TESIS DE LA UNIVERSIDAD DE ZARAGOZA

2013

147

Teresa Ubide Garralda

# The Cretaceous alkaline magmatism in northeast Iberia: igneus processes and geodynamic implications

Departamento
Ciencias de la Tierra

Director/es
Arranz Yagüe, Enrique
Lago San José, Marceliano



ISSN 2254-7606

Prensas de la Universidad
Universidad Zaragoza

Tesis Doctoral

# THE CRETACEOUS ALKALINE MAGMATISM IN NORTHEAST IBERIA: IGNEUS PROCESSES AND GEODYNAMIC IMPLICATIONS

Autor

Teresa Ubide Garralda

Director/es

Arranz Yagüe, Enrique
Lago San José, Marceliano

**UNIVERSIDAD DE ZARAGOZA**

Ciencias de la Tierra

2013

# THE CRETACEOUS ALKALINE MAGMATISM IN NORTHEAST IBERIA. IGNEOUS PROCESSES AND GEODYNAMIC IMPLICATIONS

TERESA UBIDE GARRALDA

PhD THESIS 2013

UNIVERSIDAD DE ZARAGOZA
FACULTAD DE CIENCIAS
DEPARTAMENTO DE CIENCIAS DE LA TIERRA
GRUPO DE INVESTIGACIÓN GEOTRANSFER

Supervisors
Dr. Enrique Arranz Yagüe
Dr. Marceliano Lago San José

*A mis padres*

# Contents

# Agradecimientos

Son muchas las personas que han contribuido al desarrollo de este trabajo, desde el punto de vista tanto profesional como personal, y espero que queden reflejadas (¡y no dejarme ninguna!) en este apartado.

Quiero agradecer a mis directores, los Dres. Enrique Arranz y Marceliano Lago, el haberme introducido en el fascinante mundo de la investigación en petrología ígnea, así como su apoyo y ayuda durante estos años.

Aunque no figure como codirector de esta Tesis, quiero agradecer especialmente la contribución del Dr. Carlos Galé. Como compañeros de despacho, hemos discutido juntos el enfoque y resultados obtenidos en cada una de las etapas de investigación y, además, su lado artístico me ha ayudado mucho en la presentación de resultados. ¡Gracias por todo Carlos!

También me gustaría agradecer el apoyo de Patricia Larrea, mi compañera de viaje en el doctorado y los congresos por el mundo. ¡Investigar en equipo con Carlos y Patri ha sido una experiencia increíble! Hace mucho tiempo, además, que dejaron de ser sólo mis compañeros de trabajo para convertirse en grandes amigos.

Quiero agradecer también el interés y amistad de Pablo Tierz, Laura Becerril y Tomás Sanz, que completan el auto-denominado grupo *petroZ* y que me han apoyado en innumerables ocasiones durante todo este tiempo.

Asimismo, al resto de compañeros de la cantera, arbotantes, coffee mañanero con Marta, Javi, Belén y Juan, comida en el laboratorio con Richard o Alba, cenas con Bea, Isma y Luismi, y todos aquellos con los que hemos compartido unas cenas de Navidad geniales.

I would like to give special thanks to Prof. Jan R. Wijbrans for hosting and supervising me at the *Argon Geochronology laboratory* of the VU University Amsterdam (The Netherlands) and introducing me into the $^{40}Ar/^{39}Ar$ world which I enjoyed especially during this PhD Thesis. Thank you for your time, knowledge and support Jan. I would also like to acknowledge especially the help of Roel van Elsas, who trained me on mineral separation, investigated with me the separation of amphibole from pyroxene and made work in the lab so much fun, thank you Roel!

Quisiera agradecer muy especialmente la ayuda prestada por los Dres. Carles Roqué y Lluis Pallí (Universitat de Girona) para descubrir los lamprófidos cretácicos de la Costa Brava y, concretamente, los de las boscosas zonas del interior de Girona. Sus mapas e indicaciones nos ayudaron a encontrar unas intrusiones de una riqueza petrológica y mineralógica excepcional. Gracias también a Anna Ferrer, que avisó a Carles cuando, al excavar el solar de su futura casa en Llagostera, se topó con una capa de roca negra, muy dura, que resultó ser ¡un sill de lamprófido! Sin su ayuda no hubiésemos podido describir y muestrear la sección subterránea del sill, que posteriormente volvió a quedar oculta.

Durante el trabajo de campo me gustaría destacar el apoyo incondicional de Marce y la ayuda también de Quique, Carlos, Patri, Pablo y los Dres. Andrés Gil y Óscar Pueyo (Universidad de Zaragoza). La preparación de las muestras y su estudio microscópico se llevaron a cabo en el *Servicio General de Apoyo a la Investigación-SAI* de la Universidad de Zaragoza y me gustaría destacar el trabajo de los laborantes y, en especial, el de Manolo Tricas. Gracias también a Alfredo F. Larios por su apoyo durante las interminables horas de microsonda electrónica en el *Centro Nacional de Microscopía Electrónica* de la Universidad Complutense de Madrid, así como a los Dres. José González del Tánago y David Orejana. Estoy muy agradecida a la Dra. Olga Cazalla por su ayuda e implicación en las sesiones de LA-ICP-MS en el *Centro de Instrumentación Científica-CIC* de la Universidad de Granada, así como al asesoramiento del Dr. Fernando Bea. Asimismo, agradezco al Dr. José Ignacio Gil-Ibarguchi (laboratorio *SGIker*, Universidad del País Vasco UPV/EHU) y a la Dra. Elisabeth Widom, a Dave Kuentz (*Isotope Geochemistry & Mass Spectrometry Laboratory*, Miami University, Ohio-USA) y a Patri por las determinaciones de relaciones isotópicas de Sr-Nd-Pb.

El tratamiento de los datos se realizó siguiendo metodologías clásicas pero también otras nuevas y, a este respecto, me gustaría señalar la aportación del Dr. Juan Rofes (Universidad del País Vasco UPV/EHU), quien me ayudó a comenzar en el mundo de la estadística multivariante y el análisis por componentes principales. Juntos investigamos las enormes posibilidades que podía ofrecer esta técnica, muy desarrollada en otras ramas de las Ciencias de la Tierra, al tratamiento de bases de datos geoquímicos y la interpretación de procesos magmáticos.

Gracias a mis padres, los Dres. Mª Ángeles Garralda y José Carlos Ubide, así como al Dr. Juan Zuriarrain (Universidad del País Vasco UPV/EHU) por las discusiones sobre las limitaciones cristal-químicas y termodinámicas del reparto de elementos traza entre minerales y fundidos.

La colaboración con otros grupos de investigación me ha llevado a conocer a grandes personas como la Dra. Zilda França (Universidade dos Açores) y los Dres. José López, José Barrenechea y Raúl de la Horra (CSIC y Universidad Complutense de Madrid), así como a

Belén, que conocí a raíz de su estancia con nosotros en Zaragoza y que se ha convertido en una gran amiga y un importante apoyo para mí.

Sin financiación pública, nada de lo que se refleja en esta memoria habría sido posible. Me gustaría agradecer especialmente al Gobierno Vasco la concesión de mi beca y contrato predoctorales y las ayudas adicionales para realizar las estancias en Ámsterdam. Asimismo, al Ministerio de Ciencia e Innovación por los proyectos CGL2008-06098/BTE y CGL2011-27477, necesarios para financiar la investigación. Quiero destacar también las ayudas de investigación concedidas por el Instituto de Estudios Altoaragoneses y el Instituto de Estudios Turolenses y el apoyo económico del Gobierno de Aragón al grupo de investigación *Geotransfer*, así como las numerosas bolsas de viaje para asistencia a congresos concedidas por la Universidad de Zaragoza y por los comités organizadores del Goldschmidt Conference 2012 y del Congrès des Doctorants IPGP 2013.

Dedico esta Tesis a mis padres por ser siempre mi mayor apoyo y ejemplo y porque además, han sido la mejor guía para el desarrollo de esta Tesis. Mil gracias a mi hermana, Elisa, por ser mi otra mitad, por ser genial y por animarme y apoyarme siempre.

Me considero muy afortunada de tener la familia que tengo y quiero agradecer muy especialmente a mis abuelos Carmen y Fausto, por ser increíbles y dar absolutamente todo a las personas que quieren, y a los que ya no están, Mª Asunción y Ciriaco, porque sé que esta Tesis les habría hecho una ilusión especial. Quiero agradecer también el apoyo de todos mis tíos y especialmente el de mi tía Elena que, durante este último año, ha sido mi mayor referente y acicate para terminar de escribir esta Tesis. Gracias a todos mis primos (¡y sus familias!) y, muy especialmente, a María. Y no me olvido de Conchi, que ha sido y será siempre como una hermana mayor para mí.

Todo el tiempo y experiencias que hemos vivido juntos hacen que, para mí, sean también familia Ane, Jose, Su, Katta, Roci y el resto de la *PG people*. Muchísimas gracias a todos por estar ahí, por todo, por formar parte de mi vida.

Quiero dedicar también un agradecimiento muy especial a Almu, Laura y Pilar. Por nuestra unión y amistad infinita, nuestros viajes, nuestros cafés, cenas, fiestas,… ¡un millón de gracias chicas!

También al resto de mis compañeros de promoción y especialmente a Delia, Alberto, Edu y el resto de integrantes del viaje a Islandia… Entre los que me gustaría destacar a Marian y Pablo, que hicieron que el año del Máster fuera inolvidable.

Quiero agradecer también el apoyo de Alicia y todos los de Jaca, así como de Pili y Elena, que me han animado mucho, especialmente en esta última fase. Gracias a Pilar R., por su

ánimo constante durante este tiempo. Y también quiero destacar el apoyo y afecto de José Antonio.

A Micaela, Isabel y el resto del *Cambridge team*, muchas gracias por estar ahí y por hacer, además, que un trabajo que me encanta sea aún mucho más genial.

Gracias a Ricardo, que me aportó muchísimo en una larga etapa de mi vida y particularmente al inicio de esta Tesis. También quiero agradecer el apoyo de David y todo su entorno, destacando especialmente a las Cristinas.

De las estancias de investigación en Ámsterdam me llevé, no sólo una experiencia laboral increíble, sino también unos amigos muy especiales. Placi y Nadine me acogieron en su casa con los brazos abiertos cuando aún ni me conocían. Recuerdo con mucho cariño nuestras largas conversaciones y su entusiasmo por la vida.

Tons of thanks to Anne, Kristin, Uros and Elco, because you made my stays in Amsterdam unforgettable! We became so close and had so much fun during those three months in Amsterdam and afterwards in Madrid, London, Rome, Vienna and Montreal!

Para terminar, me gustaría agradecer muy especialmente a José Manuel, por su apoyo, comprensión, cariño, ayuda, ánimos, paciencia y buen humor, que día a día me transmiten mucha paz y felicidad.

¡Gracias a todos!

Teresa

Zaragoza, 1 de octubre de 2013

# Resumen

Durante la apertura del océano Atlántico, responsable de la ruptura del supercontinente Pangea, la apertura del Golfo de Vizcaya provocó la rotación y separación de Iberia respecto de Europa. Este evento condicionó el desarrollo de un magmatismo alcalino, previo al inicio de la colisión alpina que desencadenó la elevación de la cadena pirenaica entre Iberia y Europa. Dicho magmatismo alcalino es de edad cretácica y hoy se reconoce en los Pirineos y en el margen septentrional de las Cadenas Costero Catalanas. Sin embargo, no existen, hasta la fecha, estudios completos ni comparativos de estas rocas. Esto contrasta con su enorme interés científico, pues suponen una preciada fuente de información acerca del controvertido contexto geodinámico, así como de los procesos ígneos relacionados con la generación de fundidos en el manto y su ascenso a través de la corteza.

Así, la presente Tesis Doctoral comprende la petrología, mineralogía, geoquímica y geocronología del magmatismo cretácico en todo el noreste de Iberia, incluyendo afloramientos en los Pirineos y con especial énfasis, en el margen septentrional de las Cadenas Costero Catalanas, ya que este dominio ha sido menos estudiado.

Se han obtenido nuevas edades $^{40}Ar/^{39}Ar$ que actualizan los datos previos y delimitan temporal y geográficamente la provincia ígnea. Además, la edad del magmatismo, asociado a un rifting continental, aporta nuevos argumentos a considerar para evaluar las teorías sobre la evolución geodinámica del límite Iberia-Europa, tanto respecto a la apertura del Golfo de Vizcaya como al inicio de la compresión alpina.

El estudio de la composición de las rocas en elementos mayores, elementos traza y relaciones isotópicas de Sr-Nd-Pb revela una signatura heterogénea y enriquecida del manto en este dominio, que podría haber perdurado desde el final de la orogenia varisca hasta el cuaternario.

La composición de los minerales en elementos mayores y traza, junto con las estimaciones barométricas realizadas, informan de manera muy detallada acerca del origen de las poblaciones de cristales, complejas, que se observan en las rocas, revelando procesos de recarga y mezcla de magmas en profundidad y la incorporación de cristales heredados en magmas ascendentes hacia la superficie terrestre. Estos datos permiten reconstruir la historia de los procesos que tuvieron lugar en el sistema de alimentación durante el ascenso de los magmas y su evolución en cámaras magmáticas.

En este trabajo se realiza la primera cuantificación de la influencia de cristales heredados (tipo antecristal) en la composición global de las rocas en las que se encuentran. El modelo geoquímico desarrollado muestra que la acumulación de antecristales máficos provoca modificaciones significativas en las composiciones de roca total, y esto cuestiona la interpretación tradicional de las composiciones magmáticas "primitivas", así como las ideas sobre procesos de acumulación gravitatoria de cristales y zonación composicional en cuerpos ígneos.

La aplicación, en esta tesis, de métodos matemáticos como la elaboración de modelos cuantitativos y el análisis estadístico de componentes principales al tratamiento de datos geoquímicos, es novedosa en este campo científico y abre el camino a una mejor evaluación de hipótesis petrológicas en base a datos geoquímicos completos, proporcionando una metodología de trabajo potencialmente aplicable al estudio de sistemas ígneos.

Finalmente, es importante destacar que los datos geoquímicos cobran todo su significado únicamente cuando se comprende, en detalle, la petrología de las rocas y las condiciones de equilibrio entre los minerales y el fundido que los engloba. Esto, además, lleva al cálculo, por primera vez, de un conjunto internamente consistente de coeficientes de reparto de elementos traza para clinopiroxeno y anfíbol en fundidos de tipo lamprófido alcalino (camptonita).

# Summary

During the opening of the Atlantic Ocean, which was responsible for the break-up of the Pangea supercontinent, the opening of the Bay of Biscay triggered the rotation and separation of Iberia with respect to Europe. This event conditioned the development of alkaline magmatism, prior to the onset of Alpine collision eventually leading to the formation of the Pyrenees between the Iberian and European domains. The alkaline magmatism is Cretaceous in age and is found in the Pyrenees and in the northernmost Catalonian Coastal Ranges. However there have been to date neither complete nor comparative studies of these rocks. This is in spite of their important scientific significance as a valuable source of information on what is a controversial geodynamic context, as well as on igneous processes related to melt generation in the mantle and its ascent through the crust.

Given this lack of information, the present PhD Thesis addresses the petrology, mineralogy, geochemistry and geochronology of the Cretaceous magmatism along northeast Iberia, including igneous occurrences in the Pyrenees and especially in the, less studied, northernmost Catalonian Coastal Ranges.

New $^{40}Ar/^{39}Ar$ age determinations constrain temporally and geographically previous notions about the alkaline magmatism associated to continental rifting, and provide new data to evaluate the theories about the Iberia-Europe geodynamic evolution regarding both the opening of the Bay of Biscay and the onset of Alpine compression.

The study of the major element, trace element and Sr-Nd-Pb isotope concentrations in the rocks reveals a heterogeneous and enriched mantle source signature that might have prevailed in this area from Late Variscan to Quaternary times.

The major and trace element composition of the minerals, together with calculated barometric data, inform in great detail about the origin of complex crystal populations observed in the rocks, revealing deep magma recharge and mixing processes and entrainment of inherited crystals into magma batches ascending towards the Earth's surface. This leads the way to reconstruct the history of processes taking place in the plumbing system during magma ascent and evolution in magma chambers.

The novel quantification of the influence of inherited crystals (antecrysts) on the bulk composition of the rocks they are included in, should be especially noted. It shows that

the accumulation of mafic antecrysts modifies significantly whole rock compositions, and this brings into question the traditional interpretation of “primitive” magmatic compositions, as well as notions about crystal settling processes and compositional zoning in igneous bodies.

The application in this thesis of mathematical methods such as quantitative modelling and statistical principal component analysis to the treatment of geochemical data is innovative in this field of science. It opens the way to a better evaluation of petrological hypotheses on the basis of full compositional datasets, providing a methodology potentially applicable to the study of igneous systems.

Finally, it is well recognised that geochemical data can only be fully understood when the petrology of the rocks and mineral-melt equilibrium conditions are well known. Such an in-depth analysis in this work has moreover allowed the calculation, for the first time, of a consistent partition coefficient dataset of trace elements for clinopyroxene and amphibole in alkaline lamprophyre (camptonite) melts.

*Theory guides,*
*Experiment decides*
Izaak M. Kolthoff

# 1

# Introduction

*Platja Fonda, Costa Brava*

## 1.1. Interest

The Cretaceous Era was characterised by widespread alkaline igneous activity on widely separated peri-Atlantic continental margins (Matton and Jébrak, 2009; Fig. 1.1). Magmatism concentrated in the period between 125 and 80 Ma has received the name Peri-Atlantic Alkaline Pulse (PAAP; Matton and Jébrak, 2009). In the Iberian Peninsula, it includes outcrops in southern Portugal and northern Spain (e.g., Rock, 1982; Solé et al., 2003).

Cretaceous pulses in alkaline magmatic activity were closely associated with major Atlantic tectonic events (Matton and Jébrak, 2009). In northern Spain, the opening of the Bay of Biscay (Fig. 1.1) led to the anticlockwise rotation and separation of Iberia with respect to Europe (Vissers & Meijer, 2012*a* and references therein). This was followed by the onset of Alpine collision between Iberia and Europe from the Late Cretaceous, eventually leading to the formation of the Pyrenees (Vissers & Meijer, 2012*b* and references therein).

The rifting scenario generated by the opening of the Bay of Biscay thinned the crust between the Iberian and European domains (e.g., Jammes et al., 2009). This enabled not only the ascent of alkaline magmas, but also the development of high temperature and low pressure metamorphism, hydrothermalism and mantle exhumation (Golberg et al., 1986; Lagabrielle and Bodinier, 2008; Lagabrielle et al., 2010; Montigny et al., 1986; Poujol et al., 2010; Schärer et al., 1999). Today, Cretaceous alkaline magmatism is recognised as extrusive and intrusive, mafic and felsic rocks along the Pyrenees and as isolated lamprophyre intrusions in the northern part of the Catalonian Coastal Ranges (e.g., Azambre et al., 1992; Solé et al., 2003).

In detail, this magmatism crops out in four main domains (Fig. 1.2): Basque-Cantabrian Basin in the western Pyrenees, North Pyrenean Basins, Eastern Pyrenees and northern Catalonian Coastal Ranges. In addition, there is a geographically restricted alkaline magmatism in the Central Pyrenees (Galé et al., 2000; Mey, 1968; Fig. 1.2) that could be Cretaceous on the basis of the geochemical affinity of the rocks and preliminary $^{87}Rb/^{86}Sr$ data (Galé and Arranz, 2001).

The Cretaceous alkaline magmatism in northeast Iberia has a threefold interest. Firstly, the magmatism has traditionally been related to the opening of the Bay of Biscay and allied rotation of Iberia (e.g., Montigny et al., 1986; Rock, 1982) and predates the beginning of Iberia-Europe collision (Solé et al., 2003; Vissers and Meijer, 2012*a*). Although these geodynamic events have attracted considerable interest in geoscientists, they remain poorly understood (e.g., Jammes et al., 2009; Rosenbaum et al., 2002; Vissers

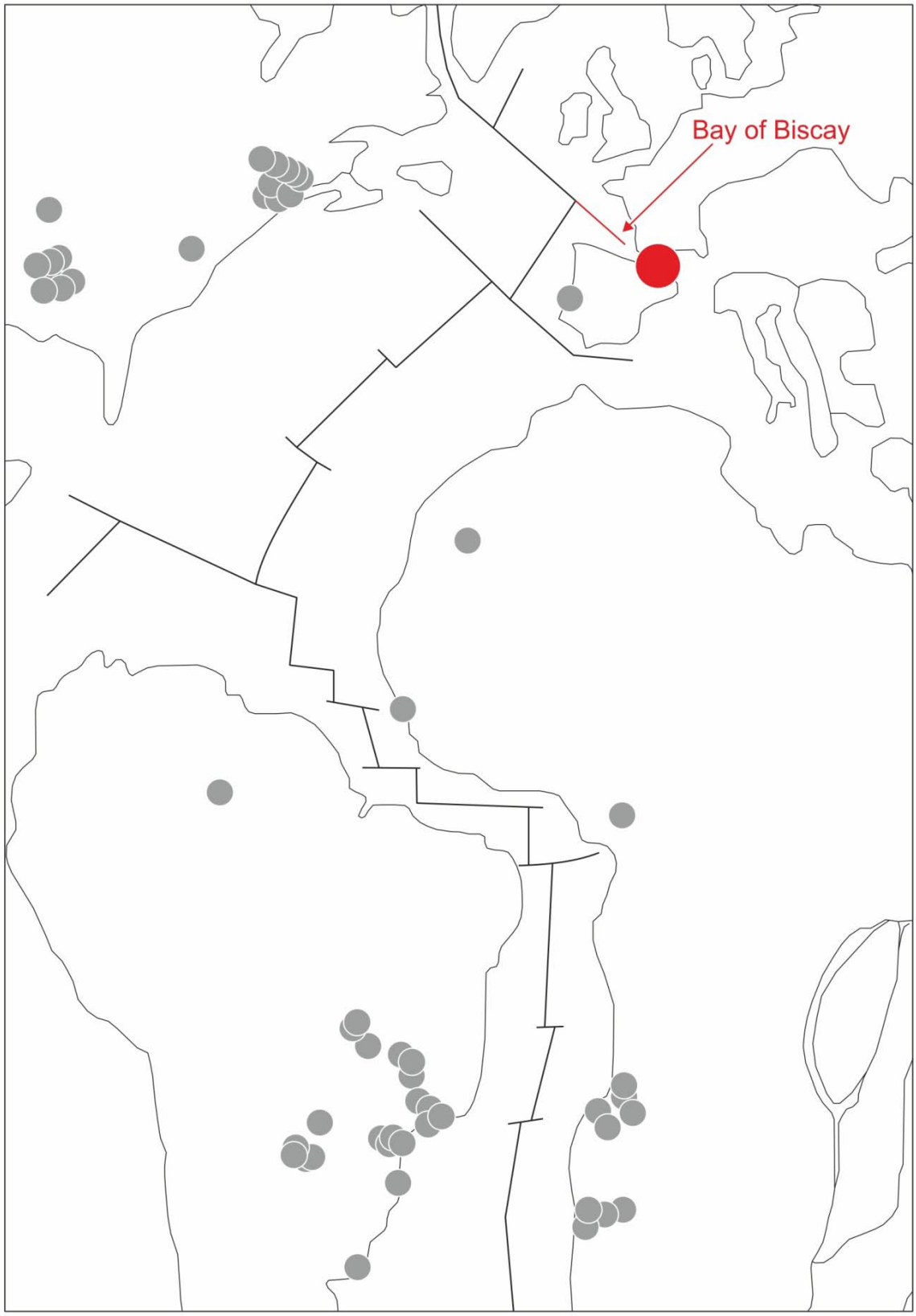


**Fig. 1.1.** Reconstruction of the peri-Atlantic realm at 100 Ma with occurrences of Cretaceous alkaline igneous rocks denoted as circles (modified after Matton and Jébrak, 2009). The magmatism studied in this PhD thesis (red circle) is related to the opening of the Bay of Biscay and predates the onset of Alpine collision between Iberia and Europe.

and Meijer, 2012*a*, 2012*b*) and the age of the magmatism could provide an alternative approach to better understand the debated Iberia-Europe kinematic evolution during the Alpine cycle.

Secondly, basic igneous rocks together with ultramafic bodies and ultramafic xenoliths suites (e.g., Bianchini et al., 2007; Downes, 2001; Galán et al., 2008) represent independent sources of information on the mantle and its evolution with geologic time. The presence of igneous typologies such as lamprophyres suggests a metasomatised mantle source, as deduced for older (e.g., Lago et al., 2004*a*; Orejana et al., 2008) and younger (e.g., Cebriá et al., 2000; Gasperini et al., 2013) magmatisms in Iberia. In the Pyrenees, ultramafic bodies are cross-cut by a late generation of amphibole-pyroxenite veins (Lagabrielle and Bodinier, 2008 and references therein) that have been interpreted as pathways for the ascent of Cretaceous alkaline magmas (Golberg et al., 1986; Bodinier et al., 1987).

Thirdly, well preserved and crystal-rich lamprophyres in the Catalonian Coastal Ranges may constitute an exceptional window into magmatic processes in alkaline igneous systems, from melt generation in the mantle to final magma emplacement in the crust, through intermediate stages of stagnation in magma chambers. Particularly, there is an increasing awareness in the igneous scientific community that large crystals (macrocrysts, megacrysts) may not be phenocrysts in equilibrium with their host glass/groundmass (e.g., Davidson et al., 2007). As highlighted in a recent review (Marsh, 2013), crystal-rich magmas when examined in any detail are messy: the crystals may have a wide range of provenances and it is only when the crystals are chemically examined in great detail that the true complexities are revealed. In many cases, large crystals are recycled from earlier stages of the magma system and have a composition either more primitive or more evolved that the liquid in which they are finally contained. They are “antecrysts”, a term introduced recently and used in a growing number of studies (Charlier et al., 2005, 2007; Davidson et al., 2007; Francalanci et al., 2012; Gill et al., 2006; Hildreth and Wilson, 2007; Jerram and Martin, 2008; Sakyi et al., 2012). This type of crystals provides a wealth of information on magma history, as they may record deep processes such as magma recharge and mixing, and their significance has just been uncorked. The entrainment of recycled crystals varies in accord to the magnitude of the eruptive power of the magma (Marsh, 2013), and may produce strong variations in whole rock compositions (e.g., Sakyi et al., 2012). In consequence, the role of these crystals needs to be carefully evaluated.

Additionally, partitioning of trace elements between minerals and melts is a longstanding issue for the interpretation of magmatic processes and there is a significant lack of data applicable to alkaline lamprophyre systems (Foley et al., 1996; Irving and Frey, 1984; Orejana et al., 2004). The Cretaceous magmatism in the Catalonian Coastal Ranges may also represent a natural laboratory for the study of trace element partitioning.

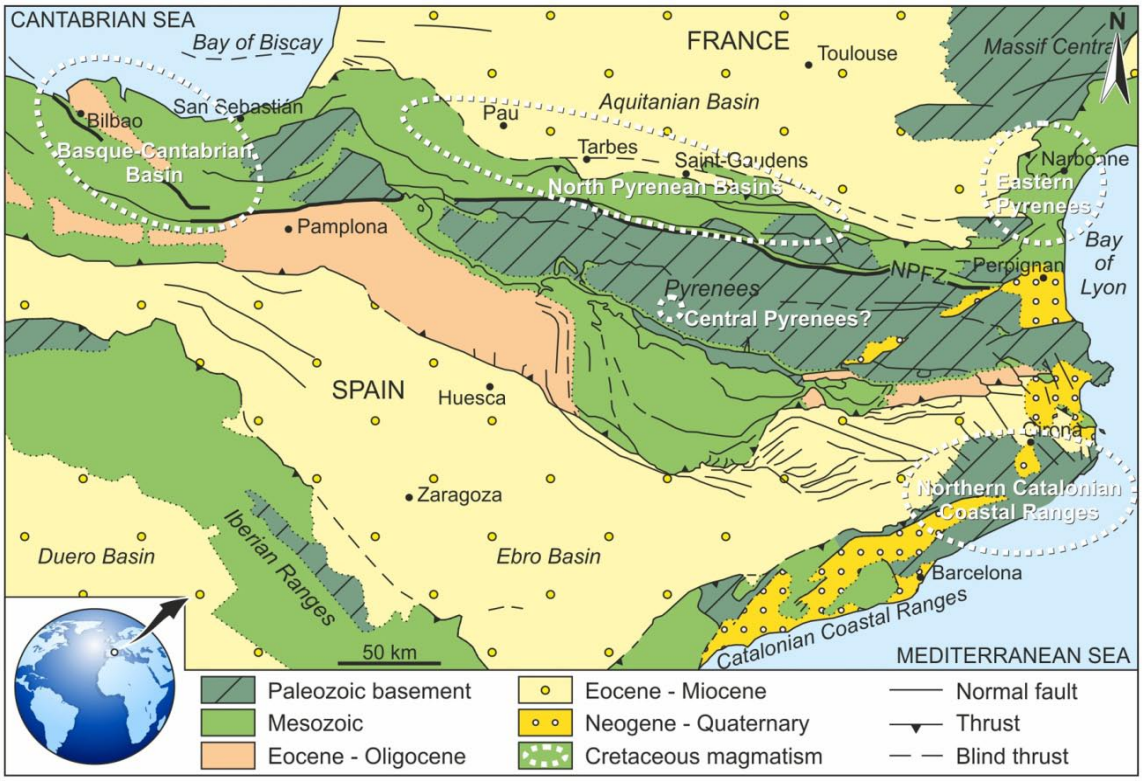


**Fig. 1.2.** Location and geological map of northeast Iberia indicating the domains where the Cretaceous magmatism crops out. From west to east: Basque-Cantabrian Basin, North Pyrenean Basins, Eastern Pyrenees and Catalonian Coastal Ranges. The alkaline magmatic occurrence in the Central Pyrenees is marked as well.

In spite of its great potential, the Cretaceous magmatism in northeast Iberia has not been investigated in depth up to now. Published studies have mainly focused on the Pyrenean realm and were carried out long ago, so geochemical analyses are relatively incomplete (Azambre et al., 1992; Cabanis and Le Fur-Balouet, 1990; Rossy et al., 1992). Volcanic series in the Basque-Cantabrian Basin have received greatest attention (Carracedo et al., 2000, 2012; Castañares et al., 1997, 2001; Castañares and Robles, 2004; Cuevas et al., 1981; Cuevas and Tubia, 1984), but these studies deal primarily with emplacement characteristics. Before the start of this PhD, the study of the Cretaceous magmatism in the Catalonian Coastal Ranges was limited to petrologic and petrographic descriptions published in the first half of the 20$^{th}$ century (Calderón et al., 1907; San Miguel Arribas, 1952; San Miguel de la Cámara, 1930, 1936; Velde and Tournon, 1970) and scarce field and preliminary compositional studies (Enrique, 2009; Gimeno, 2002). In conclusion, data available for the Cretaceous magmatism in northeast Iberia are neither complete nor comparable, and broad conclusions cannot be drawn. A detailed study of the magmatism in the Catalonian Coastal Ranges and a general study of the whole magmatic province are necessary to obtain insights into magmatic processes and the mantle source.

Regarding geochronological data, published ages were obtained long ago using the $^{40}K/^{40}Ar$ method and more rarely the $^{40}Ar/^{39}Ar$ method, and provided data with relatively high uncertainties (Golberg et al., 1986; Montigny et al., 1986; Solé et al., 2003; Vitrac-

Michard et al., 1977). A careful evaluation of published data completed with new $^{40}Ar/^{39}Ar$ ages is needed to constrain the age and chronological distribution of the magmatism and discuss the results in terms of the Iberia-Europe kinematic evolution during the Alpine cycle. Moreover, the alkaline occurrences in the Central Pyrenees need to be ascribed, or not, to the Cretaceous magmatism on the basis of reliable age data.

## 1.2. Objectives

Given the interest of the topic but the major lack of information, the present PhD project is focused on the investigation of the petrology, mineralogy, geochemistry and geochronology of the Cretaceous alkaline magmatism in northeast Iberia. This includes the study of the different domains (Fig. 1.2) with particular emphasis on the northern Catalonian Coastal Ranges, where least studies have been carried out and some occurrences may yet be unreported.

In detail, the following objectives are to be achieved:

- To determine new $^{40}Ar/^{39}Ar$ ages and evaluate previous geochronological data, in order to constrain the age distribution and geographical extent of the Cretaceous magmatism and its geodynamic implications.

- To obtain major and trace element concentrations as well as Sr-Nd-Pb isotope ratios from the whole magmatic province, in order to characterise the mantle source and its evolution from Late Variscan to Quaternary times.

- To study in great detail the Cretaceous magmatism in the northern Catalonian Coastal Ranges on the basis of the petrology, mineralogy, whole rock chemistry, mineral chemistry and barometry of already known lamprophyre intrusions as well as potential new intrusions, in order to unravel the complexities of the magmatic system from deep magma chambers to the shallow emplacement level.

- To quantitatively determine the influence of antecryst accumulation on whole rock compositions.

- To carry out statistical treatment of geochemical datasets by applying principal component analysis, to test the similarities or differences between groups of data.

- To investigate equilibrium conditions and calculate trace element partition coefficients between clinopyroxene, amphibole and alkaline lamprophyre melt.

## 1.3. Outline

This PhD dissertation is structured in thematic chapters that constitute independent but interrelated scientific contributions. After the present introductory chapter and the following chapter, devoted to the general description of the materials used and the methodologies applied, Chapters 3 to 7 are studies structured in sections such as introduction, geological context and field observations, samples and methods, results, discussion and conclusions. Finally, there is a last synthesis chapter that brings together the most relevant conclusions.

Chapters 3 to 7 are ordered from more general to more particular studies (Fig. 1.3). In order to contextualise the magmatism, Chapter 3 deals with the age of the rocks. New $^{40}Ar/^{39}Ar$ data are presented together with carefully evaluated geochronological data from previous studies. This leads to the definition of the Cretaceous magmatic province in terms of geographic and chronologic extension. Age data provide an independent approach to the much debated Iberia-Europe kinematic evolution during the Alpine cycle, including the opening of the Bay of Biscay and allied rotation of Iberia as well as the onset of Alpine compression.

Once the Cretaceous province is defined, the general petrogenetic study is presented in Chapter 4. Elemental and Sr-Nd-Pb isotope geochemistry of the Cretaceous magmatism, together with data from ultramafic exposures and older and younger magmatisms in Iberia, lead the way to a better understanding of the mantle source as well as its evolution with geologic time.

In contrast with magmatic occurrences in the Pyrenean setting, very little information has been published from the magmatism in the northern Catalonian Coastal Ranges. In this domain, Cretaceous magmas make up an alkaline lamprophyre suite rich in crystal populations and compositional zoning. Chapter 5 presents detailed petrologic, mineralogical and geochemical data that reveal a complex magma history including magma recharge and mixing processes at depth and entrainment of recycled antecrysts by ascending magmas. The variable accumulation of antecrysts in these lamprophyres makes it possible to investigate the influence of such crystals on whole rock compositions.

One of the Cretaceous lamprophyre intrusions in the Catalonian Coastal Ranges is extremely interesting because it is particularly well preserved and thin, and still shows complex compositional zoning at the macroscopic and microscopic scales. Hence, this small intrusion represents an outstanding laboratory for the study of compositional variations in igneous intrusions and compositional and barometric variations related to crystal zoning. The bulk compositional zoning across the sill is investigated in Chapter 6. This chapter includes the first quantification and statistical evaluation of the effect of

antecryst accumulation on whole rock compositions. Once macroscopic variations are controlled, Chapter 7 goes deeper into the investigation of compositional and barometric variations across single crystals.

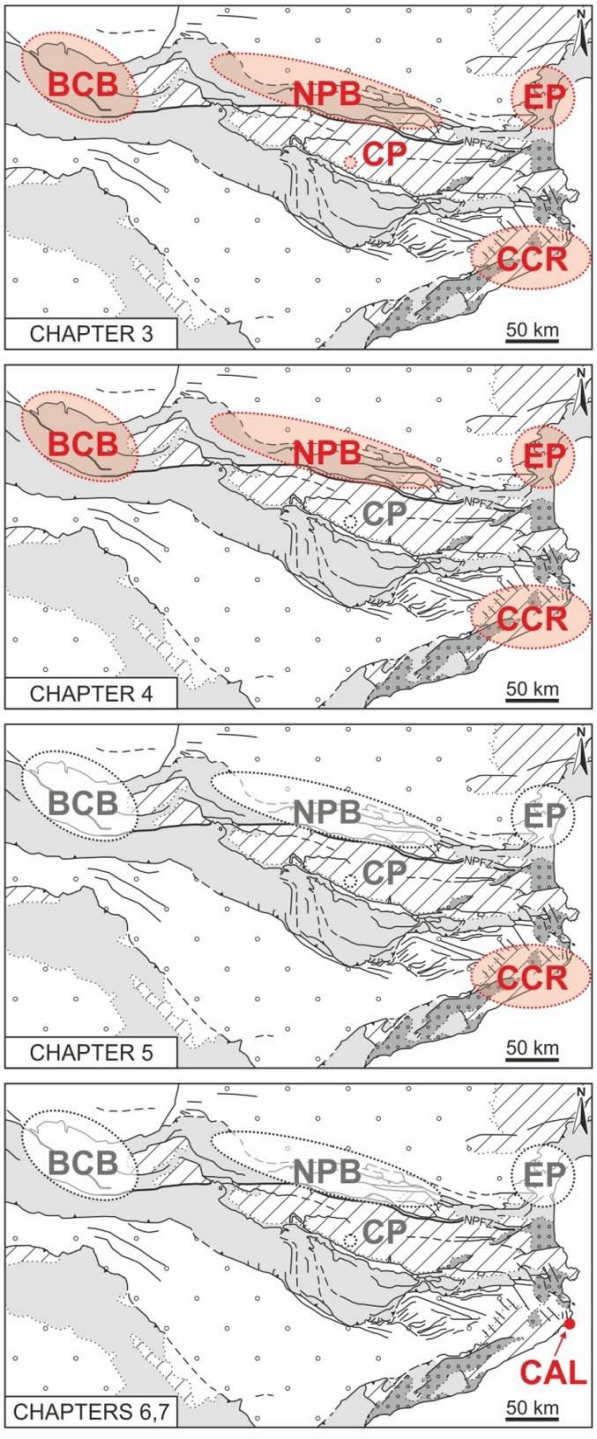


**Fig. 1.3.** Alkaline magmatic occurrences studied in each chapter of this PhD dissertation (in red). Geological map simplified from Fig. 1.2. BCB: Basque-Cantabrian Basin; NPB: North Pyrenean Basins; CP: Central Pyrenees; EP: Eastern Pyrenees; CCR: Catalonian Coastal Ranges; CAL: Calella de Palafrugell.

This leads to a detailed reconstruction of the magma plumbing system and additionally, allows for the calculation of trace element partition coefficients between clinopyroxene, amphibole and alkaline lamprophyre melt.

In some aspects, the ordering of the chapters may be reverse to the development of research. For instance, it was not until variations in whole rock chemistry and mineral chemistry in the Calella de Palafrugell lamprophyre were clear (Chapters 6 and 7) that the systematic methodologies developed for these investigations could be applied to other lamprophyres in the Catalonian Coastal Ranges, drawing broader conclusions for the whole lamprophyre suite (Chapter 5). Similarly, it was not until the magmatism in the Catalonian Coastal Ranges was investigated in depth that whole rock compositions from the whole Cretaceous magmatic province could be correctly evaluated (Chapter 4). However, the structure of this PhD dissertation is thought so that, first of all, the reader contextualises the problem with age constraints and geodynamic implications (Chapter 3) and, then, zooms (Fig. 1.3) progressively closer into what this fascinating magmatism has to offer, from regional information on the mantle (Chapter 4) to detailed information on magmatic processes (Chapters 5, 6 and 7).

# 2

# Materials and Methods

**SUMMARY**

This chapter includes a summary of the samples used as well as a general description of the methodologies applied. Field work was followed by petrological and mineralogical studies and a diversity of geochemical and geochronological analyses, for which several laboratories were used in Spain and abroad. The large amount of new data, together with a thorough review of previous studies, led to interpretations on magmatic processes, mantle sources and geodynamic conditions. During this Thesis, new sample preparation and data treatment techniques have been developed and geochemical interpretations have been closely linked to a deep understanding of the rocks.

*Punta des Mut, Costa Brava*

## 2.1. Samples

The Cretaceous magmatism in northeast Iberia crops out in several sectors across the Pyrenees and in the northern Catalonian Coastal Ranges (see Fig. 1.2). Previous studies on this magmatism were carried out with different levels of detail and the magmatism in the Catalonian Coastal Ranges was particularly unstudied. Therefore, sampling covered all the sectors but focused especially on those in the Catalonian Coastal Ranges. The samples are representative of the diversity of magmatic products, with special emphasis on mafic compositions as they are closer to the mantle source and primary magmatic processes.

A summary of samples is presented in Table 2.1. This table includes location, classification and methods applied to each sample. On the basis of macro- and microscopic examinations, the most representative and unaltered samples were selected for geochemical and geochronological analyses.

## 2.2. Methodology

### 2.2.1. Field work

After a careful review of previous studies and cartographic material, numerous field campaigns were undertaken across northeast Iberia. Field observations on the petrology, structure and emplacement characteristics of the magmatic outcrops leaded to sampling of the least altered material in each case. Field work was especially relevant in the Catalonian Coastal Ranges, given that this domain was poorly studied and several outcrops had never been reported before.

### 2.2.2. Laboratory work

This section mentions all the techniques applied during this PhD project and Chapters 3 to 7 include a detailed description of the specific samples and methods used in each study.

The samples were first studied macroscopically to select one or several areas of interest for microscopic examination. The preparation of thin sections of the samples (30 µm thickness) was ordered to the *Servicio General de Apoyo a la Investigación-SAI* of the Universidad de Zaragoza (Spain). The thin sections were studied under the petrographic microscope of the *Servicio General de Apoyo a la Investigación-SAI* of the Universidad de Zaragoza (Spain) to describe the petrography of the samples (texture, mineral assemblage, crystallisation sequence, crystal stratigraphy) and select minerals and rocks for geochemical and geochronological studies.

**Table 2.1.** Summary of samples studied and methods applied.

| Domain | Sector | Sample | Classification | Thin sections | EMP [a] | LA-ICP-MS[a] | ICP-AES ICP-MS [b] | Rb/Sr Sm/Nd Pb/Pb [b] | Ar/Ar AGE [c] |
|---|---|---|---|---|---|---|---|---|---|
| Basque-Cantabrian Basin | Bilbao | SGR | gabbro | 1 | 1 | | 1 | | 1 |
| | Guernica | FR-1 | trachybasalt | 3 | 1 | | 1 | | |
| | | FR-3 | trachybasalt | 1 | | | | | |
| | | FR-4 | trachybasalt | 1 | | | | | |
| | | FR-5 | trachybasalt | 3 | | | | | |
| | | FR-6 | trachybasalt | 2 | 1 | | | | |
| | | FR-7 | trachybasalt | 1 | | | | | |
| | | FR-8 | trachybasalt | 2 | 1 | | | | |
| | | FR-9 | trachybasalt | 1 | | | 1 | 1 | |
| | Vergara | ELG-01 | picrite | 1 | | | | | |
| | | ELG-02 | picrite | 1 | | | | | |
| | | ELG-03 | picrite | 1 | | | | | |
| | | ELG-04 | picrite | 3 | 1 | | 1 | | |
| | | ELG-05 | picrite | 1 | | | | | |
| | | ELG-06 | picrite | 1 | | | | | |
| | | ELG-07 | picrite | 1 | | | | | |
| | | ELG-08 | basalt | 1 | 1 | | 1 | 1 | |
| | | ELG-09 | basalt | 1 | 1 | | | | |
| | | MALZA-1 | trachyte | 1 | | | 1 | 1 | |
| | | MALZA-B | basalt | 3 | 1 | | 1 | | |
| | | URR | gabbro | 3 | 1 | | 2 | | |
| | | URR-2 | gabbro | 1 | | | | | |
| | | URR-3 | gabbro | 1 | 1 | | 1 | | |
| | | 8057 | basaltic trachyandesite | 1 | | | 1 | 1 | |
| | | 8058 | basaltic trachyandesite | 1 | | | | | |
| | | 8059 | basaltic trachyandesite | 2 | | | | | |
| | | 8060 | basaltic trachyandesite | 1 | | | | | |
| North Pyrenean Basins | Oloron-Sainte-Marie | AUB | monzonite | 1 | 1 | | 1 | | 1 |
| | | COG-3 | basaltic trachyandesite | 1 | | | 1 | | |
| | | COG-4 | basaltic trachyandesite | 1 | | | | | |
| | | COG-5 | monzonite | 1 | | | | | |

CP: Central Pyrenees.

Classification criteria according to Le Maitre (2002).

([a]) number of polished thin sections analysed; ([b]) number of whole rock powders analysed; ([c]) number of separated fractions analysed; ([d]) equivalent to samples 1, 2, 3, 4 and 5 in Chapters 6 and 7.

**Table 2.1** (cont)

| Domain | Sector | Sample | Classification | Thin sections | EMP [a] | LA-ICP-MS [a] | ICP-AES ICP-MS [b] | Rb/Sr Sm/Nd Pb/Pb [b] | Ar/Ar AGE [c] |
|---|---|---|---|---|---|---|---|---|---|
| Eastern Pyrenees | Corbières | CORB-1 | monchiquite | 1 | | | 1 | | |
| | | CORB-1B | monchiquite | 1 | | | | | |
| | | CORB-1C | monchiquite | 2 | | | | | |
| | | CORB-2 | monchiquite | 2 | 1 | | 1 | 1 | |
| | | CORB-3 | monchiquite | 1 | | | 1 | | |
| | | CORB-4 | monchiquite | 1 | | | | | |
| | | CORB-5 | monchiquite | 1 | | | | | |
| | | CORB-6 | monchiquite | 2 | | | 1 | | |
| | | VIN-1 | sannaite | 1 | | | 1 | | |
| | | VIN-2 | sannaite | 4 | 1 | | 1 | 1 | |
| | | VIN-3 | sannaite | 1 | | | | | |
| | | VIN-4 | sannaite | 2 | | | | | |
| | | FIT-1 | syenite | 1 | | | 1 | | |
| | | FIT-2 | syenite | 2 | 1 | | 1 | 1 | |
| | | FIT-3 | syenite | 1 | | | 1 | | |
| CP | Denuy | DEN1 | basalt | 1 | | | | | 1 |
| | | DEN2 | basalt | 4 | 4 | | | | 1 |
| Catalonian Coastal Ranges | East | AIG-04 | camptonite | 2 | 2 | | 1 | | |
| | | AIG-05 | camptonite | 1 | 1 | | 1 | 2 | |
| | | AIG-06 | camptonite | 1 | 1 | | | | |
| | | AIG-08 | camptonite | 1 | 1 | | 1 | | |
| | | AIG-12 | camptonite | 1 | | | | | |
| | | CAL-1 [d] | camptonite | 1 | 1 | 1 | 1 | | 1 |
| | | CAL-2 [d] | camptonite | 1 | 1 | | 1 | 1 | 1 |
| | | CAL-3 [d] | camptonite | 1 | 1 | 1 | 1 | | |
| | | CAL-4 [d] | camptonite | 1 | 1 | | 1 | | |
| | | CAL-5 [d] | camptonite | 1 | 1 | | 1 | | |
| | Centre | SAG-03 | camptonite | 1 | 1 | | | | |
| | | SAG-03B | camptonite | 1 | 1 | | 1 | 1 | |
| | | LLAG-01 | camptonite | 2 | 2 | | 1 | 1 | 2 |
| | West | SFB-1(r) | camptonite | 1 | 1 | | 1 | | |
| | | SFB-2(r) | camptonite | 1 | 1 | | 1 | | |
| | | SFB-3 | camptonite | 2 | 1 | | 1 | 1 | |
| | | SFB-4 | camptonite | 2 | 1 | | 1 | | |
| | | SFB-5 | camptonite | 1 | 1 | | 1 | | |
| | | SFB-6 | camptonite | 2 | 1 | 1 | 1 | 1 | 1 |

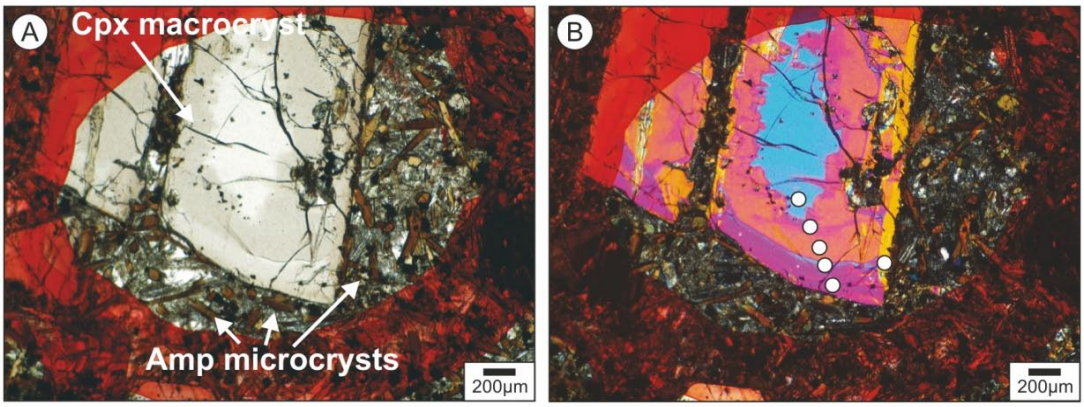


**Fig. 2.1.** Photomicrographs of a complexly zoned clinopyroxene macrocryst set in a fine-grained groundmass, which includes amphibole microcrysts. Plane-polarised (A) and cross-polarised (B) transmitted light. The area is circled in red for spot analyses. The different zones in the macrocryst (white circles) reveal different melt compositions and a complex magma history (see Chapters 5 and 7 in this volume). The rock is a Cretaceous lamprophyre from the Catalonian Coastal Ranges (sample SFB-4).

The mineral chemistry study included mineral classification and especially, a careful analysis of crystal populations. This was particularly relevant in porphyritic lamprophyres from the Catalonian Coastal Ranges, which include macrocrysts with complex zoning patterns as well as groundmass microcrysts (Fig. 2.1). Mineral compositions were analysed on polished thin sections ordered to the *Servicio General de Apoyo a la Investigación-SAI* of the University of Zaragoza (Spain). Major element concentrations were determined by electronic microprobe (EMP) at the *Centro Nacional de Microscopía Electrónica* of the Universidad Complutense de Madrid (Spain) and trace element concentrations were determined by inductively coupled plasma mass spectrometry with laser ablation (LA-ICP-MS) at the *Centro de Instrumentación Científica-CIC* of the Universidad de Granada (Spain).

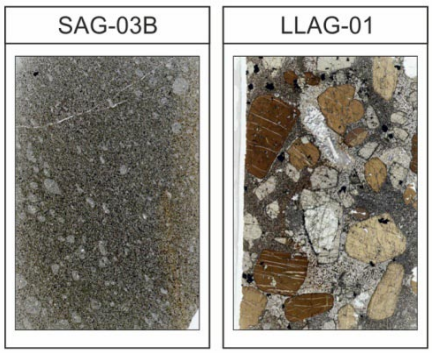


**Fig. 2.2.** Scanned thin sections of microlitic (left) and porphyritic (right) lamprophyres from the Catalonian Coastal Ranges (the width of each image is 2.5 cm). Whole rock compositions are strongly influenced by the volume fraction and type of macrocrysts (see Chapters 5 and 6 in this volume).

Samples for whole rock chemistry were carefully selected considering the nature of the rocks (primitive or evolved, porphyritic or microlitic, type of macrocryst assemblage; Fig. 2.2). Whole rock elemental and Sr-Nd-Pb isotope compositions were analysed on powders obtained by crushing, milling and splitting representative aliquots of sample at the *Servicio General de Apoyo a la Investigación-SAI* of the University of Zaragoza (Spain). Elemental analyses were ordered to the *Service d'Analyse des Roches et des Minéraux (SARM)* of the *Centre des Recherches Pétrographiques et Géochimiques* in Nancy (France). Major element concentrations were obtained by inductively coupled plasma atomic emission spectroscopy (ICP-AES), also referred to as

inductively coupled plasma optical emission spectrometry (ICP-OES). Trace element concentrations were obtained by inductively coupled plasma mass spectrometry (ICP-MS). Sr-Nd-Pb isotope analyses were ordered to the *SGIker-Geochronology and Isotopic Geochemistry* facility of the Universidad del País Vasco UPV-EHU (Spain), using thermal ionisation mass spectrometry (TIMS) and multi collector inductively coupled plasma mass spectrometry (MC-ICP-MS). Additionally, one of the samples was analysed at the *Isotope Geochemistry & Mass Spectrometry Laboratory* of the Miami University (Ohio, USA), using TIMS.

$^{40}Ar/^{39}Ar$ geochronology was carried out on mineral and groundmass separates at the *Argon Geochronology laboratory* of the VU University Amsterdam (The Netherlands). For this end, two research stays were done under the supervision of Prof. Jan R. Wijbrans. During the first research stay (January 2010), the samples were prepared for analysis by crushing, sieving and separating the fractions of interest (groundmass, amphibole or biotite, depending on the sample) using heavy liquids, Frantz® magnetic separator and Faul vibration table, as appropriate. The separated fractions were purified by HF-leaching and hand-picking under the microscope. To visually differentiate amphibole grains from clinopyronoxene, the fractions were observed over a white surface (Fig. 2.3; see details in Ubide et al., 2010*a* and Chapter 3 in this volume). The final separates were sent for irradiation to the High Flux Reactor (HFR) at Petten (The Netherlands). During the second research stay (September – December 2010), Ar isotope ratios were determined on the irradiated separates to obtain crystallisation ages. The separates were first preheated and then analysed by incremental heating with laser ablation. The gas was purified in an ultra-high vacuum extraction line and analysed with a magnetic sector noble gas mass spectrometer (see details in Chapter 3).

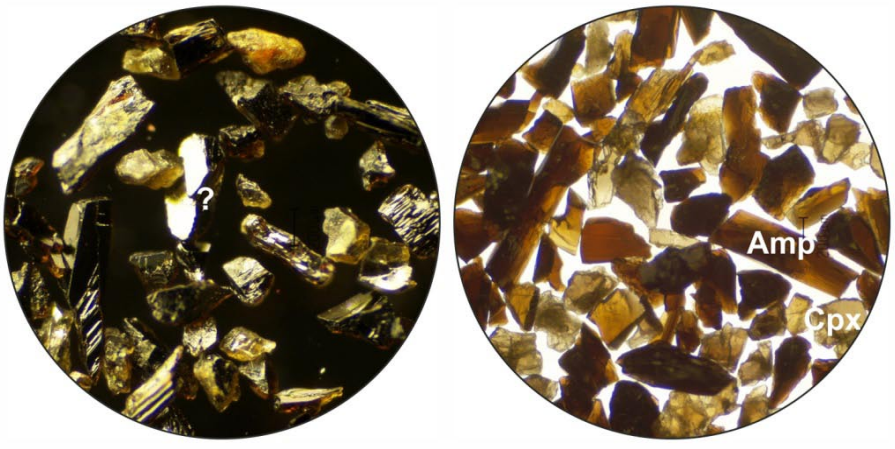


**Fig. 2.3.** Photomicrographs of a 250 – 300 µm sample fraction including clinopyroxene and amphibole. Only amphibole was of interest for $^{40}Ar/^{39}Ar$ geochronology due to its higher concentrations in $K_2O$. However, it is hard to distinguish from clinopyroxene, as they have similar physical properties and a black, shiny appearance (left image). This was solved by observing the separates over a white surface and best results were obtained adding acetone (right image): brown grains are amphibole and pale-green fragments are clinopyroxene.

### 2.2.3. Data treatment

Compositional data were mainly treated with ad-hoc built spreadsheets. Mineral compositions were recalculated to structural formulae for classification purposes. After a careful evaluation of mineral-melt equilibrium, clinopyroxene and amphibole compositions were used for thermobarometric estimates, as these minerals are unaltered and frequent in the rocks. Recalculations and normalisations were applied to whole rock compositions as appropriate, and geochemical parameters were calculated from mineral and whole rock compositions. Large geochemical datasets were constructed with new and previously published whole rock data for discussion on the mantle source.

Geochemical modelling was applied to trace element concentrations in order to quantify natural processes and therefore test petrological and mineralogical hypotheses (see Chapter 6). Specifically, the contribution and effect of macrocrysts to the whole rock composition of porphyritic rocks is quantified for the first time.

Principal component analysis was applied to trace element datasets in order to statistically test hypotheses and models (see Chapters 6 and 7). This is a method poorly exploited in igneous mineralogical-geochemical studies and provides stimulating and unbiased results. The *PAST software* (Hammer et al., 2001) was used.

Mineral-melt partition coefficients were calculated for clinopyroxene and amphibole in alkaline lamprophyre melts (see Chapter 7). They were tested by curve fitting to the lattice strain model by Blundy and Wood (1994) using the *TableCurve 2D version 5.0.1* software and compared to previous datasets in basic rocks.

Data reduction for $^{40}Ar/^{39}Ar$ geochronology (see Chapter 3) was undertaken with the *ArArCalc2.5 software package* (Koppers, 2002). Previously published age data were compiled and discussed together with new data in terms of geodynamic evolution.

### 2.2.4. Presentation of results

Petrological, mineralogical, geochemical and geochronological data was interpreted and discussed in terms of magmatic processes, mantle sources and geodynamic conditions in the context of the Iberia-Europe boundary. Some of the results have been presented in numerous national and international conferences with oral and poster presentations, several research papers in peer-reviewed journals and this Thesis dissertation.

The most relevant contributions related to the research carried out during this PhD Thesis are the summarised in the following page.

Ubide et al. (2010). A visual method for separating amphibole (kaersutite) and Mg-clinopyroxene. *Macla* 13, 217–218. Spanish Mineralogical Society Meeting (poster).

Ubide et al. (2010). The lamprophyric sub-vertical dyke swarm from Aiguablava (Catalonian Coastal Ranges): petrology and composition. *Geogaceta* 49, 83–86.

Ubide et al. (2011). Magma differentiation and recharge processes: evidence from clinopyroxene compositions (Catalonian Coastal Ranges, northeast Spain). *Geophysical Research Abstracts* 13, EGU2011-6888. EGU General Assembly (oral comm.).

Ubide et al. (2011). Subduction-related signature in late-Variscan lamprophyres from the Catalonian Coastal Ranges (northeast Spain). Abstract #1924. IUGG General Assembly (poster).

Ubide et al. (2012). Unravelling the influence of antecryst settling on the composition of a lamprophyre sill: results from geochemical modelling and principal component analysis. *Geophysical Research Abstracts* 14, EGU2012-116. EGU General Assembly (oral comm.).

Ubide et al. (2012). Enriched mantle source for the Cretaceous alkaline lamprophyres from the Catalonian Coastal Ranges (NE Spain). *Mineral. Mag.* 76 (6), 2475. Goldschmidt Conference (poster).

Ubide et al. (2012). The influence of crystal settling on the compositional zoning of a thin lamprophyre sill: A multi-method approach. *Lithos* 132-133, 37–49.

Ubide, T. (2013). New $^{40}Ar/^{39}Ar$ ages for the Cretaceous magmatism in northeast Iberia: implications for the rotation of Iberia and the onset of Pyrenean compression. Abstracts book, 61. IPGP Doctoral Students Congress Paris (invited oral comm.).

Ubide et al. (2013). Magmatic processes revealed by heterogeneous crystal populations in a lamprophyre system. *Mineral. Mag.* 77 (5), 2371. Goldschmidt Conference (poster).

Ubide et al. (under review *a*). Age of the Cretaceous alkaline magmatism in northeast Iberia: implications for the Alpine cycle in the Pyrenees. *Tectonics*.

Ubide et al. (under review *b*). Clinopyroxene and amphibole crystal populations in a lamprophyre sill: a record of magma history and a window to mineral-melt partitioning. *Lithos*.

Ubide et al. (in prep.). The relevance of crystal transfer on magma mixing processes: a case study in the Maladeta Plutonic Complex (Pyrenees, Spain). *Contrib. Mineral. Petrol*.

# 3

# Age of the Cretaceous alkaline magmatism in northeast Iberia: implications for the Alpine cycle in the Pyrenees

**SUMMARY**

New $^{40}Ar/^{39}Ar$ ages on the Cretaceous magmatism in northeast Iberia together with reviewed previous data provide new insights into geodynamic evolution in this area. The magmatism in the Pyrenees is Albian-Santonian (105-85 Ma) and developed in a tectonically unclear context after the rotation of Iberia with respect to Europe, related to the opening of the Bay of Biscay; classical kinematic models for the opening do not fit magmatic data. The magmatism in the Catalonian Coastal Ranges is Campanian (79 Ma) and could mark the onset of Alpine shortening. Finally, the magmatism in the Central Pyrenees is not Cretaceous as previously considered, but Late Triassic (232 Ma) – Early Jurassic (180 Ma) and related to rifting at the beginning of the Alpine cycle.

*Landscape near L'Aubisqué, North Pyrenean Basins*

## 3.1. Introduction

During the Cretaceous, the northeast of Iberia underwent an important geodynamic event linked to ocean-floor spreading in the North Atlantic: the V-shaped Bay of Biscay opened, leading to ca. 35º of anticlockwise rotation and consequent separation of Iberia with respect to Europe (Bullard et al., 1965; Carey, 1958; Choukroune, 1992; Gong et al., 2008; Sibuet et al., 2004; Van der Voo, 1969). This event has attracted considerable interest in geoscientists. The debate is fuelled by the fact that the main rotation of Iberia occurred between magnetic anomalies M0 and A34 (base of the Aptian and Santonian respectively, according to the recent geologic timescale by Walker and Geissman, 2009) during the Cretaceous Normal Superchron and hence, no reliable sea-floor magnetic anomalies exist to document the intermediate stages of the process (e.g., Vissers and Meijer, 2012*a*). Furthermore, there is a discrepancy between plate-kinematic models and the geological record in the Pyrenees, so the kinematics of opening of the Bay of Biscay and related Iberia rotation remains controversial (e.g., Jammes et al., 2009; Vissers and Meijer, 2012*a*).

In a recent interpretation, the entire rotation of Iberia has been confined to the Aptian period (Gong et al., 2008), and Vissers and Meijer (2012*a*) have proposed that a stagnant tectonic stage took place between the end of rotation and the beginning of Alpine collision between Iberia and Europe in the Late Cretaceous. Compression continued during the Tertiary, eventually leading to the formation of the Pyrenean chain. The exact age for the onset of shortening is however, not clear. Plate-kinematic reconstructions by Rosenbaum et al. (2002) fix the onset of Iberia-Europe convergence right at the end of the Cretaceous Normal Superchron (magnetic anomaly A34, Santonian according to Walker and Geissman, 2009). On the other hand, different geological studies in the Pyrenees report slightly different ages from the Santonian to the Maastrichtian for the onset of compression (e.g., Beaumont et al., 2000; Garrido-Megías and Ríos-Aragüés, 1972; Muñoz, 1992; Puigdefàbregas and Souquet, 1986). More recently, Vissers and Meijer (2012*a*, 2012*b*) stress that there is no geological evidence in the Pyrenees for any significant crustal shortening prior to the Campanian.

In this geodynamic scenario, magmatic activity developed at the transition between the Iberian and European domains, and is recorded today in the northeast part of the Iberian Peninsula. This magmatism crops out in several zones along the Pyrenees and as isolated intrusions in the northern part of the Catalonian Coastal Ranges. Because of its Cretaceous age and alkaline geochemical affinity, it belongs to the Late Cretaceous Alkaline Igneous Province in the Iberian Peninsula defined by Rock (1982) and it could also be ascribed to the Cretaceous Peri-Atlantic Alkaline Pulse defined by Matton and Jébrak (2009). The Cretaceous magmatism in northeast Iberia has traditionally been related to the opening of the Bay of Biscay and allied rotation of Iberia (e.g., Montigny et al., 1986;

Rock, 1982) and to the period between the end of rotation and the beginning of Iberia-Europe collision (Solé et al., 2003; Vissers and Meijer, 2012*a*). It follows that the age of the magmatism potentially gives insights on the discussed geodynamic evolution of the Iberia-Europe plate boundary during the Alpine cycle. Following this approach, Montigny et al. (1986) carried out a wide geochronological study on the Cretaceous magmatism and LP/HT metamorphism in the Pyrenees, concluding that magmatic activity took place between 110 and 85 Ma (Albian and Santonian respectively, according to the recent geologic timescale by Walker and Geissman, 2009); despite being the most complete isotopic study carried out to date, it was published more than 20 years ago and used the $^{40}K/^{40}Ar$ dating method, yielding results with relatively high uncertainties. Further isotopic dating has only been carried out in the eastern part of the Pyrenees (Golberg et al., 1986; Vitrac-Michard et al., 1977) and in the Catalonian Coastal Ranges (Solé et al., 2003) and yielded rather varying results.

The primary aim of the present study is to better constrain the age of the Cretaceous magmatism in northeast Iberia, in the light of new $^{40}Ar/^{39}Ar$ ages. Samples from the Pyrenees and the Catalonian Coastal Ranges were considered, most of them from newly studied outcrops. For certain samples, both macrocryst and groundmass separates were dated to double-check the results. The new ages, together with a careful evaluation of previous data, generate a complete geochronology for the Cretaceous magmatism in northeast Iberia. This will be used to shed some light on the longstanding debate regarding the geodynamic evolution of the area during the Alpine cycle, including the kinematics of opening of the Bay of Biscay and associated Iberia rotation, as well as the age of onset of Pyrenean shortening.

## 3.2. The Cretaceous magmatism in northeast Iberia: geological context, characterisation and previous dating results

### 3.2.1. Pyrenees

The Pyrenees belong to the long Alpine-Himalayan Tertiary collision system and formed in response to convergent motions between Iberia and Eurasia (e.g., Muñoz, 1992; Vergés et al., 2002). The Pyrenees constitute an E-W trending, bivergent mountain chain divided into several zones (Fig. 3.1; e.g., Choukroune, 1992). Due to post-orogenic erosion and exhumation (Fitzgerald et al., 1999), the Paleozoic basement crops out in the central area of the chain, in the Pyrenean Axial Zone. To the north of the Axial Zone, mainly Mesozoic uplifted sedimentary basins make up the narrow, North Pyrenean Zone. To the south, Mesozoic and Tertiary sediments make up the South Pyrenean Zone. Finally, Tertiary foreland deposits compose the Aquitanian and Ebro basins. The North

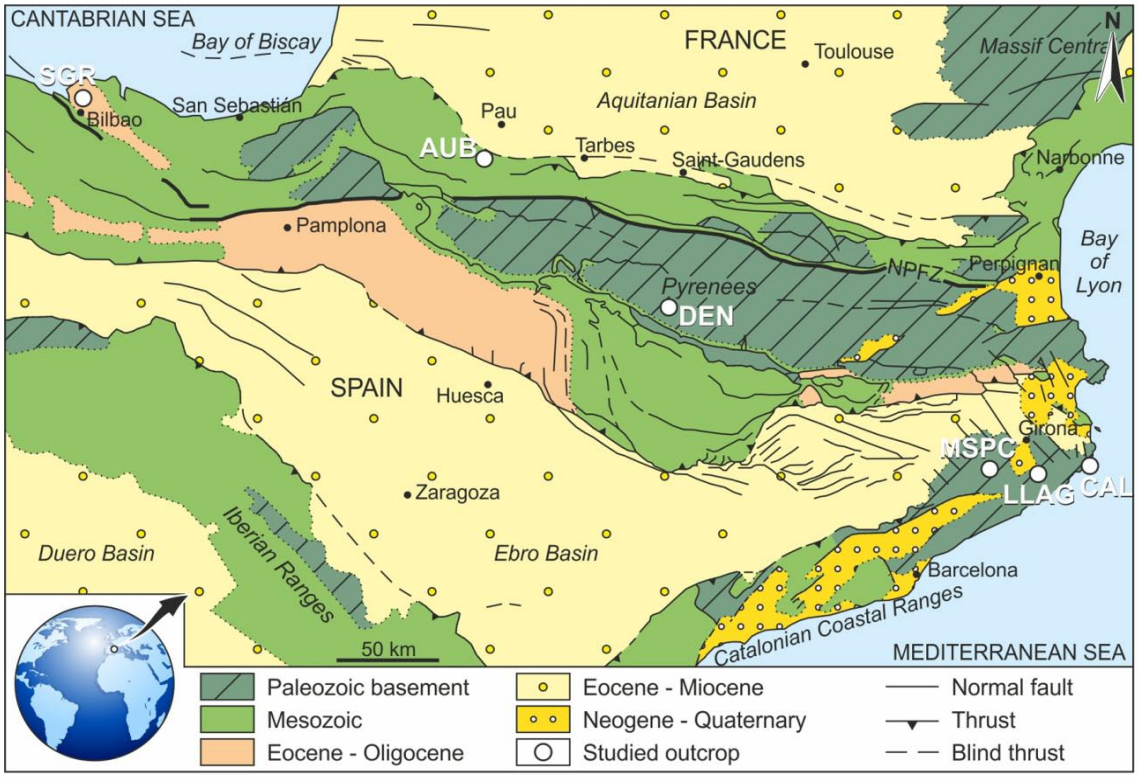


**Fig. 3.1.** Geological map of northeast Iberia (modified from Vergés et al., 2002). White circles indicate the location of the studied outcrops. SGR: San Groniz; AUB: L'Aubisqué; DEN: Denuy; CAL: Calella de Palafrugell; LLAG: Llagostera; MSPC: Monasterio de Sant Pere Cercada. NPFZ: North Pyrenean Fault Zone (thick black line).

Pyrenean Fault Zone, roughly parallel to the trend of the Pyrenees and located between the North Pyrenean Zone and the Axial Zone (Fig. 3.1), separates the Iberian and European domains (Vissers and Meijer, 2012*a*, 2012*b* and references therein).

Cretaceous magmatism crops out in several zones along the Pyrenees (Fig. 3.1), namely: the Basque-Cantabrian Basin (Bilbao-San Sebastián area in the Western Pyrenees), the North Pyrenean Basins (Pau-Tarbes area and Saint-Gaudens oil drillings) and the Eastern Pyrenees (Corbières-Fitou area, between Narbonne and Perpignan). In all the cases, the magmatism is alkaline in composition (Azambre et al., 1992; Cabanis and Le Fur-Balouet, 1990; and references therein). It was emplaced into Mesozoic sediments of the North Pyrenean Zone, to the north of the North Pyrenean Fault Zone, thus within the European domain. In the Basque-Cantabrian Basin (Western Pyrenees) the Cretaceous magmatism is widespread and comprises a great variety of rock types including acid and basic volcanic, volcanoclastic and intrusive rocks; extrusive rocks are the most common and reach more than 1000 meters in thickness (e.g., Carracedo et al., 2012). Towards the east, magmatic occurrences are progressively scarcer and no extrusive rocks are known in the Eastern Pyrenees (Corbières-Fitou area), where lamprophyre dykes, small nepheline-syenite stocks and amphibole gabbros represent the Cretaceous igneous rocks. The magmatism in the Eastern Pyrenees is silica undersaturated, in contrast with its saturated character in the rest of the chain (Azambre et al., 1992; Cabanis and Le Fur-Balouet, 1990;

Chapter 4 in this volume). These variations along the Pyrenees have been interpreted in terms of contrasting geotectonic evolution and differences in melting rate (Azambre et al., 1992; Cabanis and Le Fur-Balouet, 1990; Chapter 4) of an initially similar mantle source (Rossy et al., 1992; Chapter 4).

In the Basque-Cantabrian Basin, the oldest Cretaceous extrusive rocks are interbedded with sediments of the Early Albian (Fernández-Mendiola and García-Mondéjar, 2003 and references therein). In the interval from the Late Albian to the Santonian several extrusive stages are recognised (Castañares and Robles, 2004 and references therein). The $^{40}K/^{40}Ar$ ages obtained from the intrusive rocks in this domain range between ca. 104 and 84 Ma (Montigny et al., 1986). In the North Pyrenean Basins, extrusive rocks are dated at the Albian-Cenomanian boundary in the Pau-Tarbes area (Schoeffler et al., 1964) and have also been recognised at the Saint-Gaudens boreholes covering the Late Albian – Turonian period. Intrusive rocks cover a wide variation range between ca. 110 and 90 Ma ($^{40}K/^{40}Ar$ ages: Montigny et al., 1986). Finally, isotopic ages of the intrusive rocks in the Eastern Pyrenees range between ca. 95 and 82 Ma ($^{40}Ar/^{39}Ar$: Golberg et al., 1986; $^{40}K/^{40}Ar$: Montigny et al., 1986; $^{87}Rb/^{86}Sr$ and $^{40}Ar/^{39}Ar$: Vitrac-Michard et al., 1977).

In addition to these outcrops, Mey (1968) reported the occurrence of a small volcanoclastic basin with associated basaltic dykes in the Central Pyrenees, in the Huesca province in the Iberian domain (Fig. 3.1). Petrological studies by Galé et al. (2000) and Galé and Arranz (2001) showed the alkaline character of the basaltic lavas. This geochemical affinity may agree with a Cretaceous age. Furthermore, preliminary $^{87}Rb/^{86}Sr$ data (Galé and Arranz, 2001) suggested an age of ca. 119 Ma.

### 3.2.2. Catalonian Coastal Ranges

The Catalonian Coastal Ranges are a NE–SW trending orogen located in the northeastern Iberian plate, next to the coastline (Fig. 3.1). This orogen was constructed by intraplate propagation of the Tertiary Pyrenean compression (Juez-Larré and Andriessen, 2002, 2006; Vergés et al., 2002). The NE area of the orogen is mainly composed of Paleozoic metasediments and granitoids, whereas the SW zone basically comprises Mesozoic materials; Neogene-Quaternary deposits cover a major proportion of this mountain belt.

In contrast with the Pyrenees, the Cretaceous magmatism in the Catalonian Coastal Ranges is represented by just a few isolated, strongly alkaline lamprophyres. They intruded into the Paleozoic basement of the northern part of the ranges and crop out in three zones (Fig. 3.1; see also Chapter 5 in this volume): a western area (Pallí et al., 1993; Velde and Tournon, 1970), an eastern area on the coast (Enrique, 2009; Losantos et al., 2000, 2004; Ubide et al., 2012*a*, under review *b*) and a central area in between (see section 3.3.1 below). Similar to the rocks of the Eastern Pyrenees, these lamprophyres are

silica undersaturated (Enrique, 2009; Ubide et al., 2012*a*; Chapter 4 in this volume). They share a common mantle source (Ubide et al. 2012*b*; Chapter 4 in this volume). The available isotopic ages (Solé et al., 2003) correspond to three different lamprophyre intrusions and vary from ca. 80 to 69 Ma. Two of the intrusions were dated by $^{40}K/^{40}Ar$ and only one by $^{40}Ar/^{39}Ar$.

## 3.3. Samples and methods

### 3.3.1. Location and description of the samples

Three outcrops from the Pyrenees and three outcrops from the Catalonian Coastal Ranges were selected for dating with $^{40}Ar/^{39}Ar$ (Fig. 3.1; 3.2). A total of nine samples were analysed (Table 3.1; UTM coordinates in the electronic supplement). The Pyrenean samples comprise one sample from the Basque-Cantabrian Basin (SGR-Bt), one sample from the North Pyrenean Basins (AUB-Amp) and two samples from the Central Pyrenees (DEN1-Gr and DEN2-Gr) because it is the least accurately dated domain so far (Galé and Arranz, 2001). No samples were included from the Eastern Pyrenees, as these are the only Cretaceous alkaline rocks in the Pyrenees already dated by the $^{40}Ar/^{39}Ar$ method (Golberg et al., 1986; Vitrac-Michard et al., 1977) and most of the studies yield very consistent ages (Golberg et al., 1986; Montigny et al., 1986). In the Catalonian Ranges previous data (Solé et al., 2003) are scarcer than in the Pyrenees. Accordingly, a total of five samples (CAL-Amp, CAL-Gr, LLAG-Amp, LLAG-Gr and MSPC-Amp) were analysed from three different, geographically scattered lamprophyre intrusions that have never been dated before.

Sample SGR-Bt is a biotite separate from a gabbro located in the Basque-Cantabrian Basin near San Groniz (Bilbao). This gabbro (Fig. 3.2A) has a medium- to coarse-grained granular holocrystalline texture composed of clinopyroxene, plagioclase, opaque minerals, biotite, apatite and secondary phases including calcite, mixed phyllosilicates and analcime. Sample AUB-Amp is a separate of large amphibole crystals from a monzonite located in the North Pyrenean Basins near L'Aubisqué, south from Pau. This monzonite can be correlated to the teschenites described previously in this area (e.g., Azambre et al., 1992; Cabanis and Le Fur-Balouet, 1990). It shows a coarse-grained holocrystalline doleritic texture (Fig. 3.2B), defined by up to cm-sized crystals of feldspars, brown amphibole (kaersutite), which sometimes show green rims, clinopyroxene and opaque minerals with associated biotite; the intergranular spaces are occupied by fine-grained crystals of prehnite, chlorite, analcime and accessory epidote, green amphibole, apatite, acicular feldspars, opaque minerals and titanite. Samples DEN1-Gr and DEN2-Gr are groundmass separates from two basaltic dykes located in the Central Pyrenees near Denuy (Huesca).

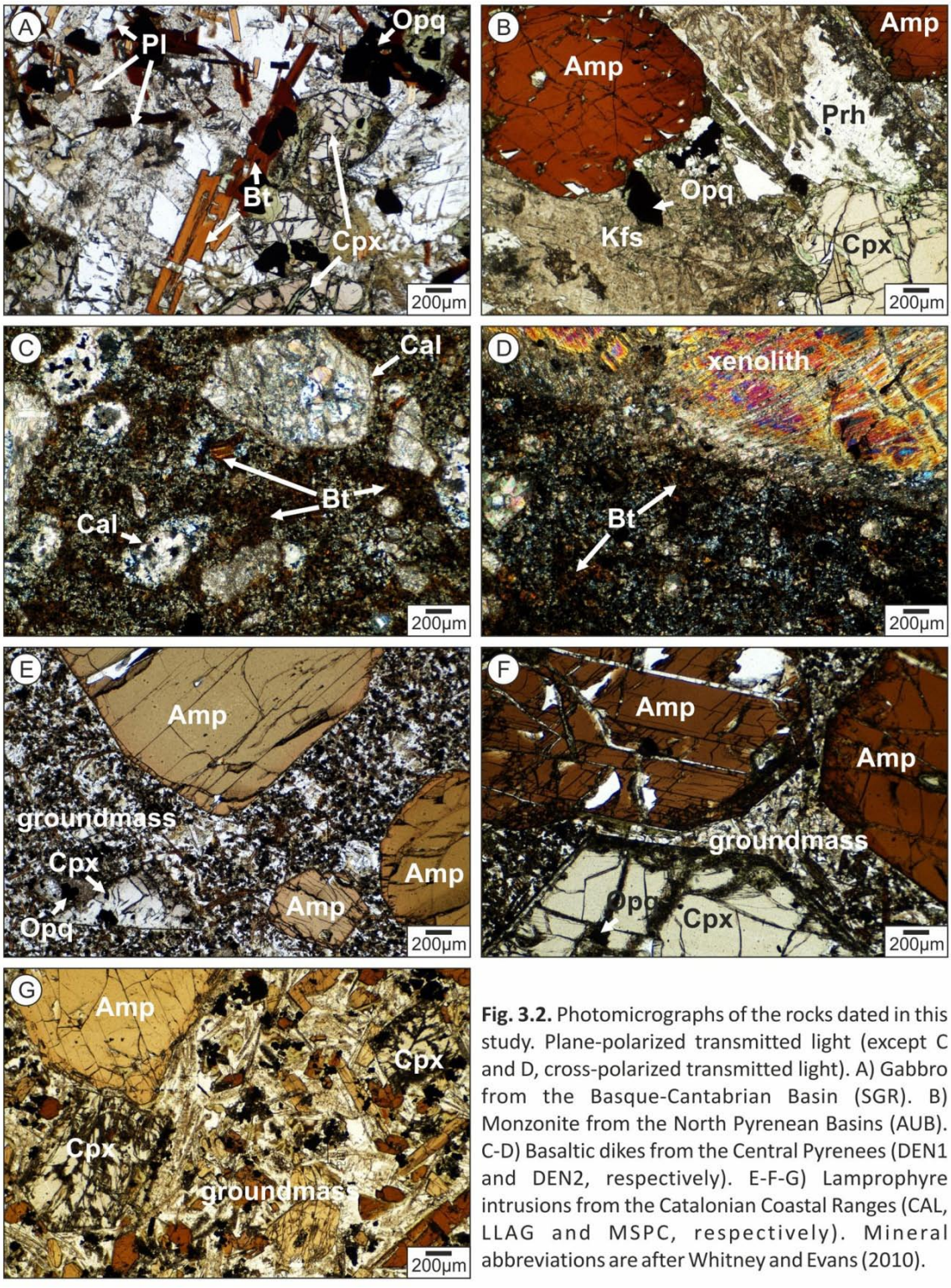


**Fig. 3.2.** Photomicrographs of the rocks dated in this study. Plane-polarized transmitted light (except C and D, cross-polarized transmitted light). A) Gabbro from the Basque-Cantabrian Basin (SGR). B) Monzonite from the North Pyrenean Basins (AUB). C-D) Basaltic dikes from the Central Pyrenees (DEN1 and DEN2, respectively). E-F-G) Lamprophyre intrusions from the Catalonian Coastal Ranges (CAL, LLAG and MSPC, respectively). Mineral abbreviations are after Whitney and Evans (2010).

These basalts (Fig. 3.2C, 3.2D) are highly vesicular fine-grained hypocrystalline porphyritic rocks, where the vesicles are filled with calcite. They carry clinopyroxene, spinel and apatite xenocrysts and spinel peridotite xenoliths. The groundmass contains plagioclase, biotite, opaque minerals, clinopyroxene, minor amounts of altered glass and accessory apatite.

**Table 3.1.** Summary of $^{40}Ar/^{39}Ar$ data; preferred ages are marked in bold. Full data tables are available in electronic format. Bt: biotite; Amp-M: amphibole macrocryst; Gr: groundmass; GAB: gabbro; MNZ: monzonite; BAS: basalt; LAMP: lamprophyre.

| Geological setting | Sample | Separated phase | Rock type | Plateau age | ±2σ | MSWD | %39Ar, n steps | Inverse isochron age | ±2σ | MSWD | K/Ca | ±2σ |
|---|---|---|---|---|---|---|---|---|---|---|---|---|
| Pyrenees | SGR-Bt | Bt | GAB | 104.82 | ±0.66 | 7.64 | 65.09 | **101.39** | **±1.24** | **3.21** | 5.602 | ±1.824 |
| | | | | | ±0.63% | | 8 | | **±1.23%** | | | |
| | AUB-Amp | Amp-M | MNZ | **102.63** | **±0.75** | **2.06** | 99.78 | 102.77 | ±0.63 | 2.29 | 0.082 | ±0.005 |
| | | | | | **±0.73%** | | 8 | | ±0.61% | | | |
| | DEN1-Gr | Gr | BAS | **231.83** | **±5.22** | **2.31** | 62.59 | 236.27 | ±5.74 | 2.45 | 0.067 | ±0.030 |
| | | | | | **±2.25%** | | 5 | | ±2.43% | | | |
| | DEN2-Gr | Gr | BAS | **179.68** | **±1.39** | **1.32** | 53.23 | 180.65 | ±1.79 | 1.62 | 0.170 | ±0.018 |
| | | | | | **±0.78%** | | 4 | | ±0.99% | | | |
| Catalonian Coastal Ranges | CAL-Gr | Gr | LAMP | 80.73 | ±1.28 | 2.43 | 74.12 | 79.07 | ±1.77 | 2.40 | 0.454 | ±0.048 |
| | | | | | ±1.58% | | 7 | | ±2.23% | | | |
| | CAL-Amp | Amp-M | | 80.37 | ±1.39 | 37.44 | 88.70 | **78.98** | **±0.50** | **2.34** | 0.130 | ±0.007 |
| | | | | | ±1.73% | | 3 | | **±0.63%** | | | |
| | LLAG-Gr | Gr | LAMP | 80.42 | ±0.79 | 2.00 | 64.30 | **79.20** | **±0.81** | **1.58** | 0.134 | ±0.017 |
| | | | | | ±0.98% | | 11 | | **±1.02%** | | | |
| | LLAG-Amp | Amp-M | | 78.06 | ±0.66 | 7.26 | 93.46 | 77.39 | ±0.86 | 7.57 | 0.128 | ±0.007 |
| | | | | | ±0.84% | | 3 | | ±1.12% | | | |
| | MSPC-Amp | Amp-M | LAMP | 79.53 | ±0.94 | 16.81 | 99.50 | **78.21** | **±0.45** | **1.63** | 0.111 | ±0.004 |
| | | | | | ±1.18% | | 6 | | **±0.58%** | | | |

The Catalonian Coastal Ranges lamprophyres are subvolcanic sills located in the province of Girona (Chapter 5). One of the selected sills is located near Calella de Palafrugell (see Chapters 6 and 7 and Ubide et al., 2012*a* for a full petrological and geochemical characterisation of this intrusion). The second one is located in Llagostera and is reported here for the first time; although there are a few meters of exposure, a less weathered underground section was studied and sampled during an excavation in the neighbouring plot, undertaken for building purposes. The third intrusion is located in the area between Santa Coloma de Farners and Sant Feliu de Buixalleu, near the Monasterio de Sant Pere Cercada (Pallí et al., 1993). The three lamprophyres are classified as camptonites and share similar petrographical features (Fig. 3.2E, 3.2F, 3.2G). They are also very similar to some of the lamprophyres dated by Solé et al. (2003). These rocks are holo- or hypo-crystalline, porphyritic due to the presence of mm- to cm-sized crystals (macrocrysts and minor megacrysts) of brown amphibole (kaersutite), clinopyroxene, opaque minerals and pseudomorphosed olivine. The groundmass is fine-grained, especially at the chilled margins of the intrusions where it gets almost aphyric and rich in vesicles. The groundmass is mainly composed of plagioclase, brown amphibole (kaersutite), opaque minerals, acicular apatite and recrystallised glass (where present). In the lamprophyre

from Llagostera there are evolved patches of groundmass that show K-rich, Ca-poor feldspars and lower volume fractions of mafic minerals. Large amphibole crystals were separated for dating from the three lamprophyres (samples CAL-Amp, LLAG-Amp and MSPC-Amp). These crystals display homogeneous cores in all the cases, slightly rounded by magmatic corrosion and overgrown by subidiomorphic rims (Fig. 3.2E, 3.2F, 3.2G). The groundmass of the lamprophyres from Calella de Palafrugell and Llagostera is especially fine-grained (Fig. 3.2E, 3.2F) and in these cases groundmass was separated as well for dating experiments (samples CAL-Gr and LLAG-Gr).

### 3.3.2. $^{40}Ar/^{39}Ar$ methodology

The selected phases (groundmass, amphibole or biotite) were separated at the mineral separation laboratory of VU University Amsterdam. Groundmass and amphibole were previously analysed in order to assure high potassium contents: $K_2O$ varies from 0.54 to 2.27 wt. % in groundmass samples –whole rock analyses- and from 1.21 to 2.07 wt. % in amphibole crystals –spot analyses- (authors' unpublished data). Alteration zones in bulk samples were removed by sawing, and the remaining materials were crushed and sieved to select the 400-500 μm fractions, which were washed with demineralised water. The LOC-50 (Liquid Overflow Centrifuge model-50; IJlst, 1973) was used for heavy liquid separations. Heavy liquids were Diiodomethane diluted with 1.2Dichlorobenzene. The Frantz® separator was used for magnetic separations. A Faul vibration table was also used when separating biotite. Subsequently, all samples were purified by handpicking under the microscope. Because amphibole and clinopyroxene have very similar physical and optical properties, a method was developed to exclude clinopyroxene grains from amphibole separates (Ubide et al., 2010*a*). The method relies on the different colour of these minerals under transmitted light: mineral separates were observed under the microscope using a transparent tray over a white surface, so that the thinnest rims of the grains revealed the colour of the mineral under transmitted light; best results were obtained adding acetone to the studied fraction, as refraction of light inside the liquid helped transmitting the light (Ubide et al., 2010*a*). Finally, the samples were cleaned in an ultrasonic bath with demineralised water. Groundmass and amphibole samples were additionally leached with HF (5 %, 10 minutes) to remove alteration from groundmass and overgrowths from amphibole crystals, and cleaned again. A summary of the mineral separation methods applied to each sample is presented in Table 3.2.

For irradiation, each sample was wrapped in an 8 mm diameter Al-foil package. About 30 mg of sample were used for biotite, ca. 50 mg for amphibole and ca. 60 mg for groundmass. Sample packages and 8-10 mg aliquots of laboratory standard sanidine DRA (25.42 Ma, calibrated following Kuiper et al., 2008) wrapped in Cu-foil were sealed in a 9 mm diameter ID quartz vial, with one standard package loaded at the top and bottom

**Table 3.2.** Separated fractions for $^{40}Ar/^{39}Ar$ analyses and mineral separation methods applied.

| Sample | Rock sample | Separated phase | Faultabel | Heavy liquids (g/cm$^3$) | Franz magnet (mA) | Sieve (μm) | Hand-picking (g) | Leaching HF | Final weight (mg) |
|---|---|---|---|---|---|---|---|---|---|
| SGR-Bt | SGR | Biotite | Yes (P) | >2.9 | 200-400 | 400-500 | 0.083 | No | ~ 30 |
| AUB-Amp | AUB | Amphibole | No | 3.05-3.3 | 410-480 | 400-500 | 0.119 | Yes | ~ 50 |
| DEN1-Gr | DEN1 | Groundmass | No | 2.9-3.05 | | 400-500 | 0.195 | Yes | ~ 60 |
| DEN2-Gr | DEN2 | Groundmass | No | 2.9- 3.05 | magnetic | 400-500 | 0.167 | Yes | ~ 60 |
| CAL-Gr | CAL-1 | Groundmass | No | 2.76 -2.9 | | 400-500 | 0.203 | Yes | ~ 60 |
| CAL-Amp | CAL-2 | Amphibole | No | 3.2-3.3 | 410-500 | 400-500 | 0.127 | Yes | ~ 50 |
| LLAG-Gr | LLAG-01 | Groundmass | No | 2.8-2.9 | | 400-500 | 0.184 | Yes | ~ 60 |
| LLAG-Amp | LLAG-01 | Amphibole | No | 3.2-3.3 | 400-500 | 400-500 | 0.115 | Yes | ~ 50 |
| MSPC-Amp | SFB-6 | Amphibole | No | 3.2-3.3 | 440-525 | 400-500 | 0.162 | Yes | ~ 50 |

positions and between every 4 sample packages. The quartz vial was sealed in a standard Al-irradiation-capsule and irradiated for 20 hrs in a Cd-lined rotating facility (RODEO) at the NRG-Petten HFR facility in The Netherlands.

$^{40}Ar/^{39}Ar$ analyses were carried out at the geochronology laboratory of VU University Amsterdam. The experiments were undertaken on multigrain samples, ca. 9 months after their irradiation, allowing for the decay of $^{37}Ar$ in Ca-rich samples (groundmass and amphibole). The samples were loaded in 6 mm wide, 3 mm deep holes of 60 mm diameter copper discs, with 21 holes per disc (half of the irradiated material was loaded per sample). The standards were loaded in 3 mm wide, 6 mm deep holes of a 185 holes copper disc (2-3 grains per hole and 7 replicates per standard). The samples and the standards were preheated to ca. 200 ºC to remove undesirable atmospheric argon. After this preheating step, they were placed in an ultrahigh vacuum extraction line. A $CO_2$ laser heating system was used for all the experiments; single fusion was applied to the standards and incremental heating to the samples. Positioning of the laser beam was achieved using an analogue Raylease scanhead fitted with a dual mirror system for X-Y adjustment and a ZnS 300 mm focusing lens. The beam delivery system achieved ca. 300 μm at the focal point and for the samples the beam was diffused in the y-direction with a 200 Hz frequency triangular current causing a +1 and -1 mm beam deflection. To ensure even heating of all the grains, the beam was applied in circles increasing in diameter for the standards and in a raster pattern for the samples. The gas was analysed isotopically with a Mass Analyzer Products LTD 215-50 noble gas mass spectrometer. Beam intensities of Ar isotopes were measured in a magnet field controlled peak-jumping mode over the mass range 40–36 on a secondary electron multiplier using switchable amplifier resistors with relative gains of $5x10^2$, 5x10 and 5 with respect to the Faraday collector ($10^{11}$ Ω resistor on the Faraday collector amplifier). For data collection, the mass spectrometer is operated with a modified version of standard MAP software. System blanks were measured every 2 (biotite) or 4 (groundmass and amphibole) sample measurements, and

at the beginning and the end of each step. The total system blanks were in the range of $6x10^{-2}$ – $9x10^{-1}$ volts for mass 40, $5x10^{-5}$ – $6x10^{-3}$ volts for mass 39, $8x10^{-6}$ – $7x10^{-4}$ volts for mass 38, $1x10^{-5}$ – $2x10^{-4}$ volts for mass 37 and $2x10^{-4}$ – $4x10^{-3}$ volts for mass 36. Mass discrimination (ca. 1.002-1.010 per atomic mass unit and 1.0045 for the main series of experiments) was monitored by frequent analysis of $^{40}Ar/^{36}Ar$ air pipette aliquots.

Data reduction was performed with the originally in-house developed ArArCalc2.5 software package (Koppers, 2002) (http://earthref.org/tools/ararcalc/). Each analysis was corrected for mass discrimination; system blanks were negligible compared to sample signals (often better than a factor of per mil). The irradiation parameter J for each sample was determined by interpolation using a second-order polynomial fitting between the individually measured standards. For the decay constants and the abundance of $^{40}K$ the values recommended by the IUGS Subcommission on Geochronology (Steiger and Jäger, 1977) were used.

## 3.4. Results

A summary of $^{40}Ar/^{39}Ar$ incremental heating results is presented in Table 3.1. Full data tables can be found in the electronic supplement, where the results are reported following recommendations by Renne et al. (2009). Age spectra, K/Ca spectra and inverse isochron plots are presented in Figs. 3.3 to 3.7, with uncertainties quoted at 2σ.

The experiments showed good, consistent results with age calculations that in most cases meet commonly accepted reliability criteria (McDougall and Harrison, 1999). Several age spectra showed elevated ages in the initial steps which may either point to loosely bound excess $^{40}Ar$ (some amphibole separates) or, alternatively, to recoil loss of $^{39}Ar$ from fine grained alteration phases (some groundmass separates) (Koppers et al., 2000; Wijbrans et al., 2007). The first steps were not considered in the age calculations if they contained abundant atmospheric argon, excess argon, were affected by recoil loss of $^{39}Ar$ or presented large uncertainties. The last steps were not considered in the age calculations if they revealed extraneous (excess or inherited) argon. Always three or more concordant, contiguous, high temperature steps were selected, representing more than 50 % of the $^{39}Ar$ released.

If the $^{40}Ar/^{36}Ar$ intercept for the trapped argon derived from the isochron treatment of the data was not significantly different from the atmospheric ratio of 295.5, excess argon was ruled out. If excess argon was detected (biotite and some amphibole separates), the inverse isochron age was preferred over the plateau age (e.g., McDougall and Harrison, 1999). If not (groundmass separates and sample AUB-Amp), the preferred age was

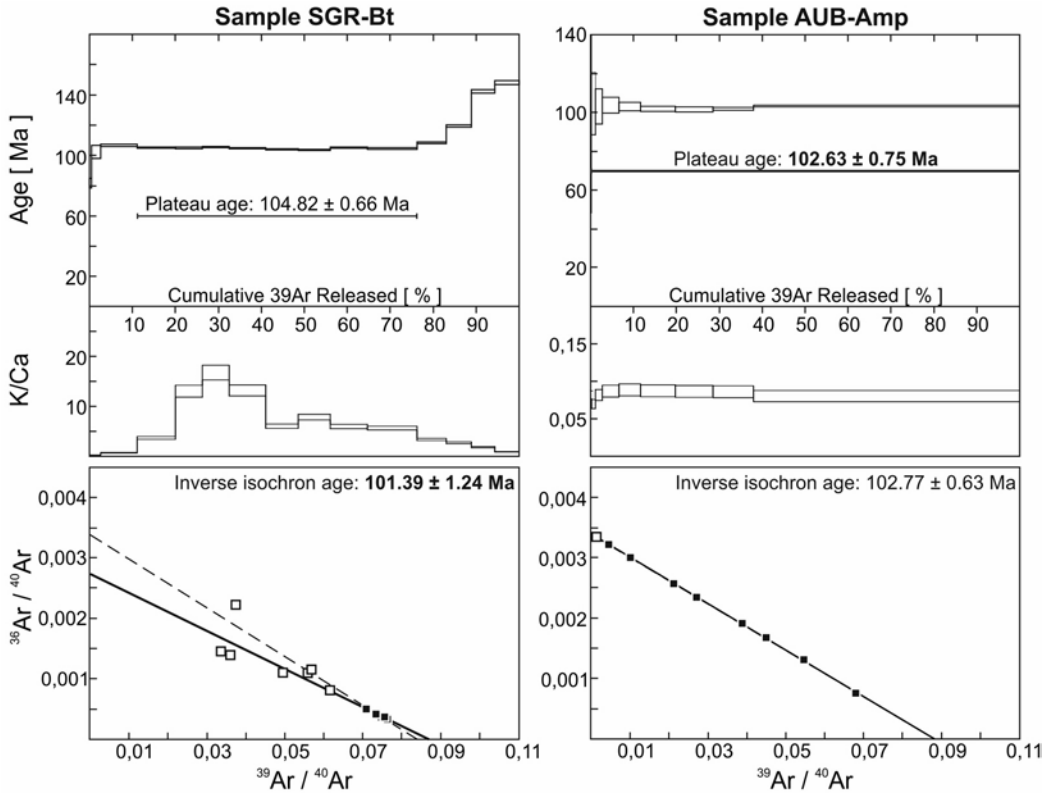


**Fig. 3.3.** $^{40}Ar/^{39}Ar$ incremental heating results for samples SGR-Bt and AUB-Amp, presented in age and K/Ca spectra and inverse isochron plots. In the age and K/Ca spectra, the thickness of the steps reflects the associated uncertainty; the horizontal line represents the plateau. In the inverse isochron diagrams, the dashed line represents the ideal atmospheric-radiogenic mixing line, whereas the solid line represents the inverse isochron calculated with the plateau defining steps (black squares); square size includes uncertainty. The preferred crystallization age is marked in bold and graphically with a thicker line.

chosen according to the mean squares of weighted deviates (MSWD) values, which measure the extent to which the scatter of data can be explained by analytical uncertainty.

Preferred crystallisation ages (plateau or inverse isochron ages) are marked in bold in Table 3.1 and Figs. 3.3 to 3.7. All preferred ages show MSWD values below the cut-off value of 2.5 (O´Connor et al., 2007) excepting sample SGR-Bt, which nevertheless presents an acceptable inverse isochron age.

From the amounts of $^{39}Ar$ and $^{37}Ar$ released during the experiments some information may be obtained on the chemical composition of the mineral phases contributing to the spectrum (Wijbrans et al., 2007). This effect is shown in the K/Ca plots (Figs. 3.3 to 3.7). The variation in K/Ca is never larger than one order of magnitude, highlighting the purity of the separates. Meanwhile, the radiogenic component of the argon in the selected steps ranges from less than 10 % to almost 100 %. It is generally very high for biotite and amphibole separates and rather low for groundmass separates, although this is not reflected in larger analytical uncertainties in the groundmass experiments.

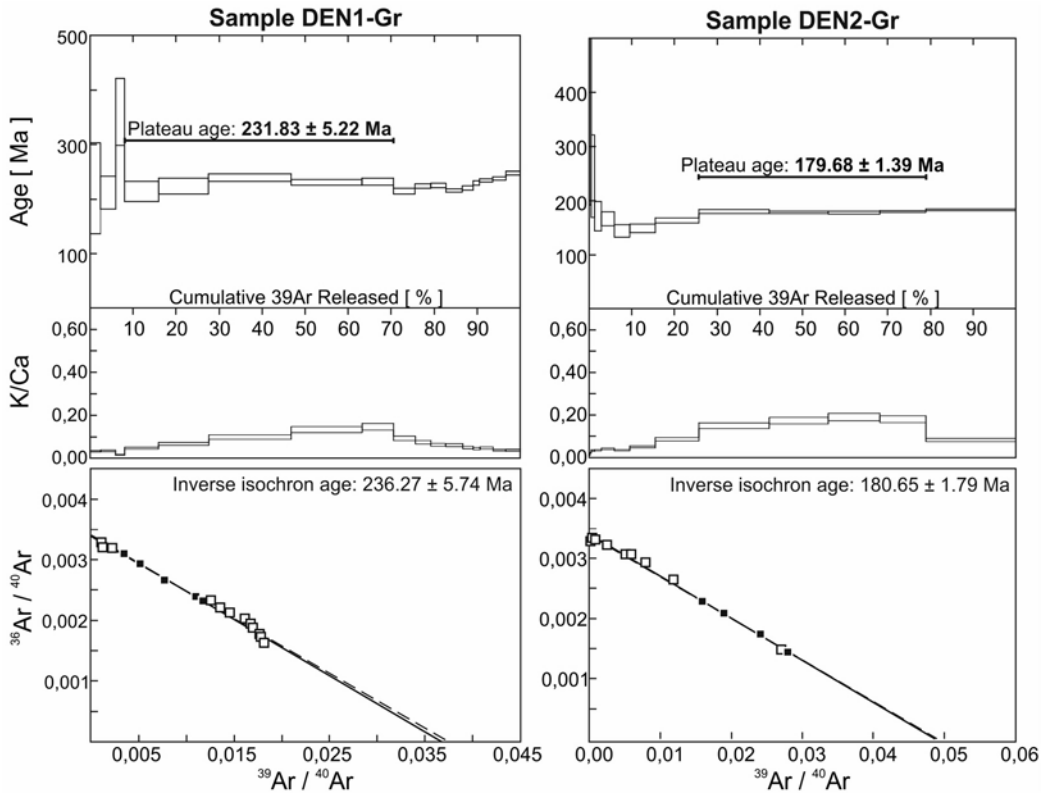


**Fig. 3.4.** $^{40}Ar/^{39}Ar$ incremental heating results for samples DEN1-Gr and DEN2-Gr. Explanation is as in Fig. 3.3.

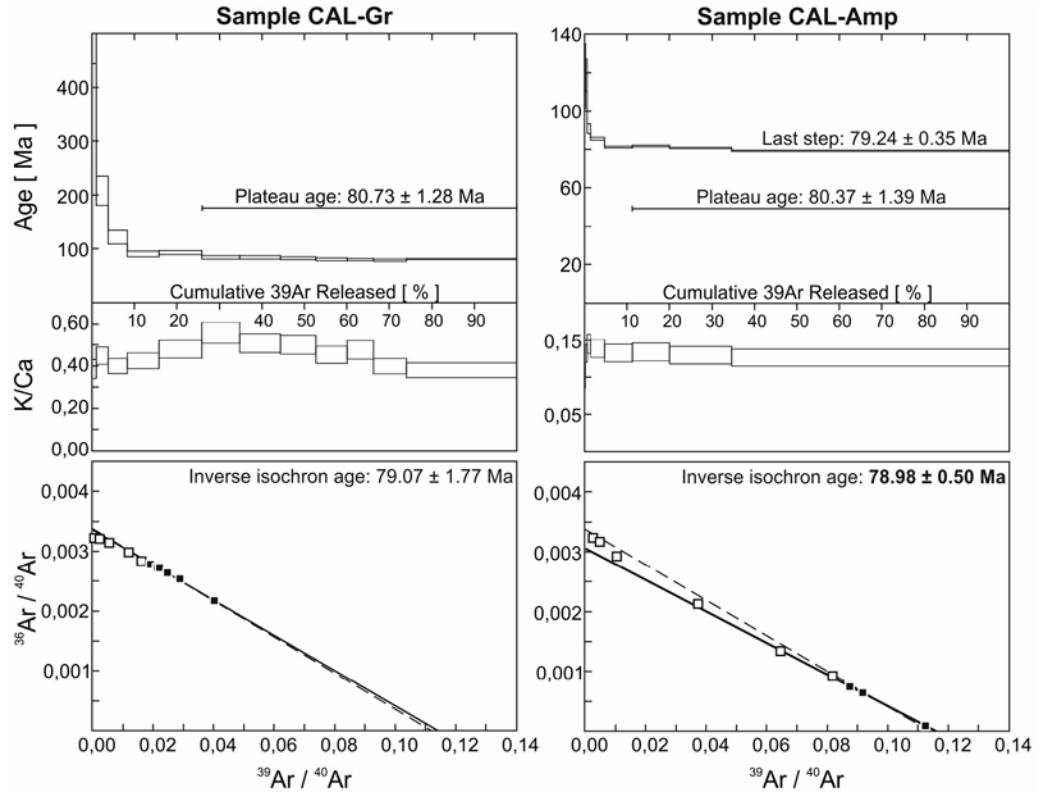


**Fig. 3.5.** $^{40}Ar/^{39}Ar$ incremental heating results for samples CAL-Gr and CAL-Amp, which represent different separates from the same lamprophyre. Explanation is as in Fig. 3.3. For the amphibole experiment, the age of the last step is included in the age spectrum.

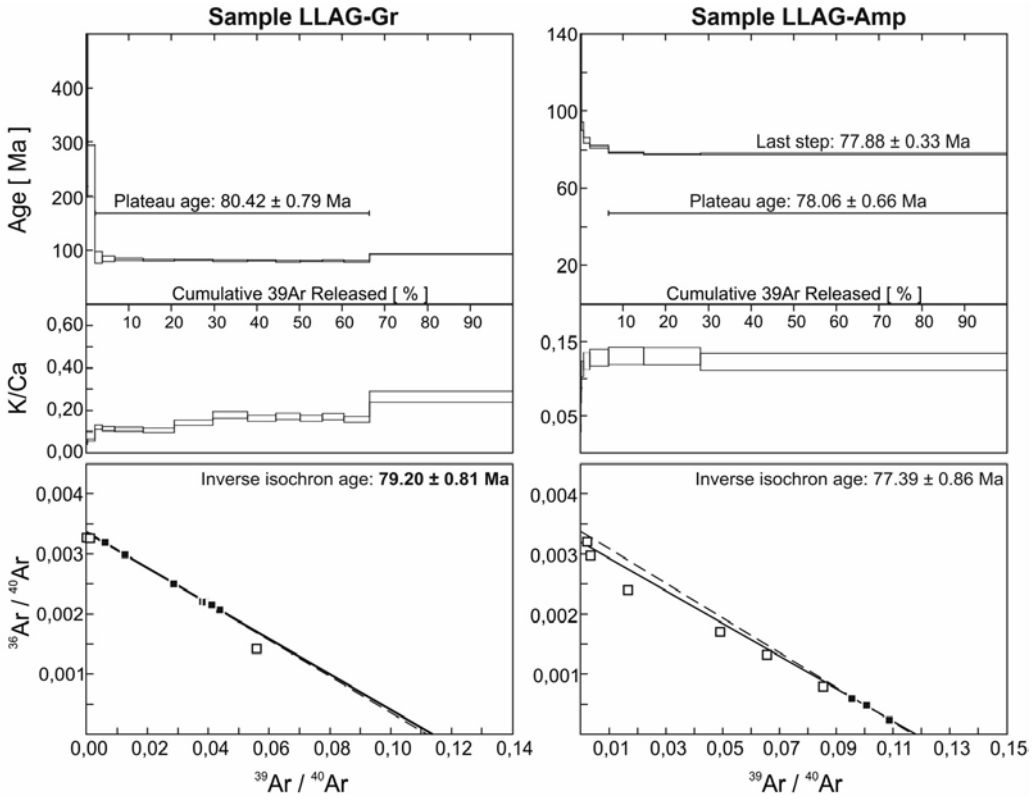


**Fig. 3.6.** $^{40}Ar/^{39}Ar$ incremental heating results for samples LLAG-Gr and LLAG-Amp, which represent different separates from the same lamprophyre. Explanation is as in Fig. 3.3. For the amphibole experiment, the age of the last step is included in the age spectrum.

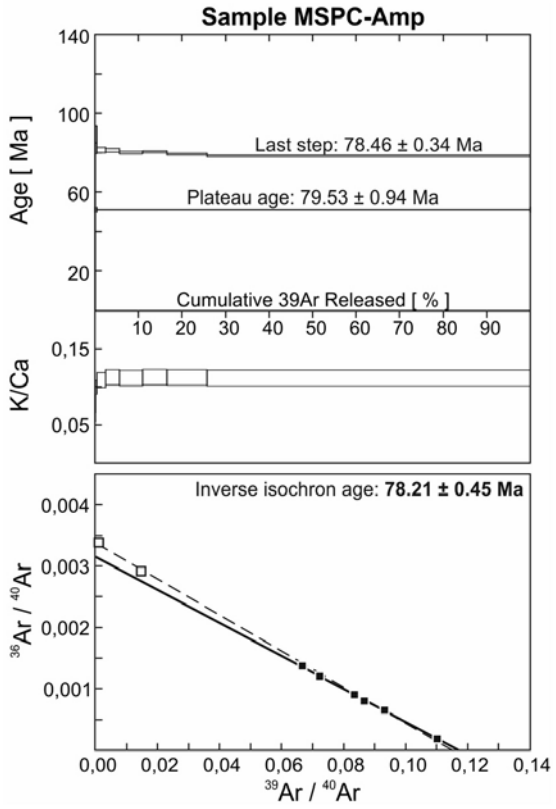


**Fig. 3.7.** $^{40}Ar/^{39}Ar$ incremental heating results for sample MSPC-Amp. Explanation is as in Fig. 3.3. The age of the last step is included in the age spectrum.

The detailed interpretation of the age results is in the Appendix (section 3.7). Sample SGR-Bt from the Basque-Cantabrian Basin and AUB-Amp from the North Pyrenean Basins yielded similar, Albian ages at 101.39 ± 1.24 and 102.63 ± 0.75 Ma, respectively (Fig. 3.3; Table 3.1). In the Central Pyrenees, samples DEN1-Gr and DEN2-Gr yielded different ages neither of them Cretaceous (Fig. 3.4; Table 3.1). The age of DEN1-Gr is 231.83 ± 5.22 Ma (Late Triassic) and that of DEN2-Gr is 179.68 ± 1.39 Ma (Early Jurassic). Finally, in the Catalonian Coastal Ranges all the experiments yielded similar, Campanian ages at ca. 79 Ma (Figs. 3.5 to 3.7; Table 3.1). Groundmass and amphibole separates yielded ages indistinguishable from each other within the uncertainty. The preferred crystallisation age for each intrusion was 78.98 ± 0.50 Ma for the lamprophyre from Calella de Palafrugell (CAL-Amp sample), 79.20 ± 0.81 Ma for the lamprophyre from Llagostera (LLAG-Gr sample) and 78.21 ± 0.45 Ma for the lamprophyre from the Monasterio de Sant Pere Cercada (MSPC-Amp sample).

## 3.5. Discussion

### 3.5.1. The Triassic-Jurassic rifting in the Central Pyrenees

The age of samples DEN1-Gr and DEN2-Gr is Late Triassic (ca. 232 Ma; Carnian) and Early Jurassic (ca. 180 Ma; Toarcian), respectively (Table 3.1). These data are in contrast with preliminary geochronological results (Galé and Arranz, 2001) and dismiss a Cretaceous age for the alkaline dykes in the Central Pyrenees. It follows that the Cretaceous magmatism in the Pyrenees is restricted to the European domain, to the north of the North Pyrenean Fault Zone (Fig. 3.1).

Two types of magmatic events are recognised in northeast Iberia during the Triassic and Jurassic. On the one hand, there is widespread tholeiitic magmatism (“ophites”) emplaced during the Triassic-Jurassic boundary in the Western and Central Pyrenees (e.g., Alibert, 1985; Azambre et al., 1987; Béziat et al., 1991; Montigny et al., 1982; Rossi et al., 2003). On the other hand, there is more restricted, geographically scattered, alkaline magmatism forming part of a Late Triassic alkaline igneous province (Lago et al., 1996; Sanz et al., 2013). Within the Pyrenean chain, the latter magmatism has only been recognised in the Eastern Pyrenees (Corbières area; e.g., Azambre and Rossy, 1981) where it has a Late Triassic, Norian age (Montigny et al., 1982).

The Triassic-Jurassic geochronological results reveal for the first time, an alkaline magmatism in the Central Pyrenees for that period. Given the affinity of these rocks, one could think they have a common origin within the alkaline igneous province. The differences in age between the samples suggest a long-living (ca. 50 Ma), although geographically restricted, magmatism. If it were related to the alkaline province, the

whole province would cover a longer time span than previously thought. This kind of enduring, sporadic, scattered, low volume and geochemically homogeneous magmatism has recently been documented in the nearby Languedoc volcanic province (Dautria et al., 2010), where alkali basaltic activity spans from 161 to 0.5 Ma. More data would be necessary to know whether the Triassic-Jurassic alkaline activity in the Pyrenees was sporadic or continued in time.

Azambre and Fabriès (1989) propose that the tholeiitic and alkaline Triassic magmatic events developed in a context of continental rifting which affected southwestern Europe after the Variscan orogeny, at the beginning of the Alpine cycle. According to these authors, the tholeiitic magmatism represents the greatest effects of rifting and intruded subsiding Triassic basins. More recently, the tholeiitic magmatism has been related to the Central Atlantic Magmatic Province (CAMP; Rossi et al., 2003). In contrast, the alkaline magmatism developed at the same time along the boundaries of the subsiding Triassic basins with adjacent blocks, and represents off-axis magmatism (Azambre and Fabriès, 1989). The subsiding basins developed from ca. 240-220 Ma to the Mesozoic and part of the Cenozoic (Azambre and Fabriès, 1989). Strikingly, the initiation age of the basins coincides with the oldest obtained result at ca. 232 Ma (Table 3.1). Therefore, assuming that the newly dated rocks are related to the alkaline magmatism, this magmatism started coevally with the subsidence at the Late Triassic and lasted (continuously or not) until at least the Early Jurassic (ca. 180 Ma, Table 3.1). Moreover, the new data demonstrate that the alkaline Triassic magmatism was not only restricted to the Eastern Pyrenees but was affecting also the Central Pyrenees.

### 3.5.2. The Cretaceous opening of the Bay of Biscay and rotation of Iberia

The results obtained for the Cretaceous alkaline magmatism in northeast Iberia are clearly arranged in two, very consistent groups (Table 3.1): the ages obtained in the Pyrenees point to ca. 102 Ma (Late Albian), whereas those from the Catalonian Coastal Ranges indicate another magmatic event at ca. 79 Ma (Campanian). The new Cretaceous ages obtained in this study have been plotted together with the results of previous geochronological studies in the chronostratigraphic chart of Fig. 3.8. New data show significantly smaller uncertainties and are within the wide range defined by previous data, most of which correspond to $^{40}K/^{40}Ar$ analyses.

This section will be focused on the Pyrenean ages. The most relevant previous study was carried out by Montigny et al. (1986) with rocks from the whole Pyrenean chain. According to these authors, magmatic activity took place between 110 and 85 Ma (Fig. 3.8), with most data within the interval between 100 and 90 Ma and younger data (ca. 90-85 Ma) restricted to samples from the western part of the belt. These authors report

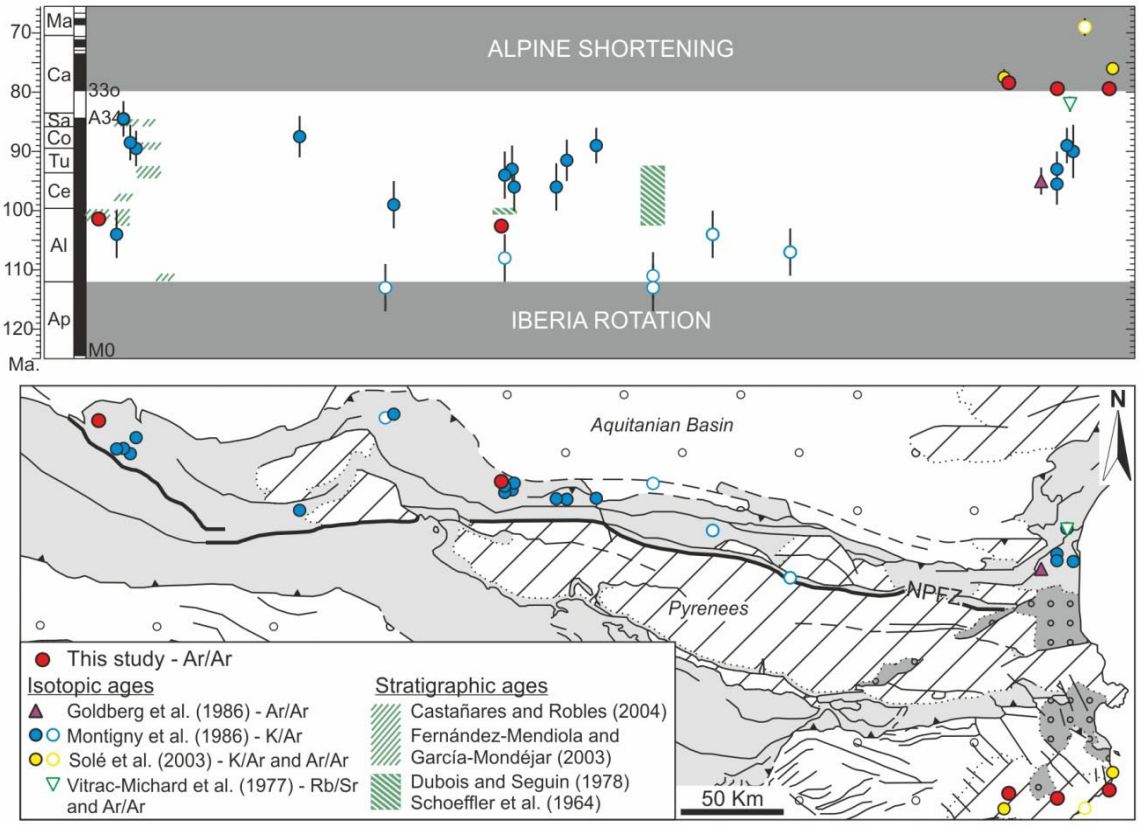


**Fig. 3.8.** Summary of ages for the Cretaceous magmatism in northeast Iberia. The horizontal position of each age correlates with its location in the geological map below (simplified from Fig. 3.1). Red circles represent the samples dated in this study. The rest of the symbols represent data from the literature (white-filled symbols represent discarded data; see sections 3.5.2 and 3.5.3). Isotopic ages correspond to intrusive rocks whereas stratigraphic ages correspond to extrusive rocks. Vertical lines represent the uncertainty associated to isotopic ages (for our data, symbol size includes uncertainty). The rotation of Iberia took place during the Aptian (Gong et al., 2008) and the mainly Tertiary Alpine compression started in the late Cretaceous (e.g., Vissers and Meijer, 2012*b*). The geological timescale and the geomagnetic polarity timescale are from Walker and Geissman (2009). Note the Cretaceous Normal Superchron between magnetic anomalies M0 and A34. Ap: Aptian; Al: Albian; Ce: Cenomanian; Tu: Turonian; Co: Coniacian; Sa: Santonian; Ca: Campanian; Ma: Maastrichtian.

six ages around 110 Ma in the central part of the North Pyrenean Zone that are problematic because they are older than their country rock (Albian-Cenomanian flysch; Dubois and Seguin, 1978) and also older than genetically related extrusive rocks (Dubois and Seguin, 1978; Schoeffler et al., 1964; see Fig. 3.8). Furthermore, they recognize excess Ar in other minerals analysed from the same rocks. Therefore, these ages will not be considered further in the discussion. In the Eastern Pyrenees, consistent data by Golberg et al. (1986) and Montigny et al. (1986) constrain the age of the magmatism to ca. 95-90 Ma (Fig. 3.8), updating a younger age obtained by Vitrac-Michard et al. (1977) that will not be considered further in the discussion. Regarding the age of the extrusive rocks, they crop out in the Basque-Cantabrian Basin and North Pyrenean Basins and their stratigraphic position agrees with the main magmatic phase at 100-90 Ma and also with the more recent ages in the Basque-Cantabrian Basin (Castañares and Robles, 2004; Dubois and Seguin, 1978; Schoeffler et al., 1964; Fig. 3.8). Also in the Basque-Cantabrian

Basin an older, Early Albian extrusive phase is recognised (Fernández-Mendiola and García-Mondéjar, 2003).

The evaluation of previous data reveals that the Cretaceous magmatism in the Pyrenees is Albian to Santonian, mostly 105-85 Ma (instead of 110-85 Ma considering the work by Montigny et al. (1986) or 110-82 Ma considering the whole dataset; Fig. 3.8). The 105-85 Ma range includes most acceptable isotopic and stratigraphic ages, and covers the Basque-Cantabrian Basin, the North Pyrenean Basins and the Eastern Pyrenees. New geochronological data obtained in the present study have uncertainties significantly lower than previous results and stress the importance of the magmatism at ca. 102 Ma (Fig. 3.8). According to the integration of new and revisited data, the magmatism must not be considered Albian to Turonian as frequently cited (e.g., Gong et al., 2009; Vissers and Meijer, 2012*a*) although the magmatic activity concentrated especially in the range ca. 100-90 Ma. Another interesting feature is that the magmatism is very limited in time in the Eastern Pyrenees (95-90 Ma), whereas multiple stages are recognised towards the west with the longest time span recorded in the Basque-Cantabrian Basin (Fig. 3.8); this is in good agreement with the propagation of the V-shaped Bay of Biscay rift.

Contemporaneous with the magmatic activity, mantle exhumation, LP/HT metamorphism and hydrothermal activity are recognised in the North Pyrenean Zone, close to the North Pyrenean Fault Zone (Golberg et al., 1986; Lagabrielle and Bodinier, 2008; Lagabrielle et al., 2010; Montigny et al., 1986; Poujol et al., 2010; Schärer et al., 1999). In particular, the sub-continental mantle crops out as restricted bodies of ultramafic rocks, cross-cut in certain areas by a late generation of amphibole-pyroxenite veins (Lagabrielle and Bodinier, 2008 and references therein). These veins are considered to represent melt conduits for the Cretaceous alkaline magmatism in the Pyrenees (Golberg et al., 1986; Bodinier et al., 1987). $^{40}Ar/^{39}Ar$ dating of amphibole from the veins provided ages of ca. 103 Ma (Albarède and Michard-Vitrac, 1978), ca. 101 Ma (Golberg et al., 1986) and ca. 108-103 Ma (Henry et al., 1998), and unpublished results of the VU argon laboratory are also similar. These data are in line with the main magmatic phase at ca. 100-90 Ma and especially with the new ages at ca. 102 Ma, supporting the link between the amphibole veins and the Cretaceous magmas.

The Cretaceous magmatism, metamorphism, hydrothermalism and mantle exhumation are related to a context of crustal extension and extreme thinning along the North Pyrenean Zone, linked to the opening of the Bay of Biscay and allied rotation of Iberia with respect to Europe (e.g., Jammes et al., 2009; Lagabrielle and Bodinier, 2008; Lagabrielle et al., 2010; Montigny et al., 1986; Poujol et al., 2010). However, considering that the rotation of Iberia has recently been confined to the Aptian (Gong et al., 2008; see Fig. 3.8), all these events are not simultaneous with the rotation as traditionally considered (e.g., Cabanis and Le Fur-Balouet, 1990; Montigny et al., 1986), but post-

rotation. They therefore developed in a tectonically unclear stage in the Iberia motion, after the Aptian rotation and before the onset of the Alpine compression in the Late Cretaceous. The ages of magmatic rocks in the Pyrenees define a time-band between both tectonic events (Fig. 3.8).

Regarding the kinematics of opening of the Bay of Biscay and consequent rotation of Iberia, two end-member models have been put forward (Fig. 3.9). Both models achieve a good fit between the shape of the northern and southern Bay of Biscay continental margins. The differences are mainly in deriving the Euler poles of the rotation, which are required for the kinematic reconstructions. The first model is based on the fit of sea-floor magnetic anomalies across the North Atlantic and Bay of Biscay and is supported by paleomagnetic data and plate-kinematic analysis (Sibuet et al., 2004; Srivastava et al., 2000; Vissers and Meijer, 2012*a*). It proposes a scissor-type opening for the Bay of Biscay which leads to ca. 35º of anticlockwise rotation of Iberia. The main drawback of this model is that it implies large-scale convergence in the Pyrenean domain, which in principle is not consistent with the subsequent development of flysch-filled basins, magmatism, metamorphism, hydrothermalism and mantle exhumation in the North Pyrenean Zone. Following geological evidence for extension, the second model proposes a dominantly left-lateral strike-slip motion between Iberia and Europe, with Iberia moving in a southeasterly direction along the North Pyrenean Fault Zone (Choukroune, 1992; Oliva-Urcia et al., 2011; Olivet, 1996). This model however, is not consistent with sea-floor reconstructions and implies significantly less than the ca. 35º anticlockwise rotation documented by paleomagnetism (Gong et al., 2008). A recent work by Vissers and Meijer (2012*a*) argues in favor of the scissor-type opening model by proposing that convergence in the Pyrenean realm was accommodated by up to 300 km of north-directed subduction underneath the European margin. According to this work, the lithosphere subducted during the Aptian rotation became gravitationally unstable during the subsequent stagnant stage and detached in the Albian, leading to asthenospheric upwelling and consequent magmatism, metamorphism and extension in the overlying European margin now exposed in the North Pyrenean Zone (Vissers and Meijer, 2012*a*). These authors relate the lack of evidence for subduction in the Pyrenees to the fact that the subducted crust was amagmatic, mantle-dominated ocean floor exhumed under conditions of ultraslow spreading during the Late Jurassic and Early Cretaceous.

An alternative kinematic model has been recently proposed by Jammes et al. (2009, 2010) based on field data in the western Pyrenees together with previous observations and numerical modelling. This model proposes a scissor-type opening for the Bay of Biscay with an inferred pole of rotation located in the Mediterranean Sea, preceded by a left-lateral strike-slip motion between Iberia and Europe during the Late Jurassic to Early Cretaceous. The main advantage of this model is that the rotation pole in the

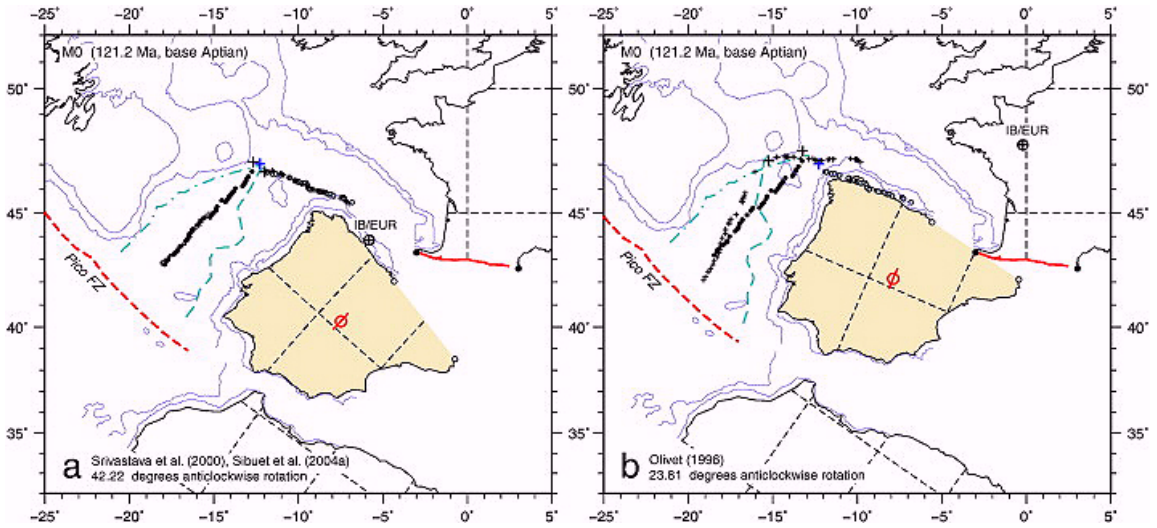


**Fig. 3.9.** Reconstructions for Iberia and surrounding plates relative to Europe for chron M0 according to end-member kinematic models. Dots represent M0 anomaly picks on the North American and European side, crosses denote M0 anomalies on the Iberian side. IB/EUR denotes total reconstruction pole for Iberia with respect to Europe. Amount of rotation is measured in Madrid (circle with bar, ϕ). Note that reconstruction in (a) implies compression in the Pyrenean domain and the reconstruction in (b) is incompatible with the seafloor anomaly data in the Atlantic and Bay of Biscay and implies a smaller degree of total counterclockwise rotation. From Vissers and Meijer (2012*a*).

Mediterranean sea produces scissor-type opening in the Bay of Biscay as well as in the Pyrenean domain, explaining extension in the North Pyrenean Zone and the formation of the Cretaceous basins. However, as in the strike-slip opening case, the model is not consistent with sea-floor reconstructions and implies significantly less than the ca. 35º anticlockwise rotation documented by paleomagnetism (Gong et al., 2008; see Vissers and Meijer, 2012*a*).

Given that the Cretaceous alkaline magmatism follows the rotation and separation of Iberia from Europe (Fig. 3.8), the temporal, geographical and petrological distribution of the igneous rocks may shed some light on the long-standing debate regarding the kinematics of opening of the Bay of Biscay. The chronological distribution of the magmatism reveals differences along the Pyrenees, with more magmatic stages and a more enduring magmatic activity towards the west (Fig. 3.8). Furthermore, the magmatism is widespread and mainly extrusive in the west (Basque-Cantabrian Basin) but becomes progressively scarcer and more intrusive towards the east, with no extrusive rocks cropping out in the Eastern Pyrenees. The nature of the magmatism is also different, with silica undersaturated rocks to the east, related to a lower melting rate of the mantle source (e.g., Cabanis and Le Fur-Balouet, 1990; Chapter 4). All these lines of evidence suggest that extension was more developed and long-lasting towards the west. Such a tectonic variability along the Pyrenees appears to support a scissor-type opening model for the Bay of Biscay.

On the other hand, the linearity of magmatic, metamorphic and mantle rock occurrences along the North Pyrenean Zone may be in favour of a strike-slip opening along the North Pyrenean Fault and a recent study on the Cretaceous Peri-Atlantic Alkaline Pulse (Matton and Jébrak, 2009) highlights the strong structural control reigning over the ascent of the alkaline magmas. However, such linearity could alternatively indicate the position of the axe of the rift and it is also possible that compression in closing the Cretaceous basins accentuated the linearisation of the outcrops.

The magmatism studied is associated to a continental rift setting. Hence, the mechanism of initiation of rifting can also be evaluated to test the kinematics of opening for the Bay of Biscay. The scissor-type opening model according to Vissers and Meijer (2012*a*) proposes that sedimentary basins and magmatism are triggered by asthenospheric upwelling, i.e. an "active rifting" scenario (e.g., Wilson, 1989). In contrast, the scissor-type opening model according to Jammes et al. (2009, 2010) as well as the strike-slip opening model (Olivet, 1996) consider magmatism to be developed in a purely extensional or transtensional setting leading to extreme crustal thinning, i.e. a "passive rifting" scenario (e.g., Wilson, 1989). Although these extreme mechanisms are too simplistic to be applied straightforwardly to the interpretation of rift systems, "active rifting" should ideally affect a broader area and lead to earlier magmatism in a rift sequence, prior to extension in surface (e.g., Winter, 2001). However, the Cretaceous magmatism in the Pyrenees (Fig. 3.8) is simultaneous or post-dates the Albian-Cenomanian flysch sequences filling the North Pyrenean Basins. Moreover, the volume of magmatism is relatively small and major focus of volcanism is restricted to the Basque-Cantabrian Basin. And there are no sub-alkaline or transitional flood basalts that would point to a thermal anomaly within the upper mantle. Finally, in the review on rift evolution by Ziegler and Cloetingh (2004) mantle upwelling is a considered a consequence of lithospheric extension and not the main driving force of rifting. Therefore, geological data point to a "passive rifting" scenario, supporting the scissor-type opening model according to Jammes et al. (2009, 2010) and the strike-slip opening model (Olivet, 1996) better that the scissor-type opening model according to Vissers and Meijer (2012*a*).

In conclusion, the varying geochronological, petrological and compositional characteristics of the magmatisms along the belt support a scissor-type opening model better than the strike-slip opening model. However, the relative timing of extension and magmatism reveal a "passive rifting" scenario that questions the model proposed by Vissers and Meijer (2012*a*). It seems therefore that none of two end-member kinematic models fit the magmatic data and an alternative model should be considered. The exposed evidence supports the scissor-type opening model proposed by Jammes et al. (2009, 2010), coherent with a "passive rifting" context. Plate-kinematic results, however, disagree with this reconstruction (Vissers and Meijer, 2012*a*). In any case, updated

geochronological and petrological information is provided to contribute to better constrain the opening of the Bay of Biscay and related rotation of Iberia.

### 3.5.3. The onset of the Alpine compression in the Late Cretaceous

Samples from the Catalonian Coastal Ranges yield the youngest ages, constraining the magmatic activity to the Campanian, at ca. 79 Ma (Fig. 3.8; Table 3.1). This datum is very well defined as macrocryst and groundmass separates produce consistent ages in all the studied intrusions (see section 3.4). The previous geochronological study by Solé et al. (2003) provided three ages, including an especially young one which is not supported by the new data and as noted by those authors, must be considered a minimum estimate.

The Cretaceous magmatism in the Catalonian Coastal Ranges is the only located in the Iberian domain, to the south of the North Pyrenean Fault Zone, and is significantly younger than the ca. 95-90 Ma age of the igneous rocks from the Eastern Pyrenees (Fig. 3.8). Strikingly, its age at ca. 79 Ma coincides with the age of magnetic anomaly 33o (e.g., Gee and Kent, 2007; Walker and Geissman, 2009; Fig. 3.8). Solé et al. (2003) stated that these magmas were emplaced in zones of crustal relaxation and/or thinning in the relatively stable tectonic transition between the rotation of the Iberian Peninsula and the Alpine collision with respect to Europe. It is however unclear when exactly Alpine compression commenced.

The change to a transpressional regime is well recorded in the Pyrenean geology by inversion of previous extensional faults and deposition of growth sequences in the south-central Pyrenees (Beaumont et al., 2000; Choukroune, 1992; García-Senz, 2002; Garrido-Megías and Ríos-Aragüés, 1972; McClay et al., 2004; Muñoz, 1992; Puigdefàbregas and Souquet, 1986). However, these authors report slightly different ages within the Late Cretaceous for the onset of compression: some give a Santonian age whereas others give a Campanian age, and others a Santonian-Maastrichtian or Campanian-Maastrichtian age range. According to plate-kinematic reconstructions based on the fit of sea-floor magnetic anomalies, Rosenbaum et al. (2002) concluded that the relative motion of Iberia and Europe changed to convergence at anomaly A34 (85 Ma, Santonian, according to the timescale by Walker and Geissman, 2009; Fig. 3.8). The recent kinematic studies by Vissers and Meijer (2012*a*, 2012*b*) emphasised that there is no geological evidence in the Pyrenees for any significant crustal shortening prior to the Campanian. Vissers and Meijer (2012*b*) proposed that the onset of collision is coeval with the latest stages of spreading in the Bay of Biscay, which involved first extension then shortening in the Pyrenean domain with a sinistral strike-slip component. Specifically, the youngest oceanic crust of the Bay of Biscay spread in the interval between anomalies A34 and 33o and provoked strike-slip extension in the Pyrenean realm; only from anomaly 33o did strike-slip shortening start in the Pyrenees (Fig. 3.10).

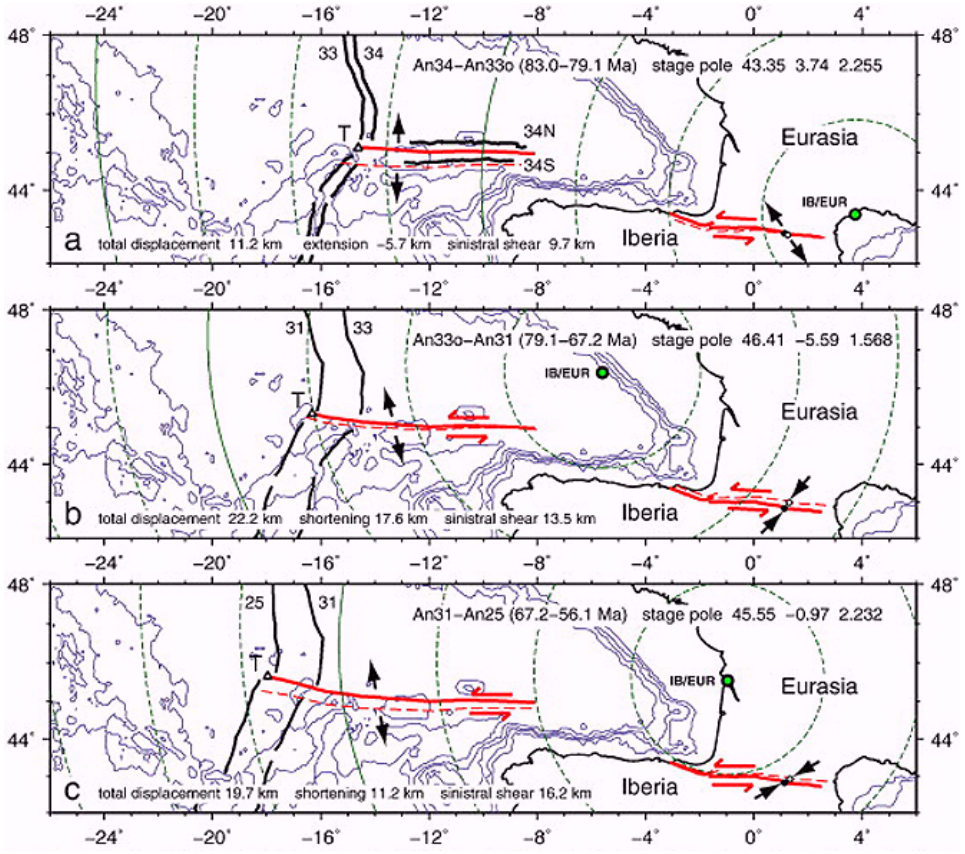


**Fig. 3.10.** Kinematics of the Bay of Biscay axis during the final stages of opening and the initial stages of Alpine shortening in northeast Iberia. From Vissers and Meijer (2012*b*).

The new geochronological results consistently point to a magmatic event at 79 Ma (Fig. 3.8). This is inconsistent with Alpine shortening starting before that time. Indeed, the timing of the magmatism coincides exactly with the abovementioned change of tectonic regime in the Pyrenean domain, related to the end of sea-floor spreading in the Bay of Biscay at anomaly 33o (Vissers and Meijer, 2012*b*). Moreover, detrital thermochronometry of foreland basin sediments gives insights on the early stage of orogenic development (e.g., Filleaudeau et al., 2011) and recent studies in the south-central Pyrenees identify a first exhumation signal at ca. 78 Ma (Whitchurch et al., 2011) and ca. 80 Ma (Filleaudeau et al., 2011), well in line with the age of the magmatism as well. Hence, the Cretaceous lamprophyres in the Catalonian Coastal Ranges could be markers of the tectonic change. In line with this hypothesis, Scarrow et al. (2011) recently concluded that lamprophyres potentially act as tectonomagmatic markers of changes in geodynamic conditions. These authors studied alkaline lamprophyres of Permian age in the Central Iberian Zone, which also are geographically restricted and small in volume. In that case, the lamprophyres were emplaced during the final stages of the Variscan orogen related to an important shift in the regional tectonic regime from transpressional to transtensional. In the case studied here, the lamprophyres appear to be related to the onset of strike-slip shortening (or to the latest stages of strike-slip extension), as lamprophyre intrusions are commonly associated to strike-slip shear zones (Pirajno, 2010

and references therein). These data suggest that Alpine shortening in the Pyrenees started in the Campanian at ca. 79 Ma.

Since Alpine compression started at the Iberia-Europe plate boundary and was propagated intraplate afterwards, the age of the magmatism in the Catalonian Coastal Ranges could alternatively be subsequent to the onset of compression at the plate margin. However, tectonic inversion in the Catalonian Coastal Ranges is considered Late Cretaceous as well (Juez-Larré and Andriessen, 2002, 2006) and the magmatism is located in the Paleozoic basement at the northernmost tip of the Ranges (see Fig. 3.1), so probably within or very close to the Pyrenean realm during Late Cretaceous times. Moreover, the Pyrenean orogen developed diachronously from east to west (Whitchurch et al., 2011 and references therein) and values for the total shortening across the belt tend to increase towards the east (e.g., Vergés et al., 2002), consistently with a small component of anticlockwise rotation of Iberia during convergence (Vissers and Meijer, 2012*b*). These data lend further support to considering the lamprophyres from the Catalonian Coastal Ranges coeval with the onset of Alpine shortening in northeasternmost Iberia.

## 3.6. Conclusions

New $^{40}Ar/^{39}Ar$ ages on the magmatism of the Pyrenees and Catalonian Coastal Ranges form three age groups: a Late Triassic (ca. 232 Ma) – Early Jurassic (ca. 180 Ma) magmatism in the Central Pyrenees that was previously thought to be Cretaceous, a Cretaceous ca. 102 Ma magmatism in the Basque-Cantabrian Basin and the North Pyrenean Basins and a Late Cretaceous ca. 79 Ma magmatism in the northern part of the Catalonian Coastal Ranges. These results, combined with a detailed evaluation of previous data, provide new insights into the geodynamic evolution of northeast Iberia during the Alpine cycle:

- The Late Triassic and Early Jurassic ages represent the first report of an alkaline magmatism in the Central Pyrenees for that time. The new ages widen temporally and geographically the alkaline magmatism associated to the continental rift setting developed in northeast Iberia and in general, southwest Europe at the beginning of the Alpine cycle.

- The Cretaceous alkaline magmatism in the Pyrenees took place from the Albian to the Santonian (mostly between 105 and 85 Ma). In contrast with traditional thinking, magmatism is not coeval but post-dates the Aptian opening of the Bay of Biscay and allied rotation of Iberia with respect to Europe. Geochronological, petrological and compositional data for the magmatism are in disagreement with

both the classical scissor-type opening model and the strike-slip opening model, and suggest that an alternative interpretation should be considered. Magmatism as well as contemporaneous metamorphism, hydrothermalism and mantle exhumation developed in a tectonically unclear stage between the rotation of Iberia and the onset of Alpine collision. Magmatic activity is especially recorded between ca. 100 and 90 Ma. It is restricted to ca. 95-90 Ma in the Eastern Pyrenees, whereas multiple stages develop towards the west with the longest time span recorded in the Basque-Cantabrian Basin. The new ages at ca. 102 Ma agree with those of amphibole in veins that cross-cut mantle exposures, supporting the interpretation that the veins represent melt conduits for the Cretaceous alkaline magmas.

- The Late Cretaceous alkaline magmatic event in the Catalonian Coastal Ranges is precisely dated at ca. 79 Ma (Campanian). This age is inconsistent with shortening starting before that time as previously considered, and could actually represent the onset of the Alpine shortening in northeast Iberia.

It is noteworthy that the alkaline magmatism in the Central Pyrenees has turned out not to be Cretaceous, so it will not be considered for interpretations on the Cretaceous magmatic province in northeast Iberia (see Chapter 4).

## 3.7. Appendix

In this section a detailed description of $^{40}Ar/^{39}Ar$ experiment results is presented. This includes the interpretation of the age spectra, K/Ca spectra and inverse isochrons as well as the criteria for the selection of crystallisation ages.

Sample SGR-Bt yielded a disturbed age spectrum with abundant atmospheric argon in the first steps and excess argon in the highest temperature steps (Fig. 3.3). The isochron treatment of the data confirmed the presence of excess argon, as the non-radiogenic intercepts were lower than atmosphere. Hence, the inverse isochron age of 101.39 ± 1.24 Ma was considered the most accurate estimate of the crystallisation age. The MSWD value was relatively high, as the result of low individual analytical step uncertainties. The K/Ca spectrum indicates a relative compositional heterogeneity, either due to compositional variations among the biotite grains or, more probably, due to contamination of the grains with other phases (e.g., other Ca-rich phases; Fig. 3.2A). The age defining fractions are the most K-rich, therefore indicating the highest biotite proportions, which retained most of the radiogenic argon (> 85 %).

Sample AUB-Amp produced linear age and K/Ca spectra where almost 100 % of $^{39}Ar$ was considered for the plateau age calculation (Fig. 3.3). No excess argon was found as the non-radiogenic intercepts were indistinguishable from atmosphere and the plateau and inverse isochron ages are concordant. The plateau age of 102.63 ± 0.75 Ma is preferred due to its lower MSWD value. Most of the gas was released in the last step, indicating the high retentivity for argon of amphibole. The K/Ca flat spectrum pointed out the purity of the sample and confirmed the compositional homogeneity of the amphibole grains, in agreement with petrographical observations (Fig. 3.2B).

Samples DEN1-Gr and DEN2-Gr yielded different ages neither of them Cretaceous (Fig. 3.4). The lowest temperature steps were somewhat irregular and showed very low K/Ca values, probably related to contamination of some groundmass grains by calcite-filled vesicles (Fig. 3.2C), which are hard to leach if they are surrounded by groundmass. The last steps were apparently affected by contamination with a Ca-rich phase (probably xenocrysts or xenoliths present in the rock, see Fig. 3.2D) which started degassing at high temperatures, as reported elsewhere for groundmass samples (e.g. De Beni et al., 2005; Koppers et al., 2000; Veldkamp et al., 2007). The fractions included in the age calculation are the most K-rich, probably related to the biotite microcrysts of the groundmass (Fig. 3.2C, 2D). No excess argon was detected and the plateau and inverse isochron ages overlapped within the uncertainty. Plateau ages were preferred due to their lower MSWD values. Therefore, DEN1-Gr and DEN2-Gr were inferred to be 231.83 ± 5.22 Ma and 179.68 ± 1.39 Ma old, respectively.

Samples CAL-Gr and LLAG-Gr yielded L-shaped age spectra with very high ages for the first step (Fig. 3.5, 3.6). Given that no excess argon was found in the inverse isochron treatment of the data, these L-shaped age spectra must be explained by recoil loss of $^{39}Ar$ from fine grained phases (Koppers et al. 2000). These are probably secondary minerals (mainly chlorite) present as late magmatic phases and, to a lesser extent, as alteration products (recrystallisation) of the glass of the rock. The total fusion ages were slightly higher than the plateau ages, also supporting recoil loss of $^{39}Ar$ (Koppers et al., 2000).

Besides, sample LLAG-Gr showed a K-rich last step. This cannot be related to contamination by large crystals because they are mafic minerals (Fig. 3.2F) which present low K/Ca ratios. This step might therefore be related to evolved, K-rich patches in the groundmass (see section 3.3.1) which started degassing at high temperatures. Inverse isochron ages show lower MSWD values than plateau ages.

Samples CAL-Amp, LLAG-Amp and MSPC-Amp (Fig. 3.5, 3.6, 3.7) produced apparently flat age spectra. In detail however, the age spectra have decreasing staircase morphology and high MSWD values and reveal excess argon in the low temperature steps. The inverse isochron treatment of the data confirmed excess argon in the samples. The excess argon was probably diffused into the crystals from the magma chamber, as reported elsewhere (e.g., Harrison and McDougall, 1980; Wijbrans and McDougall, 1988). This agrees with the compositional homogeneity of the amphibole grains, as recognised petrographically (Fig. 3.2E, 2F, 2G) and confirmed by the K/Ca spectra.

If argon diffusion into crystals is recognised, a plateau age cannot be defined; however, the purely radiogenic component from the inverse isochron corresponds to a geologically meaningful age (e.g., McDougall and Harrison, 1999). Sample LLAG-Amp however, did not produce a well defined age in any case. The steps selected for each inverse isochron represented high percentages of the gas released and high percentages of radiogenic argon in each step. Besides, the inverse isochron ages were similar to the age of the last step, presumably the least affected by argon diffusion because it most likely represents the cores of the crystals; the last step contained more than 60 % of the gas released and it was enriched in radiogenic argon over 90 %.

Groundmass and amphibole separates analysed in the lamprophyres from Calella de Palafrugell and Llagostera yielded ages indistinguishable from each other within the uncertainty. The preferred crystallisation age for each intrusion was that with the lowest associated MSWD value, namely: 78.98 ± 0.50 Ma for the lamprophyre from Calella de Palafrugell, which corresponds to the inverse isochron age from sample CAL-Amp, and 79.20 ± 0.81 Ma for the lamprophyre from Llagostera, which corresponds to the inverse isochron age from sample LLAG-Gr. The amphibole separate from the Monasterio de Sant

Pere Cercada lamprophyre yielded a very accurate inverse isochron age with almost 100 % of $^{39}Ar$ considered: 78.21 ± 0.45 Ma.

# 4

# Petrogenesis of the Cretaceous alkaline magmatism in northeast Iberia: new insights into the evolution of the mantle source

**SUMMARY**

The Cretaceous magmatism in northeast Iberia (Pyrenees and Catalonian Coastal Ranges) constitutes an alkaline igneous province with magma differentiation from ultrabasic to intermediate-acid compositions. Increasing magmatic activity and melting rates towards the west can be related to the context of opening of the Bay of Biscay that controlled the development of this magmatism. Major element, trace element and Sr-Nd-Pb isotope geochemistry reveals a common, enriched/metasomatised, heterogeneous (HIMU-EM) and asthenospheric mantle source. Comparison with a large geochemical database of magmatisms occurring in Iberia throughout the Alpine cycle indicates that the Cretaceous signature might have been present in large areas of the mantle from Permian to Quaternary times and was tapped according to favourable tectonic conditions.

*Landscape near Elgoibar, Basque Cantabrian Basin*

## 4.1. Introduction

The Cretaceous magmatism in northeast Iberia defines a geographically large, geochemically alkaline igneous province that includes outcrops along the Pyrenees and the northern Catalonian Coastal Ranges. This magmatism belongs to the larger Late Cretaceous Alkaline Igneous Province in the Iberian Peninsula (Rock, 1982) and it could also be ascribed to the Cretaceous Peri-Atlantic Alkaline Pulse (Matton and Jébrak, 2009). It is closely related to the opening of the Bay of Biscay and anticlockwise rotation and separation of Iberia with respect to Europe, which produced extreme crustal thinning between both plates (Ubide et al., under review *a* –see Chapter 3 in this volume-).

Numerous authors have focused on the Cretaceous magmatism in northeast Iberia (Azambre et al., 1992; Cabanis and Le Fur-Balouet, 1990; Rossy et al., 1992; Ubide et al., 2012*a*, 2012*b*; Chapters 5, 6 and 7 in this volume). Still, all previous studies are devoted either to the Pyrenean setting or to the Catalonian Coastal Ranges. Moreover, they were carried out with different approaches and different levels of detail, and the geochemical studies carried out long ago lack certain trace element concentrations and isotope ratios. In consequence, there is a lack of petrogenetic information comparable across the whole magmatic province.

The present chapter is the first comprehensive study on the petrology and geochemistry of the Cretaceous alkaline magmatism in northeast Iberia including the Pyrenees and the Catalonian Coastal Ranges. New data are presented and discussed in terms of the petrogenesis of these magmas as well as their links with previous and subsequent magmatisms in Iberia. The final aim is to obtain a better understanding of the mantle source and its evolution with geological time.

## 4.2. Geological context, igneous typologies and previous studies

The Cretaceous magmatism in northeast Iberia developed in the context of opening of the Bay of Biscay and anticlockwise rotation of Iberia, before the onset of the Alpine compression (Ubide et al., under review *a* –see Chapter 3-). Occurrences of this magmatism are known close to the boundary between the Iberian and European realms, in several domains (Fig. 4.1): 1) the Basque Cantabrian Basin in the western Pyrenees; 2) the North Pyrenean Basins; 3) the Eastern Pyrenees and 4) the northern part of the Catalonian Coastal Ranges.

The magmatism has an alkaline geochemical affinity and includes a great variety of rock types, from mafic to felsic compositions, with intrusive and extrusive varieties (Azambre

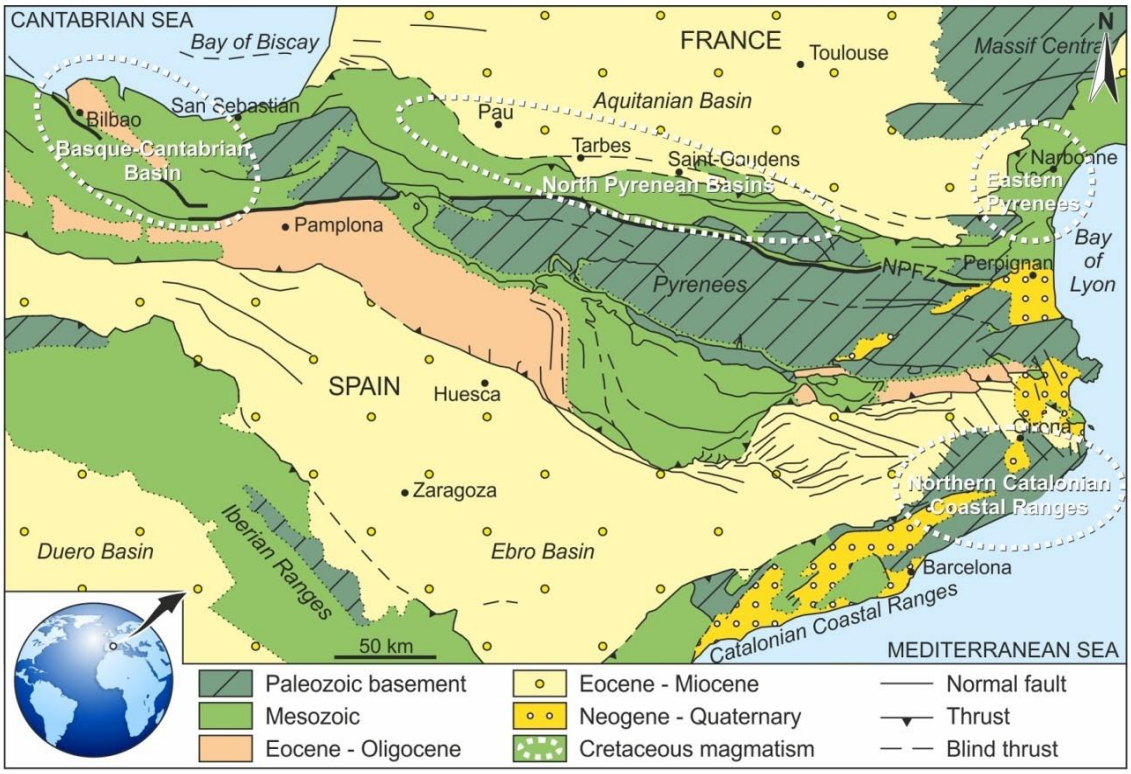


**Fig. 4.1.** Location and geological map of northeast Iberia indicating the domains where the Cretaceous magmatism crops out. From west to east: Basque-Cantabrian Basin, North Pyrenean Basins, Eastern Pyrenees and Catalonian Coastal Ranges. Cretaceous igneous rocks are progressively more intrusive, alkaline and $SiO_2$-undersaturated towards the east.

et al., 1992). The magmatism is most developed in the Basque-Cantabrian Basin, where extrusive rocks are the most common (Azambre et al., 1992; Cabanis and Le Fur-Balouet, 1990; Cuevas et al., 1981; Cuevas and Tubia, 1984). In contrast, the magmatism is restricted to scattered outcrops of intrusive rocks in the Eastern Pyrenees and the northern Catalonian Coastal Ranges (Azambre et al., 1992; Solé et al., 2003; Ubide et al., 2012*a*). Variations from western to eastern domains are progressive, so that the abundance of igneous occurrences and extrusive typologies decrease towards the east (Fig. 4.1). More details on the context, occurrences and characterisation of the magmatism can be found in Chapter 3 (section 3.2).

Previous studies on this magmatism have been carried out on very different scales. In the Pyrenees, Cretaceous igneous rocks are well documented (e.g., Montigny et al., 1986) and the characteristics of extrusive deposits have been extensively studied (e.g., Carracedo et al., 2000, 2012; Castañares et al., 1997, 2001). The petrology, mineralogy, elemental and Sr-Nd isotope geochemistry of this magmatism have been investigated in several contributions (Azambre et al., 1992; Cabanis and Le Fur-Balouet, 1990; Rossy et al., 1992). These studies however, were carried out long ago and lack relevant trace element concentrations as well as Pb isotope ratios.

In the Catalonian Coastal Ranges, alkaline lamprophyres were described since the early papers in regional geology (e.g., San Miguel de la Cámara, 1930, 1936; Velde and Tournon, 1970). However, their Cretaceous age was first confirmed by Solé et al. (2003). Until recently, investigations on these rocks were few and addressed field observations and preliminary compositional results (Enrique, 2009; Gimeno, 2002; Ubide et al., 2008, 2009). The first in-depth investigations on petrology, mineralogy and elemental geochemistry were carried out very recently for one of the intrusions (Ubide et al., 2012*a*, under review *b*) and are presented in Chapters 6 and 7 in this volume. The whole lamprophyre suite is globally studied in Chapter 5, and preliminary Sr-Nd-Pb isotope results were presented in Ubide et al. (2012*b*). Nevertheless, these rocks have never been compared to those in the Pyrenees.

## 4.3. Samples and methods

Sample collection was undertaken in numerous field campaigns across northeast Iberia to select unaltered, representative rocks of the diverse igneous materials making up the Cretaceous alkaline magmatism. Sampling was mostly focused on mafic rocks, as they potentially preserve petrogenetic information regarding the mantle source and melting processes. Acid rocks were also collected in order to evaluate magma differentiation. Poorly known sectors and those with only minor information published were more intensely sampled than those that had been previously investigated in depth.

The petrographic study led to the selection of samples for elemental and isotopic analyses. Mineral major element compositions were used for classification purposes. Polished thin sections were prepared at the *Servicio General de Apoyo a la Investigación-SAI*, Universidad de Zaragoza (Spain) and minerals were analysed by electron microprobe (EMP) at the *Centro Nacional de Microscopía Electrónica* of the Universidad Complutense de Madrid (Spain), using a JEOL JZA-8900M electron microprobe equipped with four wavelength dispersive spectrometers. Analyses were performed using an accelerating voltage of 15 kV and an electron beam current of 20 nA, with a beam diameter of 5 µm. Elemental counting times were 10 s on the peak and 5 s on each of two background positions. Corrections for inter-elemental effects were made using a ZAF (Z: atomic number; A: absorption; F: fluorescence) procedure.

A total of 37 samples were reduced to powder for whole rock elemental analyses (results in Table 4.1). They were crushed in a manganese steel jaw-crusher, milled in an agate vibrating cup mill and successively split down to few grams at the *Servicio General de Apoyo a la Investigación-SAI*, Universidad de Zaragoza (Spain). Major and trace element concentrations were determined at the *Service d'Analyse des Roches et des Minéraux*

**Table 4.1.** Location, classification and whole rock composition of the samples. Major elements expressed as wt. % and trace elements expressed as ppm.

| Domain | BCB | | | | | | | | | | |
|---|---|---|---|---|---|---|---|---|---|---|---|
| Sector | Vergara | Vergara | Guernica | Guernica | Vergara | Vergara | Bilbao | Vergara | Vergara | Vergara | Vergara |
| UTM coor. | 30T | 30T | 30T | 30T | 30T | 30T | 30T | 30T | 30T | 30T | 30T |
| | 546973 | 546810 | 516911 | 516911 | 545708 | 545072 | 504614 | 555523 | 555523 | 555523 | 545708 |
| | 4784228 | 4784613 | 4797695 | 4797695 | 4782662 | 4772677 | 4793082 | 4772385 | 4772385 | 4772385 | 4782662 |
| Rock type | Pi | B | | | | | G | | | | Tr |
| Classification | PIC | BAS | TRB | TRB | BAS | BTR | GAB | GAB | GAB | GAB | TR |
| **Sample** | **ELG-04** | **ELG-08** | **FR-1** | **FR-9** | **MALZA-B** | **8057** | **SGR** | **URR** | **UXT** [a] | **URR-3** | **MALZA-1** |
| $SiO_2$ | 37.40 | 45.46 | 47.51 | 47.69 | 39.99 | 48.50 | 43.01 | 43.32 | 42.88 | 43.46 | 61.82 |
| $TiO_2$ | 1.17 | 2.06 | 2.36 | 2.33 | 3.14 | 2.90 | 2.96 | 3.96 | 4.25 | 2.51 | 0.40 |
| $Al_2O_3$ | 6.31 | 13.70 | 15.30 | 14.72 | 13.77 | 14.93 | 14.76 | 13.27 | 13.16 | 14.94 | 18.12 |
| $Fe_2O_3^T$ | 14.77 | 9.58 | 9.59 | 9.17 | 11.77 | 12.35 | 10.44 | 15.53 | 16.91 | 10.87 | 4.16 |
| MnO | 0.21 | 0.14 | 0.15 | 0.15 | 0.25 | 0.16 | 0.13 | 0.21 | 0.21 | 0.17 | 0.17 |
| MgO | 24.97 | 8.96 | 8.74 | 8.15 | 9.66 | 4.79 | 5.65 | 5.51 | 5.81 | 8.70 | 0.72 |
| CaO | 4.86 | 9.55 | 5.71 | 5.48 | 13.00 | 3.81 | 10.24 | 10.50 | 10.76 | 9.21 | 0.80 |
| $Na_2O$ | 0.13 | 2.65 | 3.30 | 3.49 | 1.14 | 4.53 | 3.14 | 3.30 | 3.03 | 3.37 | 6.65 |
| $K_2O$ | 0.27 | 1.60 | 2.34 | 2.16 | 1.77 | 0.43 | 1.49 | < DL | < DL | 0.27 | 4.85 |
| $P_2O_5$ | 0.21 | 0.29 | 0.45 | 0.46 | 0.54 | 0.92 | 0.41 | 0.46 | 0.42 | 0.44 | 0.07 |
| LOI | 8.58 | 4.59 | 4.97 | 5.04 | 4.71 | 5.86 | 7.21 | 3.60 | 3.27 | 5.60 | 1.40 |
| Total | 98.88 | 98.58 | 100.41 | 98.81 | 99.72 | 99.18 | 99.46 | 99.65 | 100.70 | 99.55 | 99.16 |
| Mg# | 65 | 51 | 50 | 50 | 48 | 30 | 38 | 28 | 28 | 47 | 16 |
| Rb | 12.69 | 58.27 | 56.64 | 54.81 | 31.03 | 16.28 | 50.27 | 2.32 | 2.45 | 8.61 | 35.87 |
| Cs | 2.19 | 2.84 | 0.49 | 0.54 | 0.79 | 0.71 | 17.11 | 3.63 | 3.87 | 3.21 | < DL |
| Be | < DL | 1.02 | 1.11 | 2.01 | 1.10 | 2.17 | < DL | 1.22 | 1.45 | < DL | 2.51 |
| Sr | 172.60 | 1789.00 | 635.40 | 728.40 | 533.00 | 333.20 | 794.10 | 748.80 | 763.10 | 2320.00 | 321.40 |
| Ba | 129.00 | 1142.00 | 631.80 | 606.40 | 605.20 | 128.10 | 720.50 | 93.08 | 91.22 | 563.70 | 520.90 |
| V | 177.80 | 305.30 | 257.50 | 260.70 | 307.60 | 212.30 | 316.40 | 556.50 | 585.00 | 308.50 | < DL |
| Cr | 1832.00 | 401.20 | 233.40 | 248.10 | 377.90 | < DL | < DL | < DL | 7.23 | 340.50 | < DL |
| Co | 112.60 | 42.26 | 31.85 | 31.23 | 47.93 | 20.34 | 34.24 | 46.94 | 48.47 | 40.69 | < DL |
| Ni | 456.80 | 132.80 | 84.91 | 83.36 | 170.50 | < DL | 48.41 | 18.41 | 19.24 | 130.10 | < DL |
| Cu | 30.28 | 81.06 | 39.18 | 38.73 | 59.92 | 6.02 | 105.50 | 37.66 | 33.18 | 50.93 | < DL |
| Zn | 105.10 | 83.85 | 90.29 | 95.87 | 91.36 | 128.30 | 56.87 | 136.00 | 127.40 | 78.02 | 124.10 |
| Ga | 8.76 | 18.62 | 18.57 | 18.11 | 18.56 | 22.92 | 19.28 | 22.11 | 22.75 | 18.56 | 23.17 |
| Y | 7.47 | 20.10 | 22.45 | 23.58 | 23.69 | 38.61 | 20.69 | 27.67 | 26.31 | 20.08 | 32.24 |
| Nb | 14.71 | 49.24 | 66.12 | 69.55 | 58.28 | 73.30 | 54.17 | 62.07 | 56.31 | 39.69 | 175.50 |
| Ta | 1.14 | 3.48 | 5.06 | 5.18 | 5.13 | 5.39 | 4.06 | 4.70 | 4.32 | 3.03 | 12.53 |
| Zr | 47.86 | 167.80 | 196.90 | 203.80 | 163.40 | 233.40 | 167.60 | 196.80 | 190.20 | 132.10 | 529.30 |
| Hf | 1.16 | 3.75 | 4.54 | 4.62 | 4.31 | 5.25 | 4.07 | 4.61 | 4.53 | 3.14 | 9.71 |
| Mo | 0.57 | 1.33 | 1.53 | 1.23 | 2.09 | 2.20 | 1.89 | 1.77 | 1.64 | 1.43 | 0.45 |
| Sn | 0.65 | 1.39 | 2.12 | 1.58 | 2.69 | 1.63 | 1.76 | 2.62 | 1.77 | 1.17 | 4.36 |
| Pb | < DL | 1.53 | 3.84 | 1.52 | 2.89 | 3.02 | 2.17 | 1.92 | 1.74 | 1.97 | 5.76 |
| U | 0.26 | 1.01 | 1.25 | 1.36 | 0.94 | 1.36 | 1.06 | 1.18 | 1.20 | 0.84 | 1.63 |
| Th | 0.97 | 3.81 | 4.59 | 4.94 | 3.41 | 5.00 | 3.95 | 4.18 | 4.33 | 3.02 | 14.09 |
| La | 10.60 | 31.34 | 40.27 | 41.88 | 38.13 | 50.34 | 35.20 | 39.88 | 37.23 | 28.98 | 126.80 |
| Ce | 21.94 | 60.71 | 80.91 | 80.62 | 81.15 | 101.70 | 70.36 | 81.75 | 74.98 | 58.61 | 213.30 |
| Pr | 2.67 | 7.07 | 9.26 | 9.67 | 9.94 | 12.53 | 8.43 | 9.80 | 9.12 | 7.17 | 21.05 |
| Nd | 10.91 | 27.13 | 35.45 | 36.82 | 40.16 | 50.74 | 33.59 | 39.08 | 36.41 | 29.26 | 66.01 |
| Sm | 2.20 | 5.29 | 6.57 | 6.76 | 7.94 | 9.89 | 6.68 | 7.70 | 7.30 | 5.81 | 9.53 |
| Eu | 0.76 | 1.66 | 2.07 | 2.13 | 2.58 | 3.02 | 2.33 | 2.57 | 2.48 | 2.09 | 1.34 |
| Gd | 1.92 | 4.58 | 5.54 | 5.74 | 6.68 | 8.87 | 5.69 | 6.68 | 6.35 | 5.10 | 6.96 |
| Tb | 0.27 | 0.67 | 0.79 | 0.83 | 0.94 | 1.31 | 0.80 | 0.98 | 0.94 | 0.73 | 1.04 |
| Dy | 1.49 | 3.75 | 4.43 | 4.63 | 4.99 | 7.50 | 4.29 | 5.43 | 5.17 | 4.01 | 5.84 |
| Ho | 0.27 | 0.71 | 0.81 | 0.85 | 0.88 | 1.41 | 0.78 | 0.99 | 0.96 | 0.73 | 1.12 |
| Er | 0.70 | 1.88 | 2.15 | 2.28 | 2.20 | 3.68 | 2.00 | 2.65 | 2.52 | 1.92 | 3.24 |
| Tm | 0.10 | 0.27 | 0.31 | 0.32 | 0.29 | 0.52 | 0.28 | 0.37 | 0.35 | 0.26 | 0.50 |
| Yb | 0.63 | 1.73 | 2.05 | 2.14 | 1.78 | 3.22 | 1.77 | 2.37 | 2.27 | 1.69 | 3.42 |
| Lu | 0.09 | 0.27 | 0.31 | 0.31 | 0.26 | 0.48 | 0.26 | 0.36 | 0.35 | 0.26 | 0.54 |

**Table 4.1.** (cont.)

| Domain | NPB | | EP | | | | | | | | |
|---|---|---|---|---|---|---|---|---|---|---|---|
| Sector | Oloron | Oloron | Corbières | Corbières | Corbières | Corbières | Corbières | Corbières | Corbières | Corbières | Corbières |
| UTM coor. | 30T | 30T | 31T | 31T | 31T | 31T | 31T | 31T | 31T | 31T | 31T |
| | 705325 | 706293 | 495487 | 495487 | 495487 | 495487 | 485046 | 485162 | 497693 | 497693 | 497693 |
| | 4782626 | 4776055 | 4760558 | 4760558 | 4760558 | 4760558 | 4745846 | 4745844 | 4748728 | 4748728 | 4748728 |
| Rock type | B | G | L | | | | | | Sye | | |
| Classification | BTR | MNZ | MCH | MCH | MCH | MCH | SAN | SAN | SYE | SYE | SYE |
| **Sample** | **COG-3** | **AUB** | **CORB-1** | **CORB-2** | **CORB-3** | **CORB-6** | **VIN-1** | **VIN-2** | **FIT-1** | **FIT-2** | **FIT-3** |
| $SiO_2$ | 47.19 | 45.13 | 40.33 | 39.45 | 40.18 | 39.34 | 44.52 | 44.41 | 55.32 | 54.97 | 56.55 |
| $TiO_2$ | 2.20 | 2.57 | 2.88 | 2.82 | 2.89 | 2.85 | 2.49 | 2.56 | 0.21 | 0.17 | 0.12 |
| $Al_2O_3$ | 16.89 | 16.84 | 13.21 | 13.07 | 13.28 | 13.05 | 16.02 | 16.15 | 21.33 | 21.69 | 22.07 |
| $Fe_2O_3^T$ | 9.34 | 11.44 | 9.93 | 9.84 | 10.03 | 9.90 | 9.15 | 9.34 | 1.64 | 1.47 | 1.55 |
| MnO | 0.13 | 0.19 | 0.18 | 0.18 | 0.18 | 0.18 | 0.21 | 0.21 | 0.16 | 0.16 | 0.19 |
| MgO | 5.74 | 4.51 | 9.20 | 9.42 | 9.45 | 9.36 | 5.37 | 5.55 | 0.50 | 0.17 | 0.33 |
| CaO | 5.74 | 8.81 | 12.26 | 12.66 | 12.49 | 12.18 | 9.50 | 10.59 | 2.30 | 1.51 | 1.62 |
| $Na_2O$ | 5.62 | 3.68 | 2.90 | 2.66 | 2.70 | 2.86 | 3.60 | 3.02 | 6.53 | 8.05 | 6.80 |
| $K_2O$ | 0.04 | 2.32 | 1.93 | 1.85 | 1.80 | 1.74 | 3.29 | 3.57 | 5.91 | 5.54 | 6.09 |
| $P_2O_5$ | 0.78 | 0.63 | 0.66 | 0.64 | 0.66 | 0.65 | 0.68 | 0.66 | 0.05 | 0.03 | < DL |
| LOI | 5.34 | 3.14 | 6.07 | 6.12 | 5.59 | 6.84 | 4.63 | 4.09 | 5.70 | 4.95 | 3.98 |
| Total | 99.00 | 99.26 | 99.54 | 98.70 | 99.24 | 98.93 | 99.46 | 100.15 | 99.63 | 98.70 | 99.30 |
| Mg# | 41 | 30 | 51 | 52 | 51 | 51 | 39 | 40 | 25 | 11 | 19 |
| Rb | 0.62 | 39.67 | 55.51 | 51.52 | 49.30 | 51.60 | 66.36 | 73.29 | 204.00 | 173.80 | 231.00 |
| Cs | < DL | 17.96 | 5.20 | 2.85 | 3.93 | 3.87 | 41.24 | 5.15 | 1.39 | 4.08 | 2.24 |
| Be | 1.70 | 1.99 | 2.04 | 1.93 | 1.88 | 1.89 | 3.31 | 3.28 | 4.68 | 5.37 | 9.11 |
| Sr | 449.20 | 1335.00 | 1426.00 | 1562.00 | 1368.00 | 1373.00 | 1255.00 | 1947.00 | 1247.00 | 783.10 | 901.20 |
| Ba | 38.18 | 1983.00 | 930.30 | 1174.00 | 1047.00 | 1100.00 | 1284.00 | 987.40 | 733.20 | 656.70 | 210.70 |
| V | 217.30 | 207.30 | 281.80 | 268.40 | 263.40 | 262.80 | 200.20 | 200.00 | 15.43 | 13.96 | 9.63 |
| Cr | < DL | 6.09 | 355.50 | 355.80 | 340.80 | 360.70 | 111.30 | 128.10 | < DL | < DL | < DL |
| Co | 31.31 | 30.09 | 43.89 | 41.41 | 40.77 | 41.53 | 24.85 | 25.83 | 0.55 | 0.45 | < DL |
| Ni | 6.00 | 7.72 | 141.00 | 136.10 | 136.10 | 135.80 | 48.32 | 51.69 | < DL | < DL | < DL |
| Cu | 30.15 | 21.49 | 47.03 | 44.58 | 45.75 | 45.95 | 27.13 | 23.08 | < DL | < DL | < DL |
| Zn | 38.77 | 128.80 | 95.78 | 88.16 | 91.04 | 93.73 | 103.50 | 99.14 | 94.35 | 63.33 | 133.00 |
| Ga | 21.68 | 21.24 | 19.89 | 18.83 | 18.86 | 19.12 | 21.22 | 22.34 | 29.12 | 27.59 | 36.51 |
| Y | 29.18 | 28.08 | 26.44 | 24.58 | 24.90 | 24.96 | 27.58 | 26.55 | 18.90 | 16.65 | 8.65 |
| Nb | 105.30 | 83.19 | 101.30 | 98.69 | 95.79 | 97.92 | 157.80 | 144.30 | 214.80 | 183.00 | 206.70 |
| Ta | 6.99 | 5.98 | 6.81 | 6.56 | 6.57 | 6.55 | 9.35 | 8.70 | 6.43 | 5.67 | 5.54 |
| Zr | 242.30 | 225.50 | 310.10 | 289.40 | 288.80 | 291.60 | 429.00 | 417.20 | 618.30 | 542.20 | 654.70 |
| Hf | 4.16 | 4.45 | 6.18 | 5.80 | 5.84 | 5.87 | 8.43 | 8.22 | 10.43 | 8.64 | 11.05 |
| Mo | < DL | 3.12 | 7.01 | 6.03 | 6.30 | 7.36 | 5.80 | 2.41 | 2.04 | 0.92 | 1.08 |
| Sn | 2.02 | 1.96 | 2.21 | 2.13 | 2.05 | 2.08 | 1.93 | 1.92 | 0.89 | 0.72 | 0.67 |
| Pb | 5.50 | 7.59 | 6.03 | 4.11 | 4.34 | 5.72 | 7.30 | 6.10 | 11.29 | 8.58 | 20.77 |
| U | 2.12 | 2.10 | 2.34 | 2.26 | 2.28 | 2.31 | 4.63 | 4.34 | 10.34 | 8.74 | 11.44 |
| Th | 8.93 | 7.86 | 8.01 | 7.81 | 7.90 | 7.95 | 15.27 | 15.17 | 31.45 | 27.06 | 49.53 |
| La | 60.04 | 54.72 | 68.10 | 65.05 | 66.12 | 66.23 | 109.20 | 106.00 | 81.15 | 70.51 | 55.73 |
| Ce | 107.90 | 101.10 | 124.30 | 117.60 | 119.70 | 119.80 | 186.20 | 178.20 | 130.80 | 112.60 | 96.29 |
| Pr | 12.67 | 11.74 | 14.27 | 13.49 | 13.66 | 13.78 | 19.17 | 18.31 | 11.10 | 9.48 | 8.04 |
| Nd | 46.97 | 43.54 | 53.40 | 49.83 | 50.41 | 51.15 | 65.12 | 63.17 | 29.87 | 25.04 | 19.88 |
| Sm | 8.42 | 7.95 | 9.50 | 8.88 | 8.99 | 9.03 | 10.07 | 9.94 | 3.63 | 3.03 | 1.97 |
| Eu | 2.66 | 2.45 | 2.94 | 2.79 | 2.79 | 2.78 | 2.99 | 2.91 | 1.03 | 0.86 | 0.48 |
| Gd | 6.75 | 6.58 | 7.39 | 7.06 | 7.08 | 7.22 | 7.49 | 7.32 | 2.60 | 2.21 | 1.24 |
| Tb | 0.96 | 0.96 | 1.01 | 0.97 | 0.97 | 0.98 | 1.03 | 1.01 | 0.44 | 0.37 | 0.20 |
| Dy | 5.33 | 5.32 | 5.36 | 5.10 | 5.15 | 5.16 | 5.39 | 5.28 | 2.66 | 2.28 | 1.13 |
| Ho | 0.97 | 1.01 | 0.92 | 0.88 | 0.88 | 0.87 | 0.95 | 0.93 | 0.56 | 0.48 | 0.23 |
| Er | 2.65 | 2.72 | 2.42 | 2.24 | 2.27 | 2.28 | 2.59 | 2.54 | 1.83 | 1.62 | 0.76 |
| Tm | 0.38 | 0.39 | 0.32 | 0.31 | 0.31 | 0.31 | 0.37 | 0.36 | 0.33 | 0.29 | 0.14 |
| Yb | 2.52 | 2.53 | 2.07 | 1.94 | 1.98 | 1.96 | 2.46 | 2.39 | 2.57 | 2.27 | 1.15 |
| Lu | 0.39 | 0.39 | 0.31 | 0.28 | 0.29 | 0.30 | 0.38 | 0.37 | 0.43 | 0.39 | 0.22 |

**Table 4.1.** (cont.)

| Domain | CCR | | | | | | | | | | |
|---|---|---|---|---|---|---|---|---|---|---|---|
| Sector | East | East | East | East | East | East | East | East | East | Centre | Centre |
| UTM coor. | 31T | 31T | 31T | 31T | 31T | 31T | 31T | 31T | 31T | 31T | 31T |
| | 518017 | 518152 | 518082 | 515127 | 515127 | 515127 | 515127 | 515127 | 515127 | 504908 | 490826 |
| | 4643303 | 4642610 | 4643187 | 4636865 | 4636865 | 4636865 | 4636865 | 4636865 | 4636865 | 4626689 | 4629937 |
| Rock type | L | | | | | | | | | | |
| Classification | CAMP | CAMP | CAMP | CAMP | CAMP | CAMP | CAMP | CAMP | CAMP | CAMP | CAMP |
| **Sample** | **AIG-04** | **AIG-05** | **AIG-08** | **CAL-1** | **CAL-2** | **CAL-3** | **CAL-4** | **CAL-5** | **CAL-Gr** [b] | **SAG-03B** | **LLAG-01** |
| $SiO_2$ | 39.52 | 40.30 | 38.47 | 40.24 | 40.62 | 40.45 | 41.28 | 41.94 | | 45.14 | 37.72 |
| $TiO_2$ | 3.48 | 3.73 | 3.56 | 3.86 | 4.06 | 3.97 | 3.75 | 3.58 | | 3.47 | 4.17 |
| $Al_2O_3$ | 14.02 | 14.18 | 13.96 | 14.30 | 13.69 | 14.02 | 14.64 | 15.15 | | 15.11 | 12.44 |
| $Fe_2O_3^T$ | 12.95 | 13.67 | 13.98 | 14.34 | 14.73 | 14.66 | 13.66 | 12.96 | | 11.34 | 12.01 |
| MnO | 0.18 | 0.20 | 0.20 | 0.18 | 0.18 | 0.19 | 0.19 | 0.18 | | 0.16 | 0.16 |
| MgO | 4.25 | 7.42 | 4.58 | 7.33 | 8.30 | 7.87 | 7.03 | 6.55 | | 5.30 | 9.05 |
| CaO | 11.69 | 9.64 | 11.90 | 8.68 | 10.19 | 9.31 | 8.73 | 8.43 | | 7.59 | 14.34 |
| $Na_2O$ | 2.48 | 2.37 | 2.43 | 2.58 | 2.23 | 2.36 | 2.56 | 2.70 | | 3.45 | 1.95 |
| $K_2O$ | 2.80 | 2.35 | 2.59 | 2.27 | 2.01 | 2.28 | 2.54 | 2.66 | | 3.41 | 1.44 |
| $P_2O_5$ | 0.72 | 0.72 | 0.71 | 0.88 | 0.74 | 0.83 | 0.97 | 1.01 | | 0.70 | 0.24 |
| LOI | 7.75 | 5.34 | 7.48 | 5.22 | 3.43 | 4.72 | 5.08 | 4.84 | | 3.94 | 6.14 |
| Total | 99.82 | 99.91 | 99.86 | 99.88 | 100.16 | 100.67 | 100.44 | 99.99 | | 99.60 | 99.65 |
| Mg# | 27 | 38 | 27 | 36 | 38 | 37 | 36 | 36 | | 34 | 46 |
| Rb | 82.70 | 48.00 | 65.49 | 47.48 | 39.65 | 48.91 | 56.36 | 56.93 | 57.15 | 93.69 | 19.07 |
| Cs | 23.55 | 4.76 | 14.05 | 1.04 | 0.72 | 1.22 | 1.43 | 1.38 | 1.32 | 1.29 | < DL |
| Be | 1.61 | 2.09 | 3.35 | 2.42 | 1.77 | 1.91 | 2.18 | 2.27 | 2.35 | 1.91 | < DL |
| Sr | 858.10 | 812.30 | 881.20 | 784.20 | 733.70 | 739.10 | 857.40 | 902.20 | 891.18 | 631.70 | 505.60 |
| Ba | 539.10 | 543.70 | 580.90 | 531.20 | 476.80 | 499.50 | 579.10 | 599.70 | 597.89 | 984.00 | 410.80 |
| V | 344.40 | 381.80 | 366.60 | 404.80 | 432.60 | 401.40 | 359.70 | 323.80 | 369.86 | 319.50 | 461.90 |
| Cr | 48.82 | 23.39 | 13.58 | 29.56 | 54.97 | 34.47 | 12.73 | < DL | 12.77 | < DL | 59.90 |
| Co | 38.89 | 44.37 | 40.27 | 47.15 | 50.07 | 46.69 | 40.86 | 35.30 | 44.50 | 25.86 | 56.16 |
| Ni | 40.96 | 25.77 | 22.47 | 32.96 | 44.15 | 35.62 | 25.80 | 18.71 | 31.48 | < DL | 48.72 |
| Cu | 44.76 | 47.00 | 43.57 | 65.64 | 64.12 | 64.83 | 61.52 | 54.74 | 72.67 | 10.14 | 64.03 |
| Zn | 130.30 | 134.60 | 140.30 | 200.50 | 166.30 | 168.70 | 169.10 | 163.40 | 182.21 | 127.20 | 92.20 |
| Ga | 23.92 | 24.45 | 24.79 | 24.85 | 23.96 | 24.00 | 24.34 | 23.57 | 23.96 | 21.86 | 19.94 |
| Y | 25.13 | 26.75 | 27.27 | 28.53 | 26.53 | 27.21 | 29.85 | 29.72 | 30.46 | 28.08 | 18.44 |
| Nb | 61.58 | 59.71 | 62.31 | 65.21 | 55.08 | 59.56 | 70.23 | 72.88 | 73.86 | 63.92 | 27.48 |
| Ta | 4.77 | 4.54 | 4.84 | 5.06 | 4.24 | 4.61 | 5.34 | 5.46 | 5.65 | 4.86 | 2.10 |
| Zr | 272.30 | 266.70 | 277.30 | 278.60 | 243.60 | 259.60 | 293.90 | 294.40 | 301.07 | 298.40 | 149.10 |
| Hf | 6.42 | 6.30 | 6.65 | 6.66 | 6.08 | 6.40 | 6.95 | 6.77 | 6.94 | 7.01 | 4.40 |
| Mo | 5.72 | 1.13 | 1.97 | 1.24 | 1.15 | 1.55 | 1.69 | 1.62 | | 1.05 | 2.62 |
| Sn | 2.86 | 2.93 | 2.82 | 3.01 | 2.94 | 2.90 | 2.91 | 2.84 | | 3.48 | 3.66 |
| Pb | 3.84 | 8.10 | 4.52 | 10.68 | 7.48 | 9.64 | 9.11 | 7.67 | 10.24 | 10.20 | 2.27 |
| U | 1.42 | 1.37 | 1.46 | 1.49 | 1.25 | 1.36 | 1.60 | 1.66 | 1.70 | 1.89 | 0.61 |
| Th | 4.70 | 4.43 | 4.77 | 5.12 | 4.26 | 4.63 | 5.42 | 5.67 | 5.79 | 6.28 | 1.93 |
| La | 48.86 | 48.13 | 51.47 | 52.49 | 42.42 | 46.99 | 55.21 | 55.74 | 57.21 | 56.41 | 22.33 |
| Ce | 106.20 | 105.40 | 111.50 | 113.40 | 94.45 | 104.30 | 120.60 | 120.20 | 123.63 | 121.60 | 52.22 |
| Pr | 12.83 | 12.80 | 13.52 | 13.79 | 11.74 | 12.79 | 14.64 | 14.57 | 14.90 | 14.60 | 7.06 |
| Nd | 50.76 | 51.20 | 53.73 | 54.77 | 47.79 | 51.94 | 58.28 | 57.57 | 58.58 | 57.42 | 30.80 |
| Sm | 9.39 | 9.66 | 10.19 | 10.36 | 9.41 | 10.03 | 10.95 | 10.70 | 10.87 | 10.47 | 6.71 |
| Eu | 2.80 | 2.90 | 3.08 | 3.07 | 2.88 | 3.01 | 3.25 | 3.23 | 3.25 | 3.12 | 2.13 |
| Gd | 7.28 | 7.69 | 8.03 | 8.32 | 7.68 | 8.05 | 8.61 | 8.49 | 8.73 | 8.41 | 5.71 |
| Tb | 1.01 | 1.07 | 1.11 | 1.12 | 1.06 | 1.10 | 1.19 | 1.16 | 1.18 | 1.14 | 0.79 |
| Dy | 5.29 | 5.55 | 5.74 | 5.83 | 5.62 | 5.77 | 6.19 | 6.12 | 6.22 | 5.95 | 4.05 |
| Ho | 0.91 | 0.96 | 1.01 | 1.01 | 0.97 | 0.99 | 1.08 | 1.06 | 1.08 | 1.02 | 0.69 |
| Er | 2.29 | 2.43 | 2.51 | 2.58 | 2.44 | 2.53 | 2.75 | 2.74 | 2.77 | 2.55 | 1.66 |
| Tm | 0.31 | 0.33 | 0.33 | 0.34 | 0.32 | 0.34 | 0.37 | 0.37 | 0.37 | 0.34 | 0.21 |
| Yb | 1.92 | 1.98 | 2.08 | 2.10 | 2.01 | 2.05 | 2.28 | 2.30 | 2.32 | 2.14 | 1.27 |
| Lu | 0.28 | 0.29 | 0.31 | 0.32 | 0.30 | 0.30 | 0.34 | 0.34 | 0.35 | 0.31 | 0.18 |

**Table 4.1.** (cont.)

| Domain | CCR | | | | | |
|---|---|---|---|---|---|---|
| Sector | West | West | West | West | West | West |
| UTM coor. | 31T | 31T | 31T | 31T | 31T | 31T |
| | 465860 | 465860 | 466218 | 466218 | 470170 | 467387 |
| | 4629223 | 4629223 | 4629029 | 4629029 | 4630359 | 4631372 |
| Rock type | L | | | | | |
| Classification | CAMP | CAMP | CAMP | CAMP | CAMP | CAMP |
| **Sample** | **SFB-1(r)** | **SFB-2(r)** | **SFB-3** | **SFB-4** | **SFB-5** | **SFB-6** |
| $SiO_2$ | 43.29 | 41.73 | 43.38 | 42.39 | 42.60 | 44.08 |
| $TiO_2$ | 2.80 | 2.93 | 1.91 | 2.72 | 3.09 | 2.93 |
| $Al_2O_3$ | 11.36 | 11.56 | 8.24 | 10.64 | 14.09 | 14.11 |
| $Fe_2O_3^T$ | 11.26 | 11.24 | 9.78 | 11.66 | 12.09 | 11.78 |
| MnO | 0.18 | 0.13 | 0.15 | 0.14 | 0.17 | 0.19 |
| MgO | 10.03 | 9.92 | 14.03 | 11.21 | 4.39 | 6.54 |
| CaO | 11.74 | 12.37 | 13.15 | 11.87 | 10.38 | 8.64 |
| $Na_2O$ | 2.51 | 1.99 | 1.78 | 2.29 | 2.87 | 3.91 |
| $K_2O$ | 1.40 | 1.42 | 0.76 | 1.37 | 2.12 | 2.18 |
| $P_2O_5$ | 0.42 | 0.45 | 0.26 | 0.38 | 0.64 | 0.62 |
| LOI | 4.26 | 5.98 | 5.62 | 4.25 | 7.33 | 4.80 |
| Total | 99.24 | 99.72 | 99.07 | 98.92 | 99.77 | 99.79 |
| | | | | | | |
| Mg# | 50 | 50 | 61 | 52 | 29 | 38 |
| | | | | | | |
| Rb | 35.24 | 34.21 | 23.17 | 34.83 | 58.66 | 59.52 |
| Cs | 19.15 | 33.60 | 11.15 | 15.17 | 2.71 | 12.94 |
| Be | 1.16 | 1.11 | < DL | 1.06 | 1.68 | 1.52 |
| Sr | 492.50 | 357.80 | 293.10 | 444.70 | 692.70 | 507.60 |
| Ba | 435.70 | 604.60 | 627.90 | 395.60 | 644.30 | 586.70 |
| V | 314.20 | 330.70 | 239.30 | 327.00 | 301.50 | 286.50 |
| Cr | 629.20 | 606.80 | 1304.00 | 744.80 | 140.30 | 220.70 |
| Co | 51.31 | 56.18 | 56.34 | 55.89 | 35.38 | 34.03 |
| Ni | 167.00 | 167.80 | 294.30 | 213.50 | 55.03 | 85.08 |
| Cu | 92.59 | 100.60 | 160.80 | 99.56 | 24.53 | 51.56 |
| Zn | 99.95 | 139.10 | 77.34 | 101.80 | 102.70 | 155.60 |
| Ga | 18.45 | 18.86 | 13.47 | 17.94 | 23.16 | 22.03 |
| Y | 19.76 | 21.27 | 14.71 | 19.97 | 28.54 | 26.80 |
| Nb | 40.86 | 42.84 | 27.85 | 36.20 | 59.24 | 56.65 |
| Ta | 3.15 | 3.31 | 2.18 | 2.83 | 4.56 | 4.45 |
| Zr | 208.50 | 216.70 | 144.90 | 194.50 | 306.00 | 294.40 |
| Hf | 5.11 | 5.32 | 3.58 | 4.96 | 7.35 | 7.13 |
| Mo | 1.45 | 1.57 | 1.18 | 8.82 | 8.17 | 9.78 |
| Sn | 2.49 | 2.42 | 1.75 | 2.35 | 2.85 | 2.81 |
| Pb | 3.64 | 3.84 | 3.14 | 3.95 | 8.73 | 4.58 |
| U | 1.12 | 1.34 | 0.74 | 0.95 | 1.52 | 1.52 |
| Th | 3.82 | 3.82 | 2.58 | 3.32 | 5.49 | 5.43 |
| La | 35.49 | 37.66 | 24.55 | 33.18 | 55.05 | 53.44 |
| Ce | 76.45 | 82.08 | 52.78 | 72.24 | 116.40 | 113.60 |
| Pr | 9.33 | 10.12 | 6.49 | 8.92 | 14.04 | 13.59 |
| Nd | 36.85 | 40.13 | 26.05 | 36.00 | 55.48 | 52.77 |
| Sm | 7.08 | 7.67 | 5.08 | 7.04 | 10.16 | 9.67 |
| Eu | 2.16 | 2.36 | 1.57 | 2.18 | 3.06 | 2.87 |
| Gd | 5.74 | 6.26 | 4.20 | 5.73 | 8.09 | 7.63 |
| Tb | 0.79 | 0.86 | 0.59 | 0.80 | 1.12 | 1.05 |
| Dy | 4.18 | 4.48 | 3.11 | 4.16 | 5.93 | 5.60 |
| Ho | 0.72 | 0.76 | 0.53 | 0.73 | 1.04 | 0.98 |
| Er | 1.82 | 1.97 | 1.38 | 1.88 | 2.71 | 2.56 |
| Tm | 0.25 | 0.26 | 0.19 | 0.25 | 0.37 | 0.34 |
| Yb | 1.56 | 1.62 | 1.14 | 1.53 | 2.30 | 2.18 |
| Lu | 0.22 | 0.24 | 0.17 | 0.23 | 0.34 | 0.32 |

Domains: BCB - Basque-Cantabrian Basin; NPB - North Pyrenean Basins; EP - Eastern Pyrenees; CCR - Catalonian Coastal Ranges.

Rock types: Pi - Picrite; B - Basaltic rock; G - Gabbroic rock; Tr - Trachyte; L - Lamprophyre; Sye – Syenite.

Classification criteria according to Le Maitre (2002). PIC – picrite; BAS – basalt; TRB – trachybasalt; BTR – basaltic trachyandesite; TR – trachyte; GAB – gabbro; MNZ – monzonite; SYE – syenite; MCH – monchiquite; SAN – sannaite; CAMP – camptonite.

$Fe_2O_3^T$: total iron expressed as $Fe_2O_3$. LOI: Loss On Ignition.

Mg# represents magnesium number: 100 MgO / (MgO + FeO) and FeO = 0.9 $Fe_2O_3^T$.

< DL: below the detection limit.

([a]) UXT: replicate analysis of URR.
([b]) CAL-Gr: bulk trace element composition of the groundmass in the Calella de Palafrugell lamprophyre, modelled in Ubide et al. (2012*a*) –see Table 6.3-.

*(SARM)* in Nancy (France). The samples were analysed by ICP-AES for major elements and ICP-MS for trace elements. Details of the analytical procedures and detection limits are available at http://www.crpg.cnrs-nancy.fr/SARM/. The analyses cover 10 samples from the Basque-Cantabrian Basin, 2 samples from the North Pyrenean Basins, 9 samples from the Eastern Pyrenees and 16 samples from the Catalonian Coastal Ranges. A replicate of one of the samples from the Basque-Cantabrian Basin (URR) was sent for analysis with a different name (UXT) to test the reproducibility of the methods; the results were very similar (Table 4.1). In addition, the bulk composition of the groundmass of one of the lamprophyres in the Catalonian Coastal Ranges (CAL-Gr) is available from Ubide et al. (2012*a*).

From among the sample powders analysed for elemental concentrations, 13 were selected for Sr, Nd and Pb isotope analyses (results in Table 4.2). These included 4 samples from the Basque-Cantabrian Basin, 3 samples from the Eastern Pyrenees and 6 samples from the Catalonian Coastal Ranges. Measurements were carried out at the *SGIker-Geochronology and Isotopic Geochemistry* facility of the Universidad del País Vasco UPV/EHU (Spain). Regarding Sr and Nd isotope analyses, chemical procedures for sample preparation are described in Pin and Bassin (1992), Pin et al. (1994) and Pin and Santos Zalduegui (1997). Sm and Nd concentrations were determined by isotope-dilution TIMS using a mixed $^{149}Sm$-$^{150}Nd$ tracer. The $^{147}Sm/^{144}Nd$ values are precise to ± 0.2 % at the 95 % confidence level. $^{143}Nd/^{144}Nd$ ratios were measured by TIMS in a Finnigan Mat-262 instrument in static multicollection mode, and corrected for mass fractionation by normalization to $^{146}Nd/^{144}Nd = 0.7219$ (Wasserburg et al., 1981; Thirlwall, 1991). The La Jolla isotopic standard and its uncertainty (2 SD) were measured under the same conditions and gave $^{143}Nd/^{144}Nd = 0.512101 \pm 0.000003$ (n = 2). In the calculations of εNdT, $^{143}Nd/^{144}Nd_{CHUR}=0.512638$ and $^{147}Sm/^{144}Nd_{CHUR}=0.1967$ (Jacobsen and Wasserburg, 1984) were used. $^{87}Sr/^{86}Sr$ ratios were measured by MC-ICP-MS using a high-resolution Thermo Fisher Scientific Neptune instrument in static multicollection mode, and corrected for mass fractionation by normalization to $^{88}Sr/^{86}Sr = 8.375209$ (Steiger and Jäger, 1977). The reported $^{87}Sr/^{86}Sr$ ratios were adjusted to the NBS 987 standard, measured under the same conditions with a value and uncertainty (2 SD) of $^{87}Sr/^{86}Sr = 0.710270 \pm 0.000011$ (n = 3). The $^{87}Rb/^{86}Sr$ values were calculated considering the $^{87}Sr/^{86}Sr$ values and the elemental concentration in Rb and Sr (e.g., Faure, 1991). Pb isotope analyses were performed using a Neptune MC-ICP-MS instrument. Chemical procedures for Pb extraction followed those described by Manhès et al. (1987). Pb isotopes were corrected for instrumental mass bias by internal second element normalisation using known amounts of Tl and the exponential mass fractionation law, a $^{205}Tl/^{203}Tl$ ratio of 2.3889 was used. The average ratios for the NBS981 Pb standard and their uncertainties (2 SD) measured under the same conditions are $^{206}Pb/^{204}Pb = 16.9439 \pm 0.0038$, $^{207}Pb/^{204}Pb = 15.5011 \pm 0.0030$, $^{208}Pb/^{204}Pb = 36.7288 \pm 0.0071$, $^{208}Pb/^{206}Pb = 2.16767 \pm 0.00017$ and $^{207}Pb/^{206}Pb = 0.91484 \pm 0.00007$ (n = 67).

**Table 4.2.** Sr-Nd-Pb isotope composition of selected samples. Uncertainties are quoted at 2σ.

| Domain | BCB | BCB | BCB | BCB | EP | EP | EP |
|---|---|---|---|---|---|---|---|
| **Sample** | **ELG-08** | **FR-9** | **8057** | **MALZA-1** | **CORB-2** | **VIN-2** | **FIT-2** |
| $^{87}Rb/^{86}Sr$ | 0.09421 | 0.21763 | 0.14133 | 0.32276 | 0.09539 | 0.10886 | 0.64184 |
| $^{87}Sr/^{86}Sr$ | 0.70631 | 0.70575 | 0.70692 | 0.70476 | 0.70520 | 0.70502 | 0.70484 |
| | ± 0.00001 | ± 0.00001 | ± 0.00001 | ± 0.00001 | ± 0.00001 | ± 0.00001 | ± 0.00001 |
| $^{87}Sr/^{86}Sr_t$ | 0.70618 | 0.70544 | 0.70672 | 0.70431 | 0.70508 | 0.70488 | 0.70401 |
| εSr | 25.50 | 15.06 | 33.22 | -1.10 | 9.75 | 6.91 | -5.39 |
| $^{147}Sm/^{144}Nd$ | 0.1143 | 0.1103 | 0.1150 | 0.0857 | 0.1049 | 0.0929 | 0.0709 |
| $^{143}Nd/^{144}Nd$ | 0.512766 | 0.512761 | 0.512776 | 0.512782 | 0.512750 | 0.512726 | 0.512698 |
| | ± 0.000003 | ± 0.000003 | ± 0.000003 | ± 0.000003 | ± 0.000003 | ± 0.000003 | ± 0.000003 |
| $^{143}Nd/^{144}Nd_t$ | 0.512691 | 0.512689 | 0.512701 | 0.512726 | 0.512688 | 0.512671 | 0.512656 |
| εNd | 3.55 | 3.50 | 3.74 | 4.23 | 3.24 | 2.91 | 2.62 |
| $T^{Nd}_{DM}$ (Ga) | 0.59 | 0.57 | 0.58 | | 0.56 | 0.54 | |
| $^{206}Pb/^{204}Pb$ | 20.257 | 20.659 | 19.540 | 20.050 | 20.627 | 20.974 | 21.152 |
| | ± 0.004 | ± 0.007 | ± 0.004 | ± 0.004 | ± 0.004 | ± 0.004 | ± 0.004 |
| $^{207}Pb/^{204}Pb$ | 15.664 | 15.668 | 15.700 | 15.632 | 15.680 | 15.698 | 15.704 |
| | ± 0.003 | ± 0.005 | ± 0.003 | ± 0.003 | ± 0.003 | ± 0.003 | ± 0.003 |
| $^{208}Pb/^{204}Pb$ | 40.229 | 40.709 | 39.624 | 40.314 | 40.428 | 40.818 | 41.037 |
| | ± 0.008 | ± 0.013 | ± 0.007 | ± 0.007 | ± 0.007 | ± 0.007 | ± 0.007 |
| $^{208}Pb/^{206}Pb$ | 1.986 | 1.971 | 2.028 | 2.011 | 1.960 | 1.946 | 1.940 |
| $^{207}Pb/^{206}Pb$ | 0.773 | 0.758 | 0.803 | 0.780 | 0.760 | 0.748 | 0.742 |

**Table 4.2.** (cont.)

| Domain | CCR | CCR | CCR | CCR | CCR | CCR | CCR |
|---|---|---|---|---|---|---|---|
| **Sample** | **AIG-05** | **AIG-05** [a] | **CAL-2** | **SAG-03B** | **LLAG-01** | **SFB-3** | **SFB-6** |
| $^{87}Rb/^{86}Sr$ | 0.17088 | | 0.15627 | 0.42897 | 0.10907 | 0.22863 | 0.33914 |
| $^{87}Sr/^{86}Sr$ | 0.70387 | 0.70385 | 0.70376 | 0.70594 | 0.70402 | 0.70552 | 0.70582 |
| | ± 0.00001 | ± 0.00002 | ± 0.00001 | ± 0.00001 | ± 0.00001 | ± 0.00001 | ± 0.00001 |
| $^{87}Sr/^{86}Sr_t$ | 0.70368 | | 0.70358 | 0.70546 | 0.70390 | 0.70526 | 0.70543 |
| εSr | -10.30 | | -11.73 | 14.91 | -7.19 | 12.11 | 14.55 |
| $^{147}Sm/^{144}Nd$ | 0.1112 | | 0.1160 | 0.1097 | 0.1282 | 0.1149 | 0.1086 |
| $^{143}Nd/^{144}Nd$ | 0.512775 | 0.512792 | 0.512787 | 0.512777 | 0.512827 | 0.512764 | 0.512751 |
| | ± 0.000003 | ± 0.000007 | ± 0.000003 | ± 0.000003 | ± 0.000003 | ± 0.000003 | ± 0.000003 |
| $^{143}Nd/^{144}Nd_t$ | 0.512717 | | 0.512726 | 0.512720 | 0.512760 | 0.512704 | 0.512694 |
| εNd | 3.55 | | 3.73 | 3.60 | 4.39 | 3.29 | 3.10 |
| $T^{Nd}_{DM}$ (Ga) | 0.56 | | 0.57 | 0.55 | 0.58 | 0.60 | 0.58 |
| $^{206}Pb/^{204}Pb$ | 20.918 | 21.002 | 19.364 | 19.062 | 19.300 | 19.239 | 19.457 |
| | ± 0.004 | ± 0.015 | ± 0.004 | ± 0.006 | ± 0.005 | ± 0.005 | ± 0.004 |
| $^{207}Pb/^{204}Pb$ | 15.779 | 15.766 | 15.696 | 15.677 | 15.651 | 15.651 | 15.662 |
| | ± 0.003 | ± 0.020 | ± 0.003 | ± 0.005 | ± 0.004 | ± 0.004 | ± 0.003 |
| $^{208}Pb/^{204}Pb$ | 40.518 | 40.563 | 39.794 | 39.280 | 39.290 | 39.288 | 39.816 |
| | ± 0.007 | ± 0.060 | ± 0.007 | ± 0.013 | ± 0.009 | ± 0.010 | ± 0.007 |
| $^{208}Pb/^{206}Pb$ | 1.937 | | 2.055 | 2.061 | 2.036 | 2.042 | 2.046 |
| $^{207}Pb/^{206}Pb$ | 0.754 | | 0.811 | 0.822 | 0.811 | 0.813 | 0.805 |

Domains: BCB - Basque-Cantabrian Basin; EP - Eastern Pyrenees; CCR - Catalonian Coastal Ranges.
($_t$) Age of the rocks: ca. 100 Ma in the Basque-Cantabrian Basin and North Pyrenenan Basins, ca. 90 Ma in the Eastern Pyrenees and ca. 80 Ma in the Catalonian Coastal Ranges (see Chapter 3).
$T^{Nd}_{DM}$: T-depleted mantle model ages for mafic rocks.
([a]) A second aliquot of sample AIG-05 was analysed in a different laboratory.

A second aliquot of sample AIG-05 from the Catalonian-Coastal Ranges was prepared and analysed by P. Larrea and D. Kuentz at the *Isotope Geochemistry & Mass Spectrometry Laboratory* of the Miami University (Ohio, USA). Sr, Nd and Pb isotope ratios were determined by TIMS following the methods described in Larrea et al. (submitted). The results (Table 4.2) were very similar to those obtained at the *SGIker-Geochronology and*

*Isotopic Geochemistry* facility of the University of the Basque Country UPV/EHU (Spain), and most of them agree within the uncertainty. In order to keep data in the figures comparable, only data from the *IBERCRON* laboratory are plotted.

For comparison, a large geochemical database was constructed including elemental and isotopic compositions of magmatisms of Late Variscan to Quaternary age recorded in Iberia. A significant amount of data corresponds to previous studies carried out by the research group, and there are also numerous data from other authors.

## 4.4. Petrology

The samples selected for geochemical analyses cover diverse petrological typologies. The classification of all the samples is presented in Table 4.1 and detailed mineral assemblages and crystallisation sequences are available in the Electronic Supplement.

Volcanic and hypovolcanic rocks occur in the Basque-Cantabrian Basin and the North Pyrenean Basins. There are basaltic-andesitic rocks, locally picritic, as well as trachytes. Special care was exercised to obtain fresh samples, as the studied volcanic outcrops show widespread alteration.

Basaltic-andesitic samples (ELG-08, FR-1, FR-9, MALZA-B and 8057 from the Basque-Cantabrian Basin, and COG-3 from the North Pyrenean Basins) have porphyritic or intergranular textures (Fig. 4.2A), mainly composed of feldspars (30 – 75 vol. %) and clinopyroxene (Ti-rich diopside), with volume fractions that vary from very low or 0 % up to 60 %. The relative proportions of these two minerals vary with the more or less mafic character of the lavas. The mineral assemblage is completed with Fe-Ti oxides (2 – 5 vol. %), olivine pseudomorphs (0 – 6 vol. %), amphibole (mainly kaersutite; 0 – 5 vol. %), and minor amounts of biotite, titanite, apatite, epidote, calcite and chlorite. Some of the samples include chlorite and other phyllosilicates occupying intercrystalline spaces that may be interpreted as destabilised glass. In these cases, the original texture would be intersertal and thus the rock hypocrystalline.

Sample ELG-08 was extracted from a large sill that becomes locally picritic due to the accumulation of olivine crystals. The picrite, sampled as ELG-04, has a volume fraction of olivine of 70 – 80 %. This rock displays a cumulate (heteroadcumulate) texture where olivine crystals are the main cumulus phase (Fig. 4.2B). Most olivine crystals are transformed into an assemblage of serpentine group minerals and opaque grains; they frequently have a rim of bluish chlorite. Olivine relicts display homogeneous

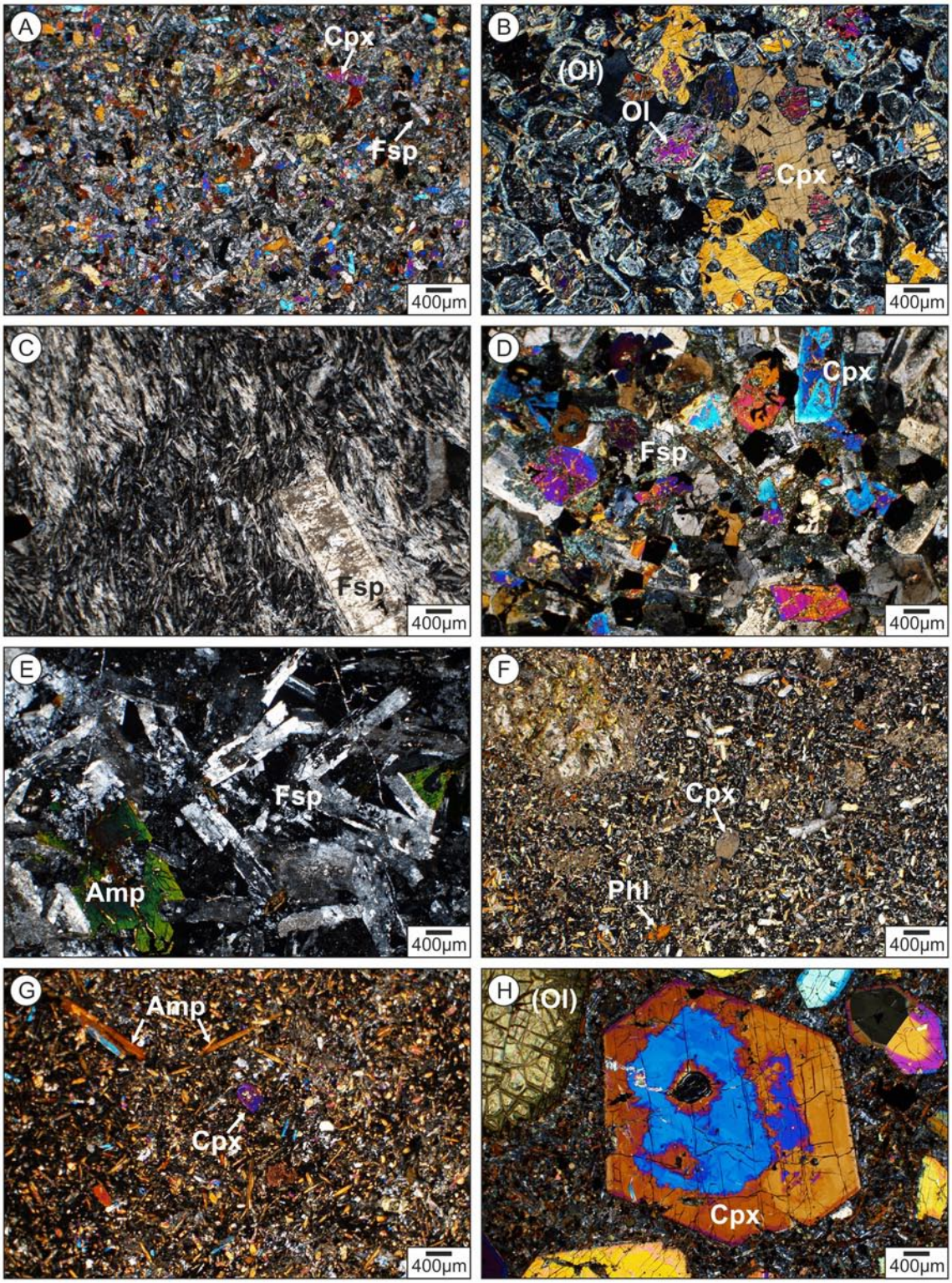


**Fig. 4.2.** Photomicrographs of representative samples. Cross-polarised transmitted light. A: Basalt ELG-08 from the Basque-Cantabrian Basin. B: Picrite ELG-04 from the Basque-Cantabrian Basin. C: Trachyte MALZA-1 from the Basque-Cantabrian Basin. D: Gabbro URR from the Basque-Cantabrian Basin. E: Syenite FIT-2 from the Eastern Pyenees. F: Monchiquite CORB-2 from the Eastern Pyrenees. G: Sannaite VIN-2 from the Eastern Pyrenees. H: Camptonite from the Catalonian Coastal Ranges. Mineral abbreviations are after Whitney and Evans (2010).

compositions, with forsterite contents of $Fo_{81-83}$. Opaque minerals (Cr-rich spinel and Fe-Ti oxides) are also present as cumulus phases (2 vol. %). Clinopyroxene (Ti-rich diopside; 10 – 15 vol. %) represents the principal intercumulus phase, developing poikilitic crystals (Fig. 4.2B). The remaining intercumulus spaces are filled with amphibole, biotite and Fe-Ti oxides that crystallised from the residual melt. The mineral assemblage is completed with minor amounts of feldspars, epidote, apatite and green chlorite.

The trachyte sample (MALZA-1 from the Basque-Cantabrian Basin) is composed almost entirely of oriented feldspar crystals (97 vol. %) with a bimodal size distribution, producing a porphyritic and trachytic texture (Fig. 4.2C). There are also opaque minerals (2 vol. %), calcite (1 vol. %) and accessory apatite.

Intrusive rocks on the other hand, are present in all the sectors. They become progressively more abundant towards the east and represent the only Cretaceous magmatics in the Eastern Pyrenees and the Catalonian Coastal Ranges. There are gabbro-monzonite-teschenite rocks as well as syenites and lamprophyre intrusions.

Mafic intrusive samples include gabbros SGR, URR/UXT and URR-3 from the Basque-Cantabrian Basin and monzonite AUB from the North Pyrenean Basins, which can be correlated to the teschenites described in previous studies (Azambre et al., 1992 and Cabanis and Le Fur-Balouet, 1990). These rocks have granular to intergranular textures (Fig. 4.2D; see also Fig. 3.2A, 3.2B) composed of feldspars (35 – 60 vol. %), clinopyroxene (Ti-rich diopside; 6 – 40 vol. %), amphibole (mainly kaersutite; up to 20 vol. %), opaque minerals (Fe-Ti oxides and rarely Cr-rich spinel; 3 – 6 vol. %) and minor abundances of olivine pseudomorphs, biotite, titanite, analcime, prehnite, apatite, epidote, calcite and chlorite. Accessory zircon is recognised in sample URR/UXT. Mafic minerals represent an important fraction (30 – 40 vol. %) of the mineral assemblage, so that samples with low proportions of clinopyroxene are especially rich in amphibole (e.g., sample AUB; see the Electronic Supplement).

Syenite samples (FIT-1, FIT-2 and FIT-3 from the Eastern Pyrenees) have an intergranular texture dominated by feldspars (ca. 70 vol. %) (Fig. 4.2E). Analcime is relatively frequent (10 vol. %) and followed in abundance by amphibole (hastingsite; 8 vol. %), clinopyroxene (aegirine-augite and minor aegirine; 4 vol. %), nepheline (3 vol. %), biotite (2 vol. %), titanite (2 vol. %) and lavenite (1 vol. %). Opaque minerals and zircon are accessory phases.

Lamprophyres crop out in the Eastern Pyrenees and the Catalonian Coastal Ranges. The Eastern Pyrenean lamprophyres are classified as monchiquites (samples CORB-1, CORB-2, CORB-3 and CORB-6) and sannaites (samples VIN-1 and VIN-2). The monchiquites show a porphyritic texture and a mineral assemblage dominated by clinopyroxene (Ti-rich

diopside; 50 – 55 vol. %) and phlogopite (25 – 30 vol. %) (Fig. 4.2F). Opaque minerals (Fe-Ti oxides and minor Cr-rich spinel) represent ca. 6 vol. % of the rock, whereas olivine pseudomorphs vary between 2 and 5 vol. %. There are also minor amounts of feldspars, nepheline, analcime, apatite, calcite and glass transformed into chlorite and other secondary products. These rocks enclose ultramafic xenoliths linked to ultramafic bodies cropping out in the Pyrenees (Azambre and Fabriès, 1989). The sannaites on the other hand, are microporphyritic and mainly composed of amphibole (25 – 40 vol. % kaersutite and minor hastingsite) and clinopyroxene (Ti-rich diopside; 20 – 25 vol. %) (Fig. 4.2G). Fe-Ti oxides (2 – 6 vol. %), feldspars (6 – 10 vol. %), glass transformed into cryptocrystalline assemblages (10 – 25 vol. %) and minor proportions of analcime, titanite, apatite and calcite complete the mineral assemblage.

In the Catalonian Coastal Ranges, lamprophyre intrusions are the only representatives of the Cretaceous magmatism. These samples (AIG-04, AIG-05, AIG-08, CAL-1, CAL-2, CAL-3, CAL-4, CAL-5, CAL-Gr, SAG-03B, LLAG-01, SFB-1(r), SFB-2(r), SFB-3, SFB-4, SFB-5 and SFB-6) are camptonites with a strongly porphyritic texture in most cases (see Chapter 5) (Fig. 4.2H; see also Fig. 3.2E, 3.2F, 3.2G, 5.8, 5.9). They consist of clinopyroxene (mainly Ti-rich diopside), which is a minor component in certain intrusions but reaches up to 50 vol. % in others, amphibole (mainly kaersutite; 25 – 55 vol. %), Fe-Ti oxides (6 – 14 vol. %), olivine pseudomorphs (up to 8 vol. %; relicts have forsterite contents of $Fo_{88-89}$), feldspars (6 – 60 vol. %) and minor amounts of biotite, apatite, analcime, calcite and chlorite. The amount of glass, which is mostly recrystallised to chlorite and other secondary products (frequently cryptocrystalline), reaches ca. 30 vol. % of the rock at the chilled margins of certain intrusions (see detailed mineral assemblages and crystallisation sequences in the Electronic Supplement).

## 4.5. Geochemistry

### 4.5.1. Classification and affinity

The classification of the samples (Table 4.1) follows criteria by Le Maitre (2002). Whole rock major element and trace element compositions are presented in Table 4.1. Loss On Ignition (LOI) values are relatively high (1.40 – 8.58 wt. %). This is due to the alteration of certain samples (e.g., the picrite sample ELG-04), but more frequently due to the abundance of hydrous minerals like amphibole or biotite, or due to the presence of calcite and hydrous minerals filling vesicles, which are widespread in lamprophyres (Ubide et al., 2012*a* –see Chapter 6-).

Irrespective of their volcanic, subvolcanic or intrusive origin, all the samples have been plotted in the Total Akalis vs. Silica diagram (TAS diagram; Le Bas et al., 1986) to evaluate

their distribution (Fig. 4.3). Based on their $SiO_2$ concentrations, most samples are basic to ultrabasic. The syenite samples from the Eastern Pyrenees (FIT-1, FIT-2 and FIT-3) are intermediate whereas the trachyte sample from the Basque-Cantabrian Basin (MALZA-1) is intermediate-acid. The high alkalis concentration in all the rocks indicates their alkaline geochemical affinity.

The distribution of the samples agrees with previous studies and defines two evolutionary trends (Fig. 4.3). Rocks from the Basque-Cantabrian Basin and the North Pyrenean Basins

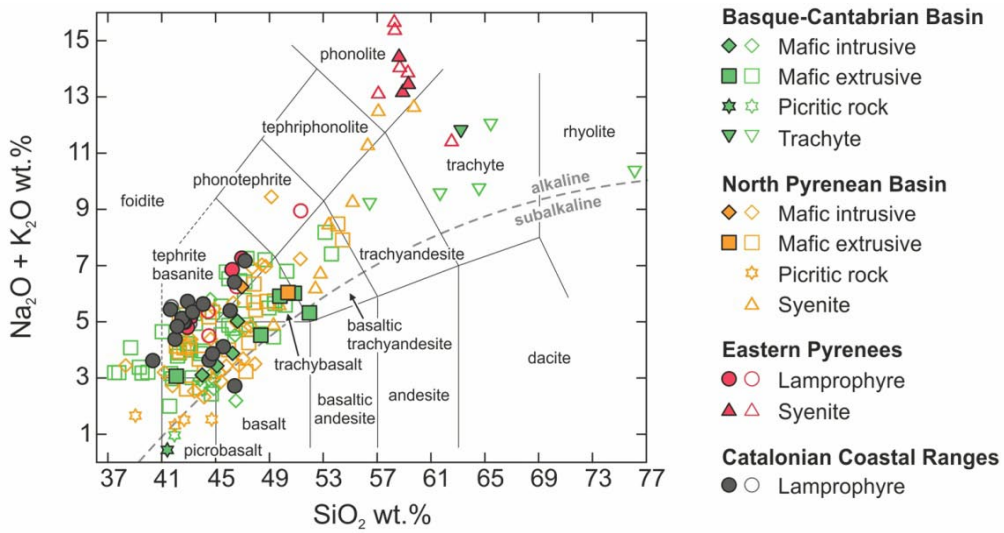


**Fig. 4.3.** Total Alkalis vs. Silica – TAS diagram (Le Bas et al., 1986; analyses recalculated to 100% on an anhydrous basis). Filled symbols represent data obtained in this study and empty symbols represent data from the literature included for comparison: data from the Basque-Cantabrian Basin and North Pyrenean basins are from Azambre et al. (1992) and Cabanis and Le Fur-Balouet (1990), data from the Eastern Pyrenees are from Azambre et al. (1992) and data from the Catalonian Coastal Ranges are from Enrique (2009). Mafic intrusives include gabbros, teschenites, syenoteschenites, dolerites and monzonites; mafic extrusives include basalts, andesites, trachybasalts and basaltic trachyandesites; picritic rocks include picrites and cortlandites; lamprophyres include monchiquites, sannaites and camptonites.

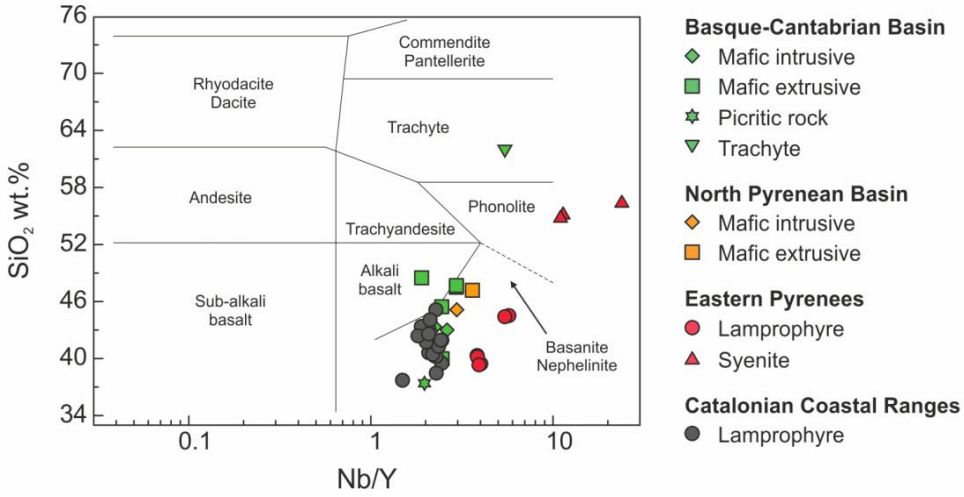


**Fig. 4.4.** $SiO_2$ vs. Nb/Y diagram (Winchester and Floyd, 1977). Data from the literature lack many trace elements including Nb and Y, so they cannot be included for comparison.

define a $SiO_2$-mildly-saturated or -undersaturated trend (with normative olivine and hypersthene or normative olivine and nepheline or leucite) with a saturated rock (trachyte MALZA-1) in the silica-rich compositions. On the contrary, rocks from the Eastern Pyrenees and the Catalonian Coastal Ranges define a steeper, $SiO_2$-undersaturated trend.

Given the high LOI values of many samples, the classification scheme proposed by Winchester and Floyd (1977), which introduces immobile elements, has been also applied. According to the $SiO_2$ vs. Nb/Y diagram (Fig. 4.4), mafic samples are classified in the basanite/nephelinite field or the alkali basalt field. Syenite samples plot outside the phonolite field whereas the trachyte sample plots in the trachyte field.

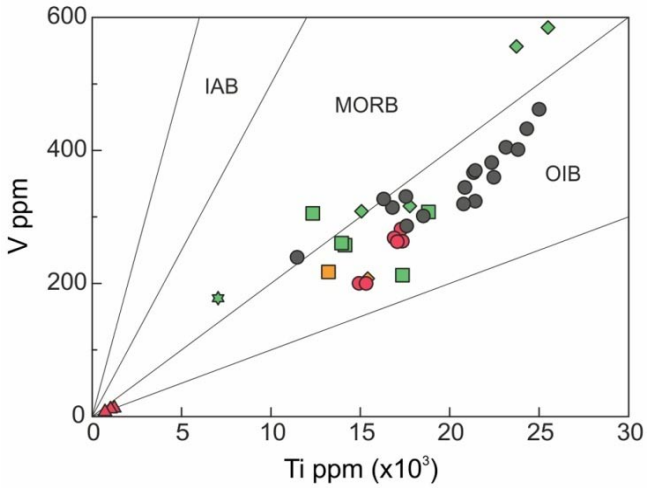


**Fig. 4.5.** V vs. Ti diagram (Shervais, 1982). Symbols are as in Fig. 4.3 and 4.4.

In the V vs. Ti diagram (Fig. 4.5), most samples plot within the OIB-type field defined by Shervais (1982). This agrees with the alkaline geochemical affinity of the rocks, as also supported by normative nepheline and no normative quartz in most compositions, high concentrations in Nb and Ta in all of the samples (Table 4.1), and mineral compositions, particularly Ti-rich mafic minerals (see section 4.4). Inferences on the geodynamic context must not be derived.

### 4.5.2. Major and trace element variations

The MgO concentrations of most samples vary between 4 and 14 wt. % (Table 4.1). The picrite sample from the Basque-Cantabrian Basin has an extremely high MgO concentration of ca. 25 wt. %, whereas the trachyte sample from the Basque-Cantabrian Basin and the syenite samples from the Eastern Pyrenees have MgO concentrations below 1 wt. %. Following these differences, most samples plot relatively grouped in bivariate diagrams vs. decreasing MgO, while the picrite sample plots to the left and the trachyte and syenite samples plot the right of the diagrams (Fig. 4.6, 4.7).

Compositional variations define evolutionary trends where $SiO_2$, $Al_2O_3$, alkalis ($Na_2O$, $K_2O$) and incompatible trace elements like the Large Ion Lithophile Elements (LILE) and the High Field Strength Elements (HFSE) increase with decreasing MgO, whereas CaO and compatible elements like the transition elements decrease with decreasing MgO, and

$TiO_2$, $Fe_2O_3^T$, $P_2O_5$, Sr and Y show an uneven distribution (Fig. 4.6, 4.7). Overall, these variations agree with magma fractionation from more primitive to more evolved compositions. The picrite sample, however, shows the effect of olivine accumulation for many elements besides MgO, as it has anomalously low concentrations in $TiO_2$ and CaO as

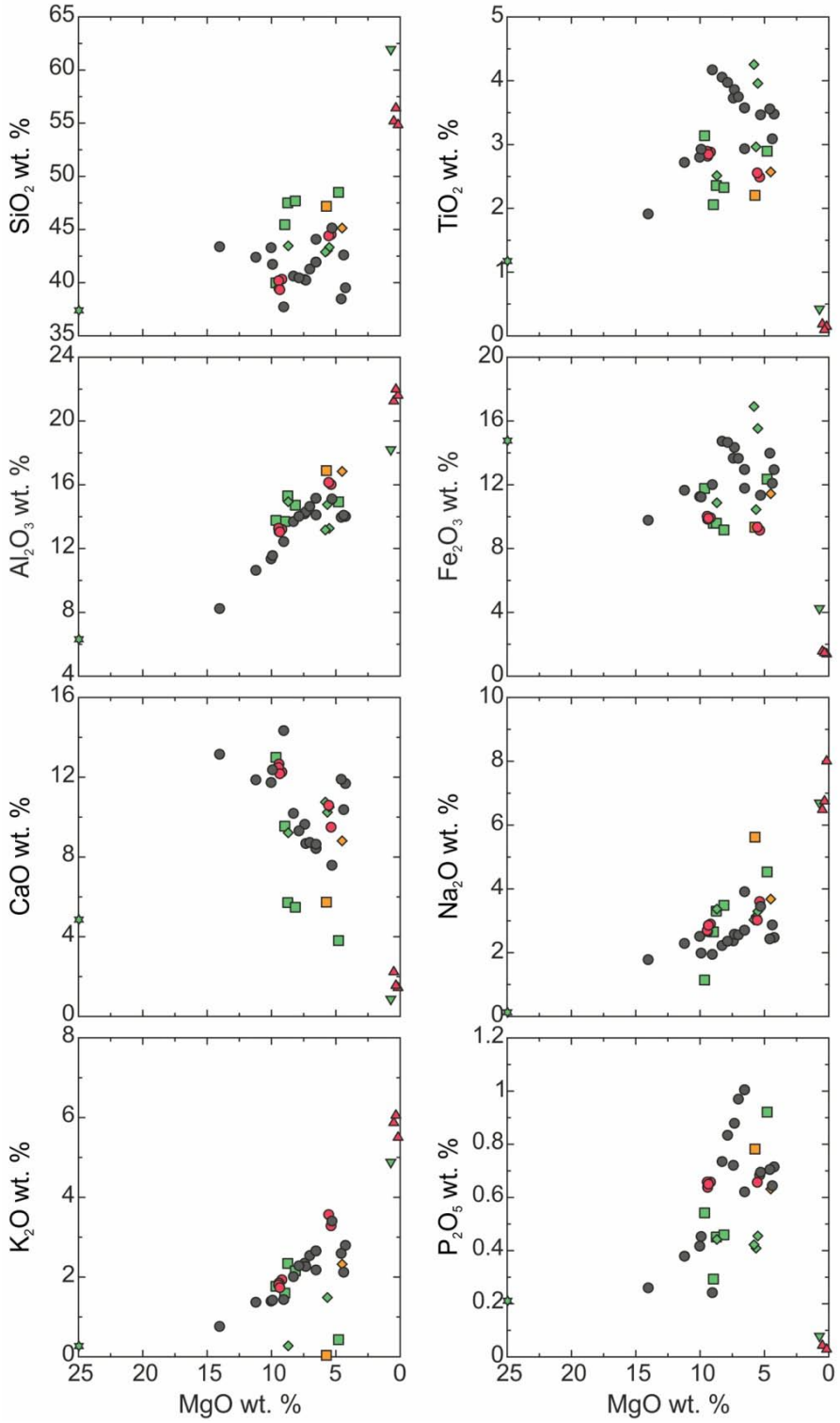


**Fig. 4.6.** Variations in major element concentrations with decreasing MgO. Symbols are as in Fig. 4.3 and 4.4.

well as extremely high concentrations in Ni and Cr. This accumulation-effect is also evident in the lamprophyres from the Catalonian Coastal Ranges. Samples with significant volume fractions of olivine macrocrysts have concentrations in MgO over 10 wt. % and high concentrations in Ni and Cr –see also Chapter 5-.

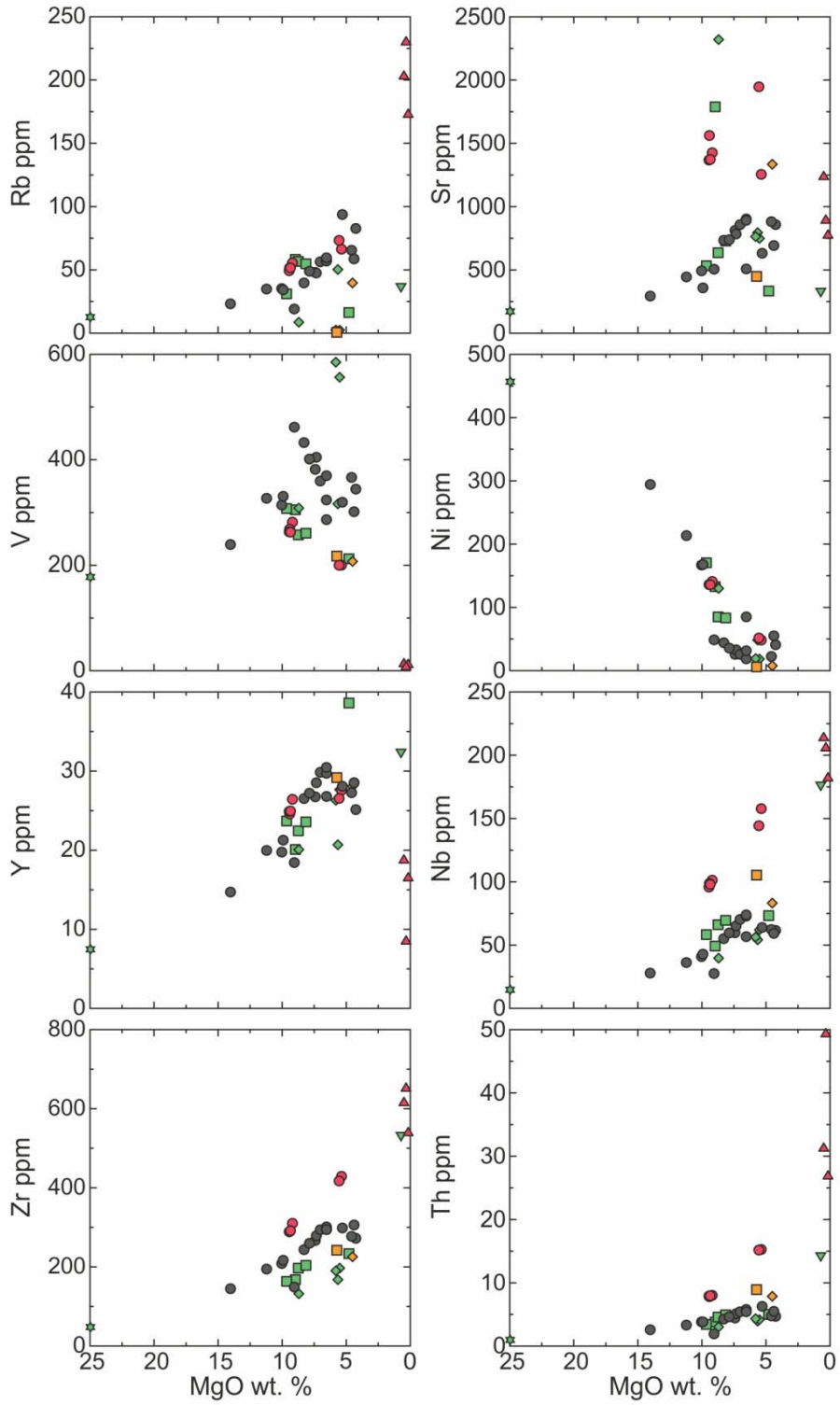


**Fig. 4.7.** Variations in trace element concentrations with decreasing MgO. Symbols are as in Fig. 4.3 and 4.4.

Normalised Rare Earth Element (REE) patterns and multielemental patterns are presented in Fig. 4.8. The rocks are significantly enriched in incompatible elements compared to the chondrite and primitive mantle compositions by McDonough and Sun (1995). They show rightwards-decreasing normalised patterns roughly parallel to each other, except for the evolved rocks. The trachyte sample from the Basque-Cantabrian basin is the only sample with a marked negative anomaly in Eu in the normalised REE pattern. This is probably

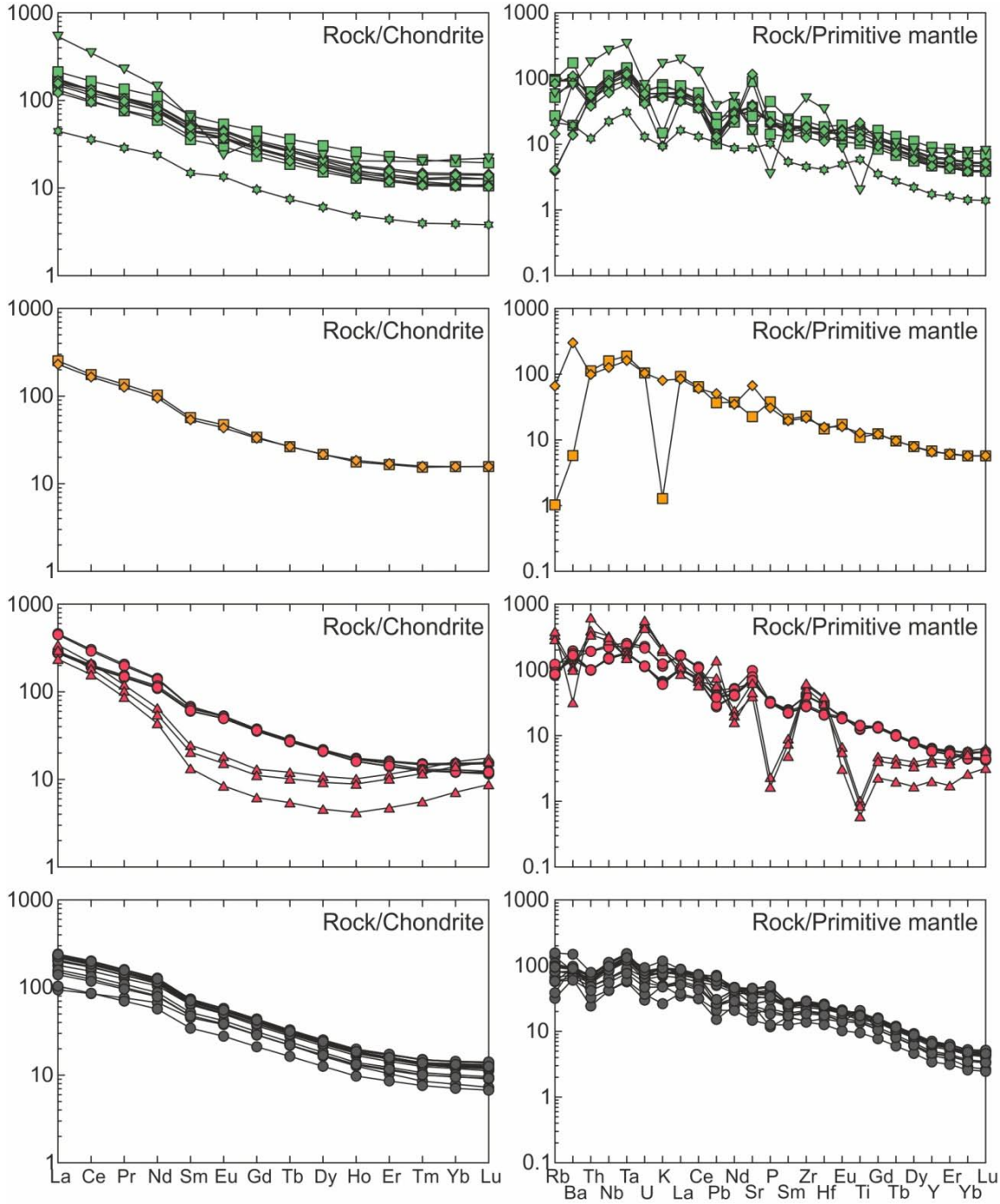


**Fig. 4.8.** Rare Earth Element (REE) concentrations normalised to the chondrite composition by McDonough and Sun (1995) and multielemental concentrations normalised to the primitive mantle composition by McDonough and Sun (1995), for the Basque-Cantabrian Basin, North Pyrenean Basins, Eastern Pyrenees and Catalonian Coastal Ranges. Symbols are as in Fig. 4.3 and 4.4.

related to fractionation of plagioclase, as suggested by Azambre et al. (1992). In contrast, the syenite samples from the Eastern Pyrenees show convex-downwards normalised REE patterns. Although Azambre et al. (1992) found no relationship between the syenites and the mafic compositions, such normalised REE patterns may be related to fractionation of clinopyroxene and/or amphibole, as these minerals have lower partition coefficients for the LREE and HREE than for the MREE (Ubide et al., under review *b* –see Chapter 7-). All of the evolved rocks (trachyte and syenites) show marked negative anomalies for Ti and P in the normalised multielemental patterns that may be related to fractionation of amphibole or Fe-Ti oxides, and apatite, respectively. Regarding the most primitive compositions, the picrite sample from the Basque-Cantabrian Basin as well as the lamprophyre samples with significant volume fractions of mafic macrocrysts from the Catalonian Coastal Ranges, show normalised patterns parallel to the other compositions but less enriched due to the influence of mafic crystals (see also Chapter 5). Finally, sample COG-3 from the North Pyrenean Basins has deep, negative anomalies for Rb, Ba and K. Given that these are mobile elements and that the normalised values are down to two orders of magnitude below the other trace elements, these depletions are most likely due to alteration.

Leaving aside outlier compositions, the Cretaceous mafic melts in northeast Iberia appear to be chemically equivalent irrespective of the domain considered (Fig. 4.8). All these compositions are significantly enriched in incompatible elements and strongly alkaline, with high $(La/Lu)_N$ values, ranging between 11 and 30. In detail, mafic rocks show $(La/Lu)_N$ values of 11 – 15 in the Basque Cantabrian Basin, 15 – 16 in the North Pyrenean Basins, 23 – 30 in the Eastern Pyrenees and 13 – 19 in the Catalonian Coastal Ranges. In normalised multielemental patterns, mafic rocks have remarkable positive anomalies for the Nb-Ta pair and lower normalised values for Th and U, defining a characteristic hill-shape for that part to the diagram. Positive anomalies in Ba are common and $(Sm/Yb)_N$ values are high (3 – 6), indicating a strong fractionation of the HREE relative to the MREE in all of the mafic rocks. On the other hand, the normalised values of K, Pb, Sr and to a lesser extent, P and Ti, are relatively variable. Some of these variations might be correlated with fractionation or accumulation of minerals such as kaersutite, plagioclase, apatite and Fe-Ti oxides.

### 4.5.3. Sr-Nd-Pb isotope composition

Isotope data are presented in Table 4.2. $^{87}Sr/^{86}Sr$ and $^{143}Nd/^{144}Nd$ ratios were recalculated taking into consideration the most recent geochronological results (~ 100 Ma in the Basque-Cantabrian Basin and North Pyrenenan Basins, ~ 90 Ma in the Eastern Pyrenees and ~ 80 Ma in the Catalonian Coastal Ranges; Ubide et al., under review *a* –see Chapter 3-) and plotted in Fig. 4.9. All of the analysed rocks yield consistent $^{143}Nd/^{144}Nd$ values

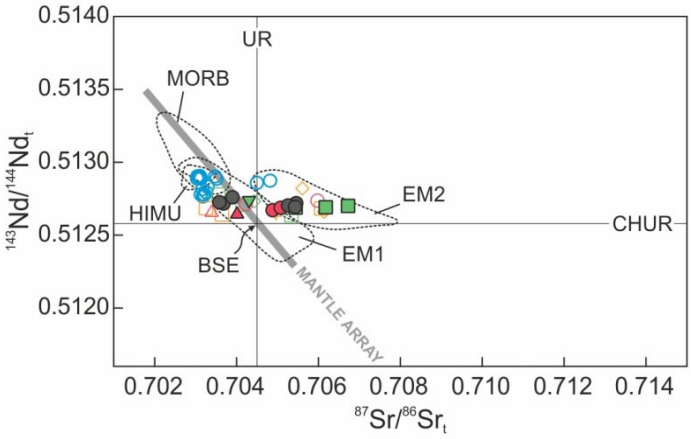


**Fig. 4.9.** Sr-Nd isotopic compositions. Filled symbols represent data obtained in this study and empty symbols represent data from the literature (Rossy et al., 1992); see the legend in Fig. 4.3. Additionally, empty blue symbols represent data from the Western Iberian Margin by Bernard-Griffiths et al. (1997). All of the data are recalculated considering the age of the rocks, as explained in the text (see section 4.5.3). Mantle component fields compiled from GEOROC database.

(0.512656 – 0.512760) enriched over the Bulk Silicate Earth (BSE), as εNd varies from +2.6 to +4.4. In contrast, $^{87}Sr/^{86}Sr$ values (0.70358 – 0.70672) and εSr values (-11.7 to +33.2) are very variable in all the domains and the samples show a horizontal scatter in the $^{143}Nd/^{144}Nd$ vs. $^{87}Sr/^{86}Sr$ diagram that is highly oblique to the mantle array. These results are in line with those obtained by Rossy et al. (1992) for the Cretaceous magmatism in the Basque-Cantabrian Basin, the North Pyrenean Basins and the Eastern Pyrenees. They are similar to those of the Cretaceous magmatism in the Western Iberian Margin with an age of 72 – 66 Ma (Bernard-Griffiths et al., 1997 and references therein), although the latter concentrate at lower $^{87}Sr/^{86}Sr$ and slightly higher $^{143}Nd/^{144}Nd$ values (Fig. 4.9).

T-depleted mantle model ages ($T^{Nd}_{DM}$) were calculated considering the obtained $^{143}Nd/^{144}Nd$ and $^{147}Sm/^{144}Nd$ isotope ratios in mafic rocks. They show a small variation range between 0.54 and 0.60 Ga (Table 4.2).

Pb isotope ratios are presented for the first time for the Cretaceous magmatism in northeast Iberia (Table 4.2; $^{206}Pb/^{204}Pb$ 19.062 – 21.152, $^{207}Pb/^{204}Pb$ 15.632 – 15.779, $^{208}Pb/^{204}Pb$ 39.280 – 41.037, $^{208}Pb/^{206}Pb$ 1.937 – 2.061, $^{207}Pb/^{206}Pb$ 0.742 – 0.822). The samples define a positive trend in Pb-Pb isotope systems (Fig. 4.10), not aligned with the Northern Hemisphere Reference Line (NHRL). The distribution of the samples is similar in all the domains. Data from the Western Iberian Margin (Bernard-Griffiths et al., 1997) agree with the least radiogenic end of the trend, where most values from the Catalonian Coastal Ranges plot. There is a sample from the Catalonian Coastal Ranges for which Pb isotope ratios appear to be outliers compared to the other data from that domain. That sample however, was re-analysed in a different laboratory with similar results (see section 4.3; Table 4.2).

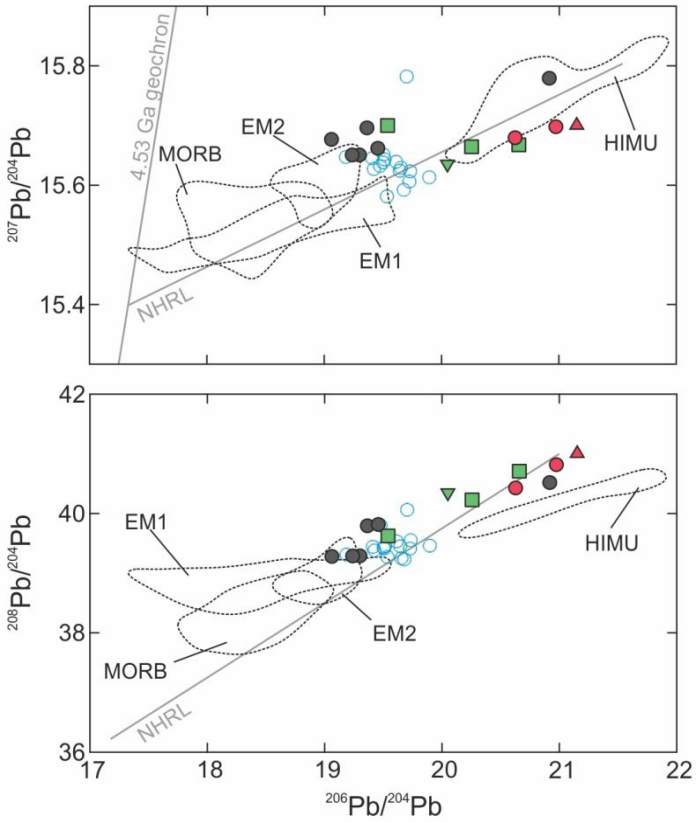


**Fig. 4.10.** Pb isotopic compositions. Data obtained in this study is represented with filled symbols (see the legend in Fig. 4.3 and 4.4). There are no previously published data from northeast Iberia, but empty blue symbols represent data from the Western Iberian Margin (Bernard-Griffiths et al., 1997). Error bars smaller than symbol size. Mantle component fields compiled from GEOROC database.

## 4.6. Discussion

### 4.6.1. Source enrichment and mantle heterogeneity

The major element, trace element and isotope composition of the Cretaceous alkaline mafic magmas are comparable across the different domains in the Pyrenees and Catalonian Coastal Ranges. It follows that these magmas may share a common mantle source. Considering the geographic extension and time span (105 – 79 Ma; Ubide et al., under review *a* –see Chapter 3-) covered by the rocks, such a source signature may affect large areas and be long-lasting in Iberia's mantle.

According to Frey et al. (1978), primary magma compositions are those with magnesium number (Mg#) > 60 – 70, MgO > 11 wt. %, Cr > 500 – 1000 ppm and Ni > 200 – 500 ppm. Only the picrite sample ELG-04 from the Basque-Cantabrian Basin and the camptonite sample SFB-3 from the Catalonian Coastal Ranges meet these criteria (Table 4.1). However, these samples have high volume fractions of olivine macrocrysts and therefore a cumulative nature (e.g., Orejana et al., 2008; Scarrow et al., 2011), so they are not

appropriate for the interpretation of primary petrogenetic processes (e.g., Larrea et al., 2013; Ubide et al., 2012*a*; see Chapters 5, 6 and 7 in this volume). Nevertheless, the other mafic samples have relatively primitive and consistent compositions. The evolved samples (MALZA-1, FIT-1, FIT-2 and FIT-3) might be related to the mafic compositions by fractional crystallisation, as indicated above (section 4.5.2).

The mafic samples have strongly fractionated normalised REE patterns (Fig. 4.8) and high $(Sm/Yb)_N$ values that are indicative of melting in the garnet stability field (e.g. McKenzie and O'Nions 1991), so at a depth greater than 60 km (e.g., Wilson, 1989; Wyllie, 1981). They are significantly enriched in incompatible trace elements (Fig. 4.8), pointing to the involvement of an enrichment process in the mantle source. The mafic samples are represented in the Th/Yb vs. Ta/Yb petrogenetic diagram proposed by Pearce (1983) in Fig. 4.11. They plot close to OIB-type compositions and suggest an enrichment of the mantle source. Thus, primary magmas of these rocks were generated by partial melting of an asthenospheric, probably metasomatised mantle.

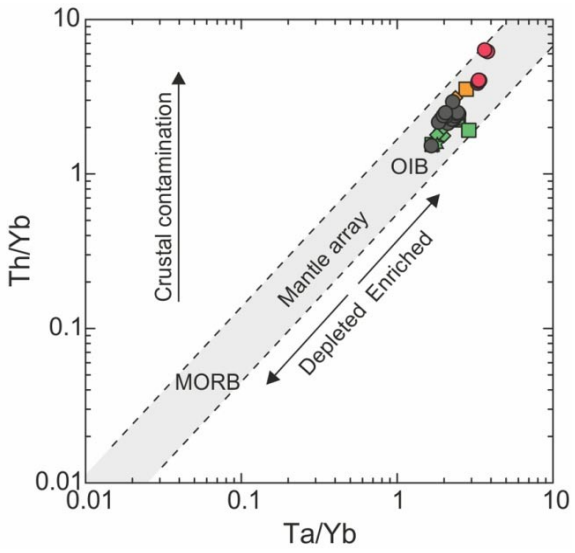


**Fig. 4.11.** Mafic compositions plotted in the Th/Yb vs. Ta/Yb petrogenetic diagram, discriminant for mantle melting array vs. arc basalts (Pearce, 1983). Symbols are as in Fig. 4.3 and 4.4.

According to Fig. 4.11, the samples are not affected by crustal contamination. In line with this, Ce/Pb ratios between 11 and 53 are closer to primitive mantle values (ca. 25; e.g., Hofmann, 1988) than to crustal values (ca. 4; e.g., Wedepohl, 1995; Gao et al., 1998). Meanwhile, the significant variation in $^{87}Sr/^{86}Sr$ isotope ratios (Fig. 4.9; Table 4.2) might reflect mantle heterogeneity or, more likely, contamination. To unveil the source of contamination to Sr isotope compositions, the samples are plotted in $^{87}Sr/^{86}Sr$ vs. MgO, $SiO_2$, Sr and 1/Sr in Fig. 4.12. It is clear from these plots that there is no correlation between these parameters and thus, crustal contamination can be ruled out as the main source of the $^{87}Sr/^{86}Sr$ variation. As proposed by Rossy et al. (1992) for the Pyrenean rocks and Bernard-Griffiths et al. (1997) for the Western Iberian Margin, the heterogeneous $^{87}Sr/^{86}Sr$ results are probably related to seawater contamination. Therefore, the most radiogenic $^{87}Sr/^{86}Sr$ data should not be considered for petrogenetic interpretations. Data within the mantle array, on the other hand, point to the potential involvement of several mantle reservoirs in the source, as they plot in between mantle components (Fig. 4.9).

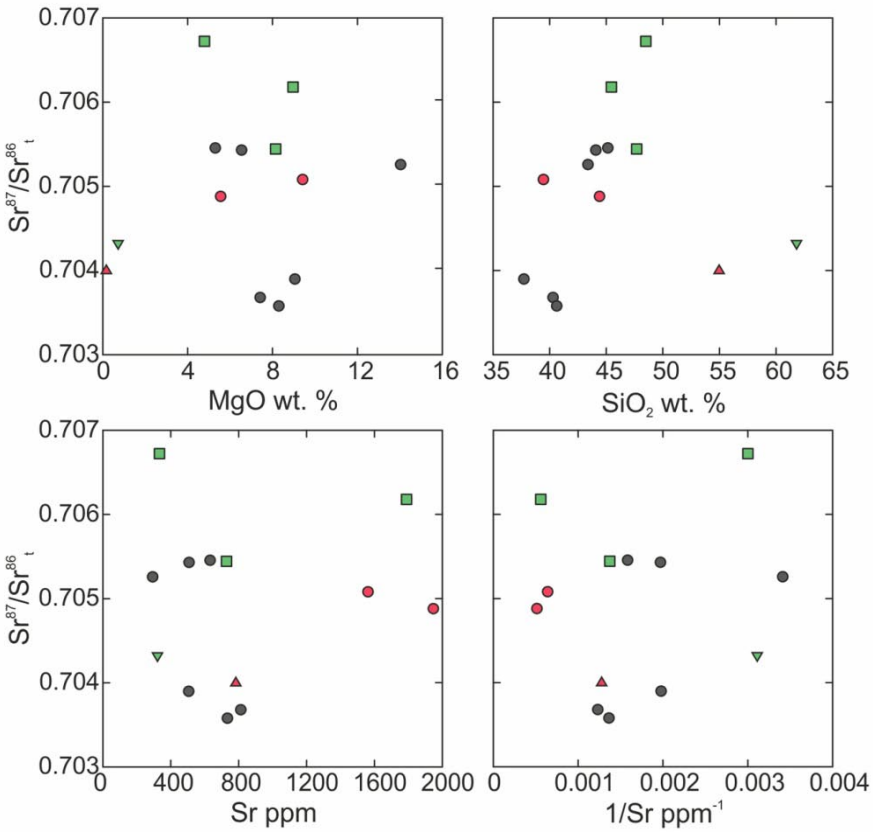


**Fig. 4.12.** Bivariate diagrams of $^{87}Sr/^{86}Sr$ vs. major and trace element parameters. Symbols are as in Fig. 4.3 and 4.4.

Rossy et al. (1992) showed that the Nd isotope composition of the Cretaceous magmatism is significantly less radiogenic than that of the ultramafic bodies cropping out in the Pyrenees (Downes et al., 1991). It is also different from the Nd isotope composition of ultramafic xenoliths included in Quaternary lavas in the Catalonian Coastal Ranges, analysed by Bianchini et al. (2007). Since these ultramafic rocks can be taken as samples of the local lithosphere, these observations agree with an asthenospheric origin for the studied magmas. The Pyrenean ultramafic bodies are cross-cut in certain areas by a late generation of amphibole-pyroxenite veins (Lagabrielle and Bodinier, 2008 and references therein) that are considered to represent melt conduits for the Cretaceous alkaline magmatism (Golberg et al., 1986; Bodinier et al., 1987). These veins are coeval with the Cretaceous magmatism (Albarède and Michard-Vitrac, 1978; Golberg et al., 1986; Henry et al., 1998; Ubide et al., under review *a* –see Chapter 3-) and have $^{143}Nd/^{144}Nd$ isotope ratios (Downes et al., 1991; Mukasa et al., 1991) of 0.512698 to 0.512874 (recalculated to 100 Ma). These values overlap with the recalculated $^{143}Nd/^{144}Nd$ ratios obtained in this study (0.512656 – 0.512760; Table 4.2), lending further support to the genetic link between the amphibole veins and the Cretaceous magmas.

In order to obtain additional constraints on the mantle source, incompatible trace elements from samples closest to primary melts need to be regarded. Only samples with MgO > 7 wt. % have been considered. In addition, rocks with high volume fractions of

large crystals have been dismissed as their composition is strongly influenced by the accumulation of the crystals (see Chapters 5 and 6). The primitive mantle-normalised multielemental patterns of the samples that meet these criteria are presented together in Fig. 4.13.

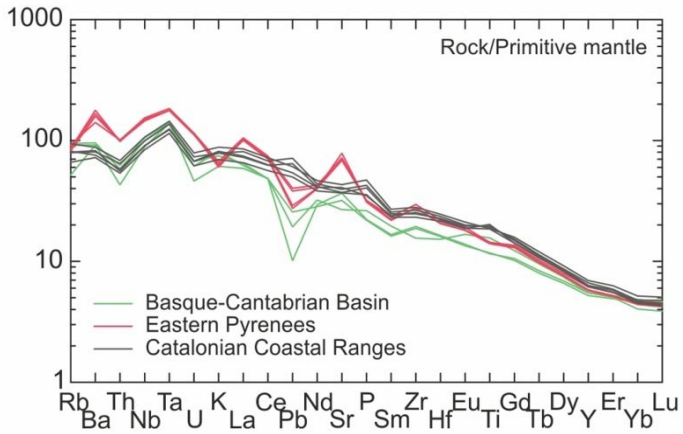


**Fig. 4.13.** Multielemental patterns of selected samples normalised to the primitive mantle composition by McDonough and Sun (1995). Note that only certain samples from the Basque-Cantabrian Basin, the Eastern Pyrenees and the Catalonian Coastal Ranges fit the criteria outlined in the preceding paragraph.

The rocks show positive anomalies for Nb-Ta and generally smaller ones for Ba; samples from the Basque-Cantabrian Basin and Eastern Pyrenees also present a negative anomaly in Pb (Fig. 4.13). These data point to an asthenospheric enriched mantle source similar to EM-1 and/or HIMU (Hofmann, 1997). Pb systematics confirms mixing of HIMU and EM-type components in a heterogeneous source (Fig. 4.10). The fact that samples from the Catalonian Coastal Ranges show no anomalies or slightly positive anomalies for Pb in trace element patterns (Fig. 4.13) may reflect a small contribution of an EM-2 component, which could be related to the incorporation of subducted crustal components into the mantle (Zindler and Hart, 1986), since crustal contamination was not important in the genesis of these magmas (Fig. 4.11, 4.12). The involvement of an EM-2 component may also contribute to the $^{207}$Pb- and $^{208}$Pb-enrichments of the samples (Orejana et al., 2008; Fig. 4.10).

The enrichment in incompatible elements and volatiles, as revealed by the trace element patterns and the abundance of lamprophyre rocks and hydrous phases, suggest a metasomatic modification of the mantle source. The nature of the metasomatic phases can be investigated through the composition in diagnostic trace elements. The samples show positive correlations in Rb/La vs. K/La plots, as well as in Ba/Nb vs. Ba/Ce plots (not shown). As explained in Orejana et al. (2008), these features might account for the presence of phlogopite in the source during partial melting as this mineral may preferentially incorporate LILE when compared to REE and HFSE. On the other hand, the

relative abundances of LILE provide alternative constraints on the composition of the source. Melts in equilibrium with phlogopite are expected to present Rb/Sr > 0.1 and Ba/Rb < 20, whereas melts in equilibrium with amphibole typically have Rb/Sr < 0.06 and Ba/Rb > 20 (Furman and Graham, 1999; McCoy-West et al., 2010). The studied mafic samples have Rb/Sr ratios of 0.00 – 0.15 and Ba/Rb ratios of 6.52 – 65.46. Although these ratios are not conclusive, they may suggest that amphibole could predominate over phlogopite in the mantle source. The high concentrations in Nb and Ta support amphibole as the main relevant phase (e.g., Ionov et al. 1997), whereas the role of phlogopite is probably less important, as this is not a frequent phase in the rocks. Finally, rocks with moderate $P_2O_5$ contents such as the studied samples (0.2 – 1 wt. %; Table 4.1) indicate that a P-rich phase, such as apatite, might have been a stable metasomatic mineral in the mantle source (e.g., Orejana et al., 2008).

Even though the trace element patterns across northeast Iberia are similar to each other, there are small differences between samples from different domains (Fig. 4.13). Samples from the Eastern Pyrenees are the most enriched in LILE and HFSE and show a deep negative anomaly for K and Pb. Their patterns are therefore the closest to HIMU (e.g., Woodhead, 1996). Their Pb isotope systematics has clear HIMU signature as well (Fig. 4.10). Regarding the alkaline character of the rocks, $(La/Lu)_N$ values are highest for the Eastern Pyrenees and Catalonian Coastal Ranges, and in the TAS diagram, these rocks define more $SiO_2$-undersaturated trends than rocks from the Basque-Cantabrian Basin and the North Pyrenean Basins (Fig. 4.3). It follows that the alkaline character decreases from east to west. Accordingly, mantle melting rates may have been higher or mantle melting pressures lower towards the west (Kushiro, 2001). Moreover, magmatic activity is more enduring and developed in the west, and progressively scarcer and more intrusive towards the east (Ubide et al., under review *a* –see Chapter 3-). All of these differences are in agreement with the geodynamic scenario of opening of the Bay of Biscay and anticlockwise rotation of Iberia that enabled the development of the studied magmatism, as this kind of setting would trigger extensional conditions increasing towards the west (Ubide et al., under review *a* –see Chapter 3-). The strong structural control on the development of the magmatism favours a non-plume scenario, as proposed by Matton and Jébrak (2009) for other Cretaceous magmatisms of the Peri-Atlantic Alkaline Pulse.

The discussion of geochemical data on the Cretaceous magmatism in northeast Iberia leads to the conclusion of a common, asthenospheric, enriched/metasomatised and heterogeneous mantle source with the involvement of HIMU and EM-1 components and a possible contribution of EM-2 component. Melting took place in the garnet stability field and responded to higher tectonic extension rates towards the west. The resulting melts have similar trace element and isotopic signatures, and it is interesting to note that elemental compositions are homogeneous whereas isotope compositions are heterogeneous, although still comparable among the different domains.

### 4.6.2. Evolution of the mantle source since the beginning of the Alpine cycle

During the Alpine cycle, the northeast of the Iberian realm was the locus of several tectono-magmatic events associated to the relative movements of Iberia (e.g., Arranz et al., 2011 and references therein). The study of the magmatisms can provide insights into the evolution of the mantle sources in the area.

First, as the Variscan compression progressively ceased favouring the emplacement of calc-alkaline plutons (Arranz and Lago, 2004; Castro et al., 2002), the tectonic regime evolved to a transcurrent and finally extensional context which resulted in thinning of the crust (Lago et al., 2004*a* and references therein). This enabled partial melting of the lithospheric mantle, triggering the emplacement of hypabyssal or even extrusive calk-alkaline and mildly alkaline magmas during the Permian. Today, these rocks are observed in the Pyrenees, the Catalonian Coastal Ranges and the Iberian Chain (Bixel, 1988; Bonin, 1988; Cabanis and Le Fur-Balouet, 1989; Debon and Zimmermann, 1993; Galé, 2005; Gil-Imaz et al., 2012; Lago et al., 2004*a*, 2004*b*, 2012; Ubide et al., 2010*b*).

The Triassic rifting stage, related to the opening and westward extension of the Tethys Ocean (e.g., Salas and Casas, 1993), enabled widespread tholeiitic magmatism ("ophites") in the western and central Pyrenean basins (Azambre et al., 1987). In addition, a Triassic alkaline magmatism was developed in the eastern Pyrenean margin (Azambre and Rossy, 1981). Ubide et al. (under review *a* –see Chapter 3-) have reported alkaline extrusive rocks of Triassic age in the Central Pyrenees as well. Alkaline mafic rocks are also recognised in the southern Catalonian Coastal Ranges and the Iberian Chain (Lago et al., 1996, 2000; Sanz et al., 2013).

Most of the Jurassic period constituted a post-rift stage (Salas and Casas, 1993) in northeast Iberia. The magmatic activity in this period is restricted to isolated, alkaline extrusive rocks cropping out in the Central Pyrenees (Ubide et al., under review *a* –see Chapter 3-) and the Iberian Chain (Martínez González et al., 1997; Ortí and Vaquer, 1980).

During the Cretaceous, the opening of the Bay of Biscay created a rifting setting favourable for the development of an alkaline magmatic province in northeast Iberia (Azambre et al., 1992; Cabanis and Le Fur-Balouet, 1990; Montigny et al., 1986; Rock, 1982; Solé et al., 2003; Ubide et al., under review *a* –see Chapter 3-). This magmatism crops out in the Pyrenees and northern Catalonian Coastal Ranges and is the focus of the present study.

Finally, the most recent magmatic activity took place during the Quaternary. An alkaline volcanic province developed to the north-northwest of the Catalonian Coastal Ranges (south of the Pyrenees) as the Iberian realm was subjected to extensional conditions after

the Alpine compression (e.g., Araña et al., 1983; Cebriá et al., 2000). This province is frequently cited as the Garrotxa Volcanic Field (e.g., Aulinas et al., 2013; Gasperini et al., 2013; Gisbert et al., 2009, 2011) and is related to the European Cenozoic rift system (Gasperini et al., 2013).

The diversity of magmatisms recorded in northeast Iberia, most of which are dominated by mafic compositions, suggests a heterogeneous mantle beneath this area. Nevertheless, when comparing the geochemistry of these magmatisms, it turns out that the asthenospheric, enriched and heterogeneous HIMU-EM signature defined for the Cretaceous magmas (see section 4.6.1) is, strikingly, present in rocks of very different age.

The primitive mantle-normalised multielemental patterns of the magmatisms with similarities to the Cretaceous magmas are presented in Fig. 4.14 (for the sake of simplicity, magmatisms with distinct compositions are not shown). In order to avoid evolved as well as cumulative compositions, only samples with MgO concentrations between 7 and 9 wt. % are plotted. Many of the oldest samples have high LOI values, but only those with contents below 5 wt. % are plotted. For comparison, the mafic compositions plotted in Fig. 4.13 are included as a grey field in the background (Fig. 4.14).

Significant similarities with the Cretaceous melts are found: in the Permian magmatism of the SE Iberian Chain (Lago et al., 2012), in the Triassic alkaline magmatisms of the eastern Pyrenean margin (Azambre and Rossy, 1981) and Iberian Chain (Lago et al., 2000), in the Jurassic magmatism of the Iberian Chain (unpublished data by the research group; see Martínez González et al., 1997 for a synthesis of this magmatism), and in the Quaternary magmatism of the Catalonian Coastal Ranges (Cebriá et al., 2000). The Permian magmatism of the SE Iberian Chain is most similar to HIMU (e.g., Woodhead, 1996), whereas the magmatisms closest in time to the Cretaceous (Jurassic and Quaternary) are also closest in composition to the Cretaceous magmatism. Other than the northeast part of Iberia, the Cretaceous compositional features are observed in the Permian magmatism of the Spanish Central System (Orejana et al., 2008) and also in the Triassic alkaline magmatism of Majorca (unpublished data by the research group; see Lago et al., 1996 for a synthesis of this magmatism).

The similarities observed in normalised multielemental patterns are reproduced in the Sr-Nd and Pb-Pb isotope systems, when measured (Fig. 4.15). Regarding the Sr-Nd isotope plot, Jurassic and Quaternary magmatisms agree with the least radiogenic Cretaceous data; the Permian and Triassic magmatisms discussed above have more scattered Sr-Nd isotope ratios, but some data agree with the Cretaceous compositions as well. Other than that, it is clear that the crustal signature decreased since the end of the Variscan orogeny, marked by the development calc-alkaline plutonism and volcanism with high $^{87}Sr/^{86}Sr$

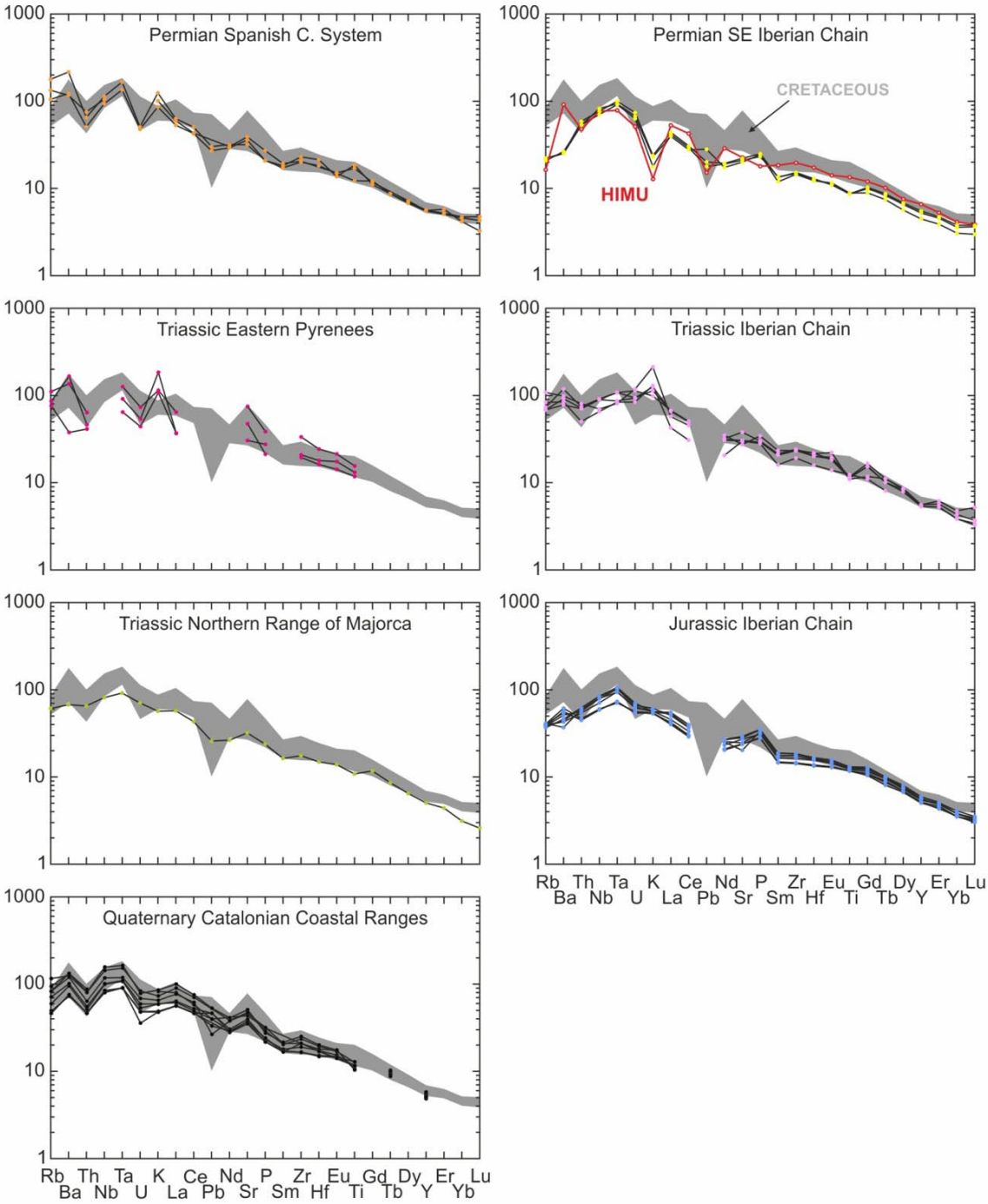


**Fig. 4.14.** Primitive mantle (McDonough and Sun, 1995) normalised multielemental patterns of Permian to Quaternary magmatisms in Iberia, to be compared to the Cretaceous compositions (see data in Fig. 4.13). Permian compositions from the Spanish Central System and the SE Iberian Chain are from Orejana et al. (2008) and Lago et al. (2012), respectively; Triassic alkaline compositions from the eastern Pyrenean margin, Iberian Chain and Majorca are from Azambre and Rossy (1981), Lago et al. (2000) and unpublished data by the research group (see section 4.6.2), respectively; Jurassic compositions from the Iberian Chain are unpublished data by the research group (see section 4.6.2); Quaternary compositions from the Catalonian Coastal Ranges are from Cebriá et al. (2000). From among the compositions provided in these studies, only those fitting the criteria outlined in the preceding page are plotted. HIMU composition from Woodhead (1996).

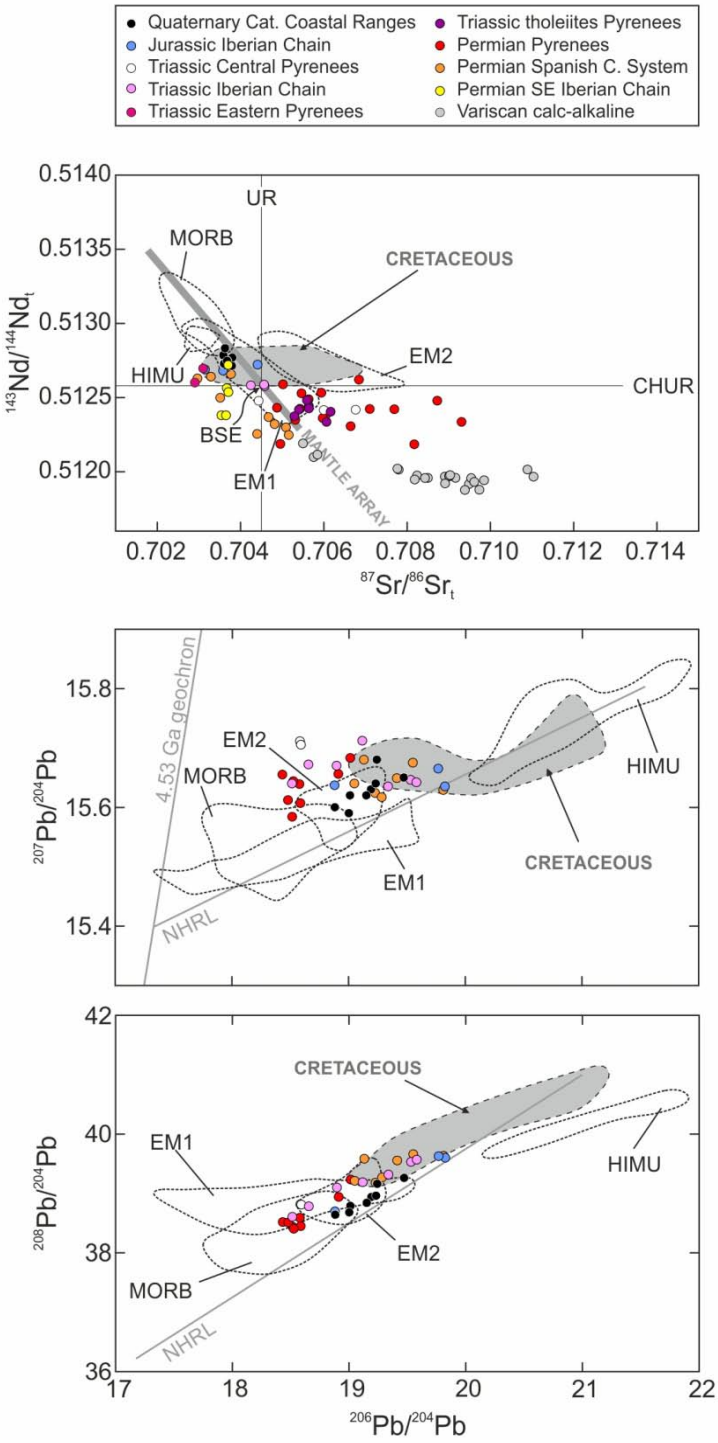


**Fig. 4.15.** Isotope systematics of Iberian magmatisms developed since the beginning of the Alpine cycle. Sr-Nd data are recalculated considering the age of the rocks. Carboniferous (Variscan) calc-alkaline plutonism in the Pyrenees from Roberts et al. (2000); Lower Permian (Variscan) calc-alkaline magmatism in the Iberian Chain from Lago et al. (2004*b*); Middle-Upper Permian magmatism in the Pyrenees, Spanish Central System and SE Iberian Chain from Galé (2005), Orejana et al. (2008) and Lago et al. (2012), respectively; Triassic tholeiitic magmatism in the Pyrenees and Triassic alkaline magmatism in the eastern Pyrenean margin from Alibert (1985); Triassic alkaline magmatism in the Central Pyrenees and Iberian Chain as well as Jurassic magmatism in the Iberian Chain are unpublished data by the research group; Cretaceous magmatism in the Pyrenees and Catalonian Coastal Ranges from this study and Rossy et al. (1992) (see data in Fig. 4.9; 4.10); Quaternary magmatism in the northern Catalonian Coastal Ranges from Cebriá et al. (2000). Mantle component fields compiled from GEOROC database.

ratios and low $^{143}Nd/^{144}Nd$ ratios (Fig. 4.15), probably due to increasing extensional conditions.

Pb isotope analyses are scarcer in previous studies (Fig. 4.15). The Permian, Triassic, Jurassic and Quaternary magmatisms discussed above are similar in terms of Pb isotopic composition to the least radiogenic Cretaceous data, supporting the petrogenetic link suggested on the basis of trace elements and Sr-Nd isotopes. Cretaceous Pb isotope ratios, however, reach most radiogenic concentrations, not recorded in any other magmatism in Iberia. The Permian magmatism in the SE Iberian Chain has normalised multielemental patterns very similar to HIMU (Fig. 4.14; Lago et al., 2012), but Pb isotope analyses have not been carried out yet.

$T^{Nd}_{DM}$ model ages have been calculated for the magmatisms with available $^{143}Nd/^{144}Nd$ and $^{147}Sm/^{144}Nd$ isotope ratios. The results are presented in Fig. 4.16 in relation to the age of the rocks. The Jurassic and Cretaceous magmatisms yield consistent model ages that overlap with each other (0.53-0.58 Ga and 0.54-0.60 Ga, respectively; see Cretaceous data in Table 4.2). Older magmatisms yield more heterogeneous model age values. Still, the youngest model ages related to the Permian and Triassic magmatisms considered above agree with the Cretaceous values. These results may reflect a Cadomian fractionation event in the mantle related to the genesis the petrogenetically linked magmas. In contrast, magmatisms unrelated to the Cretaceous signature have older model ages (Fig. 4.16). According to the variability of model age data, the Cadomian event may have affected older mantle domains, rejuvenating their isotopic compositions and probably modifying their overall composition.

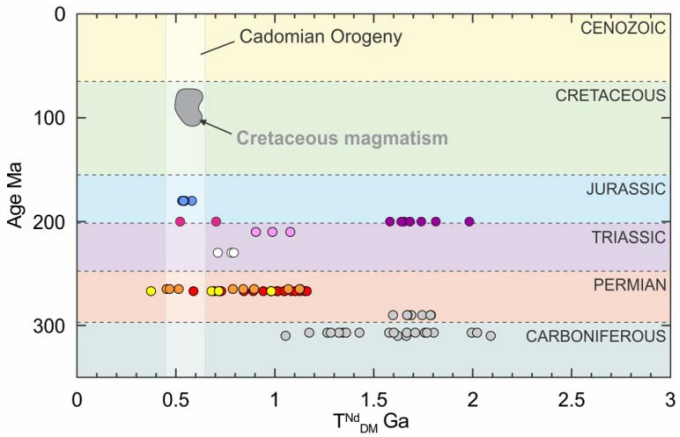


**Fig. 4.16.** Age vs. T-depleted mantle model ages ($T^{Nd}_{DM}$) plot of Iberian magmatisms developed since the beginning of the Alpine cycle. Literature data from Alibert (1985), Galé (2005), Lago et al. (2004*b*, 2012), Orejana et al. (2008) and Roberts et al. (2000). Triassic alkaline magmatism in the Central Pyrenees and Iberian Chain as well as Jurassic magmatism in the Iberian Chain are unpublished data by the research group; Cretaceous magmatism in the Pyrenees and Catalonian Coastal Ranges from this study (see data in Table 4.2). Symbols are as in Fig. 4.15.

The evaluation of trace element and isotope compositions of Iberian magmatisms since the beginning of the Alpine cycle indicates that the mantle source related to the studied Cretaceous melts probably represents a common, asthenospheric and enriched mantle domain, of considerable areal extension and long-living since Permian to Quaternary times. It is equally important to note that there are also many other signatures unrelated to this source, such as crustal signatures in the Carboniferous and Permian magmatisms (e.g., Galé, 2005; Lago et al., 2004*a*, 2004*b*; Ubide et al., 2011) or the MORB-like magmatism related to the widespread development of tholeiites during the Triassic (Azambre et al., 1987). It follows that the mantle below Iberia is heterogeneous on a large scale as well. The different mantle sources were tapped throughout the Alpine cycle according to the reigning tectonic conditions and therefore, plume-related scenarios as proposed in certain studies (e.g, Cebriá et al., 2000; Piromallo et al., 2008) are less likely. In line with this, the Cretaceous magmatism is related to extension of the lithosphere, rather than to mantle upwelling (Ubide et al., under review *a* –see Chapter 3-).

## 4.7. Conclusions

The Cretaceous alkaline magmatism in northeast Iberia is recorded in numerous outcrops in the Pyrenees and the Catalonian Coastal Ranges. The petrology and geochemistry of the rocks reveals that:

- There is a wide petrological variability including basic and acid, intrusive and extrusive rocks. Towards the west, the magmatism (and specifically volcanism) is more developed and related to higher melting rates of the mantle source. This can be correlated with extensional conditions increasing towards the west given the related geodynamic context of opening of the Bay of Biscay and anticlockwise rotation of Iberia.

- The Cretaceous melts were extracted from a heterogeneous and metasomatised, asthenospheric mantle source with the involvement of HIMU and EM-type components. The model ages reflect a Cadomian fractionation event in the mantle.

- This mantle signature is recorded in other magmatisms in Iberia with ages spanning from Permian to Quaternary. It therefore may represent an extensive and long-living source beneath the region, tapped throughout the Alpine cycle under favourable tectonic conditions.

# 5

# The Cretaceous lamprophyre suite in the Catalonian Coastal Ranges: complex antecryst populations and their effect on whole rock compositions

**SUMMARY**

The petrology, mineralogy and geochemistry of the Cretaceous lamprophyre suite in the Catalonian Coastal Ranges reveal a complex magma history related to the activity of the magma plumbing system at depth. This involved an intricate succession of magmatic processes, including recharge, magma mixing and fractionation, preserved in the complex compositional zoning patterns of large crystals (mainly antecrysts). The final intrusions cropping out today in the northern Catalonian Coastal Ranges are a mixture of 1) deep large crystals and 2) their host magma crystallised into a fine-grained groundmass. The variable entrainment of large crystals in the different lamprophyres controls whole rock chemical variations among them.

*The Aiguablava lamprophyre sill (and a thinner Late Variscan lamprophyre dyke), Costa Brava*

## 5.1. Introduction

Lamprophyres are mesocratic to melanocratic igneous rocks, usually sub-volcanic, that commonly exhibit a distinctive porphyritic texture consisting of large mafic crystals (macrocrysts) set in a fine-grained groundmass (Le Maitre, 2002; Woolley et al., 1996). In his monograph on lamprophyres, Rock (1991) pointed out that most macrocrysts are not fully cognate to the host lamprophyre melt and therefore, they are not phenocrysts in equilibrium with the enclosing groundmass. Regarding igneous rocks in general, an increasing number of studies highlight that mineral phases are commonly not in equilibrium with their host groundmass (Charlier et al., 2005, 2007; Davidson et al., 2007; Francalanci et al., 2012; Gill et al., 2006; Hildreth and Wilson, 2007; Jerram and Martin, 2008). According to these studies, phenocrysts might be an exception, rather than the rule, in macrocryst assemblages, which are instead, composed primarily of "antecrysts" partly foreign to the host groundmass but nevertheless related to the magmatic system.

Basic igneous rocks, including lamprophyres, are considered a window into the deep mantle and mantle processes, as their primitive composition, with high concentrations in MgO and compatible trace elements, might be representative of parental magmas close to the source. However, recent studies call for cautiousness when making such assumptions with strongly porphyritic rocks, as their bulk composition may be influenced by the accumulation of mafic macrocrysts and therefore, does not necessarily represent a parental melt (Larrea et al., 2013; López-Moro et al., 2007; Sakyi et al., 2012; Ubide et al., 2012*a* –see Chapter 6-).

The Cretaceous lamprophyre suite in the Catalonian Coastal Ranges consists of alkaline tabular intrusions emplaced by the end of the Mesozoic extension in northeast Iberia (Solé et al., 2003; Ubide et al., under review *a* –see Chapter 3-). Most of these lamprophyres are strongly porphyritic and include macrocrysts with complex compositional zoning patterns. These intrusions therefore constitute a natural laboratory for the study of crystal populations and the effect of macrocrysts on whole rock compositions. However, they have received little attention up to now. Some of the lamprophyres were reported in the early papers on regional geology (Calderón et al., 1907; San Miguel Arribas, 1952; San Miguel de la Cámara, 1930, 1936; Velde and Tournon, 1970), but only recently have they been object of detailed studies (Enrique, 2009; Gimeno, 2002; Solé et al., 2003; Ubide et al., 2008, 2012*a*, under review *a* and *b*) and still, they have never been investigated as a whole.

The aim of this study is to understand the petrology, mineralogy and geochemistry of the Cretaceous lamprophyre suite in the Catalonian Coastal Ranges and its implications for mineral-melt equilibrium, the contribution of macrocrysts to whole rock compositions and the complex magmatic processes taking place in the magmatic plumbing system at

depth. The present study is the first comprehensive investigation of the lamprophyre suite and includes already studied intrusions as well as unpublished exposures.

## 5.2. Geological context

The Catalonian Coastal Ranges are located in the northeastern passive margin of the Iberian plate and stretch out ca. 200 km in a NE–SW direction subparallel to the Mediterranean coastline (Fig. 5.1A). The eastern Pyrenees and their foreland Ebro basin border the Catalonian Coastal Ranges to the north and northwest, respectively, while the submerged Valencia trough defines the southeast flank. To the southwest, the Catalonian Coastal Ranges are linked to the NW–SE Iberian Ranges (Juez-Larré and Andriessen, 2002).

The Catalonian Coastal Ranges formed by intraplate propagation of the Alpine-Pyrenean compression during Tertiary times (Juez-Larré and Andriessen, 2002, 2006; Vergés et al., 2002). The northeast area of the orogen is mainly composed of Paleozoic metasediments and granitoids, whereas the southwest zone basically comprises Mesozoic materials; Neogene-Quaternary deposits cover a major proportion of this mountain belt (Fig. 5.1A).

Lamprophyre intrusions are frequent in the northeastern part of the Catalonian Coastal Ranges, intruding the Paleozoic basement. Most of these lamprophyres are Late Variscan in age (Losantos et al., 2000) and make up dense, sub-vertical dyke swarms with subalkaline to alkaline geochemical affinities (e.g., Ubide et al., 2010*b*). On the other hand, there is a Late Cretaceous lamprophyre suite (Solé et al., 2003; Ubide et al., under review *a* –see Chapter 3-) represented by a small group of isolated, strongly alkaline intrusions (Ubide et al., 2012*a*, 2012*b*; Fig. 5.1B). The Cretaceous lamprophyre intrusions have been described as subvolcanic sills. They were emplaced following well-developed structures of the country-rock (sub-horizontal joints or, less commonly, sub-vertical fractures). They sometimes cut the Late Variscan lamprophyre family (e.g., Gimeno, 2002; Pallí and Roqué, 1996).

## 5.3. Field appearance of the lamprophyres

Up to 8 sills have been found to belong to the Cretaceous lamprophyre suite in the Catalonian Coastal Ranges. They were emplaced into the Paleozoic basement of the northern part of the ranges and are exposed in the province of Girona in three sectors (Fig. 5.1B; Table 5.1): the eastern sector, the central sector and the western sector. The petrologic characteristics and UTM coordinates of the sills are summarised in Table 5.1.

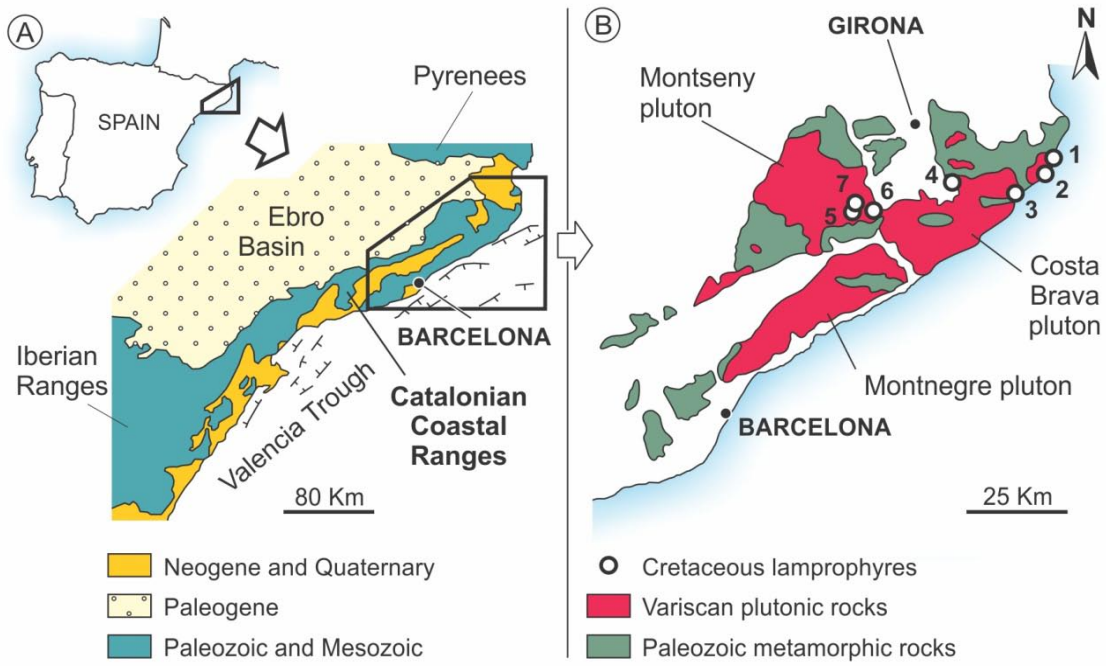


**Fig. 5.1.** A) Simplified geological map of the Catalonian Coastal Ranges (after Juez-Larré and Andriessen, 2002) and its location in the Iberian Peninsula. B) Geological map of the Paleozoic basement of the northern Catalonian Coastal Ranges (after Enrique, 1990) with indication of the Cretaceous lamprophyre intrusions. Eastern sector: 1) Aiguablava lamprophyre; 2) Calella de Palafrugell lamprophyre. Central sector: 3) S'Agaró lamprophyre; 4) Llagostera lamprophyre. Western sector: 5) Molí d'en Ponç lamprophyre and rounded blocks; 6) Molí de Dalt lamprophyre; 7) Monasterio de Sant Pere Cercada lamprophyre.

In the eastern sector, 2 intrusions crop out by the Mediterranean coast near Palafrugell: 1) the Aiguablava sill (Enrique, 2009; Gimeno, 2002; Losantos et al., 2000; Pallí and Roqué, 1991; San Miguel Arribas, 1952; San Miguel de la Cámara, 1936; Ubide et al., 2008; Fig. 5.2); and 2) the Calella de Palafrugell sill (Losantos et al., 2004; Pallí and Roqué, 1990; Ubide et al., 2012*a*; Ubide et al., under review *a* and *b*; Chapters 6 and 7 in this volume; Fig. 5.3). The central sector includes 2 intrusions: 3) the S'Agaró sill, which crops out by the coast in the vicinity of Sant Feliu de Guíxols (Pallí, 1980; Pallí and Roqué, 1996; Fig. 5.4); and 4) the Llagostera sill, which crops out inland (first reported in Ubide et al., under review *a*; Fig. 5.5). Finally, the western sector includes at least 4 intrusions located between Santa Coloma de Farners and Sant Feliu de Buixalleu: 5) the Molí d'en Ponç sill (Calderón et al., 1907; San Miguel de la Cámara, 1930; Velde and Tournon, 1970; Fig. 5.6A); 6) rounded blocks found topographically higher than the Molí d'en Ponç that potentially belong to another sill, although not found and never reported in previous studies; 7) the Molí de Dalt sill (first reported here; Fig. 5.6B, 5.6C, 5.6D); and 8) the Monasterio de Sant Pere Cercada sill (Pallí et al., 1993; Ubide et al., under review *a*; Fig. 5.6E, 5.6F).

The lamprophyres located in the coast are easily accessible using the nature trails along the coast. They show good exposures with a low alteration degree and are easily

**Table 5.1.** Cretaceous lamprophyre sills recognised in the Catalonian Coastal Ranges.

| Sector | Location | Orientation | Thickness | Texture | Macrocryst assemblage | Samples | UTM |
|---|---|---|---|---|---|---|---|
| East | Aiguablava [a] | Sub-horizontal | 2 – 0 m | Porphyritic | Amp > Cpx >> Opq > Ol | AIG-05, AIG-06 | 31T 518152 4642610 |
| | | | | | | AIG-08 | 31T 518082 4643187 |
| | | | | | | AIG-04 | 31T 518017 4643303 |
| | Calella de Palafrugell [b] | Sub-horizontal | 0.4 – 0.15 m | Porphyritic | Cpx > Amp >> Opq > Ol | CAL-1, CAL-2, CAL-3, CAL-4, CAL-5 | 31T 515127 4636865 |
| Centre | S'Agaró [c] | Sub- vertical | 0.9 m | Microitic | - | SAG-03, SAG-03B | 31T 504908 4626689 |
| | Llagostera | Sub-horizontal | 1 – 0.8 m | Porphyritic | Amp > Cpx >> Opq | LLAG-01 | 31T 490826 4629937 |
| West | Molí d'en Ponç [d] | Sub-horizontal | ~ 4 m | Porphyritic | Cpx – Ol >> Amp > Opq | SFB-3, SFB-4 | 31T 466218 4629029 |
| | | - | - | Porphyritic | Cpx > Ol >> Opq | SFB-1(r), SFB-2(r) | 31T 465860 4629223 |
| | Molí de Dalt | Sub-horizontal | ~ 4 m | Porphyritic | Cpx – Amp >> Opq – Ol | SFB-5 | 31T 470170 4630359 |
| | Mon. S.Pere Cercada | Sub-horizontal | ~ 4 m | Porphyritic | Amp – Cpx >> Opq – Ol | SFB-6 | 31T 467387 4631372 |

Mineral abbreviations are according to Whitney and Evans (2010): Ol olivine, Cpx clinopyroxene, Amp amphibole, Opq opaque minerals

UTM datum: WGS84

([a]): The Aiguablava sill was sampled in three different outcrops: Sa Planassa – Punta des Mut (samples AIG-05 and AIG-06), Cap Rubí (sample AIG-08) and Platja Fonda (sample AIG-04)

([b]): The Calella de Palafruell sill was sampled in Ses Negres

([c]): The S'Agaró sill was sampled in Cala de la Font

([d]): Near the Molí d'en Ponç lamprophyre (samples SFB-3 and SFB-4), we collected samples SFB-1(r) and SFB-2(r) from a different intrusion, although not found ("r" stands for "round stones")

recognisable as their dark brown colour contrasts with the granitic country-rock. On the other hand, the lamprophyres located inland show a yellowish hue due to alteration, which affects especially the margins of the intrusions. Moreover, these lamprophyres are harder to find as they crop out in intensely vegetated areas. Indeed, the occurrence of rounded blocks of lamprophyre near the Molí d'en Ponç sill indicates the presence of, at least, another sill in the area.

The lamprophyres are relatively thin sills (from less than 0.5 m up to more than 4 m) that show sharp contacts with the country-rock. The thickest intrusions crop out in the western sector (Table 5.1). The exact thickness of these sills however, could not be precisely measured because the sill margins were hardly recognisable due to the intense alteration of the rocks and dense vegetation in the area (see Fig. 5.6). All of the lamprophyres are sub-horizontal and have a characteristic porphyritic texture, with the exception of the S'Agaró sill, which is sub-vertical and microlitic. The porphyritic intrusions are composed of large, mm- to cm-sized mafic crystals, visible to the naked eye, embedded in a fine-grained groundmass.

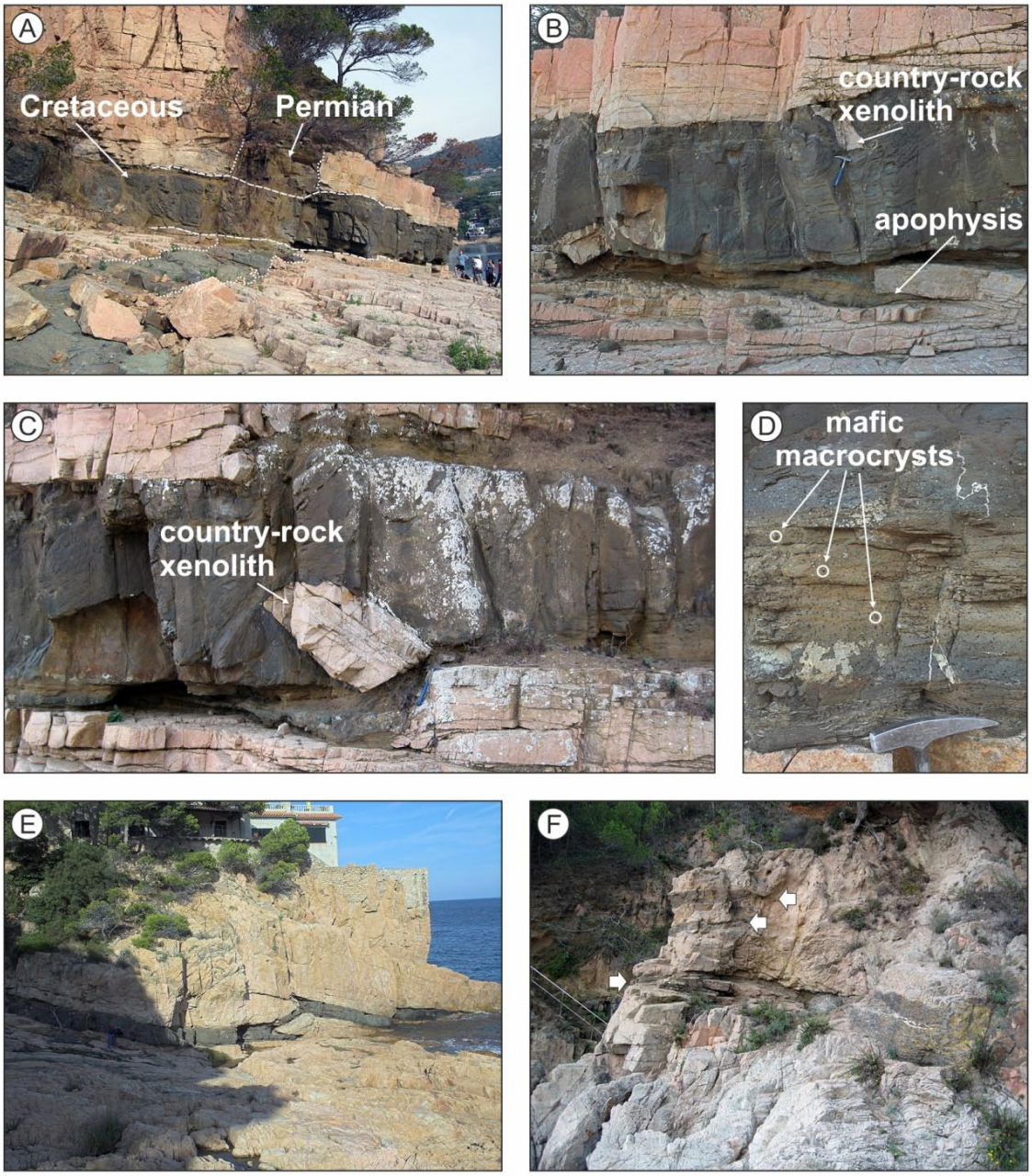


**Fig. 5.2.** Field photographs of the Aiguablava lamprophyre. A-D) Sa Planassa – Punta des Mut outcrop, where the sill cross-cuts a Late Variscan lamprophyre. E) Cap Rubí outcrop. F) Platja Fonda outcrop, where the wedge-shaped ends of the sill are observed (white arrows).

All of the sub-horizontal intrusions show a characteristic vertical zoning, as schematised in Fig. 5.7. Well developed chilled margins appear at both sides, in agreement with the difference in age between the Cretaceous magmas and the Paleozoic country-rock (e.g., Ubide et al., 2008). The chilled margins are mostly aphyric and sometimes laminated. The central facies on the other hand, displays a remarkable accumulation of large crystals towards the bottom, due to gravitational settling before solidification (Ubide et al., 2012*a* –see Chapter 6-). Vesicles are frequent in all the intrusions and reach millimetre sizes.

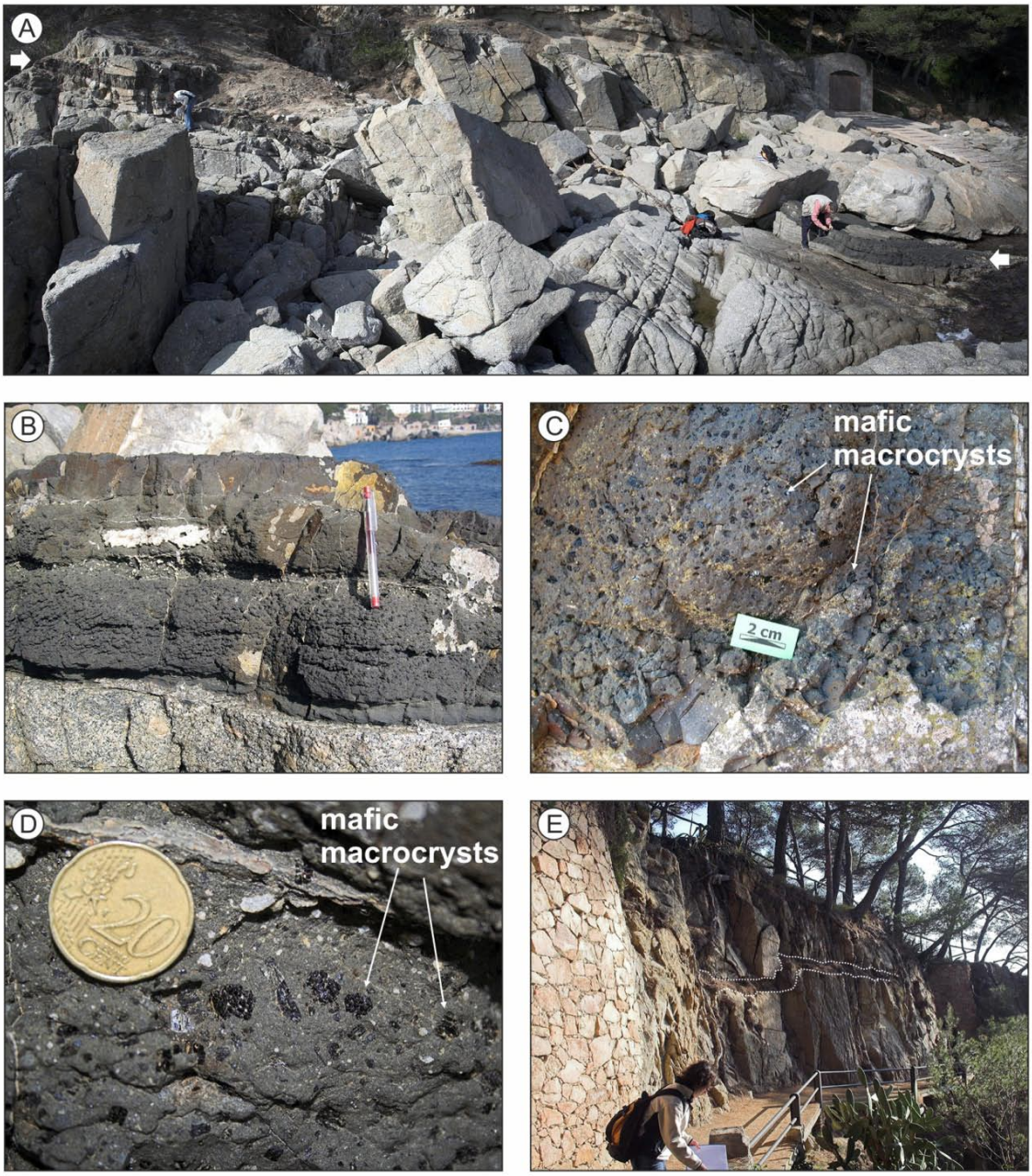


**Fig. 5.3.** Field photographs of the Calella de Palafrugell lamprophyre. A-D) Ses Negres outcrop. White arrows in A mark the ends of the sill in the picture. E) The sill crops out above the nature trail along the coast (dotted line), although it is hardly accessible and more altered than in the Ses Negres outcrop.

Vesicle alignments are commonly recognised parallel to the upper chilled margin. The abundance of vesicles together with the subhorizontal dip of most intrusions indicates a shallow level of emplacement for these magmas (Gimeno, 2002; Ubide et al., 2012*a*).

The nicest examples of vertical zoning are found in the subhorizontal sills cropping out by the shoreline, where they are clearly exposed given the absence of soil and vegetation. The sketch in Fig. 5.7 is from the Aiguablava sill. This intrusion crops out in the Aiguablava


**Fig. 5.4.** Field photograph of the S'Agaró lamprophyre, located in Cala de la Font. Note that this is the only sub-vertical intrusion of the whole lamprophyre suite. It intersects a Late Variscan lamprophyre.

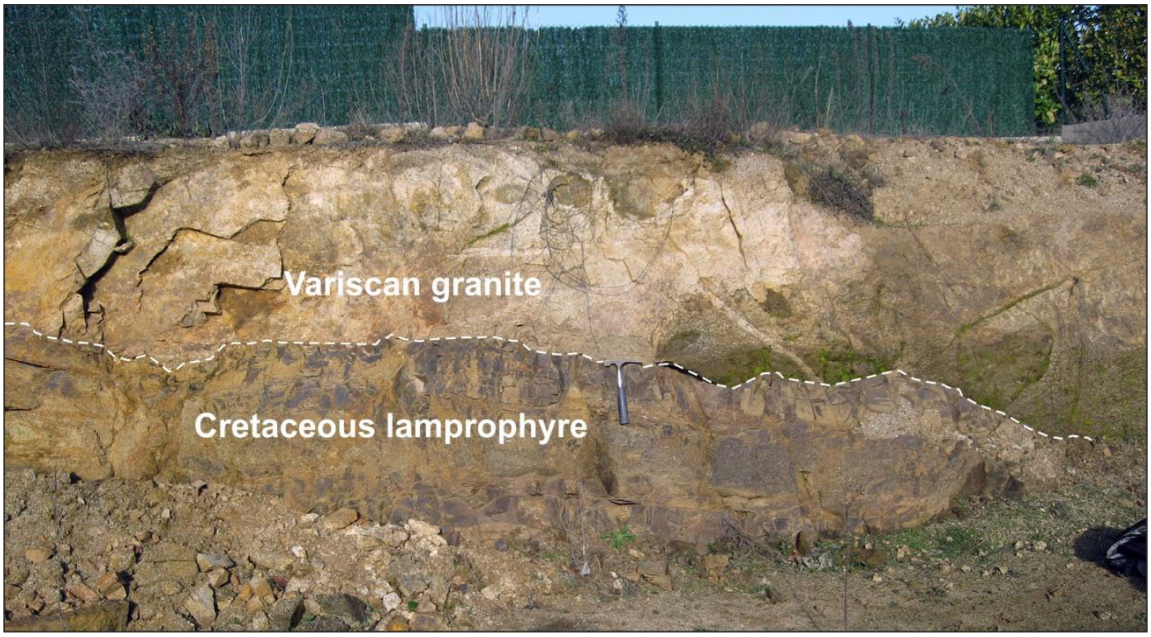


**Fig. 5.5.** Field photograph of the Llagostera lamprophyre. Although there are a few meters of exposure in the neighbouring plot, we could study and sample this less weathered underground section dug for building purposes. Nevertheless, this sill is more altered than those cropping out in the coast.

beach area, in three different locations that are less than 1 km away from each other. In the Sa Planassa – Punta des Mut outcrop the sill reaches its maximum thickness (ca. 2 m; Fig. 5.2A, 5.2B). Emplacement mechanisms are very clear in this outcrop (Gimeno, 2002), including fragments of country-rock dragged inside the intrusion during emplacement (Fig. 5.2C) and gravitational accumulation of large crystals (Fig. 5.2D). In Cap Rubí outcrop

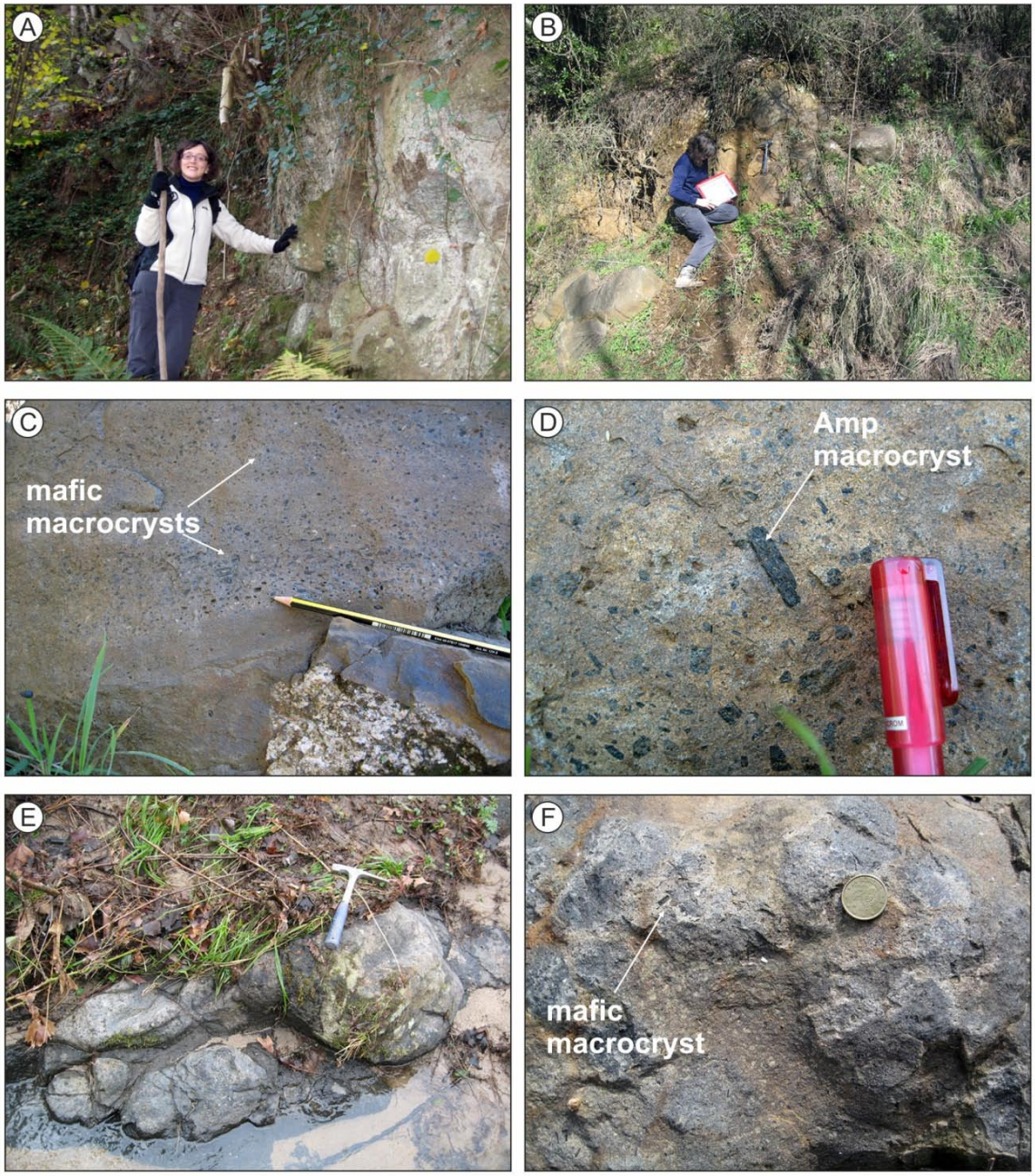


**Fig. 5.6.** Field photographs of the lamprophyres of the western sector, which is intensely vegetated. A) The Molí d'en Ponç lamprophyre. B-C-D) The Molí de Dalt lamprophyre. E-F) The Monasterio de Sant Pere Cercada lamprophyre, which crops out in a river bed. These sills are more altered than those cropping out in the coast.

the sill has an intermediate thickness and a staircase morphology indicating that the magma emplaced along pre-existing fractures (Fig. 5.2E). Finally, in Platja Fonda outcrop the wedge-shaped end of the sill can be observed (Fig. 5.2F). The groundmass crystal size decreases progressively from the Sa Planassa – Punta des Mut outcrop to the Platja Fonda outcrop, correlating with decreasing magma cooling times from the thickest to the thinnest parts of the sill (Ubide et al., 2008).

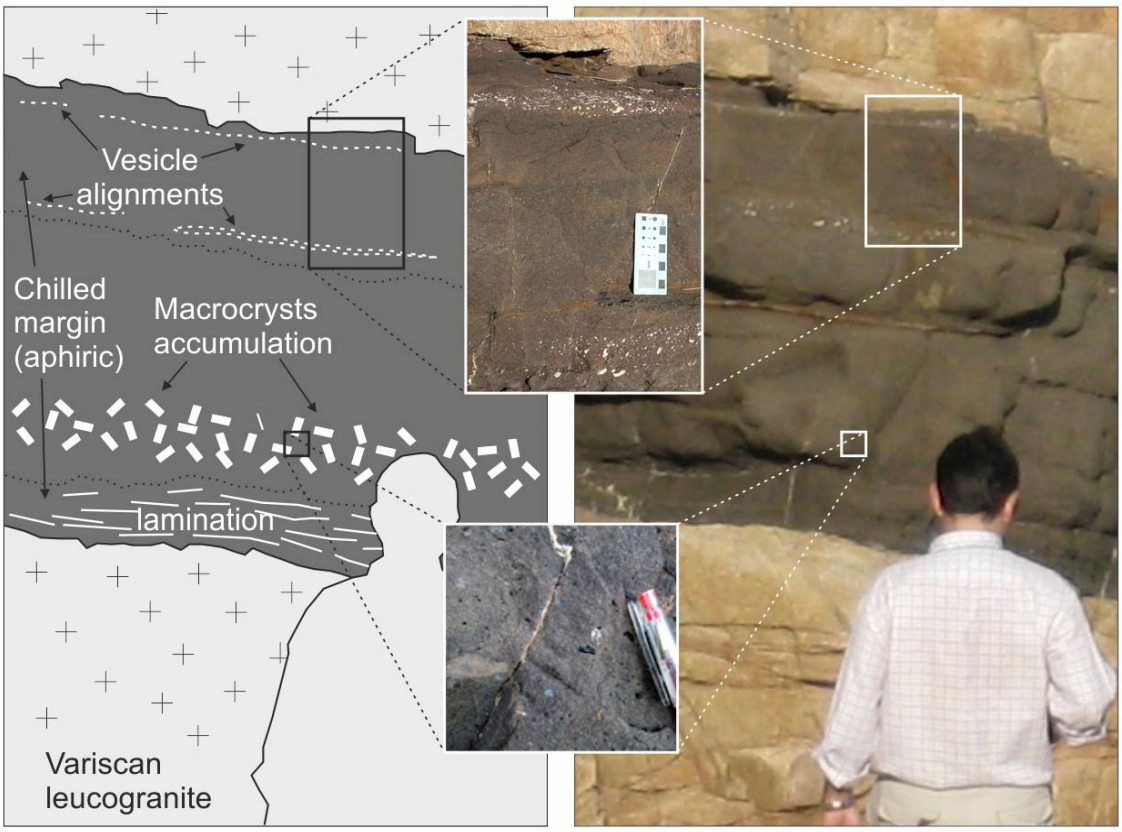


**Fig. 5.7.** Sketch and field photographs of the Aiguablava lamprophyre in Cap Rubí outcrop. Note the vertical structure of the sill, including: 1) sharp contacts with the country-rock; 2) well developed, mostly aphyric chilled margins that sometimes show lamination; 3) central facies with gravitational accumulation of large, mafic crystals towards the bottom; and 4) vesicle alignments parallel to the upper chilled margin. This structure is common to all the Cretaceous lamprophyres in the Catalonian Coastal Ranges excepting the S'Agaró lamprophyre, which is the only sub-vertical and microlitic intrusion.

The other clear example of vertical zoning is the Calella de Palafrugell sill (Fig. 5.3). This is moreover the thinnest intrusion of the whole Cretaceous lamprophyre suite (Table 5.1), allowing for a detailed study of the physical processes involved in the generation of the vertical zoning and its effects on the composition of the lamprophyre (Ubide et al., 2012*a* –see Chapter 6-).

## 5.4. Samples and methods

Several samples were collected from all lamprophyre intrusions (Table 5.1). Samples from the Aiguablava lamprophyre cover the three outcrops of the sill (see Ubide et al., 2008), whereas samples from the Calella de Palafrugell lamprophyre cover the vertical section of the sill (see Ubide et al., 2012*a*; Fig. 6.2). After a careful macroscopic examination of the samples, several sections were selected from each intrusion for microscopic examination.

Polished thin sections were prepared at the *Servicio General de Apoyo a la Investigación-SAI*, Universidad de Zaragoza (Spain). After a detailed petrographic study, thin sections were selected for *in situ*, spot analyses of major and trace elements on minerals. Major elements were analysed for all of the lamprophyres, whereas trace elements were obtained on thin sections from the Calella de Palafrugell lamprophyre and Monasterio de Sant Pere Cercada lamprophyre. Finally, whole rock analyses including major and trace element concentrations were carried out for all of the lamprophyres.

Mineral major element compositions were determined by electron microprobe (EMP) at the *Centro Nacional de Microscopía Electrónica* of the Universidad Complutense de Madrid (Spain), using a JEOL JZA-8900M electron microprobe equipped with four wavelength dispersive spectrometers. Analyses were performed using an accelerating voltage of 15 kV and an electron beam current of 20 nA, with a beam diameter of 5 µm. Elemental counting times were 10 s on the peak and 5 s on each of two background positions. Corrections for inter-elemental effects were made using a ZAF (Z: atomic number; A: absorption; F: fluorescence) procedure.

Mineral trace element compositions were determined by laser ablation ICP-MS (LA-ICP-MS) at the *Centro de Instrumentación Científica-CIC* of the Universidad de Granada (Spain), using a 213 µm Mercantek Nd-YAG laser coupled to a quadrupolar Agilent 7500 ICP-MS with a shielded plasma torch. The ablation was carried out in a He atmosphere, using a laser beam with a diameter fixed at 80 µm, a repetition rate of 10 Hz and an output energy of 0.3 mJ per pulse. The spot was preablated for 45 s using laser output energy of 50 %. The spot was then ablated for 60 s with laser output energy of 70 %. NIST-610 glass was systematically analysed as an external standard. Concentration values were corrected using the silicon concentrations obtained by electron microprobe as an internal standard. Further details on technical methods can be found in Bea et al. (2005). Data reduction was carried out by the *CIC* laboratory staff.

Samples were reduced to powder for whole rock analyses. Given the strongly porphyritic nature of most lamprophyres, large amounts of sample material were used to assure an accurate representation of the analysed powders. Samples were crushed in a manganese steel jaw-crusher, milled in an agate vibrating cup mill and successively split down to few grams at the *Servicio General de Apoyo a la Investigación-SAI*, Universidad de Zaragoza (Spain). Major and trace element concentrations were determined at the *Service d'Analyse des Roches et des Minéraux (SARM)* in Nancy (France). The samples were analysed by ICP-AES for major elements and ICP-MS for trace elements. Details of the analytical procedures and detection limits are available at http://www.crpg.cnrs-nancy.fr/SARM/. In addition, the bulk composition of the groundmass of the Calella de Palafrugell lamprophyre was modelled in Ubide et al. (2012*a* –see Chapter 6-).

## 5.5. Petrography

The Cretaceous lamprophyres in the Catalonian Coastal Ranges are classified as camptonites according to criteria by Le Maitre (2002): they have abundant large crystals of mafic minerals (mostly pale-pink clinopyroxene and brown amphibole) in a groundmass where plagioclase predominates over alkali feldspar. The complete mineral assemblage consists of brown amphibole, pale-pink clinopyroxene, feldspars, opaque minerals, pseudomorphosed olivine and accessory biotite, analcime, apatite, calcite, chlorite and recrystallised glass. Most lamprophyres have porphyritic textures, with large mafic crystals embedded in a fine-grained groundmass (Fig. 5.8). According to their size, the large crystals are considered "macrocrysts" (1 – 8 mm, commonly ca. 3 mm) or "megacrysts" (ca. 1 cm). Macrocrysts are ubiquitous, whereas megacrysts occur exclusively in the Llagostera and Molí d'en Ponç sills (Fig. 5.8); therefore, large crystals will be referred to as macrocrysts hereafter. The groundmass on the other hand, contains "microcrysts" (< 50 – 500 μm). Microcrysts are further subdivided into "microphenocrysts" (up to 500 μm in size) and "microlites" (commonly 100 – 200 μm in size). The S'Agaró lamprophyre is the only intrusion with a microlitic texture, solely composed of microcrysts, with no macrocrysts (Fig. 5.8).

### 5.5.1. The macrocryst assemblage

The macrocryst assemblage includes clinopyroxene, amphibole, opaque minerals and pseudomorphosed olivine. They sometimes cluster together into glomerocrysts. Xenocrysts of quartz and plagioclase occur occasionally. The macrocrysts accumulate towards the bottom of the central facies in all the sub-horizontal intrusions (see Fig. 5.7). Their volume fraction in the accumulation zone varies among the different intrusions and is highest for the Llagostera and Molí d'en Ponç lamprophyres, where large crystals reach more than 40 vol. % of the rock (Fig. 5.8).

The proportion of each mineral phase in the macrocryst assemblage varies among the different lamprophyres (Table 5.1; Fig. 5.8). Clinopyroxene predominates in the Calella de Palafrugell lamprophyre and in the rounded blocks that occur near Molí d'en Ponç, whereas amphibole predominates in the Aiguablava, Llagostera and Monasterio de Sant Pere Cercada intrusions. Clinopyroxene and amphibole appear in similar proportions in the Molí de Dalt lamprophyre. Finally, clinopyroxene and olivine predominate in the Molí d'en Ponç intrusion. Opaque minerals are always a minor macrocryst phase, but the highest proportions occur in the Calella de Palafrugell lamprophyre (see Fig. 5.8).

Clinopyroxene and amphibole macrocrysts have complex zoning patterns and an average size of 3 – 4 mm. Clinopyroxene macrocrysts occur in all the porphyritic lamprophyres.

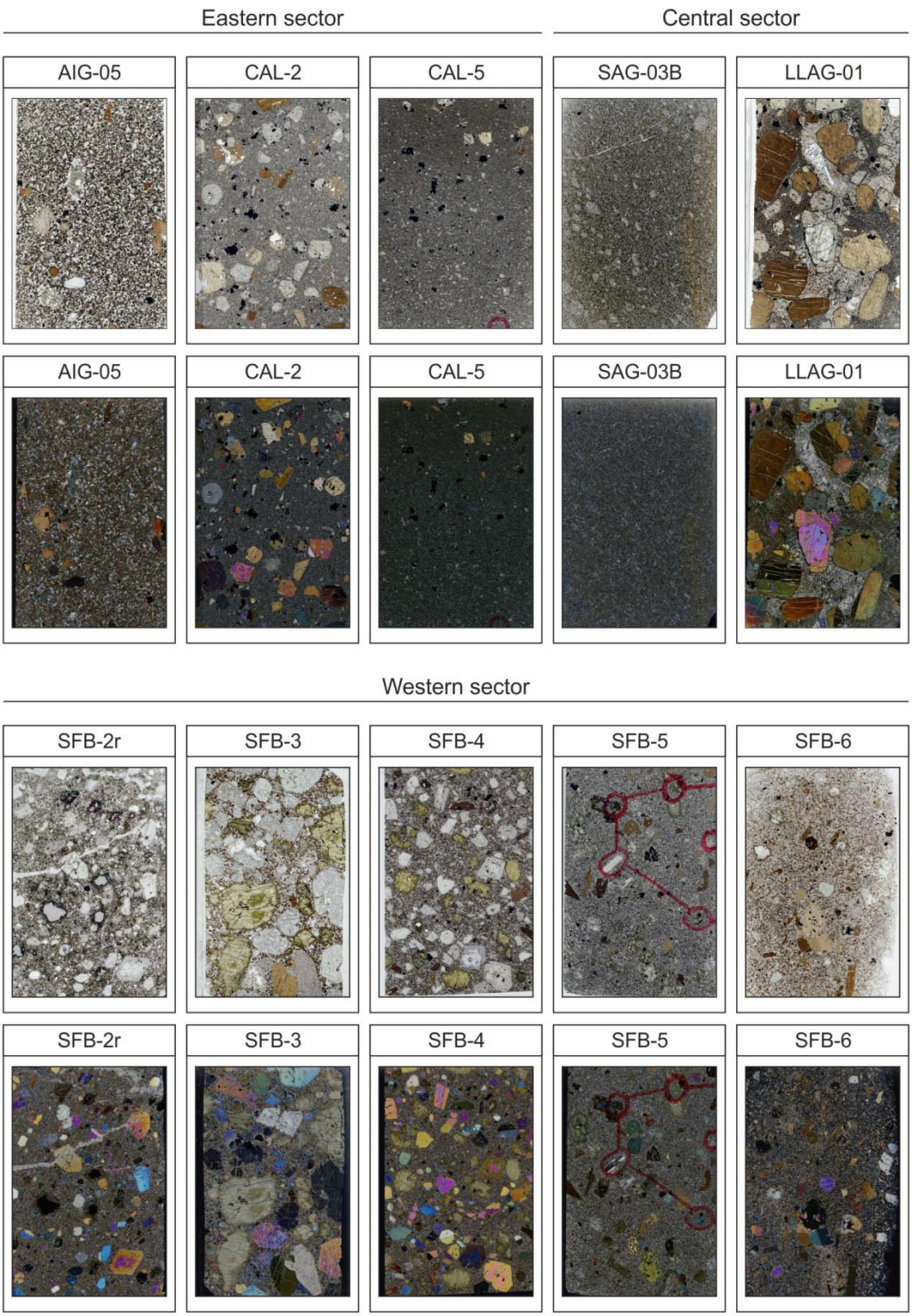


**Fig. 5.8.** Scanned thin sections of the studied lamprophyres (the width of each image is 2.5 cm). They represent the zone of accumulation of macrocrysts in each intrusion, excepting CAL-5 which belongs to the upper chilled margin of the Calella de Palafrugell lamprophyre and SAG-03B which belongs to the microlitic lamprophyre from S'Agaró. The pictures in the lower row were obtained by sandwiching the thin sections between two polarising sheets with perpendicular polarisation directions, to obtain "crossed polars" images. The thin sections from samples CAL-5 and SFB-5 show circles for mineral analysis by EMP.

Most of them are pale-pink-coloured under plane polarised light (Fig. 5.9A). They have complexly zoned subhedral to anhedral cores overgrown by euhedral to subhedral rims. In the central and western sectors, where crystals reach largest sizes (megacrysts of ca. 1 cm), there are colourless, anhedral inner cores with highly irregular contours (Fig. 5.9B). These zones of colourless clinopyroxene under plane-polarised light show second order interference colours under cross-polarised transmitted light. Particularly in the western sector, crystals with colourless inner cores show colourless thin mantles around the cores. These colourless mantles are further overgrown by pale-pink clinopyroxene, generating a striking alternation of colours (Fig. 5.9B). Moreover, there is an enclave of ca. 2 cm diameter composed of colourless clinopyroxene crystals. Meanwhile in the eastern sector, there is a pale-green, anhedral core in the Calella de Palafrugell lamprophyre; it presents resorption features, as it is corroded and displays an engulfed irregular contour (Fig. 5.9C). There are pale-green cores in the sills from the western sector as well, but they are subhedral and do not show resorption features (Fig. 5.9D).

Amphibole macrocrysts occur in all the porphyritic lamprophyres, with the exception of the rounded blocks that occur near the Molí d'en Ponç. Amphibole macrocrysts normally have homogeneous, anhedral and rounded cores and euhedral to subhedral rims. They are reddish brown-orange under plane polarised light, with different hues for the core and rim areas (Fig. 5.9E). In the eastern and western sectors, some macrocryst cores have an anhedral and rounded inner core, brown in colour (Fig. 5.9F). These inner cores are darker in the sills from the western sector than in the sills from the eastern sector. Strikingly, brown inner cores have not been recognised in the Llagostera lamprophyre (central sector), despite the fact that in this intrusion, amphibole makes up very large crystals (megacrysts of ca. 1 cm).

Opaque minerals and olivine pseudomorphs are usually smaller than clinopyroxene and amphibole macrocrysts. Macrocrysts of opaque minerals occur in all the porphyritic lamprophyres. They sometimes appear as single macrocrysts of ca. 1 mm size, especially in the Calella de Palafrugell lamprophyre (Fig. 5.8). More frequently, they are associated with macrocrysts of clinopyroxene and/or amphibole. Furthermore, alignments of sulphide inclusions occur in the inner zones of some clinopyroxene and amphibole macrocrysts. This type of inclusions has been interpreted as droplets of immiscible sulphide liquids adhering to the surfaces of rapidly growing silicate crystals (Demant et al., 2010; Peterson and Francis, 1977; Woodland and Jugo, 2007).

Olivine macrocrysts occur in all the porphyritic lamprophyres, with the exception of the Llagostera intrusion. Although olivine macrocrysts normally have a small size of ca. 1 mm, this mineral makes up megacrysts of ca. 1 cm in the Molí d'en Ponç lamprophyre. Olivine is completely transformed to secondary assemblages and unaltered relicts have only been found in a macrocryst of sample SFB-4 from the Molí d'en Ponç lamprophyre.

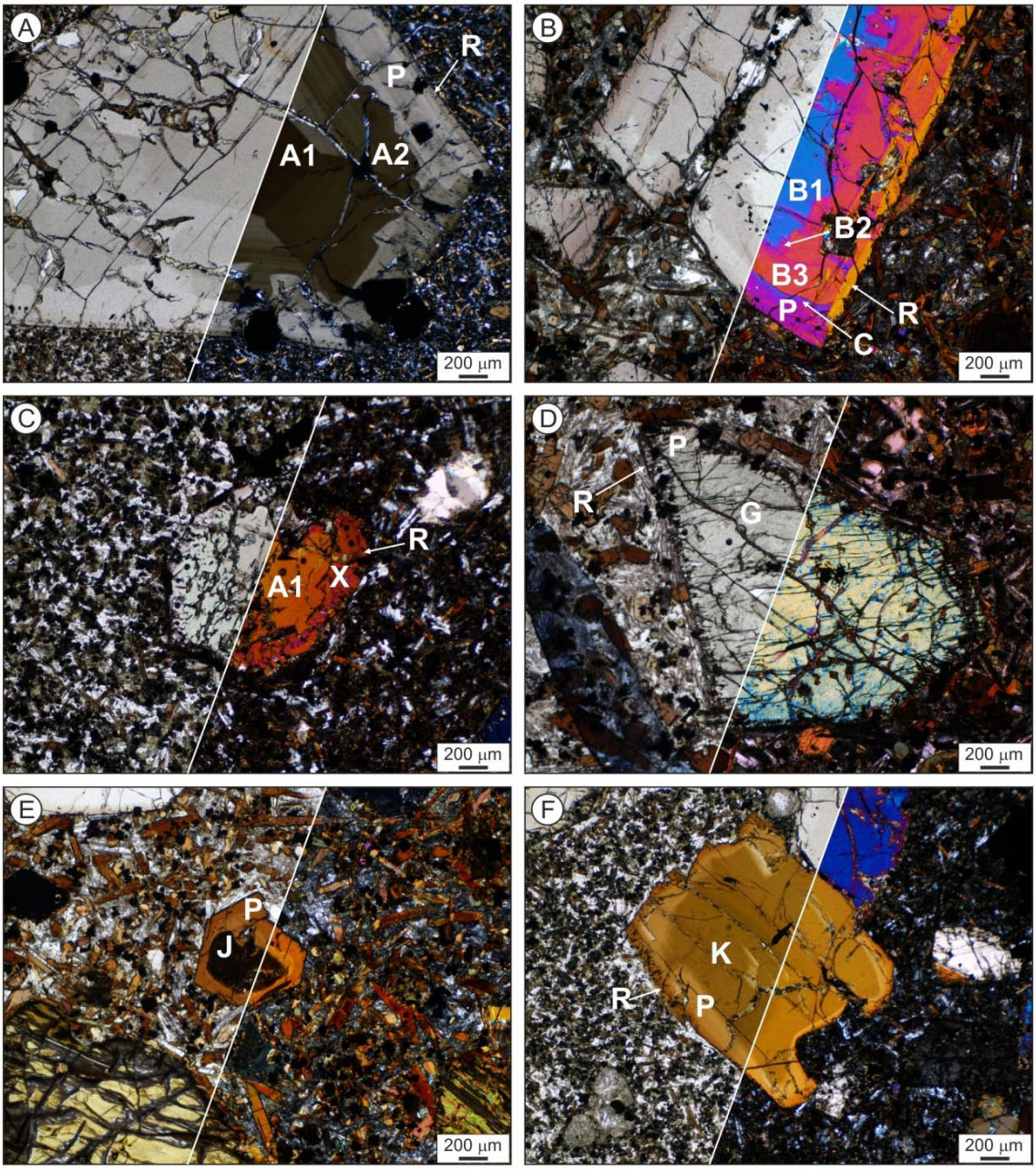


**Fig. 5.9.** Photomicrographs of clinopyroxene (A-D) and amphibole (E-F) macrocrysts. Plane-polarised (left) and cross-polarised (right) transmitted light. The same magnification was used in all the cases. Compositional types are summarised in Table 5.2.

### 5.5.2. The groundmass

The groundmass is very similar in all of the porphyritic lamprophyres and equivalent to the microlitic lamprophyre from S'Agaró (Fig. 5.10). It is composed of microcrysts of feldspars, amphibole, opaque minerals, accessory apatite and glass. The latter is mostly recrystallised to chlorite and other secondary products that are indistinguishable under the petrographic microscope. Clinopyroxene is present in minor proportions in all the lamprophyres, although in the central sector it is almost completely replaced with

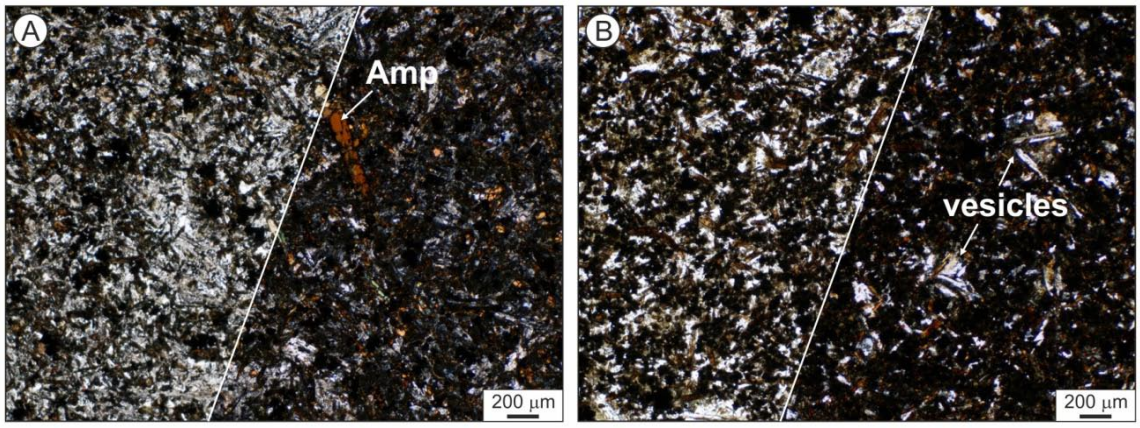


**Fig. 5.10.** Photomicrographs of the microlitic lamprophyre (A) and the groundmass of a porphyritic lamprophyres (B). Plane-polarised (left) and cross-polarised (right) transmitted light. The same magnification was used in both the cases. The arrow in A points to an amphibole microphenocryst.

chlorite. Biotite appears as an accessory phase in the lamprophyres from Aiguablava and the western sector. In the Llagostera lamprophyre there are evolved patches of groundmass with higher volume fractions of feldspars and lower volume fractions of amphibole (see whitish patches of groundmass in thin section LLAG-01; Fig. 5.8).

Most of the microcrysts are acicular microlites of amphibole and felspars, commonly 100 – 200 µm in size. The size of the microlites, however, increases as the distance increases from the sill walls, being < 50 µm at the chilled margins and up to ca. 300 µm at the centre of the intrusions. The groundmass also contains scarcer, prismatic microphenocrysts of amphibole and clinopyroxene (when present), up to 500 µm in size (Fig. 5.10A).

Vesicles are common, especially at the margins of the sills. They are mainly filled with calcite or a late magmatic assemblage including calcite, chlorite, plagioclase and amphibole (Fig. 5.10B). Occasionally, analcime-filled vesicles occur in the lamprophyres of the western sector, whereas this mineral is absent in the lamprophyres of the central and eastern sectors.

## 5.6. Mineral chemistry

### 5.6.1. Major element composition

EMP major element analyses were carried out on clinopyroxene, amphibole, feldspars, opaque minerals, olivine and accessory phases. Macrocrysts (if present) and microcrysts were analysed in all of the lamprophyres. The obtained compositional dataset includes more than 1200 analytical points and is presented with structural formulae calculations in Tables 5.I to 5.IX of the electronic supplement.

**Table 5.2.** Summary of clinopyroxene (Cpx) and amphibole (Amp) compositional types in the lamprophyres studied and locations/sectors where they appear. The colour of each compositional type is that of the symbols in figures.

| Mineral | Type | Megacrysts | Macrocrysts | Micro-phenocrysts | Microlites | Mg# mineral | Mg# liquid | AIG | CAL | SAG | LLAG | SFB |
|---|---|---|---|---|---|---|---|---|---|---|---|---|
| Cpx | B1 | Core | Core | | | 85 – 79 | ~ 55 | | | | ✓ | ✓ |
| | B2 | Core | Core | | | 78 – 72 | ~ 45 | | | | ✓ | ✓ |
| | B3 | Core | Core | | | 70 – 62 | ~ 35 | | | | ✓ | ✓ |
| | C | Core | Core | | | 78 – 72 | ~ 45 | | | | | ✓ |
| | G | | Core | | | 61 – 55 | ~ 25 | | | | | ✓ |
| | X | | Core | | | 52 – 48 | ~ 20 | | ✓ | | | |
| | A1 | | Core | | | 55 – 50 | 25-20 | | ✓ | | | |
| | A2 | | Core | | | 61 – 54 | ~ 25 | ✓ | ✓ | | | |
| | A3 | | Core | | | 67 – 59 | ~ 30 | ✓ | ✓ | | | |
| | **P** | **Mantle** | **Core** | **Core** | | **71 – 64** | **~ 35** | ✓ | ✓ | | | ✓ |
| | R | Rim | Rim | Rim | | 68 – 54 | 35 – 25 | ✓ | ✓ | | ✓ | ✓ |
| Amp | J | | Core | | | 53 – 42 | ~ 25 | | | | | ✓ |
| | K | | Core | | | 55 – 48 | ~ 30 | ✓ | ✓ | | | |
| | **P** | **Core** | **Core** | **Core** | | **62 – 53** | **~ 35** | ✓ | ✓ | ✓ | ✓ | ✓ |
| | R | Rim | Rim | Rim | Microlite | 57 – 35 | 30 – 20 | ✓ | ✓ | ✓ | ✓ | ✓ |

Mg# represents magnesium number: 100 MgO / (MgO + total iron as FeO).
Megacrysts are scarce and they are considered together with Macrocrysts in the text.
Microphenocrysts and Microlites belong to the groundmass of the lamprophyres.
Cpx-P and Amp-P (marked in bold) are in equilibrium with the bulk composition of the groundmass (see discussion).
AIG Aiguablava lamprophyre and CAL Calellade Palafrugell lamprophyre belong to the eastern sector.
SAG S'Agaró lamprophyre and LLAG Llagostera lamprophyre belong to the central sector.
SFB Sant Feliu de Buixalleu lamprophyres belong to the western sector and are considered together because they share the same compositional types.

In the case of clinopyroxene and amphibole, there are significant compositional variations among different crystal types and within single crystals. The extensive dataset and back-scattered electron images make it possible to investigate the zoning patterns observed in the petrographic study. The obtained compositional types are summarised in Table 5.2, which also includes the colours used in the figures.

*Clinopyroxene*

More than 500 analyses were obtained from clinopyroxene macrocrysts and microcrysts. They are presented in Table 5.I of the electronic supplement. Clinopyroxene macrocrysts appear in all of the porphyritic lamprophyres. Clinopyroxene microcrysts appear as microphenocrysts in all of the lamprophyres, although in the central sector they are almost completely replaced with chlorite and thus not analysable.

Most clinopyroxene compositions are classified as diopside according to criteria by Morimoto et al. (1988; Fig. 5.11), with ferrosilite contents in the range $Fs_{5\text{-}21}$. They show a wide variation range for magnesium number (Mg# = 100 MgO / (MgO + total iron as FeO)), between 48 and 85 and high $TiO_2$, $Al_2O_3$ and CaO concentrations, up to ca. 5 wt. %, 11 wt. % and 24 wt. % respectively (see Table 5.I of the electronic supplement). High CaO concentrations produce wollastonite contents over 50 (Fig. 5.11), a feature typical of alkaline rocks (e.g., Aulinas et al., 2010).

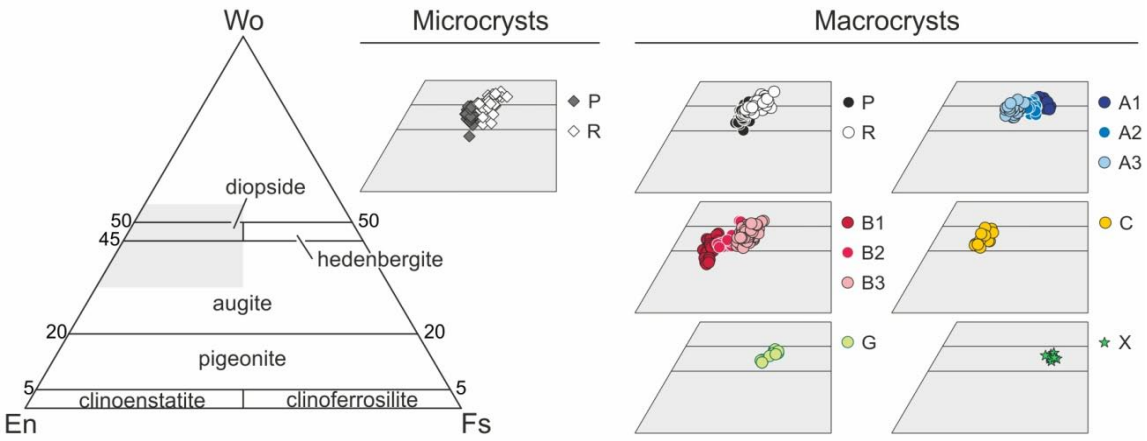


**Fig. 5.11.** Clinopyroxene classification diagram wollastonite – enstatite – ferrosilite (Morimoto et al., 1988).

All the compositions are plotted in bivariate diagrams vs. decreasing Mg# in Fig. 5.12. The complex zoning patterns observed for the macrocryst cores in the petrographic study are correlated with significant changes in composition (Table 5.2; Fig. 5.12). 10 compositional types have been defined in macrocryst cores: B1, B2, B3, C, G, X, A1, A2, A3 and P. Macrocryst rims have a distinct composition that has been named as R. Regarding the microphenocrysts of the groundmass, they show simple zoning into core and rim zones. The composition of the core is P-type and the composition of the rim is R-type. Given the complexity of compositions and the complex ways in which they are inter-related, especially in macrocryst cores, the temporal relationships between all the clinopyroxene compositions are summarised in Table 5.3, according to the relative stratigraphy between the different compositions in the analysed crystals.

P compositions occur in all of the porphyritic lamprophyres from the eastern and western sectors. They appear in the outermost zone of macrocryst cores and as microphenocryst cores. R compositions are common to all the porphyritic lamprophyres and appear as rims of macrocrysts and microphenocrysts. They are always the last compositions to crystallise (Table 5.3). P-R compositions form a common trend of decreasing $SiO_2$ and MgO and increasing $TiO_2$ and $Al_2O_3$ with decreasing Mg#, keeping rather constant and low values for $Na_2O$ and $Cr_2O_3$, the latter close to 0 (Fig. 5.12). This trend implies a normal zoning from P to R compositions, both for macrocrysts and microphenocrysts. The rest of compositions belong to macrocryst cores only and do not fit the P-R trend.

A-type and B-type macrocryst cores are the most common and are subdivided into three compositional zones, named 1, 2 and 3 in order of crystallisation. B1-B2 compositions correlate with the colourless, irregular inner cores appearing in the macrocrysts of the central and western sectors (Fig. 5.9B). B1 is the inner area and B2 is the diffused outer area of these inner cores. Some B1 compositions are classified as augite instead of

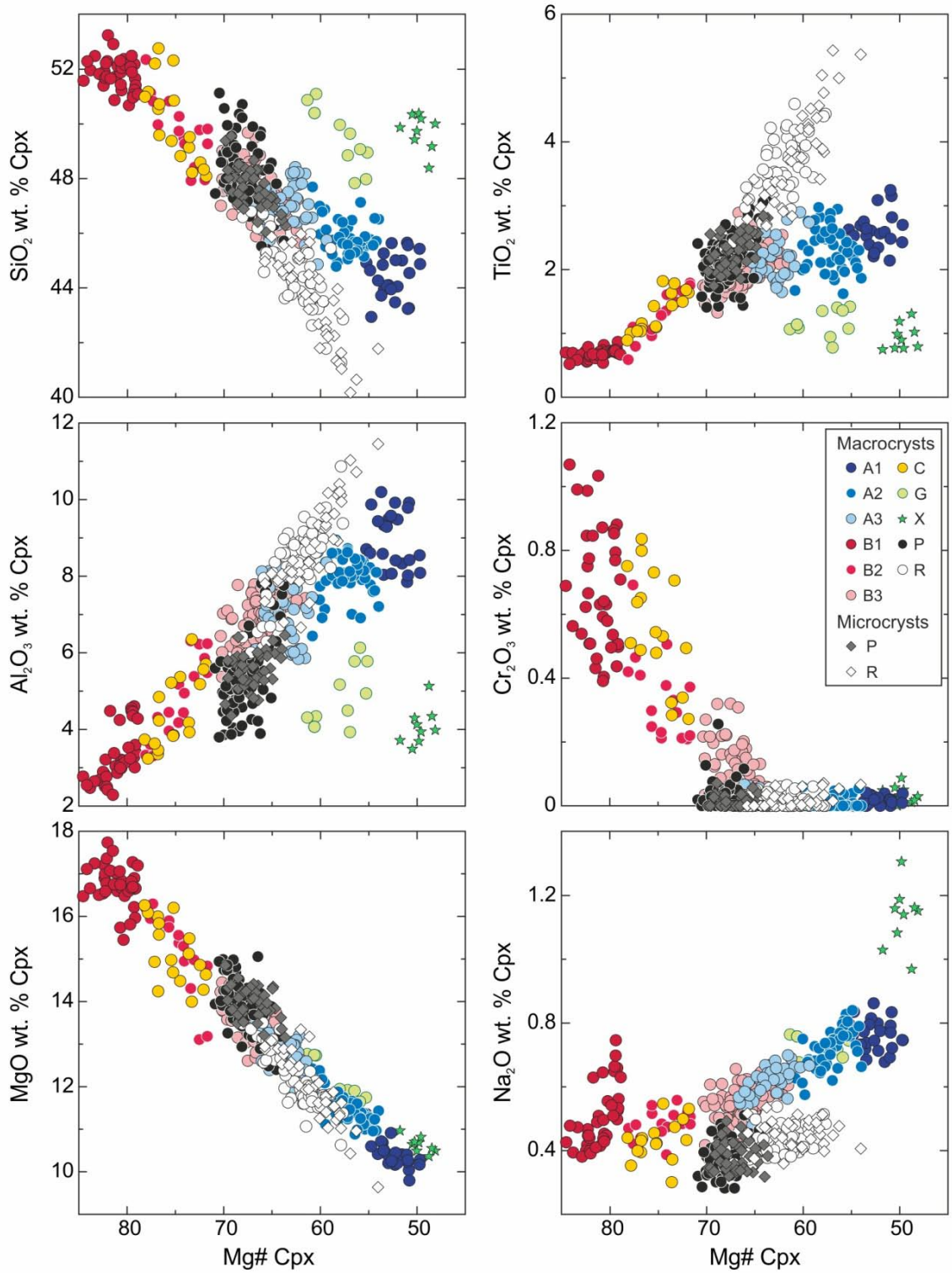


**Fig. 5.12.** Clinopyroxene major element composition in bivariate diagrams vs. decreasing Mg#.

diopside (Fig. 5.11). Colourless and anhedral B1-B2 are overgrown by pale-pink and subhedral B3. Then, in the lamprophyres from the western sector, colourless C appears as a thin zone surrounding B3, and it is followed by pale-pink P and R compositions.

**Table 5.3.** Clinopyroxene crystal stratigraphy. The compositional types are repeated in columns and rows and the ticks show the temporal relationships between them. Note that B1, G and X compositions are always inner cores, that P and R compositions overgrow most of the others and that R compositions are the last to crystallise.

| | | Mantling phases | | | | | | | | | | |
|---|---|---|---|---|---|---|---|---|---|---|---|---|
| | | B1 | B2 | B3 | C | G | X | A1 | A2 | A3 | P | R |
| Mantled phases | B1 | | ✓ | ✓ | | | | | | | | |
| | B2 | | | ✓ | | | | | | | ✓ | |
| | B3 | | | | ✓ | | | | | | ✓ | ✓ |
| | C | | | | | | | | | | ✓ | ✓ |
| | G | | | | | | | | | | ✓ | |
| | X | | | | | | | ✓ | | | | |
| | A1 | | | | | | | | ✓ | ✓ | ✓ | ✓ |
| | A2 | | | | | | | | | ✓ | ✓ | ✓ |
| | A3 | | | | | | | | | | ✓ | ✓ |
| | P | | | | | | | | | | | ✓ |
| | R | | | | | | | | | | | |

B1-B2-B3 macrocryst cores define a trend of decreasing $SiO_2$, MgO and $Cr_2O_3$ and increasing $TiO_2$ and $Al_2O_3$ with decreasing Mg#, for variable contents in $Na_2O$ (Fig. 5.12). C compositions overgrow B-type zones but strikingly, they return to a composition similar to B2 instead of continuing the Mg#-decreasing trend defined by B1-B2-B3 cores. Mg# decreases again from C to P compositions. The high contents in Mg#, MgO and $Cr_2O_3$ of B- and C-type cores are remarkably above the rest of compositions. Similarly, their contents in $SiO_2$ are relatively high and their contents in $TiO_2$ and $Al_2O_3$ relatively low, whereas $Na_2O$ concentrations fall within the range defined by the other compositions.

A1-A2-A3 compositions correlate with the pale-pink cores in the macrocrysts of the eastern sector and are overgrown by P compositions. Considering crystal stratigraphy, Mg# increases with time in A-type cores (Fig. 5.12). The Mg# increase is associated with an increase in $SiO_2$ and MgO and a decrease in $Al_2O_3$ and $Na_2O$, with fairly constant values for $TiO_2$ and $Cr_2O_3$. The A1-A2-A3-P evolution therefore defines a reverse zoning pattern. $Al_2O_3$ and $Na_2O$ concentrations are high in A-type cores, whereas $SiO_2$, $TiO_2$ and MgO concentrations are relatively low and $Cr_2O_3$ contents are close to 0.

X and G compositions belong to pale-green macrocryst cores. Only one X-type core has been recognised, in the Calella de Palafrugel lamprophyre (eastern sector). G-type cores appear in the lamprophyres from the western sector. X- and G-type cores have Mg#-poor, $Na_2O$-rich compositions (Fig. 5.12). X compositions are the most extreme, with the lowest contents in Mg# and MgO and the highest concentrations in $Na_2O$, MnO and total iron expressed as FeO ($FeO^T$) (not shown in the figure; see Table 5.I of the electronic supplement). Both the X- and G-type cores have relatively high concentrations in $SiO_2$, relatively low concentrations in $TiO_2$ and $Al_2O_3$, and $Cr_2O_3$ concentrations close to 0. The X-type core is intensely resorbed and overgrown by an A1 composition, whereas G-type cores are subhedral and directly overgrown by P compositions (Table 5.3).

The compositional variation of B-type and A-type cores points towards P compositions (Fig. 5.12). The difference is that B-type cores lose Mg# with time whereas A-type cores gain Mg# with time. C compositions overgrow B-type cores and they also appear as nuclei in macrocryst cores from the western sector; in any case, their composition is equivalent to B2 compositions and they are overgrown by P compositions, later rimmed by R compositions (Table 5.3). In contrast with the rest, X- and G-type cores do not define linear trends but plot fairly concentrated in bivariate diagrams (Fig. 5.12). These cores are unrelated to any other composition, although they have Mg# contents close to A-type cores.

*Amphibole*

More than 450 analyses were obtained from amphibole macrocrysts and microcrysts. They are presented in Table 5.II of the electronic supplement. Amphibole macrocrysts appear in all of the porphyritic lamprophyres, with the exception of the rounded blocks near the Molí d'en Ponç lamprophyre. Amphibole microcrysts appear in all of the lamprophyres and are divided into microphenocrysts and microlites.

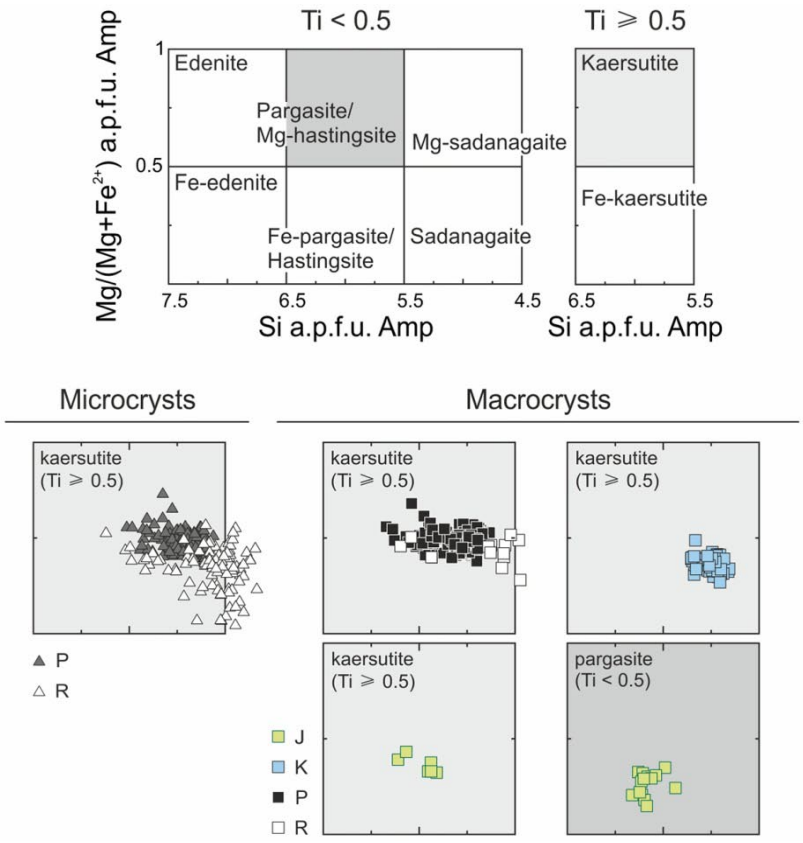


**Fig. 5.13.** Amphibole classification diagrams for calcic amphiboles with $Ca_B \geq 1.5$ and $(Na + K)_A \geq 0.5$ (Leake et al., 1997).

Most amphibole compositions are classified as kaersutite according to criteria by Leake et al. (1997; Fig. 5.13), as typical for alkaline rocks. Mg# contents vary between 35 and 62, $TiO_2$ contents reach almost 8 wt. % and $SiO_2$ contents go down to ca. 35 wt. % (see Table 5.II of the electronic supplement).

All the compositions are presented in bivariate diagrams vs. decreasing Mg# in Fig. 5.14. The petrographic zoning in amphibole, although

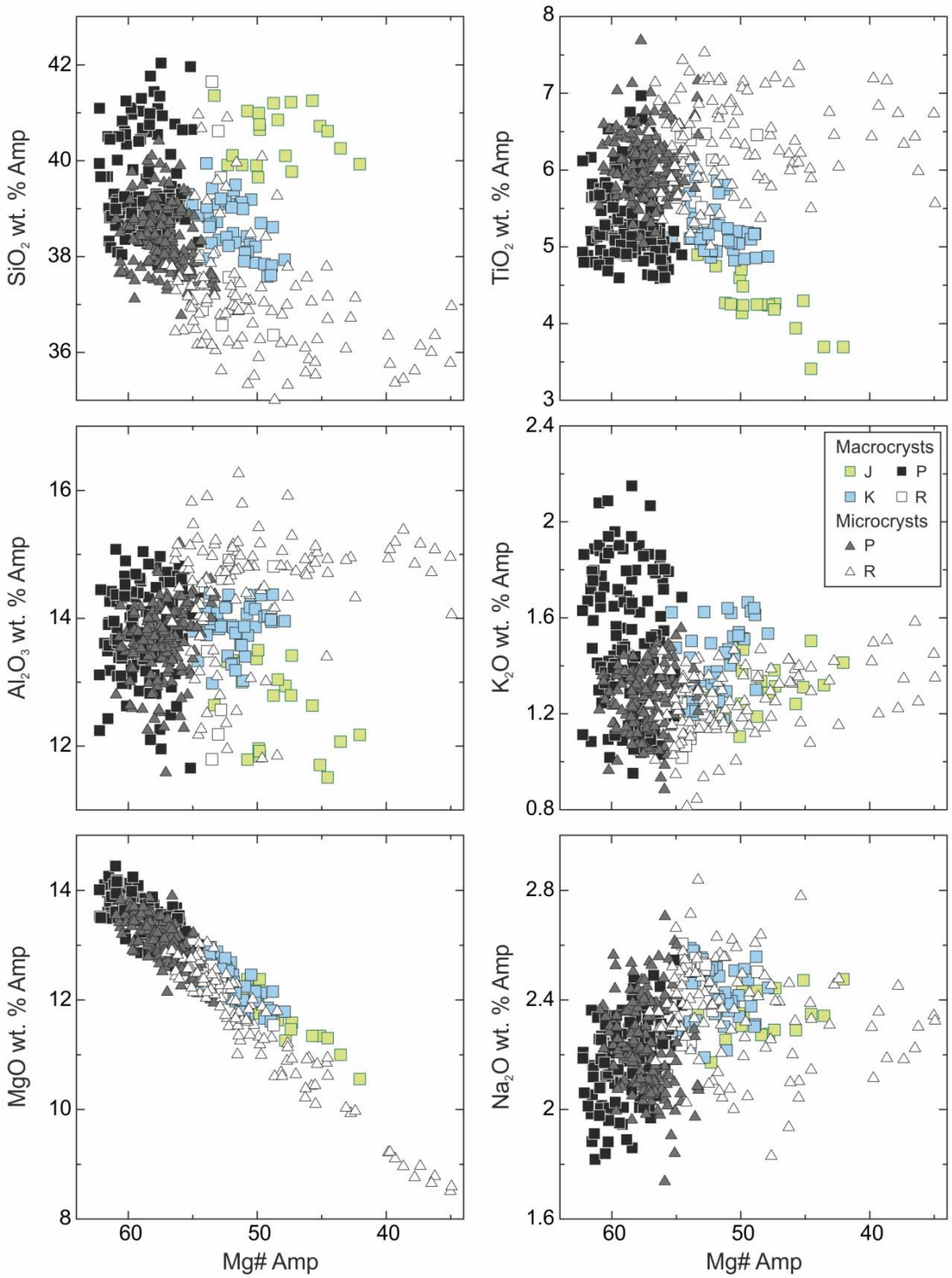


**Fig. 5.14.** Amphibole major element composition in bivariate diagrams vs. decreasing Mg#.

simpler than in the case of clinopyroxene, has a correlation with compositional changes as well (Table 5.2; Fig. 5.14). 3 compositional types have been defined in macrocryst cores: J, K and P. In contrast with clinopyroxene, most amphibole macrocryst cores, including those of the largest crystals at Llagostera (Fig. 5.8), are unzoned and composed entirely of P compositions. Macrocryst rims have a composition that has been named as

R, following the same criterion as in clinopyroxene. In the groundmass, microphenocrysts have a simple zoning into P-type cores and R-type rims. They therefore have a zoning pattern equivalent to that of most macrocrysts. Finally, the microlites are unzoned and have an R composition. The temporal relationships between the different compositional types in amphibole are presented in Table 5.4, according to their relative stratigraphy in the analysed crystals. Note that R compositions are the last to crystallise.

**Table 5.4.** Amphibole crystal stratigraphy (as in Table 5.3). Note that J and K compositions are always inner cores, that P and R compositions overgrow most of the others and that R compositions are the last to crystallise.

| | | Mantling phases | | | |
|---|---|---|---|---|---|
| | | J | K | P | R |
| Mantling pahses | J | | | ✓ | |
| | K | | | ✓ | ✓ |
| | P | | | | ✓ |
| | R | | | | |

Compositional trends in amphibole are not as clearly defined as in clinopyroxene (compare Fig. 5.12 and Fig. 5.14) and R compositions show a significant scatter because they have a slightly different slope in the lamprophyres from the central sector relative to the rest. Yet, P-R compositions define a normal zoning trend of decreasing Mg# and MgO (Fig. 5.14). P-type macrocryst cores and microphenocryst cores are similar in composition, especially considering the Mg# values. However, P compositions in macrocryst cores reach highest MgO, $K_2O$ and $SiO_2$ concentrations and lowest $TiO_2$ contents.

The rounded, brown-coloured inner cores observed in some of the macrocrysts in the eastern and western sectors (Fig. 5.9F) have a distinct composition. In the western sector, they have a dark brown colour and a composition named as J. In the eastern sector, they have a lighter brown colour and a composition named as K. Both the J- and K-type inner cores are overgrown by orange-coloured P compositions that constitute the rest of the macrocryst core.

K-type inner cores have lower Mg# and MgO contents than P compositions (Fig. 5.14). J-type inner cores reach even lower Mg# and MgO contents and moreover, higher $SiO_2$ and lower $TiO_2$ and $Al_2O_3$ concentrations. J-P and K-P macrocryst cores therefore define reverse zoning patterns. In contrast with the other amphibole compositions, J-type inner cores are mainly classified as pargasite and in a lower proportion as kaersutite (Fig. 5.13). The difference with the other compositions is especially clear for $TiO_2$, with concentrations down to ca. 3.5 wt. % in J compositions (Fig. 5.14).

*Feldspars*

More than 100 analyses were obtained from felspars, which occur as microlites in all of the lamprophyre intrusions. The analyses are presented in Table 5.III of the electronic supplement.

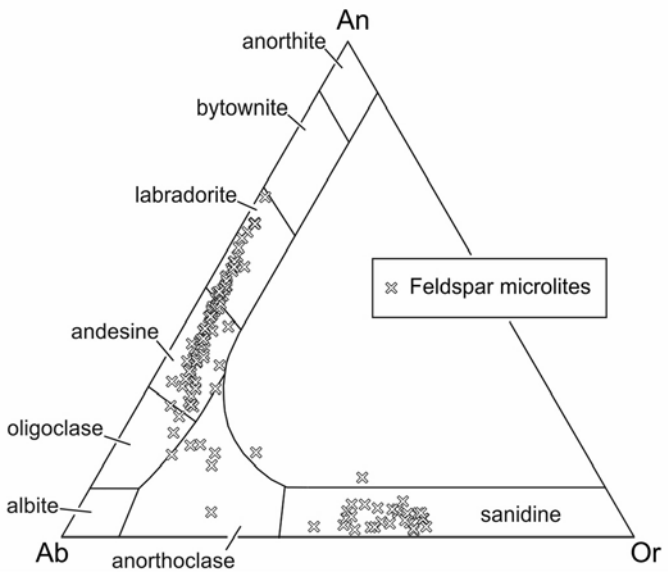


**Fig. 5.15.** Felspar classification diagram anorthite – albite – orthose.

The ternary classification diagram anorthite – albite – orthoclase is shown in Fig. 5.15. Feldspar compositions vary continuously from labradorite to sanidine ($An_{01-69}$, $Ab_{30-72}$, $Or_{01-63}$). Plagioclase-type compositions are progressively enriched in the orthoclase component as their anorthite content decreases, a feature typical of alkaline rocks.

The range of compositions is similar among the different lamprophyres. Nevertheless, most analyses from the eastern sector range from labradorite to oligoclase whereas all analyses obtained from the S'Agaró lamprophyre are classified as sanidine (see Table 5.III of the electronic supplement).

*Opaque minerals*

More than 70 analyses were obtained from macrocrysts and microcrysts of opaque minerals. They are presented in Tables 5.IV and 5.V of the electronic supplement. The macrocrysts occur in all of the porphyritic lamprophyres and the microcrysts occur in all of the lamprophyres.

Opaque minerals are mainly Fe-Ti oxides. Most of them are spinel group minerals, but there are also minor amounts of ilmenite. $Cr_2O_3$ concentrations are below 2 wt. %. Spinel group compositions are plotted in bivariate diagrams vs. decreasing MgO in Fig. 5.16. Magnetite – titanomagnetite compositions are frequent in the microcrysts and have variable $TiO_2$ concentrations between 2 and 18 wt. %. The rest of compositions, including all macrocrysts and some microcrysts, have significant amounts of MgO and $Al_2O_3$ and a correlative decrease in $FeO^T$ (not shown), indicating the involvement of the spinel end-member.

*Olivine*

Olivine pseudomorphs occur as macrocrysts in the eastern and western sectors. Analyses were carried out on the unaltered relicts found in a macrocryst core from the Molí d'en Ponç lamprophyre (sample SFB-4) and are presented in Table 5.VI of the electronic supplement.

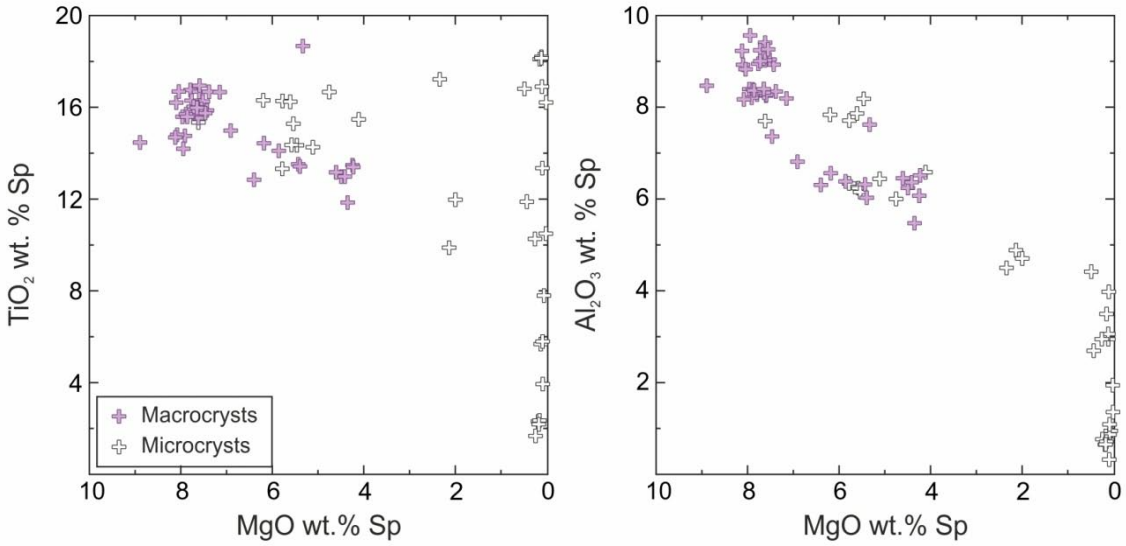


**Fig. 5.16.** Spinel group minerals major element composition in bivariate diagrams vs. decreasing MgO.

The compositions are highly homogeneous, with forsterite contents of $Fo_{88-89}$, Mg# values of 80 – 82, NiO concentrations varying in the range 0.16 – 0.26 wt. %, and CaO concentrations varying from 0.22 to 0.26 wt. %, away from compositions in peridotite (Fig. 5.17).

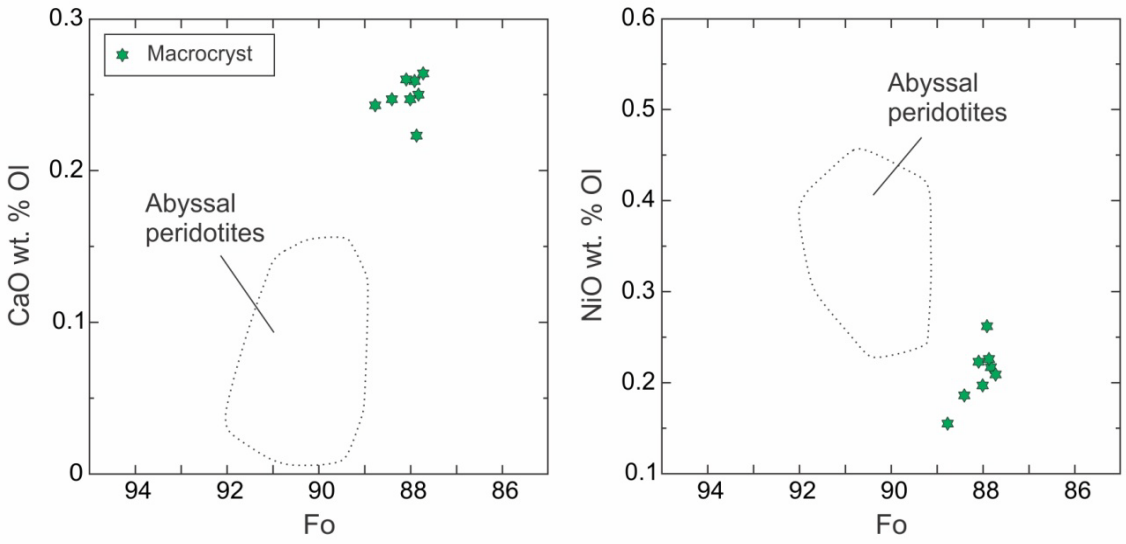


**Fig. 5.17.** Olivine major element composition in bivariate diagrams vs. decreasing forsterite. Fields for abyssal peridotites are from Sakyi et al. (2012; and references therein).

*Accessory minerals*

Analyses on accessory phases were carried out for biotite, analcime and apatite. They are presented in Tables 5.VII, 5.VIII and 5.IX of the electronic supplement.

Biotite has concentrations in MgO from 6 to 16 wt. % and concentrations in $FeO^T$ of 9 to 24 wt. %. $TiO_2$ and $K_2O$ concentrations vary in the ranges 6 – 9 and 8 – 9, respectively. The ratio $Fe^{2+}$ / ($Fe^{2+}$ + Mg) in atoms per formula unit varies between 0.24 and 0.69, with most compositions classified as biotite and few compositions classified as phlogopite according to the Mg:Fe = 2:1 division defined by Deer et al. (1966).

Analcime has $SiO_2$ and $Al_2O_3$ concentrations that range 52 – 55 and 23 – 24 respectively, with constant values for $Na_2O$ of ca. 12 wt. %.

Apatite is mainly classified as fluorapatite, with F contents of 0.12 – 2.20 wt. % and Cl contents of 0.22 – 0.45 wt. %. CaO concentrations vary from 27 to 56 wt. % and $P_2O_5$ concentrations vary from 22 to 42 wt. %.

### 5.6.2. Trace element composition

LA-ICP-MS trace element analyses were undertaken on clinopyroxene and amphibole, given the complex compositional changes recorded in the crystals of these minerals. Macrocrysts and microphenocrysts were analysed; microlites were too small to provide reliable spot analyses. A lamprophyre from the eastern sector (Calella de Palafrugell) and a lamprophyre from the western sector (Monasterio de Sant Pere Cercada) were selected for analysis.

In the case of clinopyroxene, A-, B-, G- and X-type macrocrysts cores were analysed, together with P-type compositions in macrocryst cores and microphenocryst cores. In the case of amphibole, analyses were obtained from J- and K-type inner cores in macrocrysts and P-type compositions in macrocryst cores and microphenocryst cores. Moreover, some amphibole macrocrysts in the Monasterio de Sant Pere Cercada lamprophyre have thick rims so that rim analyses could be carried out as well.

The obtained dataset includes a total of 23 compositions and is presented in Table 5.X of the electronic supplement. Primitive mantle (McDonough and Sun, 1995) normalised trace element patterns are presented in Fig. 5.18.

Clinopyroxene Rare Earth Element (REE) concentrations are up to ca. 60 times enriched over the primitive mantle (Fig. 5.18A). REE normalised patterns are convex-upwards, with the exception of the X-type green core, which presents convex-downwards patterns. Among the convex-upwards normalised patterns, B-type compositions are the least REE-enriched, P- and certain A-type cores have an intermediate composition and G- and certain A-type cores are the most REE-enriched.

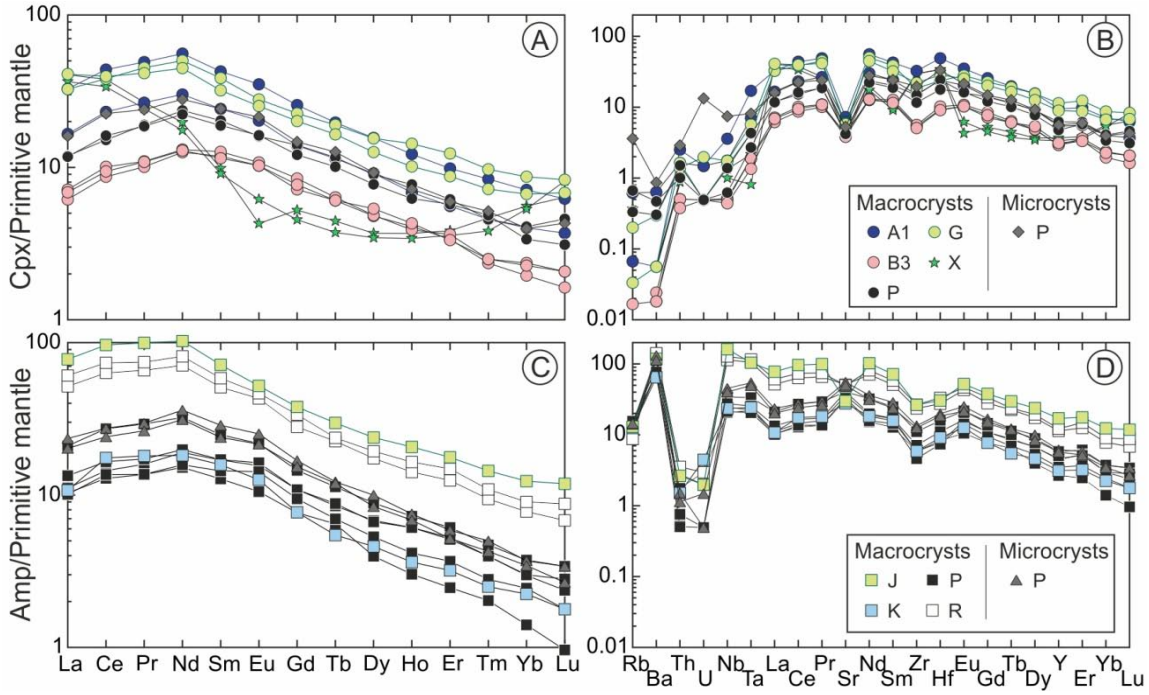


**Fig. 5.18.** Trace element composition of clinopyroxene (A, B) and amphibole (C, D), normalised to primitive mantle (McDonough and Sun, 1995). Normalised values below 0.01 were screened out.

Considering more trace elements (Fig. 5.18B), the X-type core again shows a normalised pattern different from the rest. All of the analyses however, display a negative anomaly for Sr and low concentrations in Rb and Ba, significantly below the primitive mantle in the case of X-, G-, B- and some A-type cores. Finally, the P-composition obtained from a microphenocryst shows a distinct positive anomaly for U.

Amphibole is up to ca. 100 times enriched over the primitive mantle for the REE (Fig. 5.18C). REE normalised patterns are convex-upward and fairly parallel to each other. They are similar to convex-upwards patterns in clinopyroxene (compare with Fig. 5.18A). J-type compositions are clearly the most REE-enriched, closely followed by rim compositions. K- and P-type compositions on the other hand, have lower concentrations in REE. P-type microphenocryst cores reach relatively enriched compositions.

Multielemental normalised patterns for amphibole (Fig. 5.18D) are fairly parallel with slight enrichment differences between the different compositional types, similarly to the REE-normalised patterns. Moreover, J- and R-type compositions show a negative anomaly in Sr, whereas K- and P-type compositions show a positive anomaly for this element. All of the normalised patterns show a strong negative anomaly for the U-Th pair and high normalised values for Ba.

## 5.7. Whole rock chemistry

All of the lamprophyres were analysed for whole rock compositions. The lamprophyres located inland (Llagostera and the western sector) are partly altered, especially at the chilled margins, so the analyses were carried out on the zone of accumulation of mafic macrocrysts (see Fig. 5.8). Thus, most samples have a porphyritic texture. Microlitic whole rock compositions include the lamprophyre from S'Agaró and the groundmass of the Calella de Palafrugell lamprophyre modelled in Ubide et al. (2012*a* –see Chapter 6-). The whole rock composition dataset is presented in Table 4.1 –see Chapter 4- and includes 17 analyses.

### 5.7.1. Major element composition

The lamprophyres are basic and ultrabasic rocks, silica undersaturated and rich in titanium and alkalis (Table 4.1). They are olivine- and nepheline-normative. The alteration of the samples is low and restricted to the replacement of olivine macrocrysts and glass, which are present in minor proportions, with secondary mineral assemblages (Ubide et al., 2012*a*). Nevertheless, Loss on ignition (LOI) values are relatively high due to the abundance of hydrous minerals and vesicles.

Whole rock magnesium number (Mg# = 100 MgO / (MgO + FeO) and FeO = 0.9 x total iron as $Fe_2O_3$) shows a wide variation range, between 27 and 61. However, only some samples from the central and western sectors have values over 40 and only the Molí d'en Ponç lamprophyre (western sector) has values over 50. MgO concentrations vary between 4 and 14 wt. %, with the highest values for the Molí d'en Ponç lamprophyre (Table 4.1).

Fig. 5.19 shows whole rock major element compositions plotted in bivariate diagrams vs. decreasing MgO. The samples do not define a consistent variation trend. Overall, CaO concentrations increase and $Al_2O_3$, $Na_2O$, $K_2O$ and $P_2O_5$ concentrations decrease with increasing MgO. However, $SiO_2$, $TiO_2$ and $Fe_2O_3$ define different patterns depending on the sector considered. Samples from the eastern and central sectors become more $TiO_2$-rich and $SiO_2$-poor with increasing MgO, whereas samples from the western sector show the opposite trend for $TiO_2$ and an irregular variation for $SiO_2$. Meanwhile, samples from the eastern sector and, especially, the Calella de Palafrugell lamprophyre show a significant increase in $Fe_2O_3$ with increasing MgO, whereas samples from the central sector show little variation and samples from the western sector decrease in $Fe_2O_3$ with increasing MgO.

The distribution of the samples correlates with the petrology and mineralogy of the rocks. Samples with high volume fractions of macrocrysts have high concentrations in MgO, with

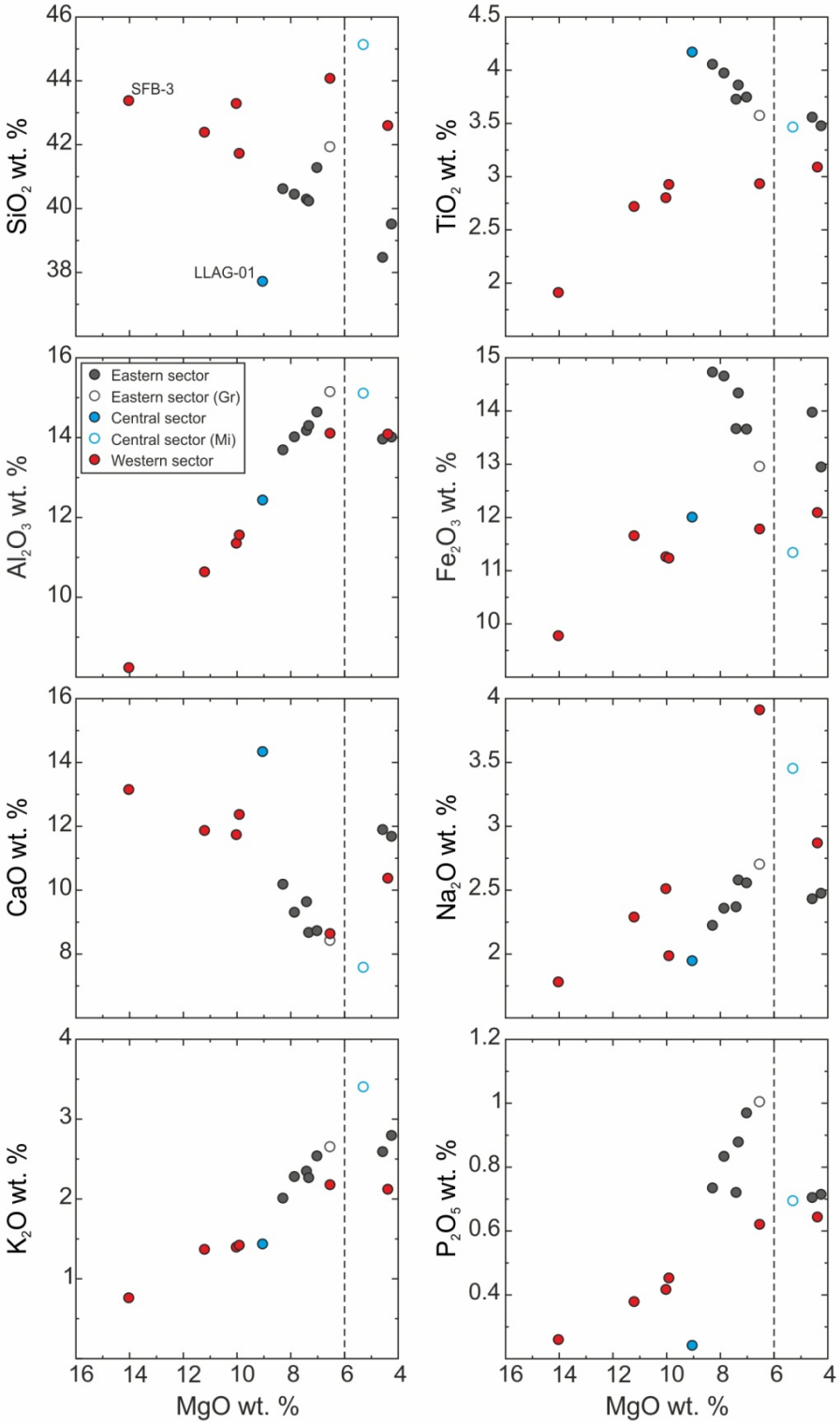


**Fig. 5.19.** Whole rock major element compositions in bivariate diagrams vs. decreasing MgO. White symbols represent macrocryst-free compositions: Gr denotes the groundmass composition of the lamprophyre from Calella de Palafrugell (Ubide et al., 2012*a* –see Chapter 6-) and Mi denotes the composition of microlitic lamprophyre from S'Agaró. The vertical dashed line may represent an average composition for the groundmass of the whole lamprophyre suite.

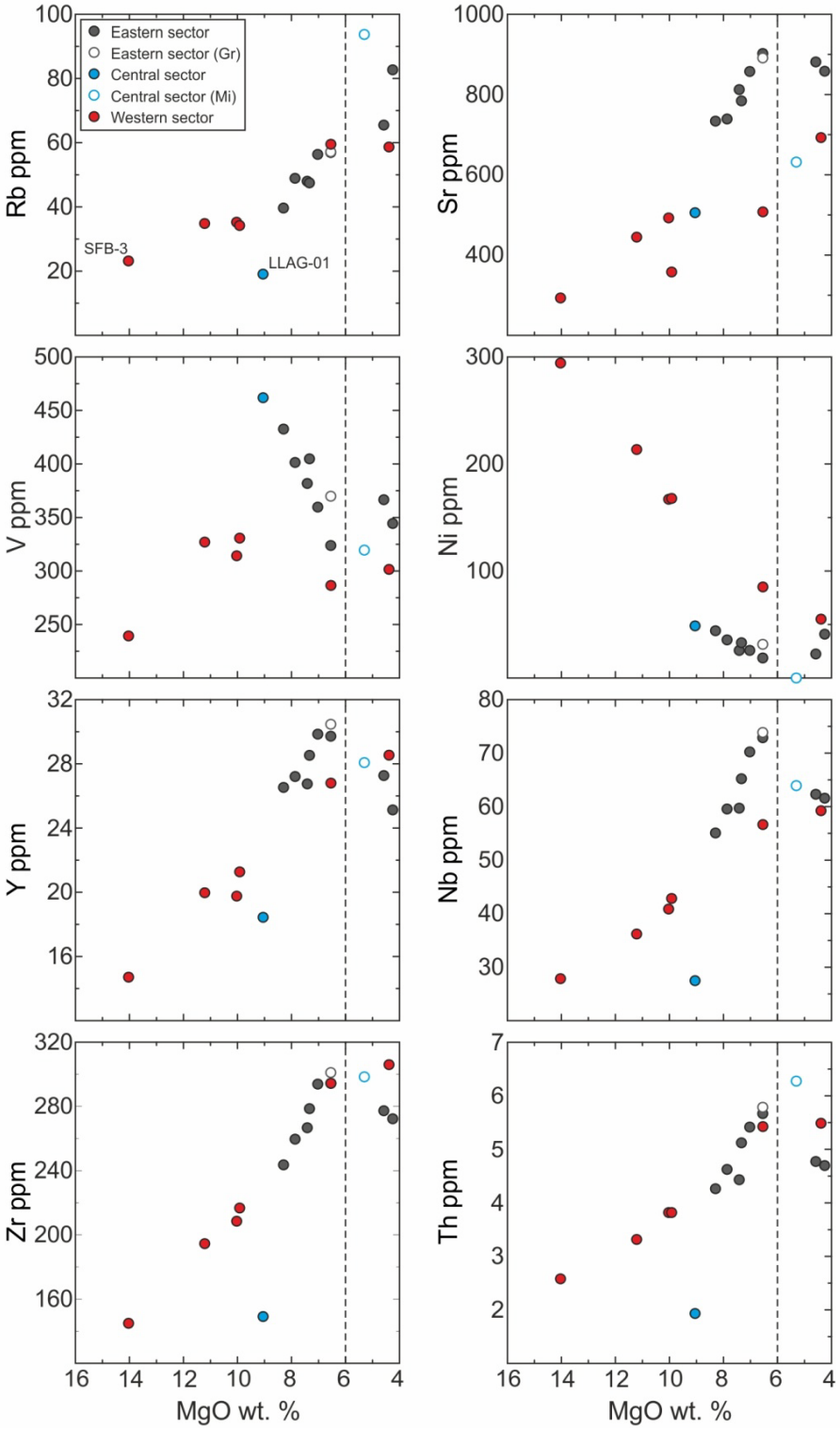


**Fig. 5.20.** Whole rock trace element compositions in bivariate diagrams vs. decreasing MgO. Explanation for the symbols is as in Fig. 5.19. The microlitic lamprophyre from S'Agaró (sample SAG-03B) has a Ni concentration below the detection limit, so it has been plotted at 0 ppm for that element. The vertical dashed line may represent an average composition for the groundmass of the whole lamprophyre suite.

the highest values for the samples with an olivine-rich macrocryst assemblage (compare Fig. 5.8 and Fig. 5.19). In contrast, microlitic compositions plot together with samples with low proportions of macrocrysts at low MgO values. Microlitic compositions share an MgO concentration of ca. 6 wt. % and an Mg# value of ca. 35 (Fig. 5.19; Table 4.1 –Chapter 4-).

### 5.7.2. Trace element composition

Representative trace elements are plotted in bivariate diagrams against decreasing MgO (Fig. 5.20). Most incompatible trace elements, including Large Ion Lithophile Elements (LILE) and High Field Strength Elements (HFSE) show an overall decrease for increasing MgO contents. Transition elements show distinct variations depending on the sector considered. Lamprophyres from the eastern and central sectors show a sharp increase in V and a smooth increase in Ni and Cr when MgO increases. In contrast, lamprophyres from the western sector show a sharp increase in Ni and Cr and irregular variations for V when MgO increases.

REE and multielemental normalised patterns are presented in Fig. 5.21. REE concentrations are enriched ca. 10 to more than 100 times over the chondrite composition by McDonough and Sun (1995). Incompatible elements are enriched up to ca. 100 times over the primitive mantle composition by McDonough and Sun (1995).

All of the lamprophyres show normalised patterns similar in shape, suggesting a common magma source. REE normalised patterns have a high slope, with $(La/Lu)_N$ values between 11 and 19. Multielemental normalised patterns show positive anomalies for Nb and Ta and minor ones for Ba; some of the samples present a negative anomaly in Pb. These data are typical of alkaline rocks with an asthenospheric, enriched mantle source similar to EM-1 and/or HIMU (Hofmann, 1997; see Chapter 4).

Strikingly, the microlitic or macrocryst-poor samples are very similar to each other in the three sectors, whereas the macrocryst-rich samples are less enriched in incompatible elements (Fig. 5.21). In the central sector, the macrocryst-rich sample (Llagostera lamprophyre) has a positive anomaly for Ti. This anomaly is also present, although smaller, for the porphyritic samples from the eastern sector.

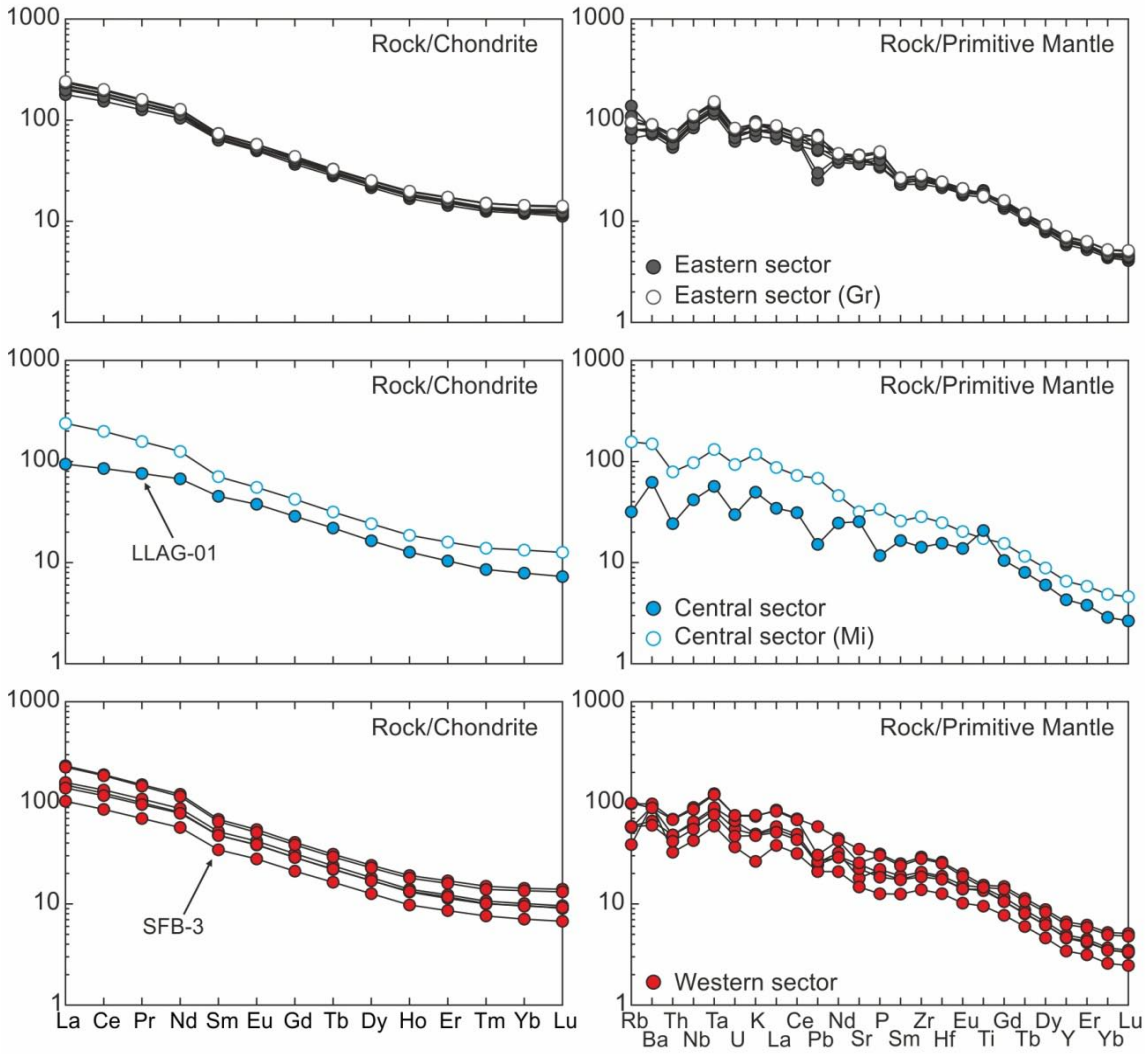


**Fig. 5.21.** Whole rock trace element compositions normalised to chondrite and primitive mantle (McDonough and Sun, 1995), for the eastern, central and western sectors. Explanation for the symbols is as in Fig. 5.19.

## 5.8. Discussion

### 5.8.1. Origin of mineral compositional variations

The Cretaceous lamprophyre suite in the Catalonian Coastal Ranges includes, at least, 7 porphyritic intrusions and 1 microlitic intrusion. The porphyritic lamprophyres are composed of large mafic crystals embedded in a fine-grained groundmass. The large crystals are mainly macrocrysts of clinopyroxene, amphibole, pseudomorphosed olivine and Fe-Ti oxides. The crystalline components of the groundmass are microcrysts, most of which are microlites of amphibole and plagioclase, and there are also scarcer microphenocrysts of amphibole and clinopyroxene. The microlitic lamprophyre is petrographically equivalent to the groundmass of the porphyritic lamprophyres.

Clinopyroxene and amphibole crystals have complex compositional variations, as shown in Fig. 5.9, 5.12 and 5.14, and summarised in Tables 5.2, 5.3 and 5.4. The macrocrysts of these minerals are composed of large cores and thin rims. In the case of clinopyroxene, A-type macrocryst cores appear in the eastern sector and define an evolutionary trend where Mg# increases with crystallisation time, towards P compositions. B-type macrocryst cores appear in the central and western sectors and decrease in Mg# with crystallisation time, also towards P compositions. B3 and P compositions are actually very similar to each other, although B3 have higher concentrations in $Al_2O_3$ and $Na_2O$ than P (Fig. 5.12). B3 and P appear together only in the western sector and a C-type zone appears in between, compositionally equivalent to B2. Meanwhile, X- and G-type macrocryst cores are scarce and have low Mg# contents. X compositions are mantled by A1 compositions whereas G compositions are mantled by P compositions.

In the case of amphibole, P compositions are the commonest macrocryst core. J-type inner cores appear in the western sector whereas K-type inner cores appear in the eastern sector and both compositions are mantled by P, implying an increase in Mg# with crystallisation time (Fig. 5.14).

P-R compositions in clinopyroxene and amphibole define evolutionary trends where Mg# decreases with crystallisation time (Fig. 5.12, 5.14). The P-R evolution is common to all the lamprophyres and can be related to progressive fractionation of the groundmass magma from more primitive to more evolved compositions. P compositions mantle the other macrocryst core compositions and they also appear as microphenocryst cores. R compositions occur as macrocryst rims, microphenocryst rims and in the case of amphibole, microlites as well.

The macrocryst assemblage could potentially comprise phenocrysts, xenocrysts, antecrysts or a mixture of these components. Phenocrysts are crystals co-genetic with their magmatic host, which is represented by the groundmass of the rock; xenocrysts are crystals foreign to the magmatic host and magma system; and antecrysts are crystals which are recycled one or several times before inclusion in the host magma but have an origin within the magmatic system (Jerram and Martin, 2008). To unravel the type of macrocryst assemblage and therefore its origin, mineral-melt equilibrium diagrams have been used (Fig. 5.22; Rhodes et al., 1979).

In equilibrium diagrams, Mg# of the mineral is plotted against Mg# of the melt (calculated as 100 MgO / (MgO + FeO) and FeO = 0.9 x total iron as $Fe_2O_3$) and the curves represent the range in which mineral and melt compositions are in equilibrium (Fig. 5.22). Mineral compositions above the curves are in disequilibrium with the melt composition and

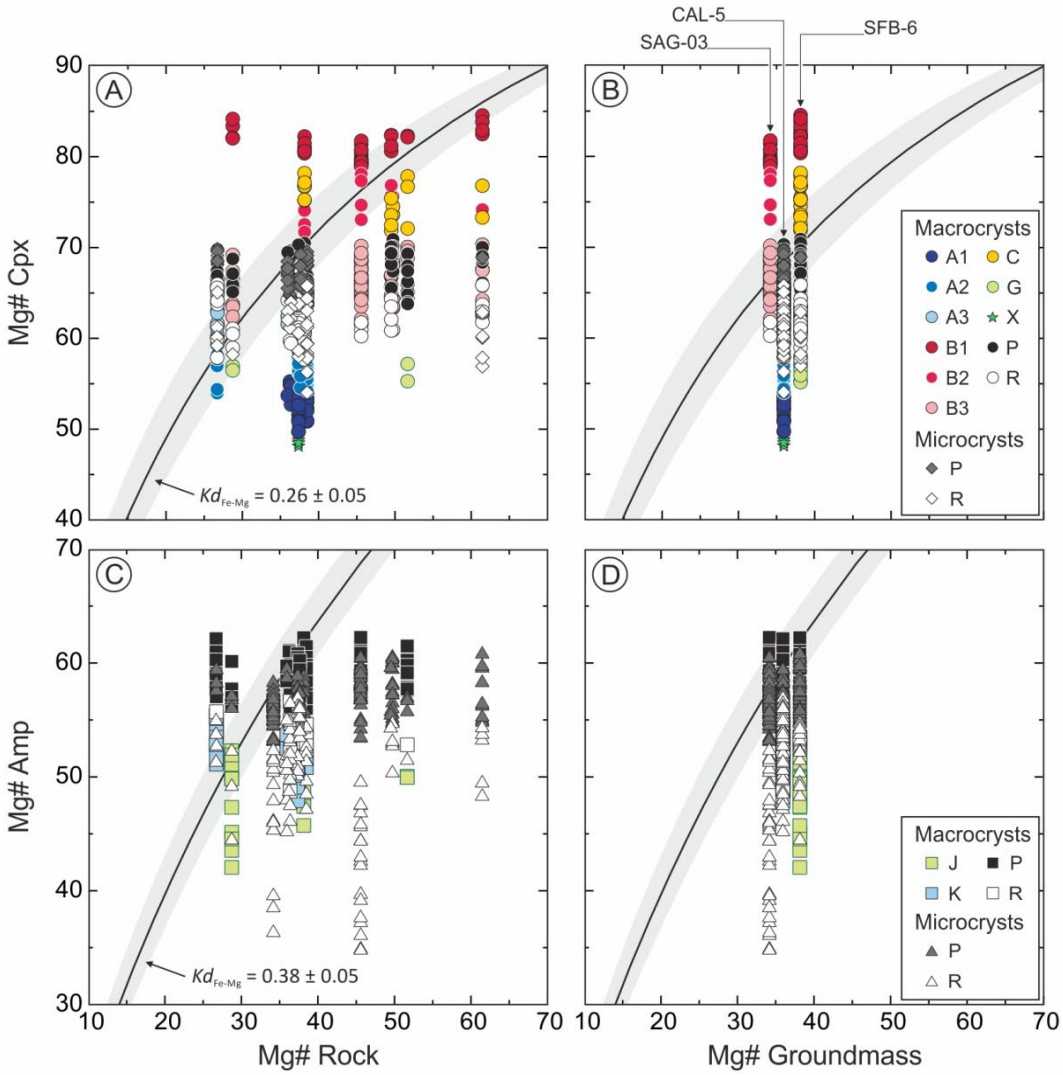


**Fig. 5.22.** Mineral-melt equilibrium diagrams for clinopyroxene (A, B) and amphibole (C, D). The curves represent the range in which mineral and melt compositions are in equilibrium based on iron-magnesium exchange (Rhodes et al., 1979).

mineral compositions below the curves are either in disequilibrium with the melt or related to fractionation. The curves are calculated according to the iron-magnesium exchange coefficient for each mineral ($Kd_{Fe\text{-}Mg}^{mineral\text{-}melt}$), which is 0.26 ± 0.05 in the case of clinopyroxene (Akinin et al., 2005) and 0.38 in the case of amphibole (LaTourrette et al., 1995); to make results comparable, an error of ± 0.05 is assumed in the latter case as well. It is common practice to use the whole rock composition of the sample containing the mineral as representative of the melt (see Fig. 5.22A and Fig. 5.22C). In addition, the bulk composition of the groundmass is used in Fig. 5.22B and Fig. 5.22D, in order to avoid the effect of the macrocrysts on the whole rock Mg# content of porphyritic rocks (Ubide et al., under review *b*; see also section 5.8.2 and Chapter 7). Groundmass Mg# contents have been approached using the whole rock composition of macrocryst-poor samples: CAL-5 in the eastern sector (Ubide et al., 2012*a* –see Chapter 6-), SAG-03B in the central sector (microlitic lamprophyre) and SFB-6 in the western sector. It is noteworthy that all

these groundmass proxies have very similar Mg# contents of ca. 35 (Fig. 5.22B, 5.22D) and very similar MgO concentrations of ca. 6 wt. % (Fig. 5.19, 5.20).

P compositions plot within or very close to equilibrium with the groundmass, both for clinopyroxene (Fig. 5.22B) and amphibole (Fig. 5.22D). This means that P compositions in both minerals are in equilibrium with each other and with the groundmass of the lamprophyre suite. P compositions can therefore be considered true phenocrysts. R compositions naturally plot below the equilibrium curves due to progressive fractionation of the groundmass magma. The remaining compositional types plot above or below the equilibrium curves. Given that they appear in macrocryst cores, they cannot have crystallised directly from their host magma. Rather, they are inherited crystals that can be either antecrysts or xenocrysts. It is noteworthy that plotted against whole rock Mg# (Fig. 5.22A, 5.22C), some of these compositions can appear to be in equilibrium with the rock they are included in. Therefore, it is necessary to be extremely cautious when interpreting equilibrium based on whole rock compositions in strongly porphyritic rocks (see also Chapter 7).

In the case of clinopyroxene, the sequence A1-A2-A3-P defines a linear evolution of increasing Mg# contents and therefore, requires repeated events of mafic recharge and magma mixing (Ubide et al., under review *b* –see Chapter 7-), that would also account for the subhedral to anhedral habit of A1, A2 and A3 zones. Given the compositional similarity with P-R compositions (Fig. 5.12), A-type cores are best described as antecrysts.

B-type cores have progressively lower Mg# contents so that actually, B3 compositions plot in equilibrium with the groundmass. B3 is overgrown by C in the lamprophyres from the western sector, implying mafic recharge and magma mixing. C compositions plot partly in equilibrium with the groundmass and are mantled by P compositions. According to their irregular shape and Mg- and Cr-rich nature, B1-B2 inner cores might be xenocrysts of mantle origin. However, B-C compositions define a trend that can be linked to the P-R evolution (Fig. 5.12) and thus, B-C-type cores are more likely antecrysts crystallised from little-differentiated melts related to more primitive stages in the magma system. These primitive antecrysts are probably linked to the Cr diopside cores described by Azambre et al. (1992) for the coetaneous magmatism in the Pyrenees.

G- and X-type cores plot noticeably below the equilibrium curves. They are mantled by more Mg#-rich compositions, implying recharge by a more mafic magma. In the case of G-type cores, their Mg# content is similar to A2 compositions and their habit is subhedral, so they are probably antecrysts related to more evolved stages of the magma system. Regarding X compositions, they appear in an only, intensely resorbed macrocryst and have extremely low Mg# contents and a major and trace element composition significantly different from the other compositional types (Fig. 5.12, 5.18). It follows that

the X-type core probably has an origin outside the magmatic system and therefore can be classified as a xenocryst. It may be linked to the green and evolved clinopyroxene xenocryst cores described in the Quaternary Garrotxa Volcanic Field (Aulinas et al., 2013; Gisbert et al., 2011), which is geographically close to the Cretaceous outcrops.

In the case of amphibole, the transition from J- or K-type inner cores to P-type mantles requires an event of mafic recharge and magma mixing that would also account for the anhedral and rounded habit of the inner cores. The Mg# content of the liquid in equilibrium with J-type inner cores is similar to the Mg# content of the liquid in equilibrium with A2 or G clinopyroxene. J compositions appear together with G compositions in the lamprophyres from the western sector and their trace element normalised patterns are similar (Fig. 5.18), so J-type amphibole may be genetically related to G-type clinopyroxene. Meanwhile, the Mg# content of the liquid in equilibrium with K-type inner cores is similar to the Mg# content of the liquid in equilibrium with A3 clinopyroxene. K compositions appear together with A-type compositions in the lamprophyres from the eastern sector and their trace element normalised patterns are similar (Fig. 5.18), so these compositional types may be genetically related as well. It follows that J- and K-type inner cores can be considered antecrysts that crystallised from evolved magmas in the magmatic system.

According to the obtained results, clinopyroxene and amphibole macrocrysts make up complex crystal populations composed mainly of antecrysts. A-, B-, C-, G-, J- and K-type cores were recycled from previous stages of the magmatic system, more primitive in the case of B-C-type cores and more evolved in the case of A-, G-, J- and K-type cores. There is also an extremely evolved X-type core that is a xenocryst accidentally incorporated into the magma from which A-type cores crystallised. All of these cores were later incorporated into the magma represented by the groundmass of the lamprophyres, from which P-R compositions crystallised. P compositions are phenocrysts in equilibrium with the bulk groundmass composition. Progressive fractionation of the groundmass magma triggered the crystallisation of R compositions.

The large difference in size between macrocrysts and groundmass microcrysts suggests different conditions of crystallisation. Clinopyroxene macrocryst cores reach higher concentrations in $Na_2O$ and lower concentrations in $TiO_2$ than groundmass microcrysts (Fig. 5.12). Meanwhile, amphibole macrocryst cores reach the highest concentrations in $K_2O$ and the lowest concentrations in $TiO_2$ (Fig. 5.14). These data suggest that macrocryst cores crystallised under higher pressure conditions than groundmass microcrysts (Adam and Green, 1994; Shaw and Eyzaguirre, 2000).

In the case of clinopyroxene, the partition of aluminium between the tetrahedral and octahedral crystallographic sites is usually a good indicator of crystallisation depth (Aoki

and Kushiro, 1968), so that higher $Al^{VI}/Al^{IV}$ ratios indicate higher depths of crystallisation. In the studied lamprophyre suite, most macrocryst cores have $Al^{VI}/Al^{IV}$ ratios higher than macrocryst rims and microphenocrysts (Table 5.I of the electronic supplement). However, B1, B2 and C compositions have variable $Al^{VI}/Al^{IV}$ ratios in spite of being overgrown by B3 compositions, which have high $Al^{VI}/Al^{IV}$ ratios. This lack of correlation between B1, B2 and C compositions and their inferred conditions of crystallisation is also evident from their low and variable $Na_2O$ concentrations (Fig. 5.14). Unfortunately, this prevents the application of barometric calibrations on these compositions.

Barometric estimates have been successfully carried out for clinopyroxene in the Calella de Palafrugell lamprophyre (eastern sector; Ubide et al., under review *b* –see Chapter 7-), indicating that A-type antecrysts crystallised in a deep magma chamber or magma conduit under a pressure of 500 – 800 MPa, equivalent to a maximum depth of ca. 25 km, whereas the X-type xenocryst crystallised under higher pressure (ca. 850 – 1000 MPa; ca. 30 km probably close to the crust-mantle boundary, also in agreement with the crystallisation conditions of green xenocrysts recognised the Quaternary Garrotxa Volcanic Field; Aulinas et al., 2013). In contrast, P compositions crystallised in polybaric conditions during ascent and emplacement of the magma from ca. 500 MPa to less than 50 MPa pressure. Finally, R compositions crystallised at the shallow emplacement level of the magma at ca. 1 km depth.

Considering the barometric results in the Calella de Palafrugell lamprophyre (Ubide et al., under review *b* –see Chapter 7-) and the qualitative results from $Na_2O$, $TiO_2$ and $Al^{VI}/Al^{IV}$ in the whole lamprophyre suite, together with the stratigraphy of the crystals, the macrocryst assemblage crystallised from deep-seated magmas that belonged a common magma system. Accordingly, clinopyroxene and amphibole macrocryst cores (excepting the evolved xenocryst) show convex-upwards normalised REE patterns (Fig. 5.18A, 5.18C) typical of deep cumulates in equilibrium with alkaline basaltic melts (Irving and Frey, 1984).

Regarding the macrocrysts of opaque minerals and olivine, their origin is probably closely related to that of the macrocrysts of clinopyroxene and amphibole given that they appear associated into glomerocrysts. The only olivine relicts occur in a macrocryst core and have a composition ($Fo_{88-89}$; NiO 0.16-0.26 wt.%,; CaO 0.22-0.26 wt.%.) that cannot be related to mantle-derived xenocrystic material (e.g., Jurewicz & Watson, 1988; Stormer, 1973; Fig. 5.17). According to the iron-magnesium exchange coefficient for this mineral ($Kd_{Fe\text{-}Mg}^{olivine\text{-}melt}$ = 0.30 ± 0.03; Roeder and Emslie, 1970), olivine compositions are in equilibrium with a liquid of Mg# ca. 55. This is similar to the liquid in equilibrium with B1-type clinopyroxene and slightly above the liquid in equilibrium with C-type clinopyroxene (Table 5.2, Fig. 5.22A, 5.22B), indicating a possible genetic relationship between olivine macrocrysts and B-C compositions in clinopyroxene macrocrysts.

### 5.8.2. Origin of whole rock compositional variations

The Cretaceous lamprophyre suite in the Catalonian Coastal Ranges has a common magma source (Ubide et al., 2012*b*; see also Chapter 4) but shows whole rock compositional variations from 4 to 14 wt. % MgO (Table 4.1 –see Chapter 4-). Samples with MgO concentrations up to ca. 7 wt. % have overall similar compositions (Fig. 5.19, 5.20), whereas samples with higher MgO contents show distinct variation trends with the increase in MgO. In the eastern and central sectors the increase in MgO is coupled with an increase in $TiO_2$ and V, a minor increase in Ni and Cr and a decrease in $SiO_2$. In the western sector the increase in MgO is stronger and coupled with a dramatic increase in Ni and Cr, a decrease in $TiO_2$ and an irregular variation for $SiO_2$ and V. $Fe_2O_3$ shows a different evolution with the increase of MgO; it increases in the eastern sector, especially for the Calella de Palafrugell lamprophyre, remains fairly constant in the central sector and decreases in the western sector. Regarding the other elements, the increase in MgO is coupled with an increase in CaO and a decrease in $Al_2O_3$, $Na_2O$, $K_2O$, $P_2O_5$ and incompatible trace elements (Fig. 5.19, 5.20, 5.21).

Whole rock variation trends can hardly respond to magma fractionation given the petrologic and mineralogic resemblance between the samples, especially regarding their groundmass. Furthermore, clinopyroxene and amphibole compositions cogenetic with the groundmass (P and R) are common to all the lamprophyres and have a similar composition in all of them. Even the inherited antecrysts are compositionally similar, when present, among different lamprophyres. Rather than magma fractionation, the significant whole rock compositional variations appear to correlate with the proportion and mineralogy of macrocrysts in the rock (see Fig. 5.8). The influence of macrocrysts on the bulk composition of porphyritic rocks has been recently highlighted in lamprophyres (Scarrow et al., 2011; Ubide et al., 2012*a* –see Chapter 6-) and basaltic rocks from ocean island settings like Hawaii (Sakyi et al., 2012) or Azores (Larrea et al., 2013).

The microlitic lamprophyre from S'Agaró and the groundmass composition from Calella de Palafrugell have very similar MgO concentrations of ca. 6 wt. %. These macrocryst-free samples, together with macrocryst-poor samples from Aiguablava and the western sector, make up the relatively homogeneous group of compositions of MgO < 7 wt. % (Fig. 5.19, 5.20), with highest concentrations in incompatible elements (Fig. 5.21). In contrast, macrocryst-rich samples have MgO > 7 wt. % and lowest concentrations in incompatible elements (Fig. 5.19, 5.20, 5.21). The volume fraction of macrocrysts is highest in the accumulation zone of the Molí d'en Ponç and Llagostera lamprophyres (Fig. 5.8) and this correlates with high MgO concentrations. In the western sector the macrocryst assemblage is olivine-rich and this accounts for the highest MgO, Ni and Cr enrichments. Amphibole is more common in the macrocryst assemblage of the eastern sector and most frequent in the Llagostera lamprophyre and that explains the $TiO_2$ and V enrichments and

the relative $SiO_2$ depletions for these samples. Finally, opaque minerals are a minor macrocryst phase but are especially frequent in the Calella de Palafrugell lamprophyre, correlating with the $Fe_2O_3$-enrichment shown by the macrocryst-rich samples from this sill. Clinopyroxene and amphibole show normalised incompatible element patterns less enriched than whole rock samples (compare Fig. 5.18 with Fig. 5.21), so that increasing volume fractions of macrocrysts in the sample may result in decreasing whole rock trace element concentrations.

The relationship between whole rock variations and macrocryst accumulation was quantitatively modelled for the Calella de Palafrugell lamprophyre in Ubide et al. (2012*a*) and Chapter 6 in this volume. In the present study, whole rock compositions have been plotted together with macrocryst core compositions in representative major element diagrams (Fig. 5.23).

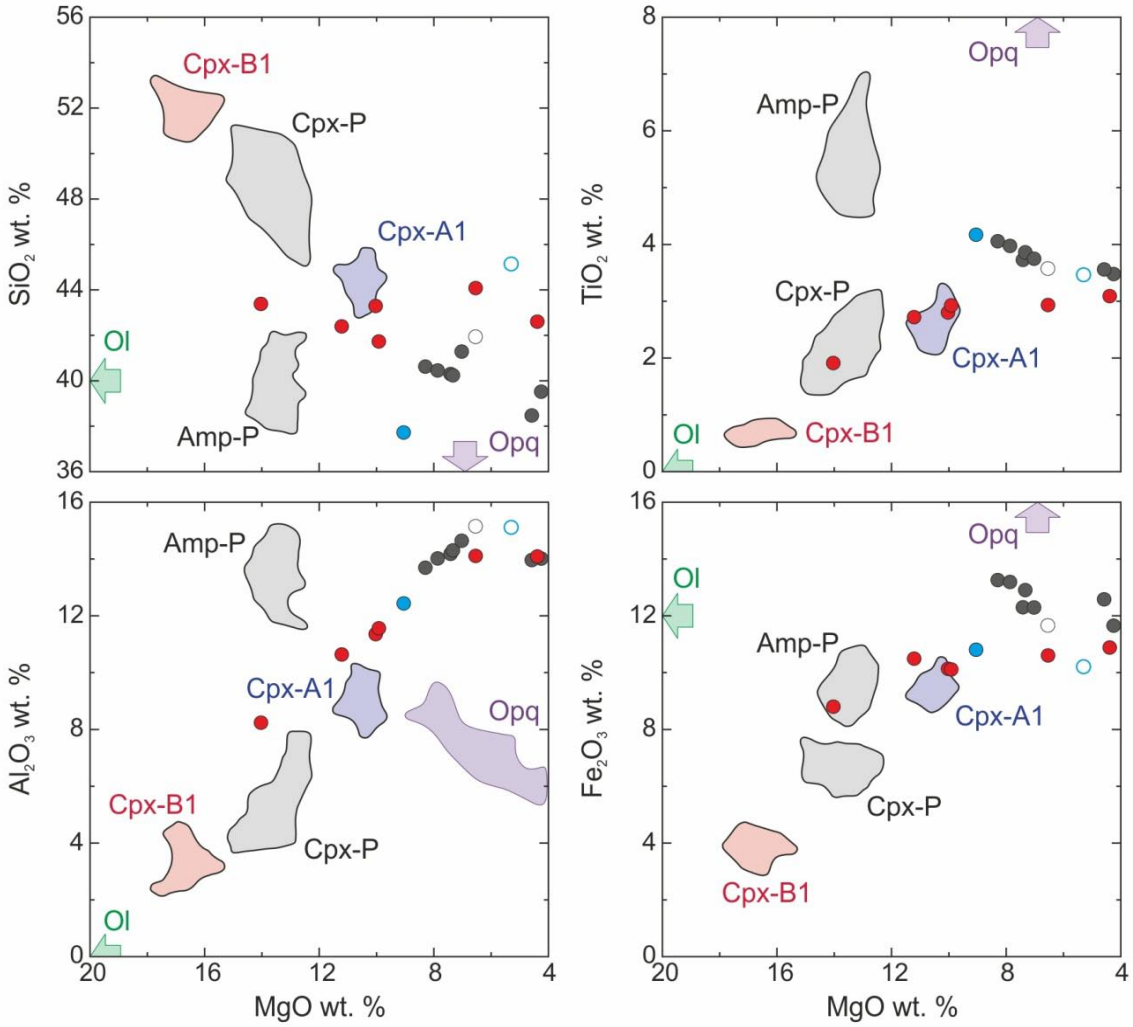


**Fig. 5.23.** Major element composition of whole rocks and representative macrocryst core types in bivariate diagrams vs. decreasing MgO. To make iron concentrations comparable, $FeO^T$ contents in whole rock are calculated as 0.9 x $Fe_2O_3^T$. Whole rock compositions are presented keeping the symbols from previous figures and mineral compositions are presented as compositional fields (or arrows when outside the diagram).

From the plots in Fig. 5.23, it is clear that clinopyroxene macrocrysts, which appear in high proportions in all the porphyritic lamprophyres (Fig. 5.8; Table 5.1), control most of the whole rock compositional variations. Amphibole is the main macrocryst phase in the Llagostera lamprophyre and it is also relevant in the Calella de Palafrugell lamprophyre and triggers $TiO_2$-enrichments and $SiO_2$-depletions in macrocryst-rich samples from these intrusions. Amphibole is also the main macrocryst phase in the Aiguablava lamprophyre and the most MgO-rich sample from Aiguablava varies along with the Llagostera and Calella de Palafrugell lamprophyres. This sample is nevertheless relatively poor in macrocrysts (Fig. 5.8) and in consequence, the macrocryst accumulation effect is minor. Olivine is especially frequent in the macrocryst-rich samples from the western sector and controls the MgO-enrichment in these samples. Opaque minerals have extreme compositions as well, but they are always a minor macrocryst phase excepting the Calella de Palafrugell lamprophyre, explaining the highest concentrations in iron of these samples.

In conclusion, the significant variations in whole rock composition among the samples from the Catalonian Coastal Ranges lamprophyres are controlled by the proportion and mineralogy of accumulated macrocrysts. The microlitic groundmass is equivalent for the whole lamprophyre suite and has MgO concentrations of ca. 6 wt. % (Fig. 5.19, 5.20) and Mg# values of ca. 35 (Fig. 5.22B, 5.22D). It represents the magma that hosted the recycled crystal populations and carried them up to the shallow emplacement levels. The variable entrainment of antecrysts in the different intrusions is the driving force that pushes whole rock geochemical variations away from groundmass compositions.

The magma represented by the groundmass of the lamprophyre suite must have undergone some fractionation prior to emplacement, either in a magma chamber or *en route* to shallower depths, as its composition cannot represent a primary magma in equilibrium with its mantle source, that would typically show Mg# > 60 – 70, MgO > 11 wt. %, Cr > 500–1000 ppm and Ni > 200–500 ppm (Frey et al., 1978). Again, the few samples with these characteristics are strongly influenced by the accumulation of macrocrysts, so they must not be considered for the interpretation of primary petrogenetic processes. The groundmass composition therefore suggests fractionation processes taking place at depth. Mineral compositions actually call for fractionation, together with mafic recharge, to explain the origin of deep, recycled antecrysts (see sections 5.8.1 and 5.8.3).

At shallower depths, slight fractionation probably affected the groundmass magma triggering minor compositional differences between the samples with MgO < 7 wt. %, as well as the development of evolved patches of groundmass in the Llagostera lamprophyre.

### 5.8.3. Reconstruction of the magmatic plumbing system

The preceding discussion has shown that the Cretaceous lamprophyre suite in the Catalonian Coastal Ranges basically represents a partly fractionated melt carrying a mush of large, recycled crystals from deep crystallisation areas. $^{40}Ar/^{39}Ar$ geochronology applied to the Calella de Palafrugell, Llagostera and Monasterio de Sant Pere Cercada lamprophyres constrained the time of emplacement to ca. 79 Ma (Ubide et al., under review *a* –see Chapter 3-). This age is Campanian and agrees with the end of the Mesozoic extension in the Late Cretaceous (see Chapter 3), when the continental crust in this area was thinned to ca. 30 km (Salas and Casas, 1993). Petrologic and geochemical data obtained in the present study make it possible to hypothesise the nature of the magma feeding system related to the lamprophyre suite, as illustrated in Fig. 5.24.

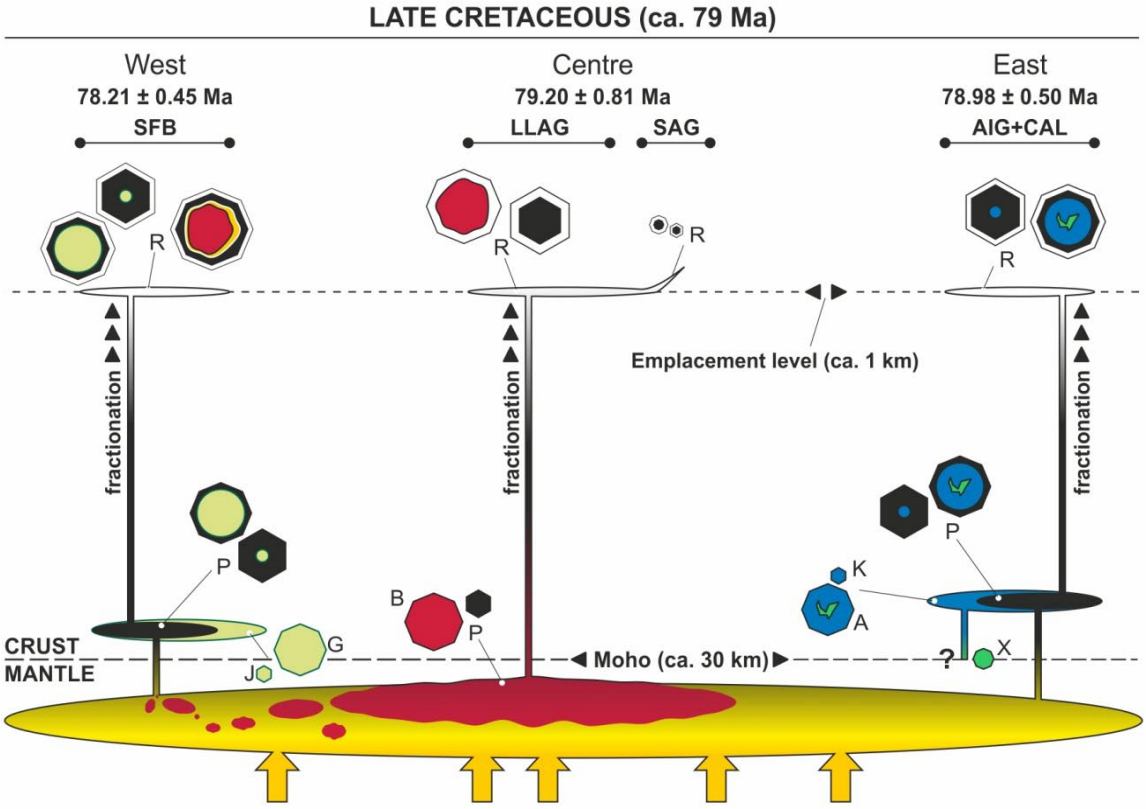


**Fig. 5.24.** Conceptual sketch of the magmatic plumbing system and magmatic processes involved in the generation of the Cretaceous lamprophyre suite in the Catalonian Coastal Ranges. Octagons represent clinopyroxene crystals in equilibrium with the melt and hexagons represent amphibole crystals in equilibrium with the melt. Rounded shapes, in contrast, represent crystals in disequilibrium with the melt. The green resorpted core represents the clinopyroxene xenocryst. Magma history in the eastern sector is further explored in Chapter 7 (see Fig. 7.12).

Because all the lamprophyres share a common groundmass that hosts different recycled crystals per sector, a large magma reservoir located below the level of crystallisation of recycled crystals might be inferred. Barometric calculations reveal that A-type clinopyroxene antecrysts and the X-type clinopyroxene xenocryst from the Calella de

Palafrugell lamprophyre crystallised in the lower part of the crust, close to the crust-mantle boundary (Ubide et al., under review *b* –see Chapter 7-). It follows that the reservoir of groundmass magma was located at a greater depth, maybe at the upper mantle-lower crust interface that constitutes a rheological discontinuity favourable for magma stagnation (e.g., Annen, 2011). The reservoir may have supplied magma to the whole lamprophyre suite and according to whole rock multielemental normalised patterns, it was fed by astenosphere-derived melts (see also Chapter 4).

The lamprophyres from the central sector are the simplest regarding mineral compositional types. In the Llagostera lamprophyre, all clinopyroxene macrocrysts have B-type cores, all amphibole macrocrysts have P-type cores and there are no olivine macrocrysts. The B1-B2-B3-R crystal stratigraphy in clinopyroxene macrocrysts can be associated with progressive evolution of the magma from more primitive to more evolved compositions. The irregular contours of B1-type inner cores, together with the presence of a diffused B2 zone between B1 and B3, suggest that B1-inner cores could have been carried with the magma filling the reservoir from lower levels. The central sector likely represents magma directly coming from the large groundmass reservoir, where macrocrysts had room and time enough to reach very large sizes. This magma may have been especially water-rich according to the abundance of amphibole macrocrysts and the lack of olivine. The S'Agaró lamprophyre is the only sub-vertical and macrocryst-free intrusion and may represent a subvertical apophysis of the Llagostera or other related sill, unreached by the deep, large and relatively heavy crystals considering the high density of clinopyroxene and amphibole. Alternatively, it could represent a shallow section of a feeder conduit with macrocrysts sinking to lower levels before solidification of the groundmass magma.

The lamprophyres from the western and eastern sectors have olivine macrocrysts as well as clinopyroxene and amphibole macrocrysts with more complex zoning patterns that include P-type zones. Moreover, amphibole macrocrysts are smaller. These differences relative to the lamprophyres from the central sector might indicate a possible recharge of the groundmass reservoir with a more primitive and water-poor magma, as detailed in the following paragraphs. Magma recharge would also explain the slight differences in mineral composition between the microlites of amphibole and plagioclase in the central sector and those in the western and eastern sectors (see section 5.6.1).

In the western sector, there are cm-sized clinopyroxene macrocrysts with B-type cores, similarly to the central sector. However, in the western sector B-type cores are surrounded by C compositions, which represent a step backwards in the evolutionary trend, back to more primitive compositions, and could be related to recharge of the groundmass reservoir with a more primitive magma. Given the high MgO and $Cr_2O_3$ concentrations in B1, B2 and C compositions, the recharging magma might be relatively

similar to the original magma entering the magma reservoir and mixed with the magma in equilibrium with B3 clinopyroxene to give rise to an intermediate C composition, similar to B2. C zones overgrow B3 and are overgrown by P, resuming the normal evolution towards more evolved compositions. Moreover, olivine macrocrysts were formed first in the crystallisation sequence, as they are in equilibrium with a liquid with Mg# similar to that producing B1 clinopyroxene and their compositions do not fit a mantle origin. In addition, the western sector lamprophyres have G-type clinopyroxene macrocryst cores and J-type amphibole macrocryst cores, which crystallised from magmas with similar Mg# contents, lower than the other antecrysts. This suggests the existence of another, more evolved magma chamber located above the groundmass reservoir. G- and J-type crystals were sampled by the groundmass magma in equilibrium with P-type clinopyroxene and amphibole ascending towards the emplacement level from the deep reservoir.

In the eastern sector there are no B-type clinopyroxene cores, indicating that the magma did not carry clinopyroxene crystals from the deep reservoir. The groundmass magma is however in equilibrium with P-type clinopyroxene and amphibole, indicating that it left the reservoir after the mafic recharge event. There are abundant macrocryst cores with A-clinopyroxene and K-amphibole compositions, both exclusive to the eastern sector lamprophyres. This suggests the presence of another evolved magma chamber located above the deep groundmass reservoir. In this case, the A1-A2-A3-P evolution in clinopyroxene macrocryst cores reveals successive inputs of magma from the deep reservoir recharging the evolved magma chamber and mixing with the resident melts. The magma in this chamber was initially more evolved and water-poor and contained a xenocryst (X-clinopyroxene) dragged from lower levels. Progressive recharge with a more primitive and water-rich magma followed by mixing with the magma resident in the crystallising chamber controlled the linear evolution of A-type clinopyroxene towards P compositions. A3-clinopyroxene crystallised coevally with K-amphibole once the water content of the mixture magma was high enough, and this was followed by the crystallisation of P-clinopyroxene and P-amphibole related to the last recharge event, which likely triggered the ascent of the groundmass magma (see also Ubide et al, under review *b* –Chapter 7-).

In all the lamprophyres, microphenocrysts and microlites crystallised in response to progressive fractionation of the groundmass magma. Microphenocryst cores may have crystallised in polybaric conditions during the ascent of the magmas, whereas rims and microlites probably crystallised at the emplacement level. The emplacement level was probably close to the surface in all the cases, as revealed by the widespread presence of vesicles, the subhorizontal dip of most intrusions implying that the magma had to support the weight of the overlying rocks and the barometric calculations in Calella de Palafrugell suggesting magma emplacement at ca. 1 km depth. (Ubide et al., under review *b* –see Chapter 7-).

## 5.9. Conclusions

The in-depth petrologic, mineralogic and geochemical study of the Cretaceous lamprophyre suite in the Catalonian Coastal Ranges has led to the following conclusions:

- Most of the studied lamprophyres are apparently simple porphyritic rocks and yet, they are composed of highly complex crystal populations that include phenocrysts, antecrysts and xenocrysts revealing deep magmatic processes. Antecrysts crystallised from earlier accumulated magmas and are predominant in the macrocryst assemblage of the lamprophyres. The obtained results imply that large crystals in porphyritic rocks must not be considered phenocrysts cognate with the host groundmass before a detailed petrographic and mineralogic study is carried out. Such assumption may otherwise lead to incorrect petrogenetic interpretations. Moreover, a deep knowledge of crystal stratigraphy and composition unveils magmatic processes that would remain misunderstood if whole rock compositions were considered alone.

- The whole rock composition of the porphyritic lamprophyres is strongly influenced by the proportion and type of macrocrysts in the sample. All of the samples have very similar groundmass compositions and yet different whole rock compositions due to the variable accumulation of macrocrysts. Importantly for petrogenetic interpretations, it follows that MgO-rich samples are not necessarily indicative of primitive compositions close to the mantle source. Rather, MgO-rich samples may arise from relatively MgO-poor melts with high volume fractions of MgO-rich antecrysts. Again, the obtained results show that a deep understanding of the samples must precede petrogenetic interpretations.

- The Catalonian Coastal Ranges Cretaceous lamprophyres are shallow exposures of a common, intricate magmatic system. Astenosphere-derived melts probably stagnated at the upper mantle – lower crust interface constituting a large magma reservoir where the largest crystals formed and from which lamprophyre magmas were extracted. Crystals from this reservoir record recharge by a new batch of primitive melt. Some of these or related magmas stagnated in the lower crust and underwent fractionation giving rise to more evolved melts. The evolved magma chambers could receive repeated influxes of primitive magma from the deeper reservoir, and the recharging magma repeatedly mixed with the magma resident in the evolved chambers. Magma upwelling from the reservoir could entrain already formed large crystals and, on its way to the shallow emplacement levels, could incorporate crystals from the evolved chambers. The result of this system is a lamprophyre family composed of a great variety of inherited large crystals in a common groundmass.

# 6

# The influence of crystal settling on the compositional zoning of a thin lamprophyre sill: a multi-method approach.

**SUMMARY**

The Cretaceous lamprophyre from Calella de Palafrugell (Catalonian Coastal Ranges) is a sub-horizontal sill with well developed chilled margins, vesicle alignments and abundant mafic macrocrysts (antecrysts) accumulated towards the bottom. These characteristics, together with a small thickness (< 0.5 m), make this intrusion an exceptional laboratory for the study of compositional zoning of igneous intrusions. Classical petrology and geochemistry are combined with mathematical modelling and multivariate statistics to quantify the influence of antecrysts on whole rock compositions. This leads to unravel the origin of the compositional zoning of the sill, as being due to gravitational settling of the antecrysts after emplacement of a single pulse of magma.

*View from ses Negres close to Calella de Palafrugell, Costa Brava*

## 6.1. Introduction

Compositional zoning is a common phenomenon in igneous intrusions, regardless of their age, geographical location, form, size, and bulk composition. Tabular intrusions (sills, dykes) are typically used to study compositional zoning, as they allow detailed observations and sampling across the intrusion, from one margin to the other, as well as recognition of gravitational settling mechanisms, where present. Thick sill-like bodies (> 50 m) have traditionally been those most studied, due to their normally better developed zoning, with cumulate layers at the lower zones and pegmatoid facies towards the top (e.g., López-Moro et al., 2007). However, some studies have also been carried out on small bodies (Brouxel, 1991; Chistyakova and Latypov, 2009*a*, 2009*b*, 2010; Kretz et al., 1985). Chistyakova and Latypov (2009*b*, 2010) highlight the need for more data in cm-scale intrusions, where compositional variations can also be recognised but there is less diversity of processes. Small (< 0.5 m thick) intrusions can therefore provide the key to a better understanding of the processes operating in more complex geological objects, such as mafic-ultramafic sills, large layered intrusions or crustal magma chambers.

Different explanations have been proposed for the origin of compositional zoning in sill-like bodies (e.g., Latypov, 2009), including single– or multi–pulse injection of crystal–free or –laden magmas, and several other hypotheses (see Chistyakova and Latypov, 2009*a* 2009*b*). Specifically, mechanical processes like crystal settling are regarded as rather irrelevant in the formation of sill zoning by some authors (e.g., Gibb and Henderson, 1992; Latypov, 2003*a*), although this process has been called on by others to explain differentiation throughout thick intrusions (e.g., Marsh, 2000). In thin (cm-scale) intrusions, the significance of crystal settling is thought to be extremely unlikely in triggering internal compositional zoning (Chystiakova and Latypov, 2009*a*, 2009*b*).

Principal component analysis (PCA) is used extensively in other fields of earth sciences, but it is not commonly applied in igneous-mineralogical or -geochemical studies where, generally, multivariate statistical methods are rarely used (e.g., Allègre et al., 1995; Cheng et al., 2011; Cortés et al., 2007; Forster et al., 1999; Janousek et al., 2004; Vogel et al., 2008). PCA reduces the dimensionality of a dataset consisting of a large number of interrelated variables, retaining as much as possible of the variation present in the dataset. This is achieved by transforming to a new set of variables, the principal components (PCs), which are uncorrelated, and ordered so that the first few retain most of the variation present in all of the original variables (Joliffe, 2002). PCA is, therefore, a powerful tool for the treatment of large geochemical datasets. It permits grouping or, on the contrary, discriminating the compositions taking into account all the elemental contents.

The present chapter is a detailed petrological and compositional study of the Calella de Palafrugell sill, which belongs to the Cretaceous lamprophyre suite in the Catalonian Coastal Ranges (studied as a whole in Chapter 5). This sill is of particular interest because it is both thin (< 0.5 m) and visibly zoned, including large, abundant antecrysts accumulated downwards. The relationships between mineral and whole rock compositions are tested by applying geochemical modelling and multivariate statistics (PCA); a combination of these methods will be used to unravel the origin of the compositional zoning of the sill, as being due to gravitational settling of the antecrysts after emplacement of a single pulse of magma.

## 6.2. Field observations

The present study is focused on the Calella de Palafrugell lamprophyre. It is an alkaline mafic intrusion cropping out on the shoreline, near Calella de Palafrugell village (UTM: 31T 515127 4636865, Fig. 6.1). It trends N065-N085, dips northwards 10-20º and was emplaced within late-Variscan granodiorites (Fig. 6.2A). The sill has sharp contacts with the country-rock and crops out for ca. 100 m. It is divided into sections by small-scale faults and is wedge-shaped, ranging from 15 to 40 cm of observed thickness. The extreme ends of the sill cannot be seen because quaternary debris deposits cover the SW part of the outcrop and the NE part of the sill disappears beneath the sea.

Fig. 6.2A-B shows the most representative section of the sill, located at the northeast part of the outcrop.

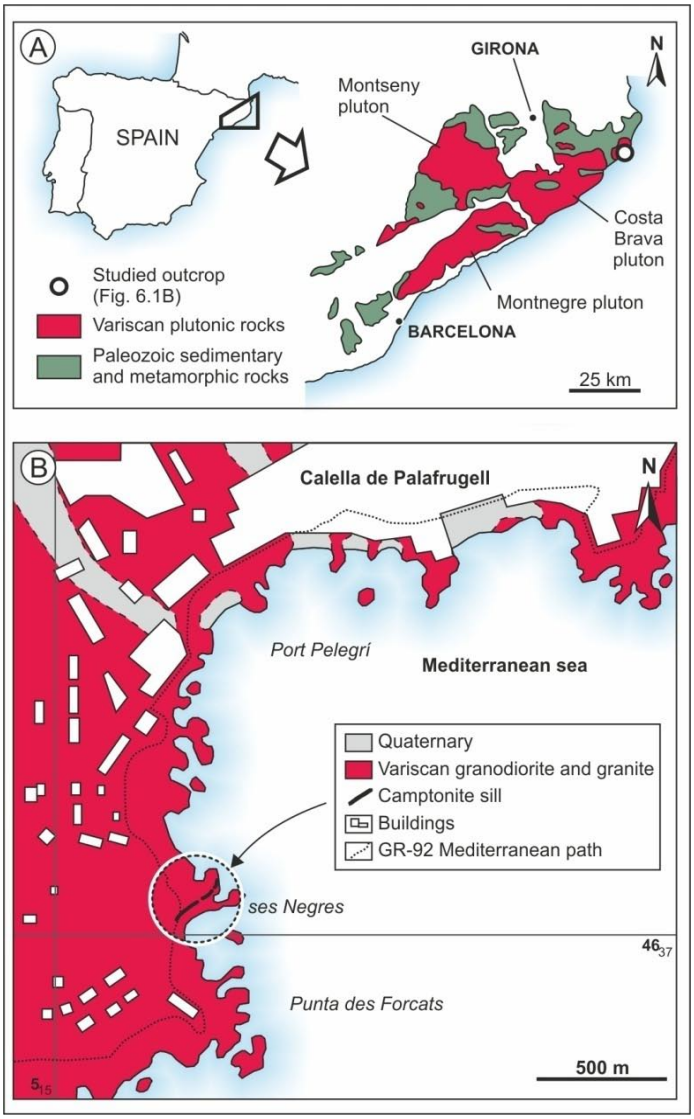


**Fig. 6.1.** Location of the studied sill, cross-cutting late-Variscan granitoids. A) Modified from Enrique (1990). B) Modified from Losantos et al. (2004); UTM grid and coordinates.

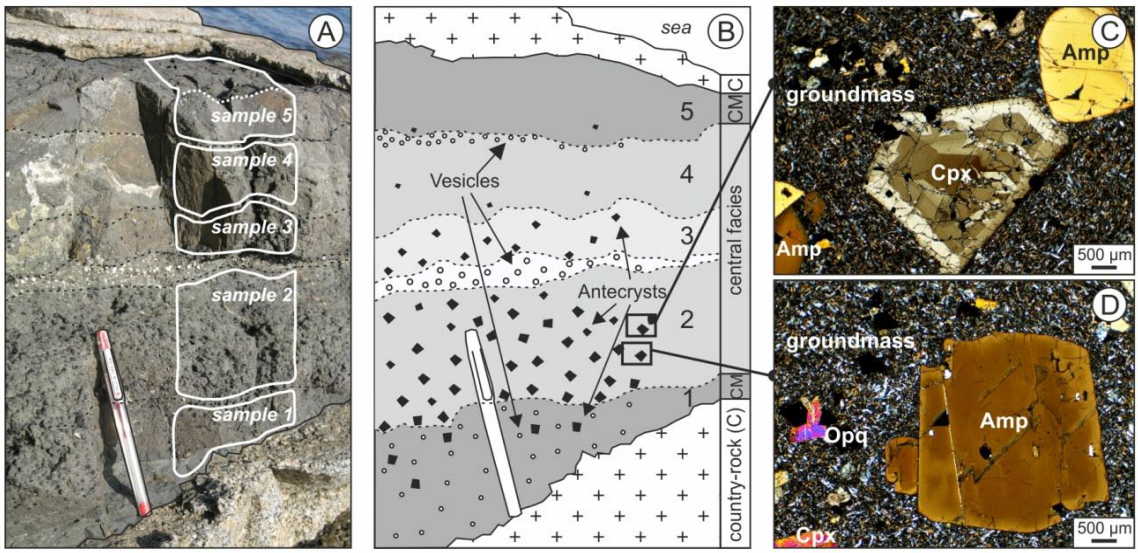


**Fig. 6.2.** A) Field photograph of the studied sill, with the location of the five studied samples. B) Scheme of A; note the vertical structure of the sill and the division in five zones; CM: chilled margin. C-D) Photomicrographs from zone 2, showing large antecrysts set in a fine-grained groundmass; cross-polarised transmitted light; mineral abbreviations after Whitney & Evans (2010).

Wide aphyric chilled margins are developed at both contacts; the upper chilled margin is usually thicker (ca. 5 cm wide), while the lower one (ca. 4 cm wide) displays an incipient lamination. The central facies is ca. 25 cm wide. It exhibits an inequigranular texture resulting from the presence of large mafic crystals measuring up to 7 mm in diameter, which are therefore visible to the naked eye. According to their size, they can be classified as macrocrysts (Le Maitre, 2002). According to their mineralogical composition (see Chapter 7 in this volume), these crystals did not crystallise from the magma in which they are now hosted, but rather represent a magma laced with a crystal cargo that has been inherited from other magmas related to the same magmatic system. Therefore, they are "antecrysts", as defined in several recent contributions (Charlier et al., 2005, 2007; Davidson et al., 2007; Gill et al., 2006; Hildreth and Wilson, 2007; Jerram and Martin, 2008). The antecrysts are concentrated at the bottom of the central facies and become progressively scarcer uptowards.

Vesicles are very common and reach 5 mm in diameter; their abundance suggests a shallow emplacement level which enabled the degassing of the magma, together with a fairly fast solidification. Vesicles are concentrated at three levels (Fig. 6.2A-B): i) the lower chilled margin, where small, irregular vesicles are scattered, ii) the contact between the upper chilled margin and the central facies and iii) the centre of the sill, where vesicles are most abundant. At levels ii and iii, the vesicles define sub-planar alignments within the sill, related to the cooling evolution of the magma at low pressure.

The particularly well developed vertical division of the sill, including wide chilled margins, vesicle alignments and varying proportions of mafic antecrysts, allows it to be divided into

the following five zones (Fig. 6.2A-B): 1) lower chilled margin; 2) lower antecryst-rich central facies; 3) upper antecryst-rich central facies; 4) homogeneous central facies; 5) upper chilled margin.

## 6.3. Samples and methods

Due to the clear vertical structure of the studied sill and its low degree of alteration, its different zones were studied separately. The whole section of the sill was sampled and then sliced using a diamond disc saw to obtain five samples, one from each zone (Fig. 6.2A). For the sake of simplicity, sample names used in this and the following chapter are 1, 2, 3, 4 and 5 instead of CAL-1, CAL-2, CAL-3, CAL-4 and CAL-5 used in previous chapters, respectively.

As many of the crystals were very large (antecrysts), almost all the sample material was used up for whole rock analyses in order to assure an accurate representation of the analysed powders. Samples were crushed in a manganese steel jaw-crusher, milled in an agate vibrating cup mill and successively split down to few grams at the *Servicios de Apoyo a la Investigación* of the University of Zaragoza (Spain). Major and trace element concentrations were determined at the *Service d´Analyse des Roches et des Minéraux (SARM)* in Nancy (France). The samples were analysed by ICP-AES for major elements and ICP-MS for trace elements. Details of the analytical procedures and detection limits are available at http://www.crpg.cnrs-nancy.fr/SARM/ and the results are presented in Table 6.1.

Polished thin sections of the five samples were prepared for petrographic observations and mineral analyses. Major element mineral compositions were determined by electron microprobe at the *Centro Nacional de Microscopía electrónica* of the Complutense University of Madrid (Spain), using a JEOL JZA-8900 M electron microprobe equipped with four wavelength dispersive spectrometers. Analyses were performed using an accelerating voltage of 15 kV and an electron beam current of 20 nA, with a beam diameter of 5 µm. Elemental counting times were 10 s on the peak and 5 s on each of two background positions. Analyses were corrected for electronic interactions using a ZAF procedure.

Mineral trace element concentrations were determined by laser ablation ICP-MS (LA-ICP-MS) at the *Centro de Instrumentación Científica (C.I.C.)* of the University of Granada (Spain), using a 213 µm Mercantek Nd-YAG laser coupled to a quadrupolar Agilent 7500 ICP-MS with a shielded plasma torch. The ablation was carried out in a He atmosphere, using a laser beam with a diameter fixed at 80 µm, a repetition rate of 10 Hz and an

**Table 6.1.** Modal proportion of antecryst cores in the studied samples and whole rock composition of the samples. The modal proportions were calculated by visual estimation under the microscope, discounting an average 15% of overgrowth rims. In the whole rock analyses, major elements are expressed as wt.% and trace elements as ppm. $Fe_2O_3^T$, LOI, <DL as in Table 4.1. ([a]): pseudomorphed antecrysts. ([b]): xenocrysts.

| | Lower chilled margin | Central facies | | | Upper chilled margin |
|---|---|---|---|---|---|
| Sample | 1 | 2 | 3 | 4 | 5 |
| % Cpx | 3.4 | 15.3 | 10.6 | 2.6 | 1.3 |
| % Amp | 2.6 | 10.2 | 4.3 | 1.3 | 1.3 |
| % Opq | 1.7 | 4.3 | 3.4 | 1.3 | 3.4 |
| % Ol [a] | 0.9 | 2.6 | 2.1 | 1.3 | 2.6 |
| % Qz [b] | << 1 | - | - | << 1 | - |
| % Cpx+Amp | 6 | 25.5 | 14.9 | 3.9 | 2.6 |
| $SiO_2$ | 40.24 | 40.62 | 40.45 | 41.28 | 41.94 |
| $TiO_2$ | 3.86 | 4.06 | 3.97 | 3.75 | 3.58 |
| $Al_2O_3$ | 14.30 | 13.69 | 14.02 | 14.64 | 15.15 |
| $Fe_2O_3^T$ | 14.34 | 14.73 | 14.66 | 13.66 | 12.96 |
| MnO | 0.18 | 0.18 | 0.19 | 0.19 | 0.18 |
| MgO | 7.33 | 8.30 | 7.87 | 7.03 | 6.55 |
| CaO | 8.68 | 10.19 | 9.31 | 8.73 | 8.43 |
| $Na_2O$ | 2.58 | 2.23 | 2.36 | 2.56 | 2.70 |
| $K_2O$ | 2.27 | 2.01 | 2.28 | 2.54 | 2.66 |
| $P_2O_5$ | 0.88 | 0.74 | 0.83 | 0.97 | 1.01 |
| LOI | 5.22 | 3.43 | 4.72 | 5.08 | 4.84 |
| Total | 99.88 | 100.16 | 100.67 | 100.44 | 99.99 |
| Mg#: Mg/(Mg+Fe) | 0.54 | 0.56 | 0.55 | 0.54 | 0.53 |
| Rb | 47.48 | 39.65 | 48.91 | 56.36 | 56.93 |
| Cs | 1.04 | 0.72 | 1.22 | 1.43 | 1.38 |
| Be | 2.42 | 1.77 | 1.91 | 2.18 | 2.27 |
| Sr | 784.20 | 733.70 | 739.10 | 857.40 | 902.20 |
| Ba | 531.20 | 476.80 | 499.50 | 579.10 | 599.70 |
| V | 404.80 | 432.60 | 401.40 | 359.70 | 323.80 |
| Cr | 29.56 | 54.97 | 34.47 | 12.73 | < DL |
| Co | 47.15 | 50.07 | 46.69 | 40.86 | 35.30 |
| Ni | 32.96 | 44.15 | 35.62 | 25.80 | 18.71 |
| Cu | 65.64 | 64.12 | 64.83 | 61.52 | 54.74 |
| Zn | 200.50 | 166.30 | 168.70 | 169.10 | 163.40 |
| Ga | 24.85 | 23.96 | 24.00 | 24.34 | 23.57 |
| Y | 28.53 | 26.53 | 27.21 | 29.85 | 29.72 |
| Nb | 65.21 | 55.08 | 59.56 | 70.23 | 72.88 |
| Ta | 5.06 | 4.24 | 4.61 | 5.34 | 5.46 |
| Zr | 278.60 | 243.60 | 259.60 | 293.90 | 294.40 |
| Hf | 6.66 | 6.08 | 6.40 | 6.95 | 6.77 |
| Pb | 10.68 | 7.48 | 9.64 | 9.11 | 7.67 |
| U | 1.49 | 1.25 | 1.36 | 1.60 | 1.66 |
| Th | 5.12 | 4.26 | 4.63 | 5.42 | 5.67 |
| La | 52.49 | 42.42 | 46.99 | 55.21 | 55.74 |
| Ce | 113.40 | 94.45 | 104.30 | 120.60 | 120.20 |
| Pr | 13.79 | 11.74 | 12.79 | 14.64 | 14.57 |
| Nd | 54.77 | 47.79 | 51.94 | 58.28 | 57.57 |
| Sm | 10.36 | 9.41 | 10.03 | 10.95 | 10.70 |
| Eu | 3.07 | 2.88 | 3.01 | 3.25 | 3.23 |
| Gd | 8.32 | 7.68 | 8.05 | 8.61 | 8.49 |
| Tb | 1.12 | 1.06 | 1.10 | 1.19 | 1.16 |
| Dy | 5.83 | 5.62 | 5.77 | 6.19 | 6.12 |
| Ho | 1.01 | 0.97 | 0.99 | 1.08 | 1.06 |
| Er | 2.58 | 2.44 | 2.53 | 2.75 | 2.74 |
| Tm | 0.34 | 0.32 | 0.34 | 0.37 | 0.37 |
| Yb | 2.10 | 2.01 | 2.05 | 2.28 | 2.30 |
| Lu | 0.32 | 0.30 | 0.30 | 0.34 | 0.34 |

output energy of 0.3 mJ per pulse. The spot was pre-ablated for 45 s using a laser output energy of 50%. The spot was then ablated for 60 s with a laser output energy of 70 %. NIST-610 glass was employed as an external standard. Concentration values were corrected using the silicon concentrations obtained by electron microprobe as an internal standard. Further details on technical methods can be found in Bea et al. (2005). Data reduction was carried out by the *C.I.C.* laboratory staff.

Data treatment and geochemical modelling were undertaken with "ad-hoc" built spreadsheets. Principal component analysis (PCA) was performed using the PAST statistical software (Hammer et al., 2001).

## 6.4. Petrography

According to its mineral assemblage, the studied lamprophyre is a camptonite (Le Maitre, 2002). It has a hypocrystalline porphyritic texture, defined by the presence of the aforementioned mafic antecrysts set in a fine-grained groundmass (Fig. 6.2C, 2D). The antecrysts are mainly clinopyroxene and amphibole, with an average crystal size of 3 mm. Smaller (ca. 1 mm) opaque and olivine antecrysts are also present, the latter transformed to chlorite-rich secondary assemblages. Occasional quartz xenocrysts are also found. The groundmass is composed of feldspars (plagioclase and minor K-feldspar), amphibole, clinopyroxene, opaque minerals (oxides and seldom sulphides), accessory acicular apatite and glass; calcite is the most common mineral filling the vesicles. Most of the groundmass consists of acicular, unzoned microlites of amphibole and plagioclase. The size of the microlites increases as the distance increases from the sill walls, being < 50 µm in the chilled margins and ca. 300 µm in the central area of the sill (zone 3). The groundmass also contains scarce, prismatic, zoned microphenocrysts of clinopyroxene and amphibole, up to 500 µm in size.

From among the antecrysts, only clinopyroxene and amphibole show clear zoning patterns. The former (Fig. 6.2C) are pale-pink crystals with subhedral to anhedral cores and thin euhedral rims. The cores show complex compositional zoning and in some cases, aligned sulphide inclusions in the inner zones. This type of inclusions has been interpreted as droplets of immiscible sulphide liquids adhering to the surfaces of rapidly growing silicate crystals (Demant et al., 2010; Peterson and Francis, 1977; Woodland and Jugo, 2007). A pale-green clinopyroxene core has also been observed. It is intensely resorpted and mantled by pale-pink clinopyroxene. Amphibole antecrysts (Fig. 6.2D) are brown-coloured and display subhedral cores and thin euhedral rims. Although the cores are generally unzoned, dark brown, anhedral and rounded inner cores are sometimes observed. Opaque antecrysts appear as single crystals or related to clinopyroxene and amphibole antecrysts.

As noted in the field (Fig. 6.2), the volume fraction of antecrysts in the different zones of the sill is variable (Table 6.1). The mafic antecrysts are especially concentrated in zones 2 and 3, whereas they are almost absent at the upper chilled margin.

## 6.5. Mineral chemistry

Major and trace element concentrations in clinopyroxene, amphibole and the other minerals are discussed in detail in Chapters 5 and 7. The analyses can be found in the electronic supplement of these chapters and include the calculation of structural formulae. In the present chapter, the mineral chemistry study focuses on compositional variations across the sill.

Clinopyroxene is classified as diopside according to Morimoto et al. (1988), amphibole as kaersutite according to Leake et al. (1997) and plagioclase mostly as andesine. Consistent with the classification of the rock as a camptonite, clinopyroxene and amphibole are Ti-rich and plagioclase is progressively enriched in the orthoclase component (up to 8%) as its anorthite content decreases. Opaque crystals are spinel group minerals. Olivine antecrysts are completely replaced by secondary minerals, so their composition could not be determined.

For a given mineral, the different crystal types recognised petrographically show different compositions. Specifically, clinopyroxene occurs as antecrysts and microphenocrysts, amphibole occurs as antecrysts, microphenocrysts and microlites, and feldspars occur as microlites. However, each crystal type keeps constant compositions across the sill, defining rectilinear vertical profiles (Fig. 6.3).

## 6.6. Whole rock chemistry

The whole rock compositions (Table 6.1), obtained from the five samples covering the vertical section of the sill (Fig. 6.2A), are silica undersaturated and rich in titanium and alkalis. They are olivine–and nepheline–normative. Loss on ignition (LOI) values are relatively high. This is probably due to the widespread presence of vesicles in the sill, given its low alteration degree, which is only evident in the replacement of olivine antecrysts and the glass (which are present in very low proportions) by chlorite and other secondary minerals. In fact, LOI values are lowest for the lower antecryst-rich central facies (zone 2), suggesting that they are not related to the alteration of mafic minerals but to the presence of vesicles, which are especially common at the chilled margins and at the homogeneous central facies (Fig. 6.2A, 2B).

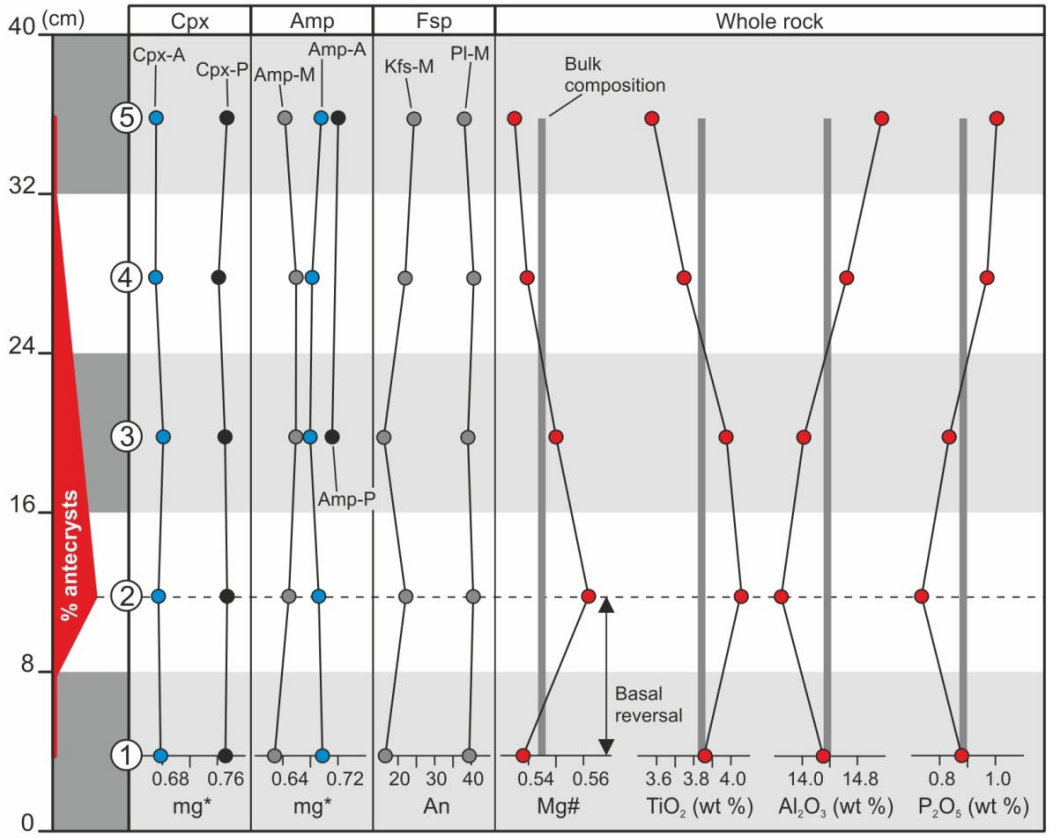


**Fig. 6.3.** Mineral and whole rock compositional variations across the studied sill. In the simplified cross section on the left side, the five zones are considered to have equivalent thicknesses; zones 3 and, especially, 2, display the highest antecryst proportions (see Table 6.1 and Fig. 6.2). The mineral profiles are constructed with the mean composition of each mineral type in each zone of the sill, considering only core compositions; suffixes -A, -P and -M indicate antecrysts, microphenocrysts and microlites, respectively; mg* represents magnesium number in minerals, calculated as Mg / ( Mg + $Fe^{2+}$ + $Fe^{3+}$ + Mn) per formula unit. In the whole rock profiles, vertical thick grey lines represent the bulk composition of the sill (mean of the composition of the five zones); Mg# represents magnesium number in whole rocks, calculated as Mg / (Mg + Fe); note that the lower chilled margin presents a more evolved whole rock composition than the lower central facies, defining a marginal reversal, not shown by mineral compositions.

Despite belonging to the same sill, the five samples display slightly different whole rock compositions (Fig. 6.3), indicating that the sill is compositionally zoned in spite of its low thickness. Among the different profile-types (S-, D- and I-shaped profiles; Fig. 6.4) described by Latypov (2003*b*), the refractory component Mg# (calculated as Mg / (Mg + Fe)) defines an S-shaped profile for the studied sill, with maximum contents in the lower antecryst-rich central facies (zone 2). $TiO_2$ behaves in a similar way as Mg#, whereas $Al_2O_3$ and $P_2O_5$ show opposite profiles, with maximum values for the upper chilled margin (zone 5). This type of profile implies a marginal compositional reversal in the lower chilled margin (basal reversal, e.g., Latypov, 2003*b*; Fig. 6.4). The bulk composition of the sill, calculated as the mean of the composition of the five zones (assuming they are similar in thickness), is very close to the composition of the lower chilled margin.

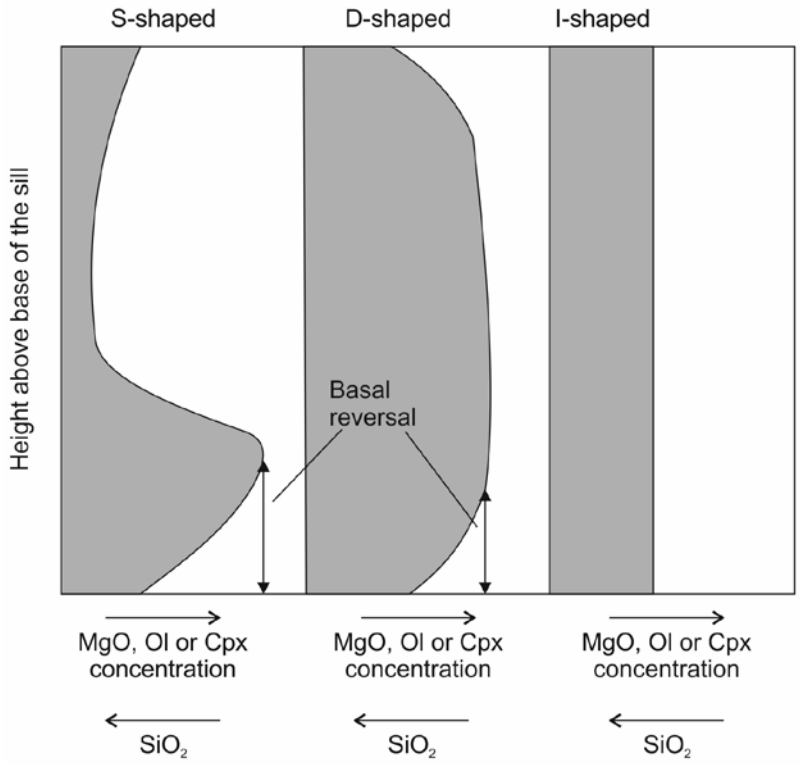


**Fig. 6.4.** Schematic vertical compositional profiles of chemical components (e.g., MgO and $SiO_2$) or modal abundances of mafic minerals (e.g., olivine) in S-, D- and I-shaped sills. Note the well developed basal reversals in the S- and D-shaped sills. From Latypov (2003*b*).

The primitive mantle-normalised REE patterns (Fig. 6.5A) are LREE-enriched, as is common in alkaline rocks. They are fairly coincident but, in detail, they range from the most to the least REE enriched in the following sequence: 5-4-1-3-2. This order is clearer at the extremes of the patterns, especially for the LREE (Fig. 6.5A inset). Accordingly, the chilled margins are overall more REE-enriched than the central facies.

The whole rock results, both for major elements and in the REE, indicate that the margins of the sill show more evolved compositions than its central facies, contrary to a normal fractionation process where cooling and crystallisation is slower inwards and, therefore, inward compositions are more evolved. Consequently, the compositional zoning of the sill cannot be explained by fractionation and some other process must be involved in its origin.

The compositional profiles and the ordering of the REE patterns correlate with the modal proportion of clinopyroxene and amphibole antecrysts in the different zones of the sill (Table 6.1): the higher these proportions, the higher the Mg# value and lower REE content. Furthermore, the higher the differences in proportion among the samples, the greater the separation of the REE patterns; for instance, samples 2 and 3 (25.5% and

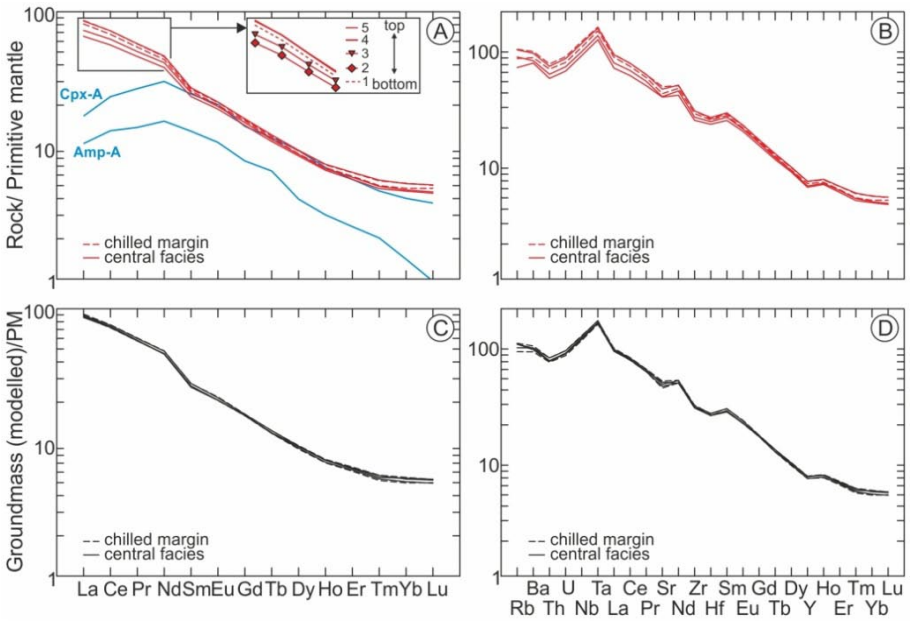


**Fig. 6.5.** Primitive mantle (McDonough & Sun, 1995) normalised Rare Earth Element (REE) and multi-element concentrations of the five zones of the studied sill (A and B respectively) and the five modelled groundmass compositions (C and D respectively). Note the high similarity among the groundmass compositions, in contrast with the whole rock compositions. Clinopyroxene and amphibole compositions used in the geochemical model are included in A.

14.9% of clinopyroxene + amphibole antecrysts, respectively) are more separated from each other than samples 4 and 5 (3.9% and 2.6% of clinopyroxene + amphibole antecrysts, respectively), which are almost coincident (Fig. 6.5A inset). These data suggest that the varying proportion of antecrysts in the different zones of the sill controls the compositional divergences among them. Accordingly, the primitive mantle-normalised REE patterns of clinopyroxene and amphibole antecrysts (Fig. 6.5A) are relatively LREE and HREE depleted compared to whole rock compositions. This means that progressively higher proportions of clinopyroxene and amphibole antecryst in the rock should generate progressively lower concentrations in LREE and HREE in whole rock; and that is the situation observed for the samples richest in antecrysts (samples 2 and 3, Fig. 6.5A inset).

## 6.7. Geochemical modelling

Proving quantitatively that the antecryst proportion controls the compositional zoning of the studied sill requires developing a mathematical model which quantifies the influence of those antecrysts on the bulk composition of the rock. From a conceptual point of view, the composition of a given sample should be a composite of the composition of its groundmass and the composition of its antecrysts, where the proportion of each member (groundmass and antecrysts) is a reflection of the proportion in which it appears in the rock. For a given trace element (*i*), the following equation is proposed:

$$C_R^i = C_{Gr}^i(1 - \sum p) + \sum(C_A^i \times p) \quad \text{eq. 1}$$

Where $C_R^i$, $C_{Gr}^i$ and $C_A^i$ represent the concentration of the element *i* in the rock (sample) *R*, the groundmass *Gr*, and the antecryst mineral *A* respectively and *p* the proportion of the antecryst mineral *A* in the rock (sample) *R*. In order to maintain the parts-per-million (ppm) units in the different terms of the equation, *p* has to be a part-per-one proportion. The summation signs refer to the possibility of having more than one antecryst mineral in the rock; each mineral developing antecrysts must be represented by a new $(C_A^i \times p)$ term in the equation, and its *p* proportion in the rock must be successively subtracted from 1 to calculate the part-per-one proportion of groundmass $(1 - \sum p)$.

In the studied case, four antecryst phases are present in a significant proportion (Table 6.1), namely: clinopyroxene (1.3-15.3%), amphibole (1.3-10.2%), opaque minerals (1.3-4.3%) and olivine (0.9-2.6%). Note that the given proportions represent only antecryst cores, as their rims crystallised in equilibrium with the groundmass (see Chapters 5 and 7) and they must be included within the groundmass proportion. As all olivine crystals are replaced, they could not be analysed and cannot be considered for the application of the equation. Fortunately, olivine is the least abundant antecryst in all the samples. In consequence, in the studied case equation 1 becomes:

$$C_R^i = C_{Gr}^i\left(1 - p_{Cpx} - p_{Amp} - p_{Opq}\right) + C_{Cpx}^i \times p_{Cpx} + C_{Amp}^i \times p_{Amp} + C_{Opq}^i \times p_{Opq} \quad \text{eq. 2}$$

Five $C_R$ compositions are available (samples 1 to 5 from bottom to top of the studied sill, Table 6.1) and, in each of the five cases, *p* values must be calculated dividing the modal percentages in Table 6.1 for clinopyroxene, amphibole and opaque minerals by 100, to obtain part-per-one values. $C_{Cpx}$, $C_{Amp}$ and $C_{Opq}$ compositions are representative trace element analyses of antecrysts of clinopyroxene, amphibole and opaque minerals, respectively (Table 6.2). Regarding the parameter *i*, 34 trace elements are available both in whole rocks (Table 6.1) and minerals (Table 6.2). Therefore, in the studied system the only unknown parameter is the composition of the groundmass ($C_{Gr}$), i.e., the composition of the whole rock subtracting the composition of the antecrysts:

$$C_{Gr}^i = \frac{C_R^i - C_{Cpx}^i \times p_{Cpx} - C_{Amp}^i \times p_{Amp} - C_{Opq}^i \times p_{Opq}}{1 - p_{Cpx} - p_{Amp} - p_{Opq}} \quad \text{eq. 3}$$

Testing the $C_{Gr}$ results for the five different $C_R$ rock compositions (and their associated *p* values) was the aim of developing this quantitative model. If, indeed, the differences in composition between the five whole rock samples ($C_R$) of the sill are due to different amounts of antecrysts in each of those samples (*p*), the five calculated groundmass compositions ($C_{Gr}$) should be the same. If they are, this model provides the composition

of the groundmass, equivalent to the composition of the magma which hosted the antecrysts and carried them to the emplacement level.

**Table 6.2.** Antecryst trace element compositions (ppm) used for geochemical modelling. Full dataset of trace element compositions in clinopyroxene and amphibole is presented in Chapter 7.

| | Cpx | Amp | Opq |
|---|---|---|---|
| Sample | 1 | 1 | 1 |
| Rb | 0.37 | 7.31 | 0.11 |
| Cs | 0.01 | 0.04 | 0.02 |
| Be | 0.77 | 0.37 | 0.10 |
| Sr | 123.28 | 611.71 | 0.70 |
| Ba | 4.17 | 486.74 | 1.41 |
| V | 308.26 | 336.23 | 1192.98 |
| Cr | 0.81 | 269.99 | 368.66 |
| Co | 23.24 | 39.98 | 103.29 |
| Ni | 0.84 | 40.00 | 125.08 |
| Cu | 0.93 | 1.31 | 5.06 |
| Zn | 64.74 | 64.39 | 338.00 |
| Ga | 18.09 | 34.04 | 29.47 |
| Y | 23.19 | 11.44 | 0.08 |
| Nb | 1.16 | 13.47 | 2.36 |
| Ta | 0.26 | 0.82 | 0.22 |
| Zr | 157.66 | 61.55 | 10.11 |
| Hf | 6.80 | 2.34 | 0.37 |
| Pb | 0.45 | 1.38 | 0.18 |
| U | 0.03 | 0.06 | 0.03 |
| Th | 0.13 | 0.14 | 0.02 |
| La | 10.74 | 6.68 | 0.05 |
| Ce | 38.76 | 21.54 | 0.10 |
| Pr | 6.75 | 3.46 | 0.01 |
| Nd | 37.60 | 18.97 | 0.04 |
| Sm | 9.82 | 5.18 | 0.01 |
| Eu | 3.12 | 1.62 | 0.00 |
| Gd | 7.55 | 4.16 | 0.02 |
| Tb | 1.13 | 0.64 | 0.01 |
| Dy | 6.16 | 2.67 | 0.03 |
| Ho | 1.02 | 0.45 | 0.00 |
| Er | 2.44 | 1.08 | 0.00 |
| Tm | 0.31 | 0.14 | 0.00 |
| Yb | 1.77 | 0.62 | 0.00 |
| Lu | 0.25 | 0.07 | 0.00 |

For each of the 34 available trace elements, eq. 3 was applied five times, one for each $C_R$ composition and its corresponding $p$ values, keeping constant $C_{Cpx}$, $C_{Amp}$ and $C_{Opq}$ compositions. The five $C_{Gr}$ compositions obtained for each trace element are presented in Table 6.3, together with their mean, standard deviation and the proportion of the standard deviation with respect to the mean value.

The five groundmass compositions ($C_{Gr}$) are highly coincident, so the proportion of the standard deviation is very low for most elements, especially for Ba, Ga, Y, Nb, Ta, Zr, Hf, U, Th and the REE (< 5%). Graphically, the primitive mantle-normalised REE and multielemental patterns of the modelled groundmass compositions are very similar to each other (Fig. 6.5C, 6.5D), in contrast with those of the whole rock samples (Fig. 6.5A, 6.5B). The highest standard deviation proportions correspond to transition elements, although only Cr and Ni exceed 20% of deviation. This means that, although their mean values are acceptable, there is a considerable dispersion among the values in each case. Taking into account that olivine antecrysts have not been considered due to their alteration, and that they have high partition coefficients for these elements (see compilation by Rollinson, 1993), the observed variations are probably caused by the variable proportions of olivine antecrysts in the different samples (Table 6.1).

The trace element compositional profiles of the whole rock and modelled groundmass compositions in the studied sill are summarised in Fig. 6.6. Regarding the whole rock values, the compatible elements (e.g., Cr) behave in a similar way as Mg# (compare with

**Table 6.3.** Groundmass modelled compositions ($C_{Gr}$; ppm) for the studied samples. The mean composition, the standard deviation and the proportion of the standard deviation with respect to the mean (%) are also shown. (*): cannot be calculated as Cr concentration in sample 5 is below the detection limit (Table 6.1).

| | $C_{Gr}$ 1 | $C_{Gr}$ 2 | $C_{Gr}$ 3 | $C_{Gr}$ 4 | $C_{Gr}$ 5 | Mean $C_{Gr}$ | Standard deviation | Proportion of standard deviation |
|---|---|---|---|---|---|---|---|---|
| Rb | 51.22 | 55.33 | 59.43 | 59.34 | 60.45 | 57.15 | 3.85 | 7 |
| Cs | 1.13 | 1.01 | 1.48 | 1.51 | 1.47 | 1.32 | 0.23 | 18 |
| Be | 2.58 | 2.30 | 2.21 | 2.27 | 2.39 | 2.35 | 0.15 | 6 |
| Sr | 827.84 | 929.36 | 856.43 | 892.65 | 949.60 | 891.18 | 50.23 | 6 |
| Ba | 561.62 | 607.48 | 585.17 | 604.06 | 631.14 | 597.89 | 26.04 | 4 |
| V | 395.77 | 427.13 | 383.97 | 350.01 | 292.40 | 369.86 | 51.34 | 14 |
| Cr | 17.60 | 16.32 | 12.53 | 4.65 | * | 12.77 | 5.83 | 46 |
| Co | 47.20 | 54.12 | 47.73 | 40.50 | 32.94 | 44.50 | 8.06 | 18 |
| Ni | 32.25 | 49.23 | 36.18 | 24.93 | 14.82 | 31.48 | 12.83 | 41 |
| Cu | 70.95 | 90.64 | 78.95 | 64.78 | 58.02 | 72.67 | 12.67 | 17 |
| Zn | 206.80 | 192.72 | 180.63 | 171.08 | 159.82 | 182.21 | 18.32 | 10 |
| Ga | 24.76 | 23.44 | 24.01 | 24.31 | 23.29 | 23.96 | 0.61 | 3 |
| Y | 29.73 | 31.07 | 29.69 | 30.69 | 31.14 | 30.46 | 0.71 | 2 |
| Nb | 70.18 | 76.11 | 71.94 | 73.83 | 77.24 | 73.86 | 2.90 | 4 |
| Ta | 5.45 | 5.85 | 5.56 | 5.61 | 5.79 | 5.65 | 0.17 | 3 |
| Zr | 294.11 | 303.08 | 293.63 | 304.71 | 309.79 | 301.07 | 7.02 | 2 |
| Hf | 6.89 | 6.82 | 6.81 | 7.11 | 7.06 | 6.94 | 0.14 | 2 |
| Pb | 11.51 | 10.35 | 11.66 | 9.57 | 8.13 | 10.24 | 1.46 | 14 |
| U | 1.61 | 1.77 | 1.66 | 1.68 | 1.77 | 1.70 | 0.07 | 4 |
| Th | 5.54 | 6.02 | 5.64 | 5.71 | 6.03 | 5.79 | 0.23 | 4 |
| La | 56.28 | 57.11 | 55.77 | 57.85 | 59.06 | 57.21 | 1.30 | 2 |
| Ce | 120.82 | 122.96 | 121.50 | 125.86 | 127.03 | 123.63 | 2.71 | 2 |
| Pr | 14.59 | 14.75 | 14.60 | 15.21 | 15.36 | 14.90 | 0.36 | 2 |
| Nd | 57.42 | 57.12 | 57.70 | 60.18 | 60.46 | 58.58 | 1.61 | 3 |
| Sm | 10.72 | 10.51 | 10.73 | 11.21 | 11.18 | 10.87 | 0.31 | 3 |
| Eu | 3.17 | 3.18 | 3.19 | 3.32 | 3.37 | 3.25 | 0.09 | 3 |
| Gd | 8.62 | 8.68 | 8.66 | 8.82 | 8.87 | 8.73 | 0.11 | 1 |
| Tb | 1.16 | 1.17 | 1.16 | 1.21 | 1.21 | 1.18 | 0.03 | 2 |
| Dy | 6.01 | 6.27 | 6.13 | 6.32 | 6.38 | 6.22 | 0.15 | 2 |
| Ho | 1.05 | 1.10 | 1.06 | 1.10 | 1.11 | 1.08 | 0.03 | 3 |
| Er | 2.67 | 2.78 | 2.72 | 2.82 | 2.86 | 2.77 | 0.08 | 3 |
| Tm | 0.35 | 0.37 | 0.36 | 0.38 | 0.39 | 0.37 | 0.01 | 4 |
| Yb | 2.19 | 2.38 | 2.24 | 2.35 | 2.41 | 2.32 | 0.09 | 4 |
| Lu | 0.34 | 0.36 | 0.33 | 0.35 | 0.36 | 0.35 | 0.01 | 3 |

Fig. 6.3), whereas the incompatible elements (e.g., La) show opposite profiles. In contrast, the calculated groundmass compositions ($C_{Gr}$) are very similar to each other, generating rectilinear profiles. This is the case even for Cr, for which the highest differences among groundmass compositions are observed (Table 6.3). The mean groundmass composition is more evolved than the bulk composition of the sill, as the latter displays higher concentrations in compatible elements and lower concentrations in incompatible elements.

Given that the developed model returns similar compositions for the groundmass ($C_{Gr}$) in all the zones of the sill, the initial hypothesis becomes supported by the data and can be numerically tested with a simple model. Furthermore, the mean $C_{Gr}$ composition (Table 6.3) can be taken to be an average composition of the groundmass of the sill.

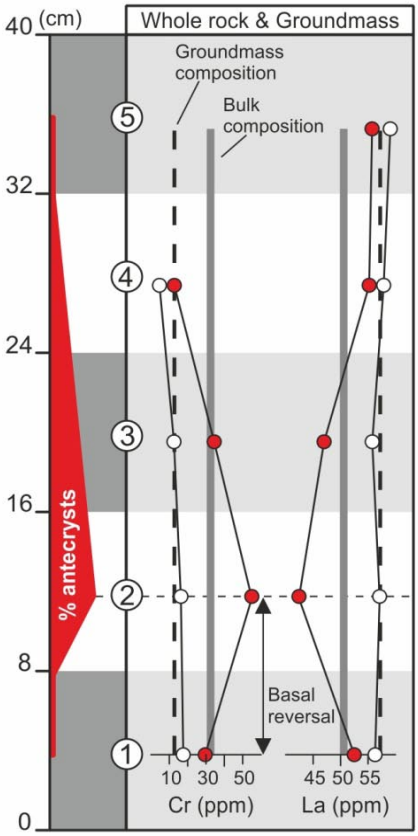


**Fig. 6.6.** Trace element variations in whole rock (black circles) and modelled groundmass (white circles) across the studied sill. Simplified cross section of the sill is as in Fig. 6.3. Cr is representative of compatible elements and La is representative of incompatible elements. The Cr concentration in sample 5 is below the detection limit. The vertical thick grey lines represent the bulk composition of the sill, whereas the vertical dashed lines represent the mean groundmass composition (Mean $C_G$). Note the high similarity among the groundmass compositions, in contrast with the whole rock compositions.

## 6.8. Principal component analysis

Principal component analysis (PCA) was applied to the compositional dataset with a twofold objective: on the one hand, to statistically test the hypothesis that the compositional zoning of the sill is due to the varying proportions of antecrysts; on the other hand, to check the validity of the modelled groundmass composition. All the 34 analysed trace elements, both in minerals and whole rock, were included in the analysis. Five whole rock compositions (Table 6.1), five antecryst compositions (including compositions in Table 6.2) and the modelled groundmass composition (Mean $C_{Gr}$, Table 6.3) were included in the analysis.

PCA transforms the original variables (elemental contents) into a new set of variables (the principal components, PCs). The first two principal components represent the greatest geochemical variation of the whole analytical dataset; therefore, the distribution of the

samples in a PC1 vs. PC2 plot (Fig. 6.7) reveals the compositional relationships among them. The five whole rocks are distributed in a linear trend between the modelled groundmass and the antecrysts. This distribution is especially developed along PC1, which clearly separates rock data (PC1 < 0) from mineral data (PC1 > 0); PC2, in turn, separates the three minerals. A closer look at the loads of the PC1 variable reveals a somewhat greater contribution of Y, Zr and most REE to the observed variability, within a general context of relative uniformity. On PC2, by contrast, the contribution of transition elements is clearly greater (see Table 6.I of the electronic supplement). Hence, incompatible elements control the maximum load on PC1, which explains 82.01% of the global variance. PC2 may have a higher load on compatible elements, but it only explains 12.29% of the variance. In consequence, incompatible elements play an important role in the statistical matrix.

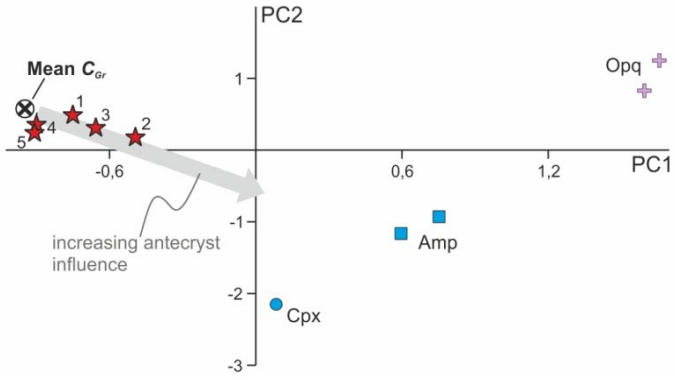


**Fig. 6.7.** Principal component analysis (PCA) of 34 trace element data in minerals and whole rock, showing the plot of component 2 against 1. The rounded cross represents the modelled groundmass of the sill; stars 1 to 5 represent the five samples collected from bottom to top of the sill; the circle, the squares and the crosses represent antecrysts of clinopyroxene, amphibole and opaque minerals, respectively. Details can be found in Table 6.I of the electronic supplement.

As for the REE patterns, the five whole rock compositions order according to their antecryst proportion (Table 6.1). Samples 4 and 5, with low volume fractions of antecrysts, plot close to the groundmass, which is antecryst-free. Samples 1, 3 and 2, with increasing volume fractions of antecrysts, plot progressively closer to the antecrysts. As the proportion of antecrysts is lower than the proportion of groundmass in all the samples, these always plot closer to the groundmass than to the antecrysts. The samples describe a linear trend that points particularly to amphibole and clinopyroxene, whereas opaque minerals, with maximum PC1 and PC2 values, fall outside this trend. This agrees with the relative proportion among antecrysts in the samples, as clinopyroxene and amphibole antecrysts (up to 25.5%) are much more common than opaque antecrysts (up to 4.3%).

The PCA results confirm the hypothesis that the small compositional divergences detected among the samples are due to the presence of different amounts of antecrysts; these differences increase with the antecryst proportion. Moreover, the calculated Mean $C_{Gr}$ (Table 6.3) is proved to represent the compositionally homogeneous groundmass of the sill and therefore, the host magma carrying the antecrysts to the emplacement level.

## 6.9. Discussion

### 6.9.1. Origin of the compositional zoning of the sill

The origin of compositional zoning in sill-like bodies has been the subject of intense debate (e.g., Latypov, 2009). Several mechanisms have been proposed for the development of sill fractionation and the creation of marginal compositional reversals (see review by Latypov, 2003*a*). Marginal reversals are common in igneous bodies regardless of their size and bulk composition, and recent studies (Chistyakova and Latypov, 2009*b*, 2010) have suggested focusing on relatively simple objects (< 0.5 m thick) such as small mafic dykes, that also commonly reveal marginal reversals, but in which most of the complicating factors can be eliminated.

In spite of its low thickness, the studied sill can be macroscopically divided into five zones (Fig. 6.2A, 6.2B). The different zones present slightly different whole rock compositions, indicating that the sill is compositionally zoned. Specifically, the vertical whole rock compositional variations reveal an S-shaped profile (Fig. 6.3, 6.6). This kind of profile implies the development of a marginal reversal in the lower chilled margin. In contrast, mineral and modelled groundmass compositions are homogeneous across the sill, generating rectilinear profiles (Fig. 6.3, 6.6).

Alteration minerals are minor in the sill and whole rock LOI contents seem to be related to the presence of vesicles (see section 6.6), which are very common in lamprophyric magmas. Thus, magmatic or subsolidus interaction with externally-derived liquids appears to be relatively unimportant. Hydrothermal alteration could have caused some scattering of the mobile elements, but is unlikely to account for the coherent variation trends observed in the sill. Therefore, the observed compositional profiles must be related to some primary process.

Igneous petrologists have suggested several mechanisms for the creation of marginal reversals, including country-rock contamination (e.g., Tyson and Chang, 1984), multi-pulse intrusion (e.g., Gibb and Henderson, 1992, 2006; Shirley, 1987), a “three-increase model” (Latypov et al. 2011), in situ crystallisation involving Soret diffusion (e.g., Latypov, 2003*a*, 2003*b*) and gravitational settling of crystals (e.g., Ariskin et al., 2003; Frenkel et al., 1989).

In the studied sill, contamination of magma by the country-rock granodiorite should be ruled out because the contacts of the sill are sharp (Fig. 6.2A) and no xenoliths or other signs of magma-rock interaction have been recognised inside the intrusion.

The well developed structure of the sill (Fig. 6.2A, 6.2B), including a central level of vesicles, may suggest multiple injections of magma. However, there are problems with this hypothesis: firstly, no chilled contacts have been recognised between the different zones; secondly, the low thickness of the sill makes this kind of complex process unlikely, although successive changes in the composition of inflowing magma have been suggested for the generation of compositional zoning in other small intrusions (Chistyakova and Latypov, 2009*b*, 2010); thirdly, mineral compositions are constant across the sill (Fig. 6.3); and finally, the modelled groundmass compositions are also constant across the sill (Fig. 6.5, 6.6). These criteria suggest a rapid, single-pulse emplacement of magma. Accordingly, the central vesicle level must be related to the isolation of volatiles at the point of final solidification, due to the inwards cooling and crystallisation of the magma. Therefore, the process responsible for the chemical zoning and basal reversal formation in the studied sill must be driven internally, not externally. These results are in agreement with recent studies (Latypov and Chistyakova, 2009) which suggest that many complex textural and compositional profiles traditionally explained by multiple magma injections may be better explained in the framework of a single-pulse magma model.

A “three-increase model” involves a combination of three processes, which become more effective with time and increasing distance from the cold country-rock: an increase in the extent of magma primitivity, an increase in the extent of chemical equilibrium among the phases and an increase in the proportion of in situ grown cumulus minerals in response to more effective removal of evolved liquid. In the studied case, the first process is discarded given the homogeneity of the groundmass compositions (Fig. 6.6), the second process is dismissed due to the homogeneity of the mineral compositions (Fig. 6.3) and the third process can be ruled out given that: a) the cumulus minerals are inherited antecrysts which crystallised below the emplacement level (see Chapter 7) and b) the low thickness of the sill implies a very rapid cooling, hindering an effective removal of liquid. In consequence, this model cannot explain the compositional zoning of the studied sill.

Soret fractionation is a single-pulse in situ process (Latypov, 2003*a*). Nevertheless, it is unlikely to produce the observed zoning given that the bulk composition of the sill agrees with the composition of the lower chilled margin (Fig. 6.3, 6.6) and that the chilled margins are fine-grained, indicating a high degree of supercooling. In any case, the small size of the intrusion would be unlikely to provide a long-lasting temperature gradient between the magma and the country-rock, which is necessary to allow for an efficient diffusion process at the sill margin.

In contrast, gravitational settling seems a likely process to take place in an antecryst-rich magmatic intrusion like the one studied here. This hypothesis is supported by: 1) the antecryst accumulation towards the bottom of the sill (Fig. 6.2); 2) the upwards differentiation (Fig. 6.3, 6.5A inset, 6.6); 3) a strongly supercooled system, reflected in the

fine-grained chilled margins, as is currently accepted for gravitational settling (López-Moro et al., 2007); 4) the similar composition of the lower chilled margin and the bulk sill composition (Fig. 6.3, 6.6); 5) the inherited origin of the antecrysts (see Chapter 7), because magmatic bodies crystallise through solidification fronts that propagate from the margins inwards and, accordingly, crystal settling can only occur in those magmas carrying crystals upon emplacement (Marsh, 2000); 6) the results of the geochemical model and the principal component analysis (PCA).

According to the geochemical model, the groundmass of the sill is homogeneous and the observed chemical zoning responds only to the influence of different proportions of antecrysts in the different zones of the sill. As a consequence, groundmass trace element profiles are rectilinear whereas sill profiles are S-shaped (Fig. 6.6), with similar compositions to the groundmass for zones with low proportions of antecrysts (zones 4 and 5) and more primitive compositions for zones with higher proportions of antecrysts (zones 2 and 3). The lower chilled margin (zone 1) seems to be the best representative of the parental magma entering the intrusion (bulk sill composition, Fig. 6.3, 6.6), probably crystallising before gravity-driven zoning was significant, due to the high degree of supercooling of the magma in contact with the country-rock. The upper chilled margin, in contrast, seems to have lost some of its initial antecrysts by gravitational settling, and its composition is closer to that of the groundmass (Fig. 6.6).

The developed PCA evaluates the relationships among the composition of the rocks, the antecrysts and the modelled groundmass. The plot of PC2 against PC1 (Fig. 6.7) clearly shows a linear trend defined by rock compositions, from the calculated groundmass composition towards the composition of the antecrysts; the higher the amount of antecrysts in the rock, the closer to the antecrysts the rock plots. Therefore, the PCA also indicates that the compositional differences recognised among the different zones of the sill are solely caused by different proportions of antecrysts.

The petrological and geochemical criteria support crystal settling as the cause of zoning. However, this process must also be physically tested. The efficiency of crystal settling depends on crystal size and density and also on the physical properties of the magma. Considering a basaltic magma of 2.875 g/cm$^3$ density and 1000 P dynamic viscosity at 1200 ºC (Petrelli et al., 2011), clinopyroxene crystals of 0.2 cm radius and 3.4 g/cm$^3$ density (average density for diopside, see www.webmineral.com) would settle with a velocity of 0.27 cm/min and amphibole crystals of the same size and 3.24 g/cm$^3$ density (average density for kaersutite, see www.webmineral.com) would settle with a velocity of 0.19 cm/min according to Stokes' law. This means that clinopyroxene and amphibole crystals would sink 20 cm (half of the sill thickness) in 73 and 105 minutes, respectively. Even though significant loads of crystals increase magma viscosity, high volatile contents

have the opposite effect and camptonite melts are richer in volatiles than basaltic melts, so these effects may compensate each other.

Meanwhile, the heat transfer approximation by Jaeger (1968) permits calculating the cooling time of the sill. For a thickness of 40 cm and a thermal diffusivity of $10^{-6}$ $m^2/s$ (Huppert and Sparks, 1980), 1 hour after the emplacement of the magma the centre of the sill started cooling; 11 hours after the emplacement of the magma cooling was substantial at the centre of the sill and about as much heat had been lost to the country-rock as remained in the sill. Taking these calculations into account, the cooling time of the intrusion was larger than the settling time of the crystals and thus, crystal settling was physically feasible.

From the above discussion it is concluded that the studied sill was formed by single injection of an antecryst-laden magma, followed by gravitational settling of the antecrysts. The latter process is the origin of the compositional zoning of the sill, creating a marginal reversal in the lower chilled margin, which crystallised immediately after the intrusion of the parental magma retaining its composition. This means that it is a "primary chilled margin", i.e., it survived from remelting and was preserved, contrary to what is usually suggested for thick intrusions (e.g., Huppert and Sparks, 1989; Latypov, 2003*a*; Latypov et al., 2007). As reported elsewhere (López-Moro et al., 2007), an important conclusion is that the samples most enriched in compatible elements do not necessarily represent the parental magma.

Gravitational settling has been suggested for the explanation of numerous cases of zoning in thick sill-like bodies (e.g., Marsh, 2000). However, its significance has been considered extremely unlikely in cm-sized dykes (Chistyakova and Latypov, 2009*a*, 2009*b*). This study proves that it is a meaningful process regardless of the size of the intrusion, as long as the parental magma carries large crystals.

### 6.9.2. Application of the geochemical model to calculate the composition of the groundmass

The studied sill displays a porphyritic texture composed of large antecrysts set in a fine-grained groundmass (Fig. 6.2). Given that the antecrysts crystallised below the emplacement level (Chapter 7) and that the sill formed by a single-pulse of magma (see section 6.9.1), the groundmass of the sill represents the crystallisation product of the magma hosting the antecrysts, i.e., the magma which incorporated the antecrysts at depth and carried them up to the emplacement level.

The composition of the groundmass or host magma has proved useful in helping to reveal the origin of the sill zoning. It will also be useful for trace element partitioning studies

with the groundmass crystals (see Chapter 7). In order to determine the composition of the groundmass in porphyritic rocks, different approaches can be undertaken. These include physical separation of the groundmass (e.g., Nakada and Motomura, 1999) or in-situ analysis with LA-ICP-MS, normally using a defocused laser beam (e.g., Thompson and Malpas, 2000). The former approach is time-consuming and there is the possibility of incomplete groundmass separation. The latter may not yield representative compositions, especially in rocks with a medium- to coarse-grained groundmass.

In this paper, the groundmass composition (Mean $C_{Gr}$, Table 6.3) has not been directly analysed but geochemically modelled and validated with PCA. In contrast with classical mass-balance models (e.g., López-Moro et al., 2007), the proposed geochemical model is applied to trace elements, uses the real proportions of crystals in the rock and returns the composition of the groundmass. The drawback however is that trace element contents must be available not only in rocks but also in minerals.

In each zone of the sill, the groundmass presents lower contents in compatible elements (e.g., Cr) and higher contents in incompatible elements (e.g., La) than the whole-rock, especially for the zones with high proportions of antecrysts (Fig. 6.6). Accordingly, the mean composition of the groundmass is more evolved than the bulk composition of the sill; the bulk composition of the sill represents the parental magma entering the intrusion, which included both the antecrysts and their host magma. However, differences between whole rock and groundmass (host magma) compositions are not large; groundmass compositions show alkaline-like, enriched primitive mantle-normalised REE and multielemental patterns (Fig. 6.5C, 6.5D) similar to whole-rock compositions (Fig. 6.5A, 6.5B). In detail, the rock compositions present a $La/Lu_N$ value ranging from 14.93 to 17.3, whereas the groundmass presents a 17.3 value is consistent with an antecryst-free composition, as clinopyroxene and amphibole antecrysts are relatively depleted in LREE compared to rock compositions (Fig. 6.5A).

The original magma which entered the intrusion is probably best represented by the lower chilled margin, which shows the highest resemblance to the bulk sill composition (Fig. 6.3, 6.6); on the other hand, the closest rock composition to that of the groundmass is apparently that of the upper chilled margin (Fig. 6.5, 6.6), which presents very low amounts of antecrysts (zone 5, Table 6.1). Hence, the modelled trace element composition of the groundmass or host magma (Mean $C_{Gr}$, Table 6.3) can be completed with the major element composition in sample 5 (Table 6.1).

The host magma must have undergone some fractionation prior to emplacement, either in the magma chamber or in the ascending conduit, as its composition cannot represent a primary magma in equilibrium with its mantle source, that would typically show Mg# > 0.6-0.7, MgO > 11 wt.%, Cr > 500-1000 ppm and Ni > 200-500 ppm (Frey et al., 1978). This

suggests the existence of some magmatic processes affecting the studied system at depth. Besides fractionation, magma recharge and mixing processes were probably involved, as they may explain the origin of the antecryst cores (see Chapters 5 and 7).

## 6.10. Conclusions

The petrologic and geochemical study of a thin (< 0.5 m) porphyritic lamprophyre has led to conclusions on compositional zoning of igneous intrusions and the influence of antecrysts on whole rock compositions. Mathematical modelling and principal component analysis have enriched the interpretation of geochemical results.

- The lamprophyre sill is visibly zoned, with chilled margins, volatile unmixing and downwards accumulation of mafic antecrysts. It was formed by single-pulse emplacement of an antecryst-laden magma followed by gravitational settling of the antecrysts before solidification.

- Mineral compositions as well as groundmass compositions are constant across the sill. In contrast, whole rock compositions change in response to varying volume fractions of antecrysts.

- It follows that crystal settling is able to trigger compositional zoning even at cm-scale intrusions.

- Another important conclusion is that samples enriched in MgO and compatible elements do not necessarily represent parental magmas. Rather, they may represent a relatively evolved magma with abundant mafic antecrysts.

- The geochemical model makes it possible to calculate with accuracy the trace element composition of the groundmass in porphyritic rocks. Besides this study, the groundmass composition will be used for the calculation of mineral-melt partition coefficients (Chapter 7).

- Multivariate statistical principal component analysis (PCA) permits establishing interpretations based on the whole analytical dataset and can become a powerful tool in geochemical studies.

# 7

# Clinopyroxene and amphibole crystal populations in a lamprophyre sill: a record of magma history and a window to mineral-melt partitioning

**SUMMARY**

In this chapter the Cretaceous lamprophyre in Calella de Palafrugell is further investigated at the mineral-scale, as this small intrusion contains a large diversity of crystal populations. Detailed observation of clinopyroxene and amphibole macrocrysts and microcrysts reveals complex zoning patterns that correlate with unexpected compositional changes. Major and trace element concentrations record the involvement of different melts, processes and depths of crystallisation, providing the pieces necessary to reconstruct the complex magma history. Equilibrium conditions between minerals and melts are carefully evaluated and lead to the calculation of a consistent dataset of trace element partition coefficients for clinopyroxene and amphibole in camptonite melts.

*View from a window in the Monasterio de Sant Pere Cercada, northern Catalonian Coastal Ranges*

## 7.1. Introduction

Minerals respond texturally and compositionally to changing magmatic environments, so they can preserve in their crystal growth stratigraphy a wealth of information regarding their past history of magmatic processes and compositions (e.g., Streck, 2008 and references therein). Accordingly, investigations of mineral textures and compositional zoning from core to rim of the crystals provide a window to magmatic evolution including open-system processes such as magma mixing, contamination and recharge. This, linked to barometric studies (e.g., Aulinas et al., 2010; Putirka, 2008) makes it possible to reconstruct the whole magmatic plumbing system associated to volcanic and subvolcanic exposures.

There is an increasing awareness that mineral phases are commonly not in equilibrium with their host glass/groundmass (e.g., Davidson et al., 2007). Large crystals in porphyritic rocks, which have traditionally been referred to as phenocrysts, can be shown in many cases to be antecrysts, a term introduced recently to denote phases that did not crystallise from the magma in which they are now contained, but rather were recycled from earlier stages of the same magma system (Charlier et al., 2005, 2007; Davidson et al., 2007; Francalanci et al., 2012; Gill et al., 2006; Hildreth and Wilson, 2007; Jerram and Martin, 2008). It follows that many apparently simple porphyritic rocks can actually contain heterogeneous crystal populations sampled and accumulated from disparate crystallisation levels in the pathway of the ascending magma (e.g., Shane and Smith, 2013; Walker et al., 2013). Importantly, the entrainment of a crystal cargo affects significantly the bulk composition of the rock, obscuring the identification of magmatic processes (Larrea et al., 2013; Sakyi et al., 2012; Ubide et al., 2012*a*; see also Chapters 5 and 6 in this volume). It is therefore necessary to check the equilibrium state between minerals and melt and complement bulk-rock compositions with detailed mineralogical studies.

Assessment of mineral-melt equilibrium is crucial for the investigation of trace element partitioning as well. For this reason, most partition coefficients *D* between mineral and melt (where *D* represents concentration ratios; Beattie et al., 1993) have been calculated from experimentally crystallised phases (e.g., Adam and Green, 2006; Bottazzi et al., 1999; Dalpé and Baker, 2000; Hart and Dunn, 1993; Hauri et al., 1994; LaTourrette et al., 1995; Tiepolo et al., 2000, 2001). *D* values are strongly dependant on the composition of the melt and also on the pressure and temperature conditions (e.g.; Adam and Green, 1994; Blundy and Wood, 2003; Hill et al., 2011) and the experimental approach provides an accurate control of these parameters. Some authors, however, warn that applying experimentally determined partition coefficients to natural rock systems can be problematic (Francis and Minarik, 2008; Fulmer et al., 2010; Thompson and Malpas, 2000). The difficulties, coupled with great improvements in analytical techniques, have

triggered a reappraisal of studies on naturally occurring phenocryst-melt pairs, provided that mineral-melt equilibrium conditions are assured (Fulmer et al., 2010). *D* values are required for quantitative modelling of magmatic processes. While there is significant data available for basaltic systems, very little studies have focused on lamprophyre melts (Foley et al., 1996; Irving and Frey, 1984; Orejana et al., 2004).

Alkaline lamprophyre magmas were emplaced as sills of camptonite during the Late Cretaceous in what today constitutes the Catalonian Coastal Ranges in northeast Iberia (Solé et al., 2003; Ubide et al., 2012*a*, under review *a*; see Chapters 3 and 5 in this volume). A particularly interesting sill crops out in the vicinity of Calella de Palafrugell, by the Mediterranean shoreline (UTM: 31T 515127 4636865; see Ubide et al., 2012*a* or Chapter 6 for details). This sill is thin (< 0.5 m) and porphyritic, including macrocrysts of clinopyroxene and amphibole with complex zoning patterns, and represents a natural laboratory for the study of mineral-melt equilibrium and open-system magmatic evolution. In the preceding chapter, the petrological zoning of the sill was unravelled to be due to the uneven accumulation of macrocrysts (antecrysts). Moreover, the bulk composition of the groundmass was calculated with geochemical modelling. In the present chapter, a deep compositional and barometric study of clinopyroxene and amphibole is carried out to gain insights into the feeding magmatic system as well as to investigate mineral-melt trace element partitioning in alkaline lamprophyres.

## 7.2. Methodology

The whole section of the sill was sampled and then sliced using a diamond disc saw to obtain five samples, named 1 to 5 from bottom to top of the sill (see Fig. 6.2A). For the sake of simplicity, sample names used in the preceding and this chapter are 1, 2, 3, 4 and 5 instead of CAL-1, CAL-2, CAL-3, CAL-4 and CAL-5, respectively. Polished thin sections were prepared at the *Servicio General de Apoyo a la Investigación-SAI*, Universidad de Zaragoza (Spain). First, a detailed petrographic study was carried out. Then, mineral major and trace elements where determined with *in situ* spot analyses.

Major element compositions were determined by electron microprobe (EMP) at the *Centro Nacional de Microscopía Electrónica* of the Universidad Complutense de Madrid (Spain), using a JEOL JZA-8900M electron microprobe equipped with four wavelength dispersive spectrometers. Analyses were performed using an accelerating voltage of 15 kV and an electron beam current of 20 nA, with a beam diameter of 5 µm. Elemental counting times were 10 s on the peak and 5 s on each of two background positions. Corrections for inter-elemental effects were made using a ZAF (Z: atomic number; A: absorption; F: fluorescence) procedure.

Trace element concentrations were determined by laser ablation ICP-MS (LA-ICP-MS) at the *Centro de Instrumentación Científica-CIC* of the Universidad de Granada (Spain), using a 213 µm Mercantek Nd-YAG laser coupled to a quadrupolar Agilent 7500 ICP-MS with a shielded plasma torch. The ablation was carried out in a He atmosphere, using a laser beam with a diameter fixed at 80 µm, a repetition rate of 10 Hz and an output energy of 0.3 mJ per pulse. The spot was preablated for 45 s using a laser output energy of 50 %. The spot was then ablated for 60 s with a laser output energy of 70 %. NIST-610 glass was employed as an external standard. Concentration values were corrected using the silicon concentrations obtained by electron microprobe as an internal standard. Further details on technical methods can be found in Bea et al. (2005). Data reduction was carried out by the *CIC* laboratory staff.

Curve fittings of the calculated mineral-melt partition coefficients to the lattice strain model by Blundy and Wood (1994) were obtained with the TableCurve 2D version 5.0.1 software. Statistical treatment of data (principal component analysis) was undertaken using the PAST software (Hammer et al., 2001).

## 7.3. Results

### 7.3.1. Petrography

The lamprophyre is classified as a camptonite according to criteria by Le Maitre (2002). It is hypocrystalline and porphyritic, with large mafic crystals set in a fine-grained groundmass (see Fig. 6.2C, 6.2D). Most large crystals are clinopyroxene and amphibole, with an average crystal size of 3 mm. There are also opaque minerals and olivine pseudomorphs, with an average crystal size of 1 mm. For the moment, the large crystals will be described with the purely descriptive term “macrocryst”. Clinopyroxene and amphibole macrocrysts sometimes cluster together or with opaque minerals into glomerocrysts. Occasional quartz xenocrysts are also found. The groundmass on the other hand, is composed of “microcrysts”. Most of the microcrysts are acicular microlites of amphibole and plagioclase. They are smaller than 50 µm at the margins of the sill and increase in size up to ca. 300 µm towards the centre of the sill. The groundmass also contains scarce, prismatic microphenocrysts of clinopyroxene and amphibole, up to 500 µm in size. Opaque minerals, minor K-feldspar, accessory apatite and glass complete the groundmass mineral assemblage. Vesicles are common, especially in samples belonging to the margins of the sill, and they are mainly filled with calcite.

Clinopyroxene and amphibole are the main constituents of the rock and the only minerals showing complex zoning patterns. Clinopyroxene is the principal macrocryst phase, reaching ca. 15 % volume fraction of the rock in the centre of the sill (see Table 6.1).

Clinopyroxene macrocrysts show complexly zoned subhedral to anhedral cores and in some cases, aligned sulphide inclusions in the inner zones. They are overgrown by a thin euhedral rim. Under plane-polarised transmitted light, clinopyroxene macrocrysts are pale-pink in colour. Moreover, a pale-green anhedral core has been observed; it presents resorption features (it is corroded and displays an engulfed irregular contour) and is mantled by pale-pink clinopyroxene. Clinopyroxene is also present in the groundmass of the rock as euhedral to subhedral microphenocrysts. These are pale-pink in colour and show a slight optical zoning.

Amphibole is brown coloured and makes up three different crystal groups. Firstly, amphibole macrocrysts reach ca. 10 % volume fraction of the rock in the centre of the sill (see Table 6.1). They show subhedral cores and thin euhedral rims. Although the cores are generally unzoned, in certain macrocrysts dark brown, anhedral and rounded inner cores are observed. Secondly, amphibole microphenocrysts are observed in the groundmass. They are euhedral to subhedral crystals with a slight optical zoning. Finally, unzoned microlites of amphibole are the commonest mafic component of the groundmass.

### 7.3.2. Major element composition: EMP results

More than 300 EMP major element analyses were obtained from the different populations of clinopyroxene and amphibole crystals. They can be found in Tables 7.I and 7.II of the electronic supplement. There are significant compositional variations among different crystal types and within single crystals. The extensive dataset and back-scattered electron (BSE) images have served to investigate the zoning patterns recognised in the petrographic study. The obtained compositional types are summarised in Table 7.1. This table includes acronyms and colours used hereafter. Composition of other mineral constituents or bulk-rock can be found in Ubide et al. (2012*a*) and Chapters 5 and 6 in this volume.

*Clinopyroxene*

Clinopyroxene is classified as diopside according to criteria by Morimoto et al. (1988). It is rich in $TiO_2$, $Al_2O_3$ and CaO, up to ca. 5 wt. %, 11 wt. % and 24 wt. % respectively, and poor in $Cr_2O_3$, always below 0.1 wt. % (see Table 7.I of the electronic supplement).

Fig. 7.1 shows compositional profiles obtained across three macrocrysts and one microphenocryst. Macrocryst cores show complex compositional variations correlating with the optical zoning (Fig. 7.1A, 7.1B). There are four compositional types within macrocryst cores, named as A1, A2, A3 and P. They are ordered based on crystal

**Table 7.1.** Summary of clinopyroxene (Cpx) and amphibole (Amp) compositional types in the lamprophyre studied.

| Mineral | Type | Macrocrysts | Microphenocrysts | Microlites | Habit | Mg# range |
|---|---|---|---|---|---|---|
| Cpx | X1 | Core | | | Anhedral | 52-48 |
| | X2 | Core | | | Anhedral | 53-50 |
| | A1 | Core | | | Subhedral | 55-51 |
| | A2 | Core | | | Anhedral | 60-54 |
| | A3 | Core | | | Subhedral | 65-61 |
| | **P** | **Core** | | | **Subhedral** | **70-66** |
| | | | **Core** | | | **70-64** |
| | R | Rim | | | Euhedral | 67-59 |
| | | | Inner Rim | | | 66-61 |
| | | | Outer Rim | | | 62-54 |
| Amp | K | Core | | | Anhedral | 54-48 |
| | **P** | **Core** | | | **Subhedral** | **61-55** |
| | | | **Core** | | | **60-57** |
| | R | Rim | | | Euhedral | 57-49 |
| | | | Rim | | | 57-48 |
| | | | | Microlite | | 57-45 |

Mg# represents magnesium number: 100 MgO / (MgO + total iron as FeO) in wt. % oxides.
Microphenocrysts and Microlites belong to the groundmass of the rock.
Cpx-P and Amp-P (marked in bold) are the only compositions in equilibrium with the bulk composition of the groundmass (see discussion).

stratigraphy, so that A1 crystallised first, followed by A2, A3 and finally P. In some cases, A1-type cores show aligned sulphide inclusions representing droplets of immiscible sulphide liquids adhering to the surfaces of rapidly growing silicate crystals (Ubide et al., 2012*a* and references therein). From A1 to P, compositions are progressively richer in magnesium number (Mg# = 100 MgO / (MgO + total iron as FeO)) and $SiO_2$, poorer in $Al_2O_3$, $Na_2O$ and total iron as FeO ($FeO^T$) and roughly constant for $TiO_2$. Macrocryst cores are frequently overgrown by a thin rim (zone R). Compared to P, R compositions have lower concentrations in Mg# and $SiO_2$, higher concentrations in $TiO_2$, $Al_2O_3$ and $FeO^T$ and similar concentrations in $Na_2O$ (Fig. 7.1B). Regarding the green-coloured core recognised in the petrographic study, it is significantly enriched in $SiO_2$, $Na_2O$, $FeO^T$ and MnO and depleted in Mg#, $TiO_2$ and $Al_2O_3$ compared to the other clinopyroxene compositions; it has been named as X1 (Fig. 7.1C). The green core is intensely resorbed and replaced with a pale-pink core (X2) compositionally similar to A1-type cores. An R-type rim overgrows both X1 and X2 compositions (Fig. 7.1C). Finally, compositional profiles across groundmass microphenocrysts reveal two different zones that correlate with the core and rim of the crystal (Fig. 7.1D). The core is compositionally equivalent to the final crystallisation zone in macrocryst cores (P-type). The rim is R-type, with decreasing Mg# and $SiO_2$ and increasing $TiO_2$, $Al_2O_3$ and $FeO^T$ towards the edge of the crystal. $Na_2O$ contents are similar in the core and rim (Fig. 7.1D) as well as in P- and R-type zones in macrocrysts (e.g., Fig. 7.1B). The main textural and compositional characteristics of the different compositional types are summarised Table 7.1.

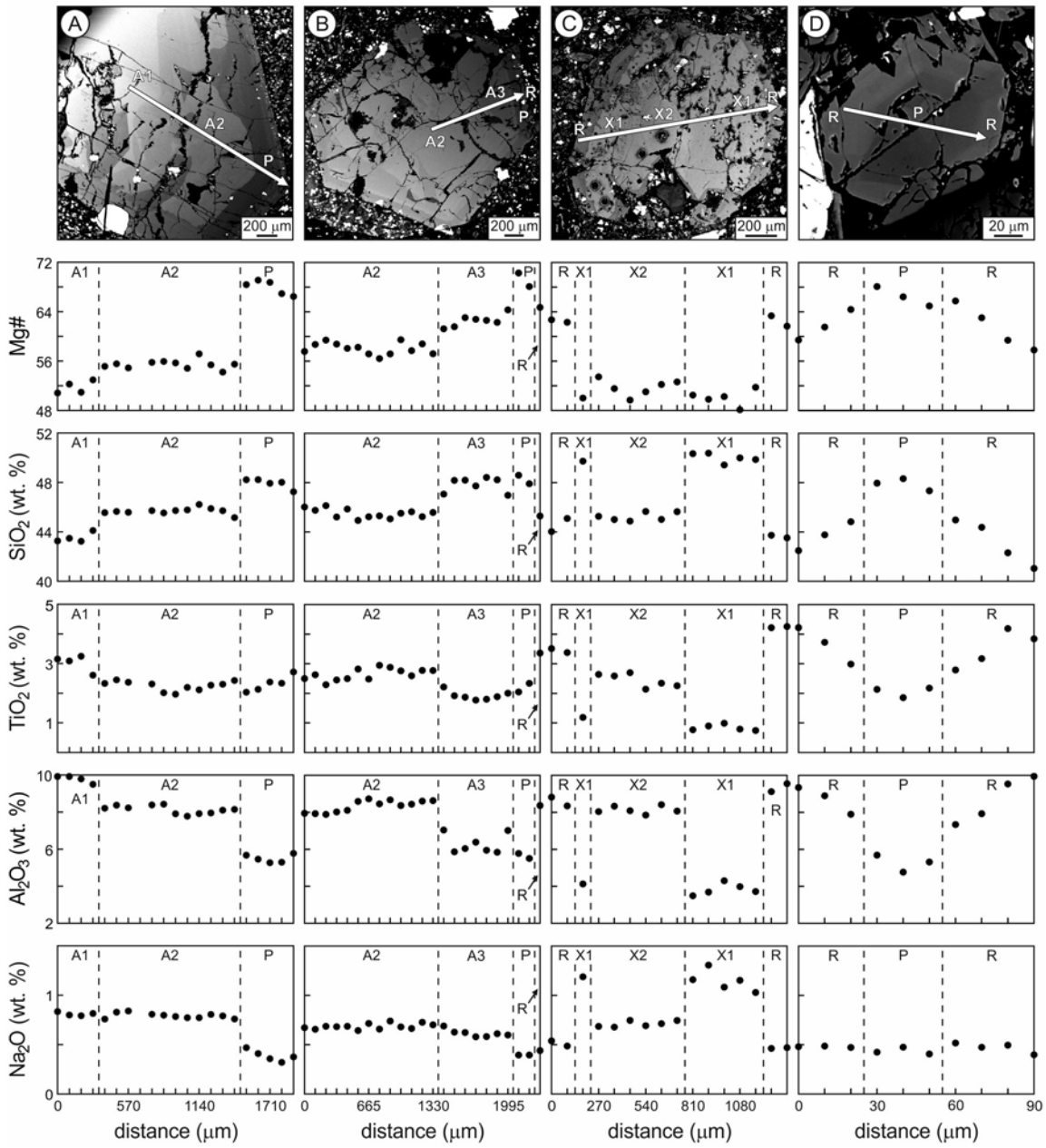


**Fig. 7.1.** Major element compositional profiles across clinopyroxene crystals. Note the complex zoning patterns in the BSE images, with different compositions as summarised in Table 7.1. A-B) Macrocrysts. C) Macrocryst with a green, corroded area in the core; note the laser pits for trace element analysis. D) Microphenocryst.

All clinopyroxene analyses were plotted together in bivariate diagrams against decreasing Mg#. Representative diagrams are presented in Fig. 7.2. The compositional types defined on the basis of profiles across individual crystals (Fig. 7.1) are best differentiated considering the whole dataset (Fig. 7.2). The green core (X1) shows a distinct, extreme composition, whereas the remaining core of the crystal (X2) shows a composition similar to A1. The rest of analyses arrange in two variation trends with different slopes that merge together in P compositions. On the one hand, A1, A2 and A3 macrocryst cores are progressively richer in Mg# and constitute a trend of increasing $SiO_2$ and decreasing $Al_2O_3$,

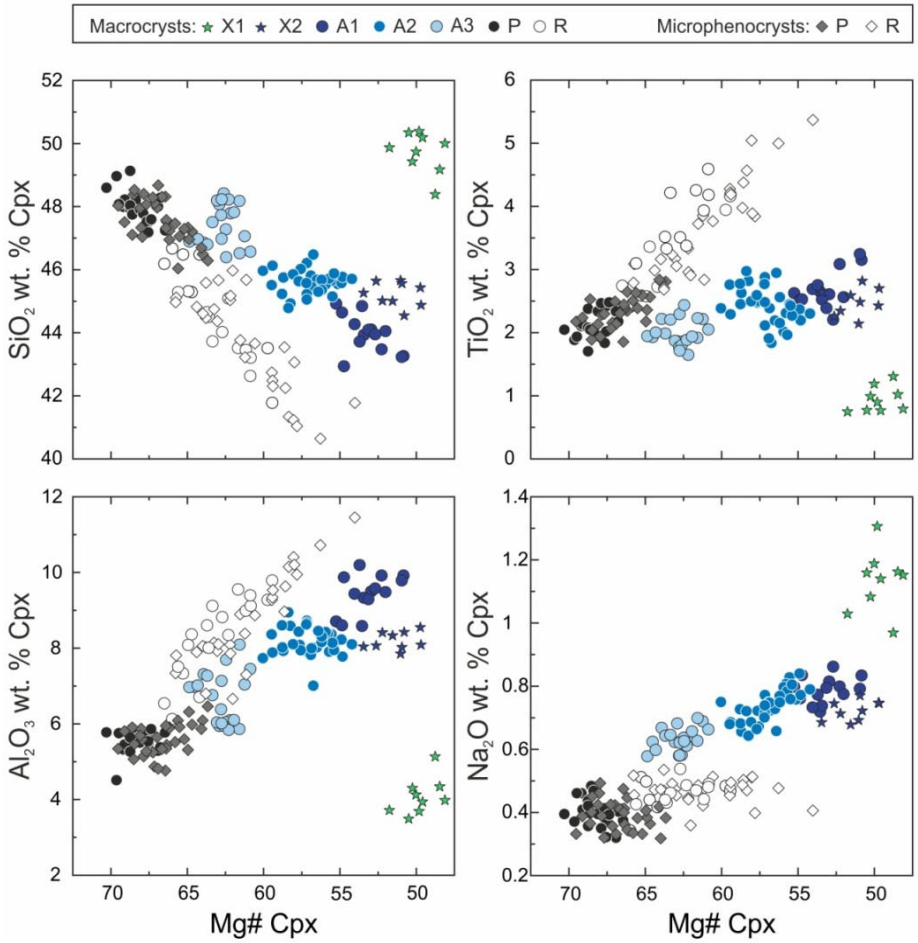


**Fig. 7.2.** Major element variation diagrams for clinopyroxene in the studied lamprophyre. Legend at the top.

$Na_2O$ and $FeO^T$ with increasing Mg#, towards P compositions; in this variation trend $TiO_2$ concentrations are low and fairly constant. On the other hand, P compositions in macrocryst cores and microphenocryst cores and R compositions (macrocryst rims and microphenocryst rims) make up a different trend of decreasing $SiO_2$ and increasing $TiO_2$, $Al_2O_3$ and $FeO^T$ with decreasing Mg#; in this variation trend $Na_2O$ contents are fairly constant and lower than in A-type and X-type macrocryst cores.

*Amphibole*

Amphibole is classified as kaersutite according to criteria by Leake et al. (1997). $TiO_2$ contents reach more than 7 wt. %, with $SiO_2$ contents down to ca. 35 wt. % (see Table 7.II of the electronic supplement).

Fig. 7.3 shows compositional profiles obtained across two macrocrysts, one microphenocryst and one microlite. Macrocryst cores are generally unzoned and have slightly higher concentrations in Mg#, $SiO_2$ and $K_2O$ and slightly lower concentrations in $TiO_2$, $Al_2O_3$, $FeO^T$ and $Na_2O$ than macrocryst rims; core compositions have been named as

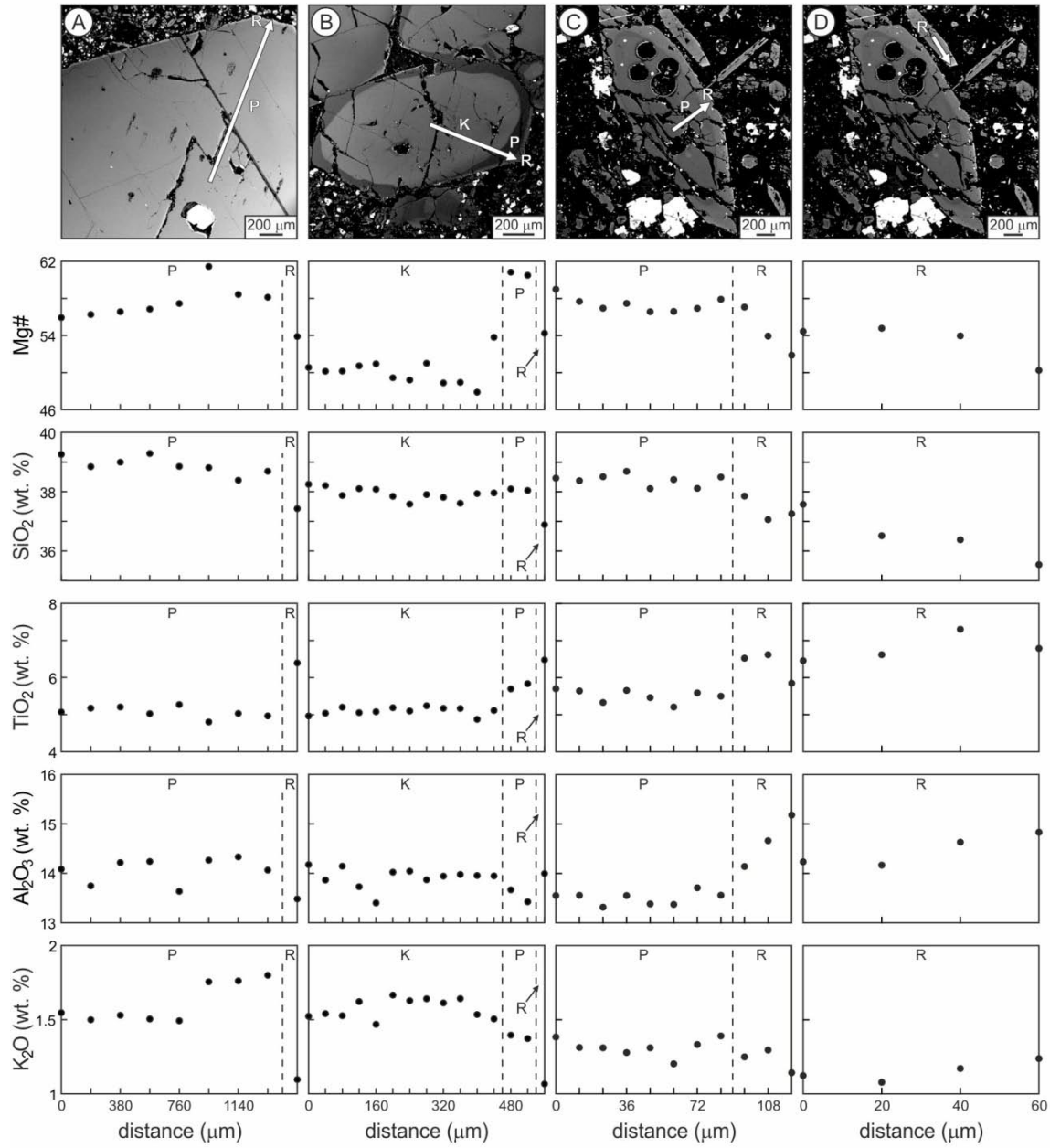


**Fig. 7.3.** Major element compositional profiles across amphibole crystals. Note the complex zoning patterns in the BSE images, with different compositions as summarised in Table 7.1. A) Macrocryst. B) Macrocryst with a rounded inner core. C) Microphenocryst; note the laser pits for trace element analysis. D) Microlite.

P and rim compositions as R (Fig. 7.3A) following the same criterion as in clinopyroxene. There are certain crystals however, with rounded inner cores as recognised under the petrographic microscope. The inner cores show a distinct composition (zone K; Fig. 7.3B) with lower contents in Mg#, higher contents in $FeO^T$ and similar contents in $SiO_2$, $TiO_2$, $Al_2O_3$, $K_2O$ and $Na_2O$ compared to P-type cores. K-type cores are mantled by P-type compositions, overgrown by R-type rims (Fig. 7.3B). In the groundmass of the sill, amphibole microphenocrysts are slightly zoned with P-type cores and R-type rims (Fig. 7.3C). Amphibole microphenocrysts therefore show a zoning pattern equivalent to that of most macrocrysts (e.g., Fig. 7.3A). Finally, microlites display a fairly constant R-type

composition across the crystal (Fig. 7.3D). The main textural and compositional characteristics of the different compositional types are summarised Table 7.1.

All amphibole analyses were plotted together in bivariate diagrams against decreasing Mg#. Representative diagrams are presented in Fig. 7.4. The compositional types defined on the basis of profiles across individual crystals (Fig. 7.3) are best differentiated considering the whole dataset (Fig. 7.4). From among the macrocryst cores, inner cores (K) have lower Mg# contents and higher $FeO^T$ contents than P-type cores; both compositional types are roughly equal for $SiO_2$, $TiO_2$, $Al_2O_3$, $K_2O$ and $Na_2O$. P compositions (macrocryst cores and microphenocryst cores) followed by R compositions (macrocryst rims, microphenocryst rims and microlites) constitute a common variation trend of decreasing $SiO_2$ and increasing $TiO_2$, $Al_2O_3$ and $FeO^T$ with decreasing Mg#. This trend is therefore similar to that of P-R compositions in clinopyroxene (compare with Fig. 7.2); in the case of amphibole however, R compositions are more scattered and hence the trend is less well defined than in the case of clinopyroxene. Finally, it is noteworthy that macrocryst cores (both K- and P-types) reach higher concentrations in $K_2O$ and lower contents in $TiO_2$ than microphenocryst cores (P), rims and microlites (R).

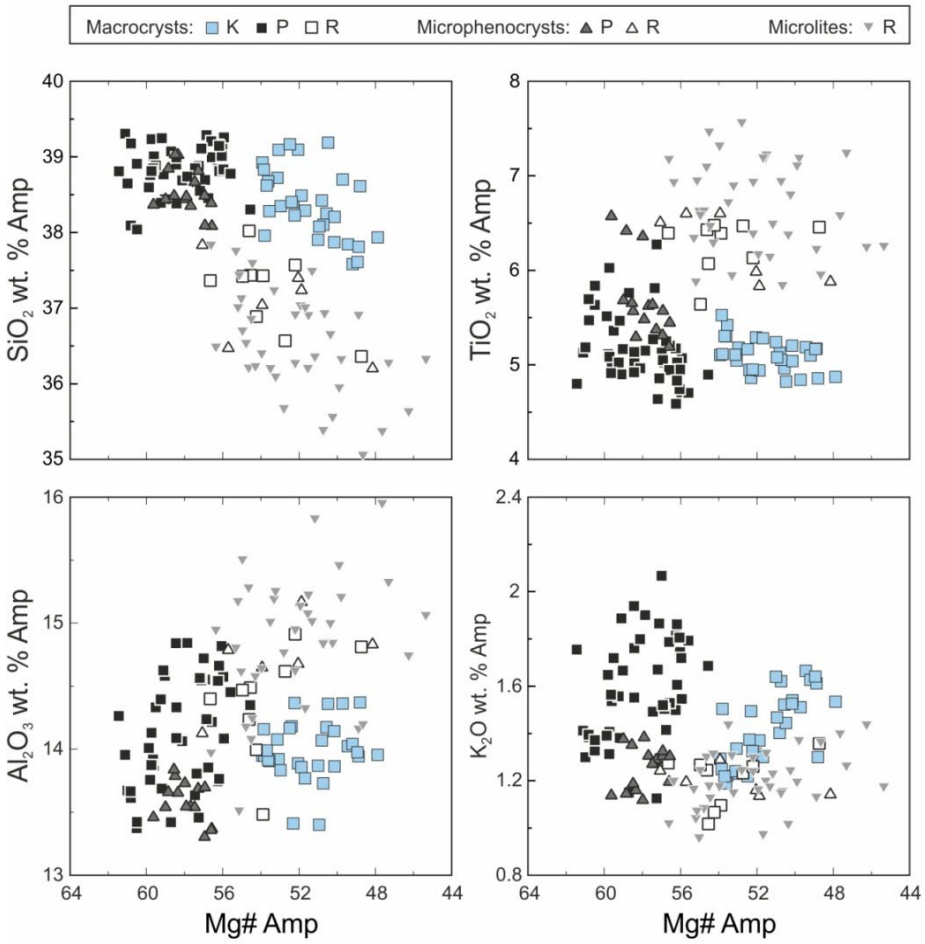


**Fig. 7.4.** Major element variation diagrams for amphibole in the studied lamprophyre. Legend at the top.

### 7.3.3. Trace element composition: LA-ICP-MS results

Clinopyroxene and amphibole were analysed with LA-ICP-MS for concentrations in trace elements. Macrocryst and microphenocryst cores were analysed; their rims, as well as amphibole microlites, were too small to provide reliable spot analyses. The results are presented in Table 7.2. Regarding clinopyroxene macrocrysts, an A1-type zone was analysed given that it represents the beginning of the variation trend of macrocryst cores (Fig. 7.2). The green macrocryst core, which shows a very extreme composition in major elements (Fig. 7.2), was analysed as well; two analyses were carried out in the green area of the core (X1) and another one in the pale-pink area (X2), which is similar to A1-type cores in major elements (Fig. 7.2). Concerning the crystals from the groundmass, the core of a microphenocryst (P) was analysed. In the case of amphibole, the K-type inner core and the P-type core from a macrocryst were analysed. Furthermore, the core of a microphenocryst (P) was analysed; it was large enough to carry out two analyses in order to double-check results. The trace element composition of the groundmass is constant across the sill and best obtained by geochemical modelling (Ubide et al., 2012*a* –see Chapter 6-). Still, LA-ICP-MS analyses of the groundmass were undertaken in samples from the lower chilled margin and the centre of the sill (samples 1 and 3) to support previous data. The results are presented in Table 7.2, which also contains the composition calculated by modelling. Primitive mantle (McDonough and Sun, 1995) normalised trace element patterns are presented in Fig. 7.5.

Rare Earth Element (REE) concentrations in clinopyroxene are 4 to 50 times enriched over the primitive mantle (Fig. 7.5A). REE normalised patterns are convex-upwards except for the green core (X1), which presents convex-downwards patterns. Despite having different major element compositions, A1 and P are coincident in REE. On the contrary, X2 shows a parallel but more enriched REE normalised pattern. Considering more trace elements (Fig. 7.5B), X1 again shows a distinct normalised pattern from the rest of compositions. All the analyses however, display a negative anomaly for Sr and low concentrations in Rb and Ba, significantly below the primitive mantle in X1 and X2. Finally, the multielemental patterns of A1 and P show small differences, not reflected in the REE patterns alone.

Amphibole is up to 30 times enriched over the primitive mantle for the REE (Fig. 7.5C). REE normalised patterns are convex-upward and fairly parallel to each other. They are similar to those of pale-pink clinopyroxene (compare with Fig. 7.5A). Amphibole macrocryst cores are slightly less enriched in REE than amphibole microphenocryst cores, irrespective of the compositional type. For instance, the P-type core of a macrocryst is less enriched than the P-type core of a microphenocryst. Multielemental normalised patterns (Fig. 7.5D) are fairly parallel with slight differences between macrocryst and microphenocryst cores as well. All the normalised patterns show a strong negative

**Table 7.2.** Trace element compositions obtained by LA-ICP-MS on clinopyroxene cores (Cpx), amphibole cores (Amp) and groundmass (Gr).

| Phase | Cpx | | | | | Amp | | | | Gr | | Gr [a] |
|---|---|---|---|---|---|---|---|---|---|---|---|---|
| | Macrocrysts | | | | Microp. | Macrocryst | | Microp. | | | | |
| Type | X1 | X1 | X2 | A1 | P | K | P | P (I) | P (II) | | | |
| Sample | 3 | 3 | 3 | 1 | 3 | 1 | 1 | 3 | 3 | 1 | 3 | modelled |
| Rb | 0.22 | 0.00 | 0.04 | 0.37 | 2.16 | 7.46 | 7.31 | 8.68 | 8.43 | 33.23 | 43.24 | 57.15 |
| Cs | 0.00 | 0.00 | 0.02 | 0.01 | 0.31 | 0.00 | 0.04 | 0.06 | 0.00 | 1.78 | 2.86 | 1.32 |
| Be | 2.70 | 2.87 | 1.69 | 0.77 | 0.89 | 0.44 | 0.37 | 0.64 | 0.84 | 2.12 | 2.79 | 2.35 |
| Sr | 76.43 | 94.55 | 144.79 | 123.28 | 104.81 | 551.50 | 611.71 | 996.95 | 1102.21 | 576.37 | 916.28 | 891.18 |
| Ba | 0.05 | 0.36 | 0.37 | 4.17 | 5.71 | 426.56 | 486.74 | 746.22 | 867.65 | 442.39 | 741.49 | 597.89 |
| V | 183.84 | 175.15 | 297.29 | 308.26 | 268.98 | 348.82 | 336.23 | 532.37 | 525.26 | 235.10 | 405.97 | 369.86 |
| Cr | 0.00 | 6.84 | 3.11 | 0.81 | 0.00 | 103.03 | 269.99 | 1.75 | 2.47 | 36.03 | 1.45 | 12.77 |
| Co | 12.34 | 12.79 | 18.36 | 23.24 | 29.52 | 39.00 | 39.98 | 59.89 | 65.31 | 50.74 | 35.44 | 44.50 |
| Ni | 0.12 | 0.11 | 0.13 | 0.84 | 15.48 | 13.30 | 40.00 | 26.85 | 41.46 | 14.65 | 13.38 | 31.48 |
| Cu | 0.18 | 0.31 | 1.42 | 0.93 | 0.78 | 2.42 | 1.31 | 11.74 | 41.50 | 61.12 | 8.65 | 72.67 |
| Zn | 221.48 | 205.20 | 91.70 | 64.74 | 38.37 | 71.18 | 64.39 | 64.03 | 63.39 | 95.48 | 183.75 | 182.21 |
| Ga | 13.95 | 14.75 | 23.79 | 18.09 | 13.46 | 32.51 | 34.04 | 84.36 | 93.71 | 37.91 | 88.47 | 23.96 |
| Y | 15.89 | 14.51 | 40.64 | 23.19 | 24.12 | 13.40 | 11.44 | 24.54 | 26.40 | 19.94 | 32.30 | 30.46 |
| Nb | 0.66 | 0.88 | 2.36 | 1.16 | 4.89 | 15.48 | 13.47 | 26.46 | 29.78 | 56.98 | 83.65 | 73.86 |
| Ta | 0.03 | 0.08 | 0.63 | 0.26 | 0.30 | 0.90 | 0.82 | 1.83 | 2.01 | 3.13 | 4.36 | 5.65 |
| Zr | 313.72 | 311.01 | 341.01 | 157.66 | 205.49 | 61.85 | 61.55 | 131.59 | 141.08 | 206.84 | 462.11 | 301.07 |
| Hf | 9.65 | 9.58 | 13.87 | 6.80 | 9.38 | 2.58 | 2.34 | 5.21 | 5.61 | 4.74 | 11.94 | 6.94 |
| Pb | 0.10 | 0.16 | 0.01 | 0.45 | 1.83 | 1.59 | 1.38 | 0.37 | 2.37 | 12.45 | 11.78 | 10.24 |
| U | 0.00 | 0.00 | 0.03 | 0.03 | 0.27 | 0.09 | 0.06 | 0.03 | 0.01 | 1.68 | 1.56 | 1.70 |
| Th | 0.00 | 0.07 | 0.20 | 0.13 | 0.23 | 0.12 | 0.14 | 0.09 | 0.12 | 4.64 | 5.61 | 5.79 |
| La | 26.24 | 23.71 | 21.23 | 10.74 | 10.41 | 6.96 | 6.68 | 13.11 | 15.20 | 52.52 | 58.62 | 57.21 |
| Ce | 63.32 | 56.63 | 73.39 | 38.76 | 37.75 | 29.35 | 21.54 | 40.37 | 45.90 | 117.80 | 125.78 | 123.63 |
| Pr | 6.78 | 6.18 | 12.47 | 6.75 | 6.09 | 4.58 | 3.46 | 6.69 | 7.51 | 12.94 | 15.11 | 14.90 |
| Nd | 24.68 | 21.91 | 69.75 | 37.60 | 34.97 | 22.75 | 18.97 | 39.03 | 45.03 | 55.75 | 76.44 | 58.58 |
| Sm | 4.00 | 3.69 | 17.30 | 9.82 | 9.84 | 6.41 | 5.18 | 9.68 | 11.65 | 10.50 | 15.35 | 10.87 |
| Eu | 0.66 | 0.95 | 5.40 | 3.12 | 3.29 | 1.94 | 1.62 | 3.32 | 3.88 | 3.18 | 4.19 | 3.25 |
| Gd | 2.85 | 2.47 | 13.95 | 7.55 | 8.00 | 4.19 | 4.16 | 8.34 | 9.15 | 6.76 | 11.16 | 8.73 |
| Tb | 0.44 | 0.37 | 1.95 | 1.13 | 1.25 | 0.54 | 0.64 | 1.18 | 1.21 | 0.75 | 1.36 | 1.18 |
| Dy | 2.49 | 2.33 | 10.53 | 6.16 | 6.23 | 3.10 | 2.67 | 5.66 | 6.73 | 4.26 | 7.47 | 6.22 |
| Ho | 0.55 | 0.51 | 1.82 | 1.02 | 1.07 | 0.54 | 0.45 | 1.02 | 1.12 | 0.77 | 1.16 | 1.08 |
| Er | 1.68 | 1.57 | 4.31 | 2.44 | 2.61 | 1.40 | 1.08 | 2.27 | 2.57 | 1.87 | 2.61 | 2.77 |
| Tm | 0.32 | 0.26 | 0.57 | 0.31 | 0.35 | 0.17 | 0.14 | 0.29 | 0.34 | 0.28 | 0.37 | 0.37 |
| Yb | 2.46 | 2.35 | 3.14 | 1.77 | 1.75 | 0.99 | 0.62 | 1.52 | 1.63 | 1.54 | 1.93 | 2.32 |
| Lu | 0.43 | 0.55 | 0.42 | 0.25 | 0.29 | 0.12 | 0.07 | 0.18 | 0.23 | 0.22 | 0.27 | 0.35 |

([a]): Groundmass composition of the sill calculated by geochemical modelling in Ubide et al. (2012*a*; see "Mean $C_{Gr}$" in Table 6.3, Chapter 6 of this volume).
(I) (II) in order to differentiate two spot analyses on the core of a single microphenocryst.

anomaly for the U-Th pair and the highest normalised values for Ba. The two analyses obtained from a microphenocryst core yield almost equal compositions (Fig. 7.5C, 7.5D).

The groundmass of the sill is ca. 4 to more than 100 times enriched over the primitive mantle for all the trace elements in normalised diagrams (Fig. 7.5E, 7.5F). It shows a rightwards-descending normalised pattern for the REE and the highest normalised values for the Nb-Ta pair, as typical of alkaline rocks. The modelled composition shows an intermediate concentration value between the two spot analyses for most elements (Fig. 7.5E, 7.5F; see also Table 7.2). Moreover, the modelled composition has normalised patterns more regular and closer in shape to bulk-rock compositions from the sill (see Fig. 6.5). It should also be noted that spot analyses cover groundmass areas without

microphenocrysts, whereas the modelled composition in Ubide et al. (2012*a* –see Chapter 6-) represents the whole groundmass, including microlites and (scarcer) microphenocrysts.

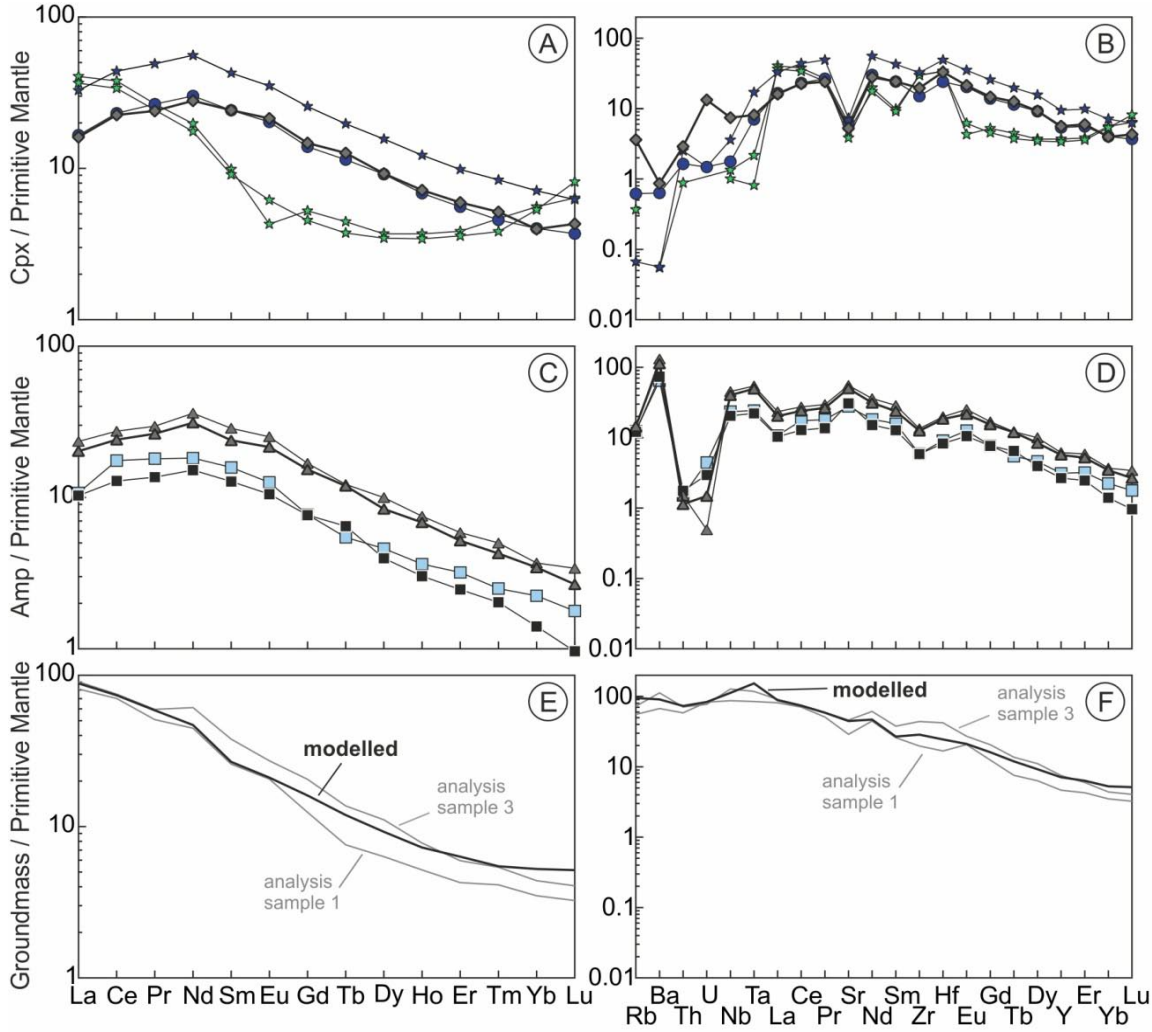


**Fig. 7.5.** Primitive mantle (McDonough and Sun, 1995) normalised trace element composition of clinopyroxene (A, B), amphibole (C, D) and groundmass (E, F). Normalised values below 0.01 were screened out. Legend for symbols is in Fig. 7.2 and 7.4. Thick lines highlight analyses used in the calculation of mineral-melt partition coefficients.

## 7.4. Discussion

### 7.4.1. Mineral-melt equilibrium: origin of clinopyroxene and amphibole crystal populations

Clinopyroxene and amphibole are the main constituents of the sill and make up heterogeneous crystal populations showing complex zoning patterns (Fig. 7.1, 7.3), with different compositions as summarised in Table 7.1. Understanding the genetic

relationship between the different compositional types and the melt is crucial for reconstructing magma history as well as studying mineral-melt partitioning.

Clinopyroxene is present as macrocrysts and groundmass microphenocrysts. Major element variations (Fig. 7.2), together with crystal stratigraphy recorded in zoning patterns, define two evolutionary trends: A1-A2-A3-P in macrocryst cores and P-R in groundmass crystals. P compositions represent the link between both trends and include the outermost zone of macrocryst cores as well as the core zone of groundmass microphenocrysts. R compositions include rims overgrowing macrocrysts and microphenocrysts. Only P-R compositions define an evolution that can be related to progressive fractionation of the groundmass magma, involving the decrease of Mg# with time from more primitive to more evolved compositions. The A1-A2-A3-P evolutionary record in macrocryst cores, in contrast, reveals an increase in Mg# with time. The transition between each zone suggests a mafic recharge event that would also explain the anhedral or subhedral habit of A-type cores. Therefore, A-type macrocryst cores did not crystallise directly from the magma that eventually formed the groundmass of the sill. Finally, the green macrocryst core (X1) displays a different composition (Fig. 7.2, 7.5A, 7.5B) and does not fit either of two evolutionary trends, suggesting an exotic origin. The remaining core of that particular macrocryst (X2) is similar to A1-type cores and thus can be included into the A1-A2-A3-P evolutionary trend.

Given that A-type macrocryst cores did not crystallise from the magma that eventually formed the groundmass of the sill, they cannot be considered “phenocrysts” in the genetic sense of the term. However, considering the small compositional differences with groundmass crystals (compare with P-R compositions in Fig. 7.2, 7.5A, 7.5B) their origin lies within the magmatic system. Therefore, these crystals are “antecrysts” (Charlier et al., 2005, 2007; Davidson et al., 2007; Francalanci et al., 2012; Gill et al., 2006; Hildreth and Wilson, 2007; Jerram and Martin, 2008; Larrea et al., 2013; Sakyi et al., 2012; Ubide et al., 2012*a*). P-R compositions on the other hand, are cogenetic with the groundmass magma and therefore P compositions can be considered true phenocrysts. They either nucleated new cores (microphenocryst cores) or mantled previous, A-type cores (P-type macrocryst cores). Note that even though macrocrysts are mainly composed of antecryst phases, this detailed compositional study reveals mantles of phenocryst material (P composition) in the outermost cores. Finally, the single green core recognised in the sill (X1) has a resorbed texture (Fig. 7.1C) and a composition significantly different from the rest (Fig. 7.2, 7.5A, 7.5B), so it probably crystallised from a magma unrelated to the magmatic system and was accidentally included as a xenocryst. It was first partially replaced with an antecryst composition (X2) and, once included in the groundmass magma, it was overgrown by an R-type rim.

Amphibole is present as macrocrysts as well as groundmass microphenocrysts and microlites. The composition of P-type macrocryst cores and microphenocryst cores is followed by the composition of macrocryst rims, microphenocryst rims and microlites in a common P-R fractionation trend where Mg# decreases with time, from more primitive to more evolved compositions (Fig. 7.4). P and R compositions therefore crystallised from the groundmass magma and P compositions are true phenocrysts. In contrast with clinopyroxene, P compositions in amphibole can constitute entire macrocryst cores. K compositions are found as inner cores in some macrocrysts and have a more evolved composition, with Mg# values lower than P-type cores. Therefore, a mafic recharge event is needed to explain the transition from K to P. This would also explain the anhedral, rounded habit of K-type inner cores. Given the compositional similarity of both types of macrocryst cores (Fig. 7.4, 7.5C, 7.5D), K-type inner cores most likely crystallised from a related progenitor magma, so they can be considered antecrysts.

To check mineral-melt equilibrium between mineral compositions and the melt that hosts them, equilibrium diagrams have been applied (Fig. 7.6; Rhodes et al., 1979). Mg# of the mineral is plotted against Mg# of the melt (calculated as 100 MgO / (MgO + FeO) and FeO = 0.9 $Fe_2O_3$) and the curves represent the range in which mineral and melt compositions are in equilibrium. The curves are calculated according to the iron-magnesium exchange coefficient for each mineral ($Kd_{Fe\text{-}Mg}^{mineral\text{-}melt}$), which is 0.26 ± 0.05 in the case of clinopyroxene (Akinin et al., 2005) and 0.38 in the case of amphibole (LaTourrette et al., 1995); to make results comparable, an error of ± 0.05 has been assumed in the latter case as well. It is common practice to use the whole rock composition of the sample containing the mineral as representative of the melt (Fig. 7.6A, 7.6B, 7.6D, 7.6E). However, Ubide et al. (2012*a* –see Chapter 6-) showed that bulk-rock compositions are affected by the presence and proportion of mafic antecrysts in the rock, implying that samples with a significant accumulation of antecrysts yield anomalously high Mg# values. This effect has also been recognised in other settings (e.g., Larrea et al., 2013; Sakyi et al., 2012). To dismiss the effect of the antecrysts, mineral compositions are plotted against the bulk composition of the groundmass in Fig. 7.6C and Fig. 7.6F. The major element composition of the groundmass is best represented by the whole rock composition of the upper chilled margin of the sill (sample 5), which contains a small volume fraction of antecrysts (Ubide et al., 2012*a* –see Chapter 6-).

As shown in Fig. 7.6, only P compositions plot within the equilibrium curves, both for clinopyroxene and amphibole. In detail, some P compositions plot slightly below the curves and therefore appear not to be in equilibrium with the melt (Fig. 7.6A, 7.6B, 7.6D, 7.6E). However, these compositions were analysed in samples with high Mg# contents due to antecryst accumulation.

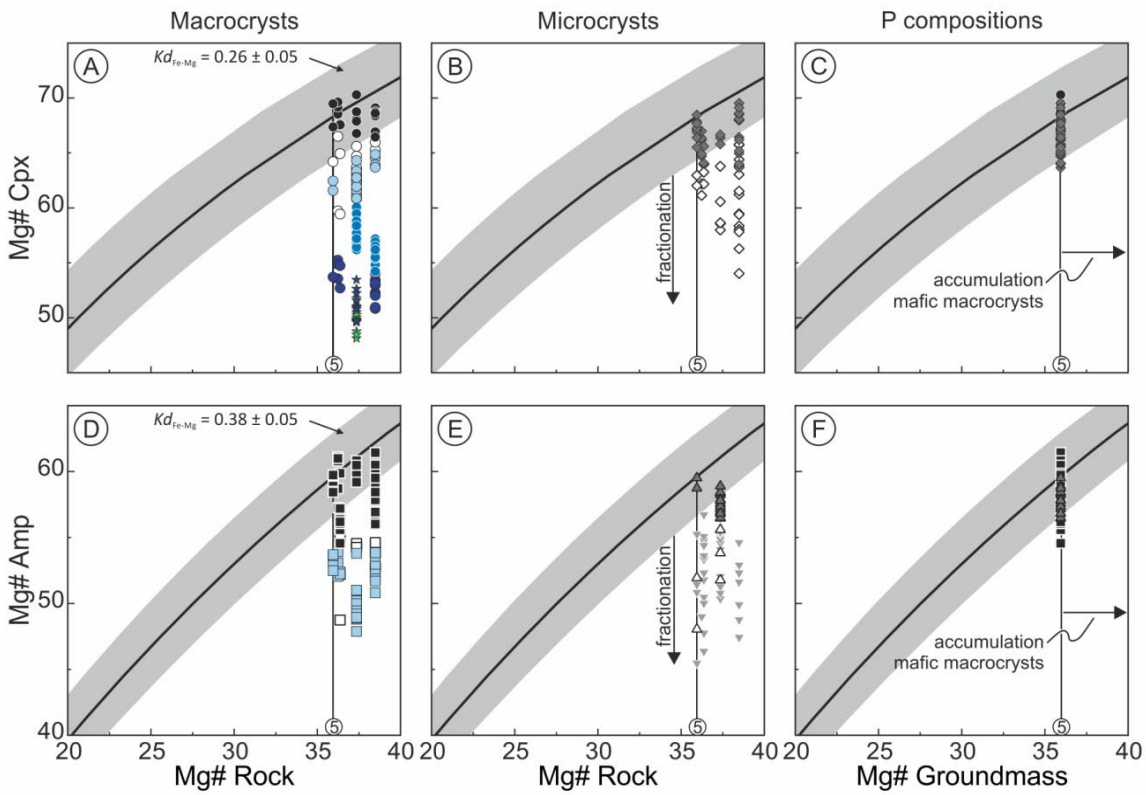


**Fig. 7.6.** Mineral-melt equilibrium diagrams for clinopyroxene (A, B, C) and amphibole (D, E, F). The curves represent the range in which mineral and melt compositions are in equilibrium based on iron-magnesium exchange (Rhodes et al., 1979). Legend for symbols is in Fig. 7.2 and 7.4. Whole rock compositions (*x* axes) are from Table 4.1. The whole rock composition of the upper chilled margin of the sill (sample 5) is marked as a reference in all the diagrams; the rest of whole rock compositions across the sill have higher Mg# values.

Considering the groundmass composition instead (Fig. 7.6C, 7.6F), P compositions plot within or very close to equilibrium, confirming they are true phenocryst phases. R compositions naturally fall below the equilibrium lines due to progressive fractionation of the magma. In contrast, xenocryst and antecryst compositions (X, A and K) are in clear disequilibrium with the melt and plot below the equilibrium curves given their low Mg# contents. In the case of clinopyroxene, A1 and X2 compositions are in equilibrium with melts of Mg# 20-25, A2 compositions with melts of Mg# ca. 25 and A3 compositions with melts of Mg# ca. 30, whereas X1 compositions are equilibrium with melts of Mg# ca. 20 (Fig. 7.6A). Meanwhile, K compositions in amphibole are in equilibrium with melts of Mg# 25-30 (Fig. 7.6D) with most analyses pointing towards the highest values of the range, in agreement with the melt in equilibrium with A3 compositions. It follows that amphibole antecrysts (K) and A3-type clinopyroxene antecrysts crystallised from a similar magma and could have a common origin. The lack of amphibole compositions in equilibrium with melts producing X1, X2, A1 and A2 clinopyroxene compositions, on the other hand, suggest lower contents in volatiles during the initial stages of crystallisation of clinopyroxene.

In conclusion, the mineral chemistry of the different crystal populations reveals a complex magma history despite the small thickness of the sill cropping out. X-, A- and K-type macrocryst cores represent inherited xenocryst and antecryst material incorporated into the magma that eventually crystallised as groundmass. Clinopyroxene antecrysts reveal several events of mafic recharge, whereas amphibole antecrysts crystallised before the last recharge event, probably related to an increase in the volatile content of the melt. Only P and R compositions are cognate with the groundmass magma. Among these, only P compositions are phenocrysts in equilibrium with the bulk composition of the groundmass (Fig. 7.6C, 7.6F).

### 7.4.2. Mineral-melt partitioning: calculation of trace element partition coefficients between clinopyroxene, amphibole and camptonite melt

Trace element partition coefficients (*D*) between mineral-melt equilibrium pairs are necessary for quantitative modelling of magmatic processes. *D* values are strongly dependant on the composition of the melt and also on the pressure and temperature conditions (e.g.; Adam and Green, 1994; Blundy and Wood, 2003; Hill et al., 2011) and most partitioning studies focus on basaltic melts under high *P-T* conditions relevant for partial melting in the mantle (e.g., Adam and Green, 2006; Bottazzi et al., 1999; Dalpé and Baker, 2000; Hart and Dunn, 1993; Hauri et al., 1994; McKenzie and O'Nions, 1991; LaTourrette et al., 1995; Sun and Liang, 2012; Tiepolo et al., 2001; Yao et al., 2012). There are scarce data however, available for alkaline lamprophyre melts (Foley et al., 1996; Orejana et al., 2004). Moreover, some datasets were obtained long ago and lack elements relevant for petrogenesis. In addition, calculation of consistent datasets including several minerals in equilibrium is often not possible.

In the studied lamprophyre P-type clinopyroxene and amphibole are in equilibrium with the bulk composition of the groundmass (Fig. 7.6C, 7.6F). Under this premise, a set of consistent mineral-melt partition coefficient data can be calculated with trace element compositions analysed by LA-ICP-MS. P compositions occur in some macrocryst cores and as microphenocryst cores. To avoid chemical diffusion effects with antecrysts, as well as the possible effects of crystallisation under different conditions, microphenocrysts have been used. They are unaltered and inclusion-free, and despite being zoned into core and rim, the core area has been considered as it is compositionally homogeneous and represents the first crystallisation product of the groundmass magma. Regarding the bulk composition of the groundmass, the modelled composition in Ubide et al. (2012*a* –see Chapter 6-), checked here with spot analyses on samples from the lower chilled margin and the centre of the sill (Fig. 7.5E, 7.5F), has been used. The compositions used are in Table 7.2 and the calculated *D* values are in Table 7.3.

**Table 7.3.** Calculated mineral-melt partition coefficients for clinopyroxene (Cpx) and amphibole (Amp). Preferred datasets are marked in bold. The last column contains mineral-mineral partition coefficients between clinopyroxene and amphibole. The compositions used for the calculations are in Table 7.2.

| | *D* Cpx/Melt | *D* Amp/Melt | | *D* Cpx/Amp |
|---|---|---|---|---|
| | **Cpx-P/ Gr**[a] | **Amp-P(I)/ Gr**[a] | Amp-P(II)/ Gr[a] | Cpx-P/ Amp-P(I) |
| Rb | 0.04 | 0.15 | 0.15 | 0.25 |
| Cs | 0.23 | 0.05 | 0.00 | 5.17 |
| Be | 0.38 | 0.27 | 0.36 | 1.39 |
| Sr | 0.12 | 1.12 | 1.24 | 0.11 |
| Ba | 0.01 | 1.25 | 1.45 | 0.01 |
| V | 0.73 | 1.44 | 1.42 | 0.51 |
| Cr | 0.00 | 0.14 | 0.19 | 0.00 |
| Co | 0.66 | 1.35 | 1.47 | 0.49 |
| Ni | 0.49 | 0.85 | 1.32 | 0.58 |
| Cu | 0.01 | 0.16 | 5.71 | 0.07 |
| Zn | 0.21 | 0.35 | 0.35 | 0.60 |
| Ga | 0.56 | 3.52 | 3.91 | 0.16 |
| Y | 0.79 | 0.81 | 0.87 | 0.98 |
| Nb | 0.07 | 0.36 | 0.40 | 0.18 |
| Ta | 0.05 | 0.32 | 0.36 | 0.16 |
| Zr | 0.68 | 0.44 | 0.47 | 1.56 |
| Hf | 1.35 | 0.75 | 0.81 | 1.80 |
| Pb | 0.18 | 0.04 | 0.23 | 4.95 |
| U | 0.16 | 0.02 | 0.01 | 9.00 |
| Th | 0.04 | 0.02 | 0.02 | 2.56 |
| La | 0.18 | 0.23 | 0.27 | 0.79 |
| Ce | 0.31 | 0.33 | 0.37 | 0.94 |
| Pr | 0.41 | 0.45 | 0.50 | 0.91 |
| Nd | 0.60 | 0.67 | 0.77 | 0.90 |
| Sm | 0.91 | 0.89 | 1.07 | 1.02 |
| Eu | 1.01 | 1.02 | 1.19 | 0.99 |
| Gd | 0.92 | 0.96 | 1.05 | 0.96 |
| Tb | 1.06 | 1.00 | 1.02 | 1.06 |
| Dy | 1.00 | 0.91 | 1.08 | 1.10 |
| Ho | 0.99 | 0.94 | 1.03 | 1.05 |
| Er | 0.94 | 0.82 | 0.93 | 1.15 |
| Tm | 0.94 | 0.78 | 0.91 | 1.21 |
| Yb | 0.76 | 0.66 | 0.70 | 1.15 |
| Lu | 0.83 | 0.52 | 0.66 | 1.61 |

Fig. 7.7 shows calculated *D* values in REE and multivariate plots, together with previous datasets. New *D* values for clinopyroxene are relatively high for the middle REE (MREE), with compatible values for Eu, Tb and Dy (Fig. 7.7A). The most compatible value corresponds to Hf whereas Ba is highly incompatible (Fig. 7.7B). The shape of REE and multivariate patterns agrees with that of previous datasets in basic rocks, although many of them are incomplete. The similarity is especially clear with the other dataset in camptonites (Orejana et al., 2004). Clinopyroxene incorporates U preferentially over Th in camptonite melts, in contrast with basalt and basanite melts (e.g., Hauri et al., 1994).

Results for REE, U, Th, Zr and Hf are higher than those by other authors in similar compositions, and approach data from acid rocks (see phonolite dataset by Olin and Wolff, 2010), which nevertheless are different in shape. High values could be related to

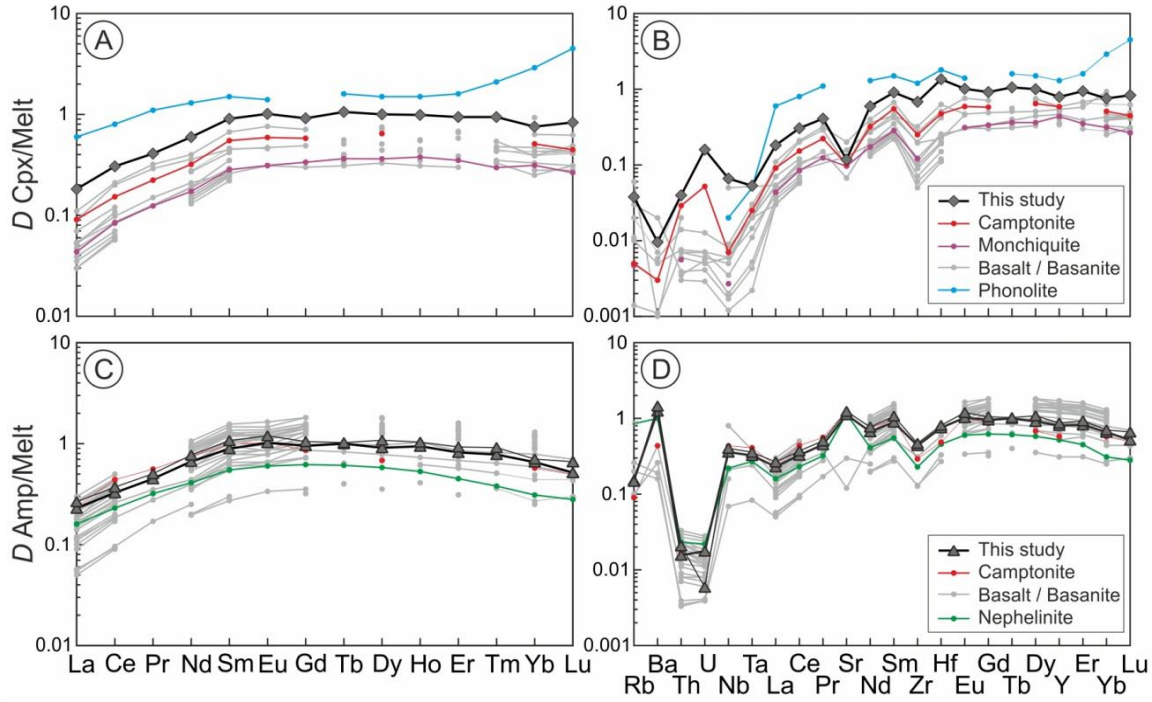


**Fig. 7.7.** Calculated mineral-melt partition coefficients for clinopyroxene (A, B) and amphibole (C, D). The thick line in amphibole-melt plots highlights the preferred dataset. Previously published *D*-values are included for comparison. In clinopyroxene, partition coefficients in camptonite were obtained by Orejana et al. (2004), in monchiquite by Foley et al. (1996), in basalt and basanite by Adam and Green (2006), Hart and Dunn (1993), Hauri et al. (1994), McKenzie and O'Nions (1991) and Thompson and Malpas (2000) and in phonolite by Olin and Wolff (2010); values below 0.001 have been screened out. In the case of amphibole, partition coefficients in camptonite were obtained by Orejana et al. (2004), in basalt and basanite by Adam and Green (2006), Bottazzi et al. (1999), LaTourrette et al. (1995), McKenzie and O'Nions (1991) and Tiepolo et al. (2000) and in nephelinite by Fulmer et al. (2010); values from evolved experiments by Tiepolo et al. (2000) have been screened out.

the fact that the studied microphenocrysts crystallised under lower pressures (see section 7.4.3) than the majority of data from the literature.

Two *D* datasets were calculated for amphibole, given the two analyses available in the mineral. Both datasets are very similar to each other and are well in line with published data in basic rocks (Fig. 7.7C, 7.7D), despite frequently incomplete. New *D*-s are high for MREE and compatible for Eu, Tb, Ba, Sr, Ga and the transition elements V and Co (Table 7.3). U and Th on the other hand, are highly incompatible and retained preferentially in the melt. It is noteworthy the strong resemblance with data in camptonite obtained by Orejana et al. (2004). It is equally interesting that the obtained REE and multivariate patterns are very similar in shape to the dataset in nephelinite by Fulmer et al. (2010), which is complete and was built with high-precision isotope dilution analyses of high field strength elements and LA-ICP-MS analyses.

Given that clinopyroxene and amphibole microphenocryst cores are both in equilibrium with the bulk composition of the groundmass, they probably co-precipitated in mutual equilibrium and therefore clinopyroxene-amphibole partition coefficients can be

calculated (Table 7.3). Because they are very similar in trace elements (Fig. 7.5), clinopyroxene-amphibole partition coefficients are close to 1 for many elements, especially Y and the REE. Clinopyroxene preferentially incorporates Cs, Pb, U and Th, whereas Ba and some transition elements are controlled by amphibole.

In order to test the obtained mineral-melt partitioning data on a crystal-chemical basis, the lattice-strain model by Blundy and Wood (1994) has been applied. Partitioning of a trace element ion into a specific crystallographic site is dependent on the radius and charge of the ion matching the radius and charge of the lattice site (Goldschmidt, 1937). For an isovalent series of ions *i*, the logarithm of the partition coefficient $D_i$ varies near-parabolically with ionic radius $r_i$ (Onuma et al., 1968; Fig. 7.8). The peak of the parabola provides the ideal radius of the crystallographic site ($r_0$) and therefore the least amount of strain in the crystal lattice upon substitution, triggering the maximum partition coefficient ($D_0$); as the difference in radius between the substituting ion and the crystallographic site increases, so does the crystal strain, and therefore the partition coefficient decreases (Fig. 7.8). This relationship was rationalised by Blundy and Wood (1994), based on the model strain energy caused by replacement of ions (Brice, 1975), into the lattice-strain model, so that the partition coefficient $D_i$ is expressed as:

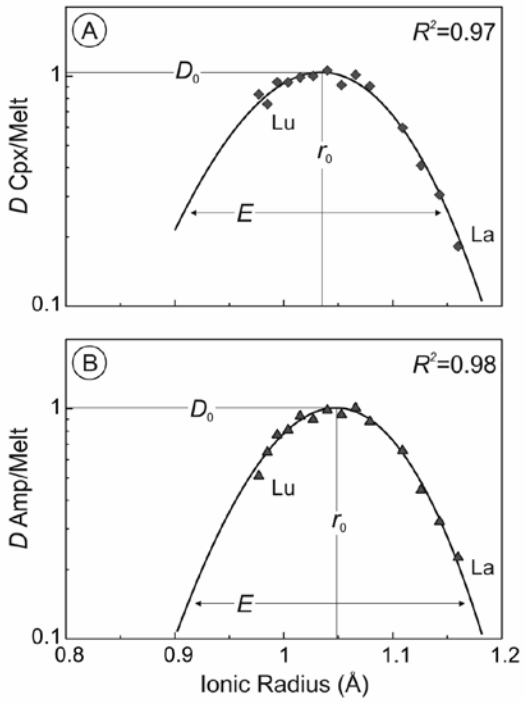


**Fig. 7.8.** Calculated mineral-melt REE partition coefficients plotted *vs.* ionic radius for clinopyroxene (A) and amphibole (B). Ionic radii are for 3+ valence and VIII-fold coordination in both minerals (Shannon, 1976). Fitting curves were obtained by non-linear least-squares regression to the lattice-strain equation by Blundy and Wood (1994) and the coefficients of determination, $R^2$, are very close to 1. Fit parameters are given in the text.

$$D_i = D_0 \exp\left[\frac{-4\,\pi\,E\,N_A\left[\frac{r_0}{2}(r_i - r_0)^2 + \frac{1}{3}(r_i - r_0)^3\right]}{R\,T}\right]$$

where $N_A$ is the Avogadro's number, $R$ is the universal gas constant, $T$ is the temperature in degrees Kelvin and $E$ is the Young's Modulus for the site, which is a measure of the tightness of the partitioning parabola, representing the local elasticity of the crystal lattice.

The REE trivalent series provides numerous partition coefficients and varied ionic radii for the construction of Onuma diagrams (Fig. 7.8). Mineral-melt partitioning in clinopyroxene and amphibole can be modelled by assuming that all $REE^{3+}$ are substituting for VIII-fold coordinated $Ca^{2+}$, in the M2 crystallographic site in the case of clinopyroxene (e.g., Wood and Blundy, 1997) and in the M4 crystallographic site in the case of amphibole (e.g., Dalpé and Baker, 2000). The calculated partition coefficients are extremely well described by the crystal lattice-strain model (Fig. 7.8). The value of the coefficient of determination, $R^2$, for curve lines, is always above 0.95.

In the case of clinopyroxene, microphenocryst cores crystallised at a temperature of 1193 – 1068 ºC (Table 7.I of the electronic supplement) according to the clinopyroxene-only thermometer by Putirka (2008; equation 32d), based on the activity model by Nimis and Taylor (2000). Fitting $REE^{3+}$ partition coefficients ($D_i$) and their corresponding ionic radii ($r_i$) by non-linear least-squares regression to the lattice-strain equation by Blundy and Wood (1994) considering T = 1100 ºC, produced $r_0$ = 1.034 ± 0.003 Å, $D_0$ = 1.04 ± 0.02 and $E$ = 280 ± 25 GPa (Fig. 7.8A), in excellent agreement with crystal lattice-strain model expectations. These values are broadly consistent with those found in previous studies (see compilation in Sun and Liang, 2012).

In the case of amphibole, the two *D* datasets provided good fits to the lattice strain model and the dataset with the best fits is preferred (marked in bold in Table 7.3 and with a thicker line in Fig. 7.7C and 7.7D; the LA-ICP-MS analysis is plotted with a thicker line in Fig. 7.5C and 7.5D). According to the thermometric calibration by Ridolfi and Renzulli (2012), amphibole microphenocryst cores crystallised at temperatures of 1066 – 1011 ºC (Table 7.II of the electronic supplement). Using the preferred *D* dataset, fitting $REE^{3+}$ partition coefficients ($D_i$) and their corresponding ionic radii ($r_i$) by non-linear least-squares regression to the lattice-strain equation by Blundy and Wood (1994) considering T = 1050 ºC, yielded $r_0$ = 1.048 ± 0.002 Å, $D_0$ = 1.01 ± 0.02 and $E$ = 322 ± 19 GPa (Fig. 7.8B), in excellent agreement with crystal lattice-strain model expectations. These results are in line with published data (e.g., Adam and Green, 2006; Bottazzi et al., 1999; Dalpé and Baker, 2000; Fulmer et al., 2010).

The calculated *D* sets of data agree with the lattice-strain model supporting equilibrium between microphenocryst cores and the groundmass. In contrast, macrocryst cores produce partition coefficients with poor correlations in Onuma diagrams (not shown) and/or unrealistic fit parameters to the lattice-strain equation by Blundy and Wood (1994). This highlights the need to carefully evaluate the equilibrium state when using naturally occurring mineral-melt pairs for D calculations (see also Fulmer et al., 2010), especially when the crystals are much coarser than the groundmass.

The calculated *D* sets of data may constitute the first extensive and internally consistent mineral-melt partition coefficients for clinopyroxene and amphibole in camptonite melts. Additionally, mineral-mineral partition coefficients are provided. The conditions of application of these data are the conditions of crystallisation of microphenocryst cores, as explored in the following section. In contrast with most partitioning studies focused on conditions relevant for partial melting in the mantle, data presented in this study are applicable to geochemical modelling of processes taking place during the ascent and shallow emplacement of magmas, like e.g., crystal fractionation.

Fig. 7.9 shows the effect of the REE *D* dataset (Table 7.3) on a process of fractional crystallisation (Rayleigh, 1896) applied to the bulk composition of the groundmass (Table 7.2), taken as a representative alkaline lamprophyre. Modelling crystallisation of clinopyroxene or amphibole in steps of 10%, from 90% to 10% melt generates liquids progressively more enriched in LREE and HREE. Given the high *D* values for the MREE, close to 1 (Fig. 7.7, 7.8), concentrations in these elements remain fairly constant during fractionation (Fig. 7.9). Note that the effect of crystallising clinopyroxene or amphibole is very similar.

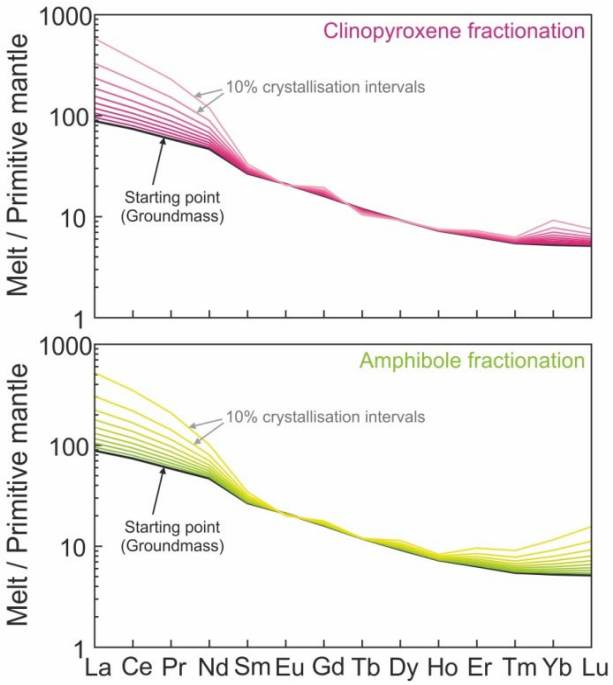


**Fig. 7.9.** Variation in REE composition (normalised to primitive mantle; McDonough and Sun, 1995) of melts undergoing fractional crystallisation of clinopyroxene or amphibole, according to calculated partition coefficient data (Table 7.3). The starting point is the bulk composition of the groundmass (black line; Table 7.2) and fractionation is modelled in steps of 10% crystallisation (coloured lines), up to 90%.

### 7.4.3. Mineral formation conditions

The different crystal populations of clinopyroxene and amphibole in the sill studied include recycled macrocrysts revealing several events of magmatic recharge. In addition, the significant differences in size between macrocrysts and microcrysts, coupled with their compositional differences in certain elements, suggest differences in the conditions of crystallisation. In the case of clinopyroxene, $Na_2O$ concentrations can be related to pressure conditions (e.g., Adam and Green, 1994) so that the higher $Na_2O$ contents in X- and A-type macrocryst cores (Fig. 7.2) might indicate crystallisation under higher pressure

than P and R compositions related to the groundmass. Moreover, X1 compositions show the highest concentrations in $Na_2O$ and the lowest concentrations in $TiO_2$, so they might represent the highest pressure conditions (Adam and Green, 1994; Shaw and Eyzaguirre, 2000). Regarding amphibole (Fig. 7.4), K- and P-type macrocryst cores reach the highest concentrations in $K_2O$ and the lowest concentrations in $TiO_2$, indicating crystallisation at higher pressure (Adam and Green, 1994) than P and R compositions in microphenocrysts, microlites and rims. Major element data in clinopyroxene and amphibole thus suggest that macrocryst cores could have crystallised at greater depths than crystals related to the groundmass of the sill. Given that clinopyroxene and amphibole macrocrysts are sometimes associated in glomerocrysts, their crystallisation was probably closely related and therefore took place at the same depth.

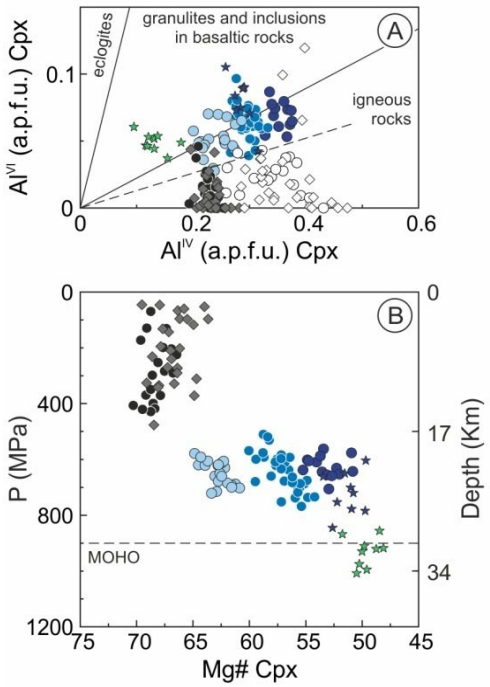


**Fig. 7.10.** Clinopyroxene barometry. A) Variation in $Al^{VI}$ vs. $Al^{IV}$ atoms per formula unit (a.p.f.u.) in clinopyroxene, with fields for eclogites, granulites and inclusions in basaltic rocks and igneous rocks from Aoki and Kushiro (1968); the discontinuous line separates X- and A-type compositions from P and R compositions. B) Pressure estimates from clinopyroxene composition and water content in the melt, according to equation 32b by Putirka (2008), vs. Mg# content in clinopyroxene. The vertical right axis shows the equivalence of pressure in depth (see text in the next page). Legend for symbols is in Fig. 7.2.

Clinopyroxene shows the most complex zoning patterns (Fig. 7.1) and therefore records most completely the magma history in the sill. Accordingly, clinopyroxene compositions will be used to infer the conditions of crystallisation of the different crystal populations. Apart from the contents in sodium and titanium as discussed in the paragraph above, the partition of aluminium between the tetrahedral and octahedral sites is a good indicator of crystallisation depth (e.g., Orejana et al., 2007 and references therein). Fig. 7.10A shows the plot of $Al^{VI}$ vs. $Al^{IV}$ atoms per formula unit, with the pressure fields defined by Aoki and Kushiro (1968). X-type compositions plot in the field of granulites and inclusions in basaltic rocks, A-type compositions plot at the boundary between the field of granulites and inclusions in basaltic rocks and the field of igneous rocks and finally, P and R compositions plot in the field of igneous rocks. X- and A-type macrocryst cores show a greater $Al^{VI}/Al^{IV}$ ratio than P macrocryst and microphenocryst cores, indicating crystallisation under higher pressure conditions (see discontinuous line in Fig. 7.10A). R compositions formed latest in the crystallisation sequence and show most variable compositions. Thus, they will not be considered further for barometric estimates.

The clinopyroxene-only barometer developed by Nimis (1995) and revised more recently by Putirka (2008) has been applied to quantify crystallisation depths. Putirka (2008) proposed an additional calibration that takes into account the water content of the liquid in equilibrium with clinopyroxene (equation 32b in Putirka, 2008), applied here to account for the significant amount of volatiles in lamprophyre magmas (e.g., Le Maitre, 2002). To calculate the water content in the melt the equations by Ridolfi and Renzulli (2012) were applied to amphibole compositions, obtaining $H_2O_{melt}$ values in the range from ca. 3 to 6 wt. % (see Table 7.II of the electronic supplement). These values are well in line with the Loss On Ignition (LOI) content in whole rock (varying from ca. 3 to 5 wt. %; Tables 4.1 and 6.1), which is related to the volatile content of the melt given the widespread presence of vesicles in the sill and its low alteration degree (Ubide et al., 2012*a* –see Chapter 6-). Provided that clinopyroxene types A3 and P crystallised from melts that produced amphibole types K and P, respectively (see section 7.4.1, Fig. 7.6), a water content of 4 wt. % has been assumed for the melt in equilibrium with these compositions. Clinopyroxene types X1, X2, A1 and A2, on the other hand, crystallised from magmas that did not produce amphibole (see section 7.4.1, Fig. 7.6) and therefore, a water content of 2 wt. % has been assumed for these compositions.

The results of applying equation 32b by Putirka (2008) to clinopyroxene core compositions can be found in Table 7.I of the electronic supplement. The pressure dataset is graphically represented vs. Mg# in Fig. 7.10B. This diagram includes the equivalence in depth of pressure values, considering a density of 3 g/cm$^3$ for the continental crust. At the time of emplacement of the lamprophyre sill in the Late Cretaceous (Ubide et al., under review *a* –see Chapter 3-) the thickness of the crust in the study area was ca. 30 km (Salas and Casas, 1993; Fig. 7.10B). It is clear from the results that A-type and X2 compositions crystallised under similar pressure conditions of ca. 500 – 800 MPa, equivalent to a maximum of ca. 25 km depth, and that X1 compositions crystallised under higher pressure (ca. 850 – 1000 MPa; ca. 30 km close to the crust-mantle boundary). P compositions on the other hand, crystallised under varying pressure conditions from ca. 500 to less than 50 MPa (ca. 15 to less than 1.5 km depth). The lowest pressure values indicate the maximum level of emplacement of the sill. Therefore, a shallow emplacement level at ca. 1 km depth can be inferred. This agrees with the degassing of the magma and formation of vesicles (Ubide et al., 2012*a* –see Chapter 6; Fig. 6.2-).

Quantitative barometric data as shown in Fig. 7.10B provide petrogenetic information on varied stages of the magmatic history. Firstly, the high pressure results for the green macrocryst core (X1) support its xenocryst origin. The extremely evolved composition of this crystal would agree with an intense fractionation process in a magma chamber located at the lower crust or the mantle-crust transition. Fractionation of clinopyroxene and/or amphibole would drive down the Mg# content of the melt in this magma

chamber, which would moreover become enriched in LREE and HREE relative to the MREE (e.g., Fig. 7.9) and then produce clinopyroxene with the composition observed in the X1 xenocryst (Fig. 7.2, 7.5A). Secondly, the X1 clinopyroxene was incorporated into an ascending magma batch that stagnated in a magma chamber or magma conduit at ca. 25 km depth. At this level the inherited X1 xenocryst was partially replaced by the X2 composition and the rest of clinopyroxene and amphibole macrocryst cores crystallised. In fact, the convex-upwards normalised REE patterns of macrocryst cores (Fig. 7.5A, 7.5C) are typical of deep cumulates in equilibrium with alkaline basaltic melts (Irving and Frey, 1984). Thirdly, microphenocryst cores and P-type mantles around previous macrocryst cores crystallised under polybaric conditions, during the ascent of the magma from the deep magma reservoir towards the shallow emplacement level. Rims and microlites (R compositions) most likely crystallised at the emplacement level.

### 7.4.4. Magma mixing and fractionation

The compositional evolution observed for the antecrysts (Fig. 7.2, 7.4) could indicate a process of progressive mixing between the magma from which antecrysts started to crystallise and a more primitive magma entering the crystallisation level at ca. 25 km depth (Fig. 7.10B), presumably a magma chamber or magma conduit were these crystals had enough time to grow into their large size. The final mixture would rise towards the shallow emplacement level, crystallising into microphenocrysts and rims cogenetic with the groundmass of the sill.

In order to check the evolutionary trends observed in Harker-type diagrams, multivariate statistical analysis was applied to EMP compositional data. Specifically, principal component analysis (PCA) was used. PCA reduces the dimensionality of a dataset by transforming the original variables (elemental concentrations) into a new set of variables (the principal components, PC-s), which are uncorrelated and ordered so that the first few retain most of the variation present in all of the original variables (Joliffe, 2002). In this way, the first two principal components of a group of compositions represent the greatest geochemical variation, and a PC2 vs. PC1 plot allows to statistically group or discriminate the compositions, as well as to identify possible variation trends among them. The interpretation of the results includes evaluating which elements have greater loads on each PC and, therefore, what group of elements each PC mainly represents. PCA was applied to clinopyroxene compositions and to amphibole compositions. Input data were all EMP analyses, with all the analysed major elements (see EMP data in Tables 7.I and 7.II of the electronic supplement). The results are detailed in Tables 7.III and 7.IV of the electronic supplement. Plots of PC2 vs. PC1 are shown in Fig. 7.11, with compositions grouped according to the types defined in Table 7.1.

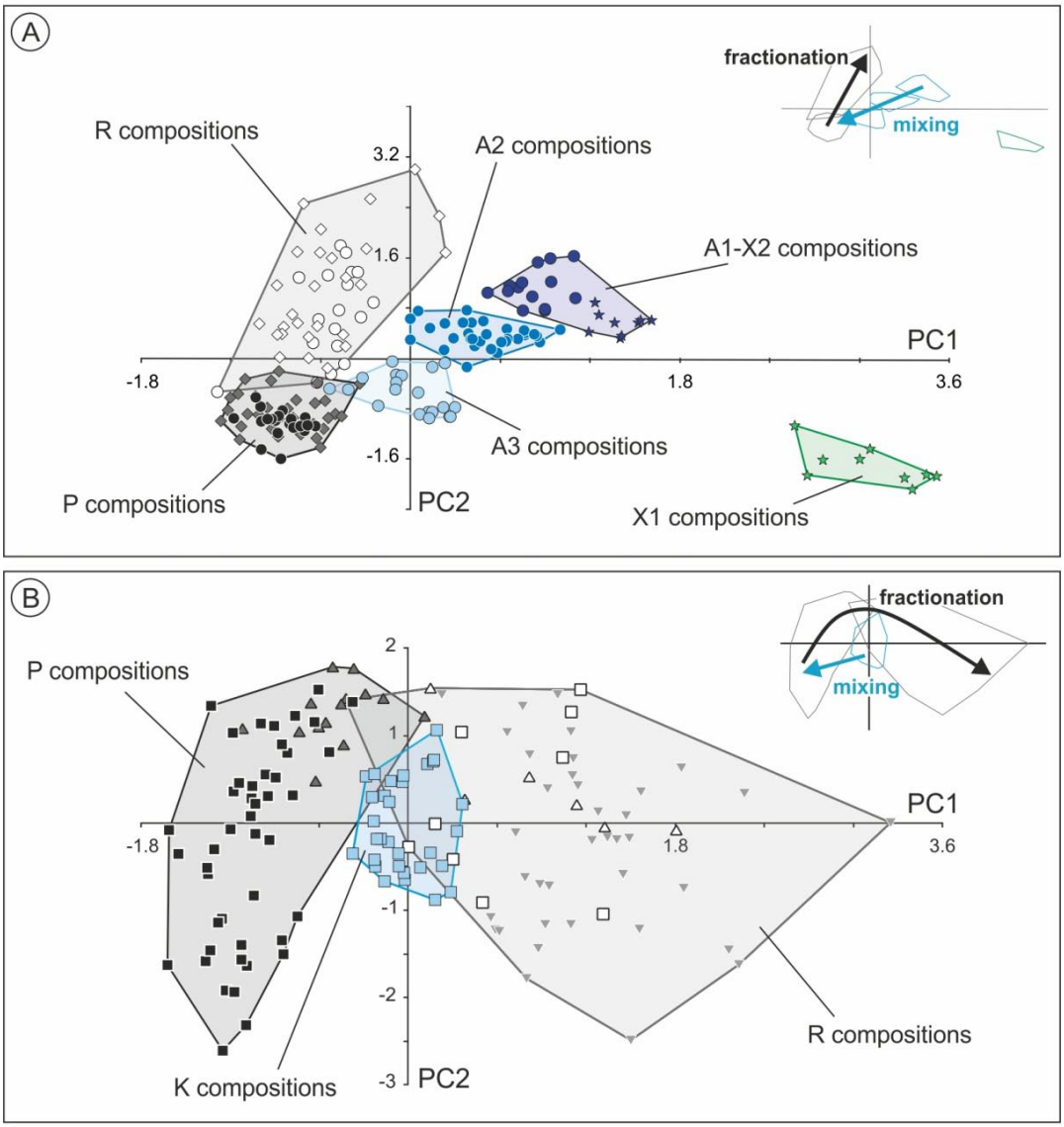


**Fig. 7.11.** Results of principal component analysis (PCA) applied to major element compositions in clinopyroxene (A) and amphibole (B). Principal component 2 (PC2) is plotted against principal component 1 (PC1). Convex hulls (polygons) link analyses of the same compositional type. Legend for symbols is in Fig. 7.2 and 7.4. Axes and convex hulls are minimised at the top right corner of each figure (inset), where the interpretation in terms of magmatic processes is highlighted.

Clinopyroxene compositions (Fig. 7.11A) plot in excellent agreement with the types defined in Table 7.1, reproducing the A1(X2)-A2-A3-P and P-R evolutionary trends from Harker-type diagrams (Fig. 7.2). Similarly, the xenocryst (X1) plots isolated with the highest PC1 values and low PC2 values. An analysis of the distinct weights of the elements on PC1 reflects a greater contribution of $Na_2O$, $FeO^T$, MgO and MnO to the observed variability, whereas the loads of NiO, F and Cl are insignificant. In contrast, PC2 shows greater loads for $SiO_2$, $Al_2O_3$ and $TiO_2$ and a low contribution of $Cr_2O_3$, CaO and $Na_2O$. PC1 explains 26 % of the total variance and PC2 explains 23 % (see Table 7.III of the electronic supplement).

Amphibole compositions (Fig. 7.11B) plot in agreement with the types in Table 7.1 as well, although the values overlap in both PC1 and PC2 and therefore, differences in composition are less clear than in the case of clinopyroxene. R compositions (macrocryst rims, microphenocryst rims and microlites) define the widest polygon, correlating with the compositional scatter recognised in Harker-type diagrams (Fig. 7.4). From among P compositions, it is noteworthy that microphenocryst cores concentrate towards the highest PC1 and PC2 values, whereas macrocryst cores show a wide variation range in PC2 for a smaller variation range along PC1. A closer look at the loads of the PC1 variable reveals a slightly higher contribution of $SiO_2$, MgO and $TiO_2$ to the observed variability, within a general context of relative uniformity. On PC2, by contrast, the contribution of $Al_2O_3$, $Cr_2O_3$, $K_2O$ and F is especially high whereas NiO has very little effect. PC1 explains the 33 % of the global variance whereas PC2 explains the 15 % (see Table 7.IV of the electronic supplement).

In general, the evolutionary trends recorded by mineral compositions are best recognised using all elemental contents simultaneously, as provided by PCA. The results support the interpretation that the magma from which A1 (and X2) clinopyroxene crystallised mixed with progressive inputs of a more primitive magma, giving rise to the crystallisation of A2, A3-K and P compositions with increasing fractions of the incoming magma in the mixture (see the insets in Fig. 7.11). The fact that the crystallisation of amphibole started later than the crystallisation of clinopyroxene suggests that the incoming magma may be more water-rich as well. Hence, the composition of the melt in the magma chamber changed in response to open-system behaviour, where successive recharges of magma were followed by mixing with the resident magma. With the last recharge and mixing event the final magma rose towards the emplacement level becoming a closed-system composed of a crystal cargo inherited from the magma chamber and a melt that would eventually transform into the groundmass of the sill. Fractionation of this melt during ascent and emplacement is recorded by P-R compositions.

### 7.4.5. Reconstruction of the magmatic plumbing system

Detailed mineral chemistry investigation of the Calella de Palafrugell lamprophyre reveals a complex magma history in the plumbing system (Fig. 7.12).

Most macrocryst cores are antecrysts crystallised at depth (ca. 25 km; Fig. 7.10B) in a magma chamber that received repeated supplies of a more primitive and water-rich magma. The melts in this chamber were already partly fractionated, because whole rock compositions cannot represent a primary magma in equilibrium with its mantle source (Ubide et al., 2012*a* –see Chapter 6-). The first magma recorded by mineral compositions produced the crystallisation of A1 clinopyroxene. This magma contained an older green clinopyroxene xenocryst (X1) crystallised from an extremely fractionated melt at the

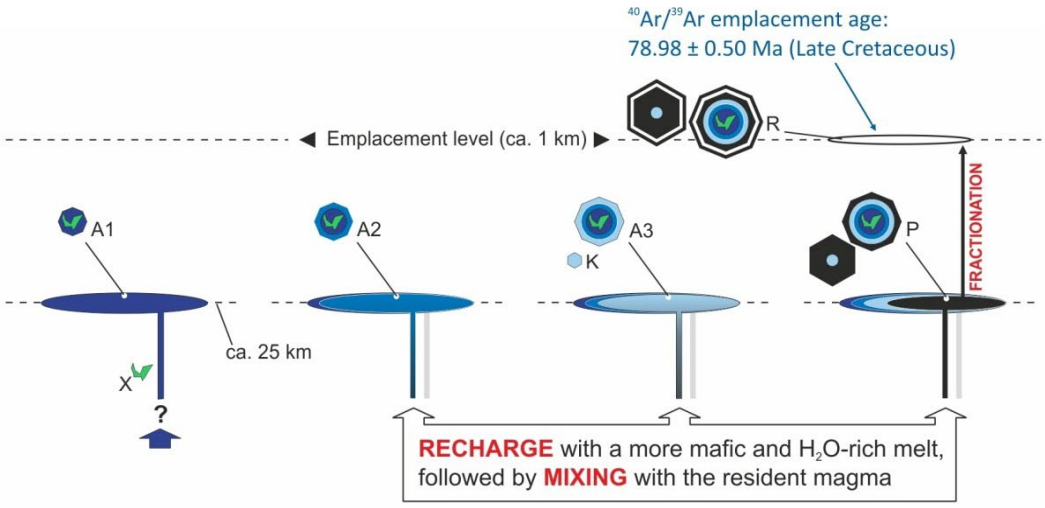


**Fig. 7.12.** Conceptual sketch of deep magmatic processes and magma history related to the Calella de Palafrugell lamprophyre. Octagons represent clinopyroxene crystals in equilibrium with the melt and hexagons represent amphibole crystals in equilibrium with the melt. Rounded shapes, in contrast, represent crystals in disequilibrium with the melt. The green resorpted core (X) represents the clinopyroxene xenocryst X1. Meanwhile, X2 compositions are included as A1.

lower part of the crust and afterwards sampled by a liquid ascending to the magma chamber. The xenocryst was corroded in contact with the new host magma and partially replaced with A1 clinopyroxene (named X2 in this case). A recharge and mixing event in the magma chamber produced a second melt composition responsible for the crystallisation of A2 clinopyroxene, either mantling previous A1 cores or nucleating new crystals. A new recharge and mixing event produced a third melt composition from which A3 clinopyroxene and for the first time, amphibole (K compositions) crystallised. Amphibole started to crystallise only when the water content of the melt was high enough, after previous events of recharge and crystallisation of anhydrous clinopyroxene. The magma chamber was becoming progressively more crystal-rich, as revealed by the fact that most glomerocrysts include both clinopyroxene and amphibole. At the same time, the melt was becoming progressively more primitive and water-rich, producing disequilibrium with previous crystals, which in consequence developed subhedral to anhedral habits (Fig. 7.12). The final recharge and mixing event was responsible for the fourth and final melt composition, in equilibrium with clinopyroxene and amphibole phenocrysts (P compositions). Mafic recharge is commonly invoked as a principal mechanism for triggering volcanic eruptions (Freeley et al., 2008; Martel et al., 2006; and references therein) and in the case studied, the final recharge into the magma chamber probably triggered the ascent of the magma towards the surface.

P compositions crystallised in polybaric conditions from the magma chamber to the emplacement level, located at a shallow depth of ca. 1 km (Fig. 7.10B). Finally, R compositions crystallised at the emplacement level, together with the final crystallisation of the groundmass of the sill (Fig. 7.11). As shown in the preceding chapter and Ubide et al. (2012*a*), the melt reaching the emplacement level carried a variety of inherited mafic

antecrysts that accumulated downwards due to gravitational settling, controlling variations in whole rock composition across the sill.

$^{40}Ar/^{39}Ar$ dating has been applied to separates of groundmass and amphibole macrocrysts from the sill (Ubide et al., under review *a* –see Chapter 3-). The results are indistinguishable from each other within the uncertainty and the inferred emplacement age is 78.98 ± 0.50 Ma. This age is Late Cretaceous (Campanian) and corresponds to a context of thinned crust by the end of the Mesozoic extension, right before the onset of the Pyrenean orogeny (Salas and Casas, 1993; Solé et al., 2003; Ubide et al., under review *a* –see Chapter 3-; Vergés et al., 2002).

## 7.5. Conclusions

Clinopyroxene and amphibole crystals record a complex magmatic history involving magma mixing and fractionation. Barometric calculations on clinopyroxene locate magmatic processes and unravel the nature of the feeder magmatic system at depth. And a consistent dataset of partition coefficients is presented. The conclusions are:

- There is a significant load of recycled crystals in the camptonite studied, in spite of the small thickness of the sill cropping out. Macrocrysts are not necessarily phenocryst phases, so it is crucial to assess mineral-melt equilibrium between the minerals and their host magma. For this end, it is important to understand that whole rock compositions may be biased by the accumulation of inherited phases and therefore, fine-grained groundmass or glass compositions may be better representatives of closed-system melts.

- In the studied case, macrocrysts are complexly zoned and provide evidence for open-system magmatic behaviour in the feeding system at depth. They are mainly composed of antecryst cores crystallised in a deep (ca. 25 km) magma chamber that received repeated injections of a more primitive and water-rich magma that mixed with the resident magma. There is also an extremely evolved xenocryst originally formed at the lower part of the crust.

- The xeno/antecryst population was incorporated into an ascending magma batch that reached the shallow emplacement level (ca. 1 km) and eventually transformed into the groundmass of the sill. During ascent and emplacement, mantles and rims overgrowing inherited cores record progressive fractionation of the groundmass magma.

- Crystal heterogeneity is therefore an important feature and tracks a complex magma history involving phases from disparate levels within the crust. It follows that mineral compositions record information which would be inaccessible using whole rock compositions alone.

- Equilibrium between phenocryst compositions and the bulk composition of the groundmass makes it possible to calculate for the first time, a consistent partition coefficient dataset for clinopyroxene and amphibole in alkaline lamprophyre melts. In contrast with most studies focused on high *P-T* conditions, data presented in this study are best applicable to shallow depths.

- Clinopyroxene-melt and amphibole-melt partition coefficients are overall consistent with data from basic rocks. Clinopyroxene partition coefficients for Rare Earth Elements, U, Th, Zr and Hf are higher than data from basalt and basanite melts.

- Clinopyroxene and amphibole show a similar partitioning behaviour for most trace elements. In the case of the REE, fractional crystallisation triggers enrichments in LREE and HREE in the melt, for fairly constant concentrations in the MREE.

# 8

# Conclusions

*View of Punta des Mut in Aiguablava, Costa Brava*

The present PhD Thesis is the first comprehensive study on the petrology, mineralogy, geochemistry and geochronology of the Cretaceous magmatism in northeast Iberia. It has allowed for a better understanding of the mantle source and its evolution with time, and it has helped to constrain the geodynamic context that conditioned the development of the magmatism, including the opening of the Bay of Biscay and the beginning of the Alpine compression. This research has also led to broader conclusions on the petrological and geochemical implications of crystal recycling, crystal settling and antecryst accumulation in mafic rocks. Consistent mineral-melt partition coefficients have been obtained for the first time in camptonite melts. Additionally, specific sample preparation methodologies have been developed and the treatment and interpretation of geochemical datasets have been enhanced by using mathematical techniques with potential applications to other igneous studies.

## 8.1. General characteristics

The Cretaceous alkaline magmatism in northeast Iberia crops out in four domains: 1) Basque-Cantabrian Basin in the western Pyrenees; 2) North Pyrenean Basins in the North Pyrenean Zone; 3) Eastern Pyrenees; 4) northern Catalonian Coastal Ranges. Preliminary studies proposed an additional outcrop in the Central Pyrenees, but $^{40}Ar/^{39}Ar$ geochronology revealed it has an older age.

The magmatism is more developed volumetrically, more extrusive and long-lasting towards the western domains. In the Eastern Pyrenees and northern Catalonian Coastal Ranges, in contrast, the magmatism is restricted to small intrusive outcrops such as lamprophyre intrusions, limited in time and more alkaline in composition.

## 8.2. Age and geodynamic implications

New $^{40}Ar/^{39}Ar$ ages and revisited geochronological data constrain the age of the Cretaceous magmatism in the Pyrenean setting to the Albian – Santonian range (ca. 105 – 85 Ma). Magmatic activity is especially recorded between ca. 100 and 90 Ma. It is restricted to ca. 95 – 90 Ma in the Eastern Pyrenees, whereas multiple stages developed towards the west with the longest time span recorded in the Basque-Cantabrian Basin. Cretaceous magmatism as well as contemporaneous metamorphism, hydrothermalism and mantle exhumation, postdate the most recent geochronological estimates for the opening of the Bay of Biscay that consider that the anticlockwise rotation of Iberia took place in the Aptian. Magmatism developed in a context of thinned crust, in a tectonically unclear stage between the rotation of Iberia and the onset of Alpine collision.

Regarding the debate on the kinematics of opening of the Bay of Biscay, data from the magmatism do not support either of two classical end-member models: scissor-type opening (based on the fit of magnetic anomalies in the Atlantic and Bay of Biscay) vs. strike slip opening (based on geological data in the Pyrenees). Progressive variations in the petrology and geochronology of the rocks along the Pyrenees yield further support to the scissor-type opening model. However, such model implies either compression or extension by asthenospheric upwelling in the Pyrenean realm, and the magmatism in contrast, postdates the rifting event. Magmatic data therefore suggest that an alternative model might be regarded. Strike-slip followed by scissor-type opening with a pole of rotation located to the east, instead of to the north of Iberia, might be a scenario compatible with the characteristics and evolution of the Cretaceous magmatism. Nevertheless, more studies are necessary and this investigation contributes to the debate with updated geochronological and petrological information.

The Cretaceous magmatism in the northern Catalonian Coastal Ranges is precisely dated with $^{40}Ar/^{39}Ar$ at ca. 79 Ma (Campanian). It is therefore the youngest Cretaceous magmatism in northeast Iberia. Lamprophyres are good markers of changes in geodynamic conditions and their 79 Ma age can be proposed as the onset of Alpine shortening in northeast Iberia, which was unclear up to now.

## 8.3. Mantle source

The Cretaceous magmatism in northeast Iberia shares a common magma source, given that trace element concentrations in mafic and not cumulative samples as well as Sr-Nd-Pb isotope ratios are comparable. Slight differences between domains suggest melting at lower rates or higher pressure conditions towards the east. Evolved magmas can be related to mafic compositions by fractional crystallisation.

Incompatible elements significantly enriched over primitive mantle compositions, together with the widespread presence of hydrous phases, suggest a metasomatised source. Amphibole and apatite were probable metasomatic phases.

Normalised trace element patterns together with Sr-Nd-Pb isotope ratios reveal the involvement of HIMU- and EM-type components in a heterogeneous source. In detail, EM-1 seems to have a more significant contribution than EM-2, but the latter could also be involved.

The mantle source was probably asthenospheric. Highly fractionated, normalised REE patterns suggest melting in the garnet-stability field. Sr-Nd isotope ratios more enriched than values from ultramafic massifs in the Pyrenees (e.g., Lherz), which are taken as

representative of the lithospheric mantle in the region, support a deeper generation level for the Cretaceous melts. Meanwhile, amphibole-rich veins cutting the ultramafic massifs in the Pyrenees have Sr-Nd isotope ratios closer to those of the Cretaceous magmatism. And the age of these amphibole-rich veins coincides with the age of the magmatism. These results support the interpretation that amphibole-rich veins represent pathways for the ascent of the Cretaceous alkaline magmas.

The mantle signature related to the Cretaceous magmatism is recognised in older and younger magmatisms in Iberia, suggesting a long-living mantle domain since Permian to Quaternary times. Model ages in genetically related magmatisms reveal a Precambrian (Cadomian) fractionation event in the mantle.

## 8.4. The Cretaceous lamprophyre suite in the Catalonian Coastal Ranges. Insights into complex crystal populations and the influence of antecrysts on whole rock compositions

At least 8 camptonite intrusions have been recognised intruding Paleozoic materials of the northern Catalonian Coastal Ranges. They are mafic, relatively thin (cm- to m-scale) and crop out as isolated sills in three sectors: east (Aiguablava and Calella de Palafrugell lamprophyres), centre (S'Agaró and Llagostera lamprophyres) and west (Molí d'en Ponç, Molí de Dalt and Monasterio de Sant Pere Cercada lamprophyres, plus rounded blocks found topographically over Molí d'en Ponç that point to the presence of, at least, another intrusion in the area). All of the lamprophyre intrusions are subhorizontal and strongly porphyritic, excepting the S'Agaró lamprophyre which is subvertical and microlitic.

Porphyritic lamprophyres are composed of large crystals (macrocrysts and scarcer megacrysts) embedded in a fine-grained groundmass that includes microcrysts and minor glass. Gravitational accumulation of the macrocrysts, together with well developed chilled margins and vesicle alignments parallel to the margins, produce well defined vertical zoning of the sills.

The macrocrysts are clinopyroxene, amphibole and to a lesser extent, opaque minerals and pseudomorphosed olivine. They are complexly zoned and mainly composed of antecrysts in disequilibrium with the host magma. Antecrysts are related to previous magmatic stages within the same magma system and crystallised at depth. They were incorporated into ascending magmas that crystallised into the groundmass of the sills, and they are mantled by phenocryst material that crystallised in equilibrium with these new host magmas. It follows that large crystals in apparently simple porphyritic rocks are not necessarily phenocrysts, so it is crucial to assess mineral-melt equilibrium between the minerals and their host magma.

The lamprophyres show significant variations in whole rock compositions but homogeneous groundmass compositions. Whole rock compositions particularly enriched in MgO and compatible elements correlate with rocks with high volume fractions of mafic antecrysts. Accumulation of mafic antecrysts in a rock artificially modifies whole rock compositions and makes them more primitive, as demonstrated by quantitative modelling and statistical analysis of the contribution of the antecrysts to the global compositional budget of the rock. It follows that samples most enriched in compatible elements do not necessarily represent primary magmas closest to their mantle source. Rather, they may represent relatively evolved melts that accumulated primitive, recycled antecrysts.

Given the petrological and compositional similarity between the groundmass of all the porphyritic lamprophyres and the microlitic lamprophyre, a large reservoir supplying magmas to the whole lamprophyre suite is inferred. It is hypothesised that this magma reservoir may have underplated the lower crust. The largest antecrysts formed in this reservoir or deeper levels and some of them record a primitive recharge event into the reservoir. These antecrysts were incorporated into certain batches of ascending magmas. In their journey upwards, ascending magmas could sample additional antecrysts from related, more evolved magma chambers located in the lower crust. Some of the evolved antecrysts record successive magma mixing events as magmas from the reservoir recharged the more evolved chambers.

As a result of this intricate, deep plumbing system, magmas ascending towards the emplacement levels carried heterogeneous populations of inherited antecrysts and underwent fractionation. Phenocrysts in equilibrium with ascending melts probably crystallised in polybaric conditions. Most of the lamprophyre magmas intruded into subhorizontal fractures located at shallow depths. Cooling and crystallisation were fast according to the small size of the intrusions. The magma developed chilled margins in contact with the country-rock and the load of macrocrysts (mostly antecrysts) accumulated downwards due to gravitational settling, producing the vertical zoning of the lamprophyre sills. It is therefore shown that crystal settling is a meaningful process in triggering zoning of igneous intrusions, even at the cm-scale.

Besides the characterisation of the magmatic system and processes, the study of the Cretaceous lamprophyre suite in the Catalonian Coastal Ranges has shown that a deep understanding of mineral zoning unveils magmatic processes that would remain misunderstood if whole rock compositions were considered alone. Moreover, the accumulation of antecrysts influences whole rock compositions significantly, so a careful petrographic evaluation is needed before considering samples richest in MgO and compatible elements as most representative of primitive melts.

## 8.5. Trace element partitioning between clinopyroxene, amphibole and camptonite melt

The first consistent partition coefficient dataset for clinopyroxene and amphibole in alkaline lamprophyre melts has been calculated with phenocryst-groundmass and phenocryst-phenocryst equilibrium pairs in natural samples from the Cretaceous lamprophyre suite in the Catalonian Coastal Ranges. The results are in excellent agreement with lattice-strain model expectations.

Amphibole-melt partition coefficients are overall consistent with data in basaltic systems, whereas clinopyroxene-melt partition coefficients are slightly higher than data in basaltic systems. Clinopyroxene and amphibole show similar partitioning for most trace elements. In the case of the Rare Earth Elements, fractional crystallisation of these minerals triggers enrichments in LREE and HREE in the melt, for fairly constant concentrations in the MREE.

## 8.6. Multi-method approach

In addition to classical methodologies for the study of geochemical results, quantitative modelling and principal component analysis (PCA) have been applied to compositional datasets.

Modelling quantitatively the contribution of antecrysts to whole rock compositions has proved the hypothesis that whole rock compositions are significantly influenced by antecryst accumulation and whole rock compositional variation can be explained on the basis of the volume fraction and typology of antecrysts in the sample. For given trace element concentrations in antecrysts and rock, the model returns the bulk composition of the groundmass. This composition has been very useful for the study of compositional zoning of igneous bodies, as well as mineral-melt equilibrium and partitioning.

Principal component analysis (PCA) is a powerful tool for statistical treatment of large geochemical datasets. This multivariate method evaluates the relationships between compositional data taking into account all the elemental contents of interest. It therefore enhances classical bivariate evaluation of data and allows for unbiased interpretations of magmatic processes.

Regarding sample preparation, a very simple, cheap and effective method is proposed for the optical separation of kaersutite-type amphibole grains and Mg-rich clinopyroxene grains, which otherwise have very similar physical properties. This method may have diverse applications and has been used in this PhD project to purify amphibole separates for $^{40}Ar/^{39}Ar$ dating experiments.

# Conclusiones

En la presente Tesis Doctoral se ha estudiado, por primera vez en su conjunto, y de forma detallada, la petrología, mineralogía, geoquímica y geocronología del magmatismo cretácico en el noreste de Iberia. Se han obtenido conclusiones acerca de la fuente de manto y su evolución, y también acerca del contexto geodinámico que condicionó el desarrolló del magmatismo, incluyendo éstas últimas, tanto la apertura del Golfo de Vizcaya como el inicio de la compresión alpina. Además, a una escala más global, esta investigación ha profundizado en las implicaciones petrológicas y geoquímicas del reciclaje de cristales profundos y la acumulación de antecristales en intrusiones de magmas básicos. Por primera vez, se han obtenido coeficientes de reparto completos entre minerales máficos y fundidos alcalinos de tipo camptonita. En el ámbito metodológico, se han desarrollado técnicas específicas de preparación de muestras y se han aplicado metodologías matemáticas para el tratamiento e interpretación de datos geoquímicos, con aplicaciones potenciales a otros estudios en sistemas ígneos.

## 8.1. Características generales

El magmatismo alcalino cretácico en el noreste de Iberia aflora en cuatro dominios: 1) Cuenca Vasco-Cantábrica en los Pirineos occidentales; 2) Cuencas Norpirenaicas en la Zona Norpirenaica; 3) Pirineos orientales; 4) Cadenas Costero Catalanas septentrionales. Estudios preliminares llevados a cabo en un afloramiento ígneo alcalino de los Pirineos centrales habían propuesto su adscripción al magmatismo cretácico, pero los datos geocronológicos obtenidos en el presente trabajo por el método $^{40}Ar/^{39}Ar$ han revelado que dicho afloramiento es de edad más antigua.

El magmatismo cretácico aparece más desarrollado en cuanto a volumen de magma, es de naturaleza más extrusiva y presenta un desarrollo temporal mayor en los dominios occidentales. Por el contrario, en los Pirineos orientales y en las Cadenas Costero Catalanas septentrionales el magmatismo aparece restringido a pequeños afloramientos intrusivos, tales como sills de lamprófido, que presentan una edad más constreñida y una composición más alcalina.

## 8.2. Edad e implicaciones geodinámicas

La edad del magmatismo ha sido definida a partir de las nuevas edades $^{40}Ar/^{39}Ar$ obtenidas, así como de una evaluación exhaustiva de edades obtenidas por autores previos. El magmatismo cretácico en el noreste de Iberia se desarrolló entre el Albiense y el Santoniense (ca. 105 – 85 Ma) y especialmente entre los 100 y los 90 Ma. En los Pirineos orientales, la actividad magmática se restringe al rango entre los 95 y los 90 Ma, mientras que, hacia el oeste, en la Cuenca Vasco-Cantábrica, el número de episodios

magmáticos y el rango temporal que abarcan es mayor. Tanto el magmatismo cretácico como el metamofismo, el hidrotermalismo y la exhumación del manto contemporáneos, son posteriores a las estimaciones geocronológicas más recientes para la apertura del Golfo de Vizcaya, que consideran que la rotación anti-horaria de Iberia tuvo lugar durante el Aptiense. El magmatismo debió desarrollarse en un contexto de corteza adelgazada, después de la rotación de Iberia y antes del inicio de la colisión alpina, en una etapa relativamente confusa desde el punto de vista tectónico.

Respecto a la cuestión candente de la cinemática de apertura del Golfo de Vizcaya, los datos obtenidos a partir del magmatismo parecen no estar de acuerdo con ninguno de los dos modelos clásicos propuestos: apertura en tijera (basado en anomalías magnéticas en el Atlántico y el Golfo de Vizcaya) vs. apertura de tipo "strike-slip" (basado en datos geológicos del Pirineo). Las variaciones en la petrología y geocronología de las rocas ígneas cretácicas a lo largo de la cadena pirenaica apoyan, en mayor medida, el modelo de apertura en tijera. Sin embargo, dicho modelo implica compresión en la región pirenaica o, alternativamente, extensión debida a un ascenso astenosférico. Cualquiera de estas dos posibilidades no parece factible atendiendo a los resultados del presente estudio puesto que el magmatismo post-data el evento de "rifting". Así, los datos obtenidos a partir del magmatismo sugieren la posibilidad de considerar un modelo alternativo. En esta línea, un desplazamiento en "strike-slip" seguido de una apertura en tijera con un polo de rotación situado al este, en lugar de al norte de Iberia, podría representar un escenario compatible con las características y la evolución del magmatismo cretácico. En cualquier caso, queda patente la necesidad de profundizar en el estudio para este contexto y edad; los datos aportados para el magmatismo contribuyen al debate a través de información actualizada sobre la geocronología y petrología de las rocas ígneas.

El magmatismo cretácico en las Cadenas Costero Catalanas septentrionales se ha datado de forma muy precisa por el método $^{40}Ar/^{39}Ar$ y tiene una edad restringida de ca. 79 Ma (Campaniense). Se trata por tanto, del magmatismo cretácico más joven en el noreste de Iberia. Dado que las intrusiones de lamprófido se consideran buenos marcadores de cambios en las condiciones geodinámicas, es razonable proponer una edad de 79 Ma como el momento de inicio del acortamiento alpino en el noreste de Iberia, que era confuso hasta la fecha.

## 8.3. Caracterización de la fuente

El magmatismo cretácico del noreste de Iberia comparte una fuente de manto común, dado que las concentraciones en elementos traza en muestras máficas y no cumulativas, así como las relaciones isotópicas de Sr-Nd-Pb en todas las muestras analizadas, son

comparables. Se han reconocido ligeras diferencias entre los distintos dominios en los que aflora el magmatismo, que sugieren que la fusión se produjo a menores tasas o en condiciones de mayor presión hacia el este. Las composiciones más evolucionadas pueden relacionarse con las composiciones máficas por cristalización fraccionada.

Las concentraciones en elementos incompatibles, significativamente enriquecidas respecto al manto primitivo, así como la presencia generalizada de fases hidratadas en las rocas, sugieren una fuente afectada por procesos metasomáticos. Es probable que minerales como el anfíbol y el apatito estuviesen presentes en la fuente como fases metasomáticas.

Las pautas de elementos traza normalizadas y las relaciones isotópicas de Sr-Nd-Pb revelan una mezcla entre componentes de tipo HIMU y EM en una fuente heterogénea. En detalle, el componente EM-1 pudo tener una relevancia mayor que el componente EM-2, aunque no se descarta la participación de éste último.

El manto relacionado con el magmatismo objeto de estudio fue probablemente de tipo astenosférico. Las pautas de tierras raras normalizadas muestran un alto grado de fraccionación, que sugiere que la fusión se produjo en la zona de estabilidad del granate. Además, las relaciones isotópicas Sr-Nd del magmatismo son más enriquecidas que aquellas de los macizos ultramáficos pirenaicos (e.g., Lherz), considerados representativos del manto litosférico de la región, lo cual apoya que el magmatismo estudiado tenga un origen más profundo. Por otro lado, las venas ricas en anfíbol que atraviesan los citados macizos ultramáficos pirenaicos han sido interpretadas como conductos de ascenso de los magmas alcalinos cretácicos. La composición isotópica y edad de estas venas es similar a la composición isotópica y edad obtenidas para el magmatismo, de forma que se refuerza la posible conexión genética entre ambos.

La signatura mantélica definida para el magmatismo cretácico en el noreste de Iberia se ha reconocido en magmatismos ibéricos más antiguos y más modernos, lo cual sugiere la presencia de un dominio de manto de estas características prevalente bajo Iberia desde el Pérmico hasta el Cuaternario. Las edades modelo calculadas para los magmatismos relacionados con esta fuente indican, de forma consistente, un evento de fraccionación del manto de edad precámbrica (Cadomiense).

## 8.4. El cortejo de lamprófidos cretácicos en las Cadenas Costero Catalanas. Poblaciones de cristales complejas e influencia de los antecristales en las composiciones de roca total

Se han reconocido al menos 8 intrusiones de camptonita dentro del cortejo de lamprófidos cretácicos de las Cadenas Costero Catalanas. Se trata de sills aislados, de potencia reducida (escala centimétrica a métrica) y composición máfica, que afloran en tres sectores: este (lamprófidos de Aiguablava y Calella de Palafrugell), centro (lamprófidos de S'Agaró y Llagostera) y oeste (lamprófidos del Molí d'en Ponç, Molí de Dalt y Monasterio de Sant Pere Cercada, además de al menos otra intrusión aguas arriba del Molí d'en Ponç, donde se han encontrado bloques sueltos de camptonita). Todas las intrusiones de lamprófido son sub-horizontales y fuertemente porfídicas, excepto el lamprófido de S'Agaró, que es sub-vertical y de textura microlítica.

Los lamprófidos porfídicos se componen de cristales grandes (macrocristales y en menor medida megacristales) en una mesostasia de tamaño cristalino fino, formada por microcristales y menores proporciones de vidrio. La acumulación gravitatoria de los macrocristales hacia las zonas inferiores de los sills, así como el desarrollo de bordes enfriados y alineaciones de vesículas paralelas a los contactos, producen una zonación vertical de las intrusiones muy bien definida.

Los macrocristales corresponden fundamentalmente a clinopiroxeno y anfíbol, aunque también hay minerales opacos y pseudomorfos de olivino. Presentan zonaciones centro-borde muy complejas y están compuestos fundamentalmente por antecristales en desequilibrio con el magma que los engloba. Los antecristales se formaron en profundidad, relacionados con etapas previas del sistema magmático, y fueron incorporados posteriormente en pulsos de magma que ascendían hacia los niveles de emplazamiento y que cristalizaron formando la mesostasia de los lamprófidos que reconocemos hoy en día. Los núcleos de tipo antecristal fueron, además, recrecidos por mantos de tipo fenocristal en equilibrio con el nuevo magma en el que fueron incorporados. De estos resultados se extrae la conclusión, importante, de que los cristales grandes en rocas porfídicas aparentemente sencillas, no tienen por qué ser fenocristales, por lo que resulta crucial evaluar las condiciones de equilibrio entre los minerales y el magma que los engloba.

Los lamprófidos estudiados muestran composiciones de roca total significativamente variables, a pesar de presentar composiciones de mesostasia homogéneas. Las muestras con concentraciones elevadas en MgO y elementos compatibles presentan también proporciones modales elevadas de antecristales máficos. Así, la acumulación de antecristales máficos en una roca modifica las composiciones de roca total haciéndolas más primitivas, tal y como se ha demostrado y cuantificado mediante el modelo

geoquímico y el análisis estadístico de la contribución de los antecristales a la composición global de la roca. Hay que tener en cuenta, por tanto, que aquellas muestras más enriquecidas en elementos compatibles no tienen por qué ser las más próximas a la composición de la fuente, sino que pueden representar fundidos relativamente evolucionados que han acumulado una cantidad significativa de antecristales máficos.

Dada la similitud petrológica y composicional entre la mesostasia de todos los lamprófidos porfídicos y también con el lamprófido microlítico, se deduce que un gran reservorio magmático común pudo proporcionar fundidos a todo el sistema de lamprófidos. Hipotéticamente, dicho reservorio pudo localizarse bajo el límite corteza-manto. Los antecristales más grandes (tamaño megacristal) se formarían en este reservorio o en niveles más profundos y algunos de ellos registrarían la entrada de un fundido primitivo recargando el reservorio. Estos antecristales se incorporarían en determinados pulsos de magma ascendentes hacia niveles superiores de la corteza. Durante su ascenso, estos magmas podrían incorporar, asimismo, antecristales de cámaras más evolucionadas y someras, relacionadas también con el sistema magmático. En detalle, algunos de los antecristales evolucionados registrarían entradas sucesivas de fundidos máficos provenientes del reservorio profundo, seguidas de procesos de mezcla con el fundido residente en las cámaras más evolucionadas y someras.

Como resultado del complejo sistema magmático en profundidad, los magmas ascendentes hacia niveles de emplazamiento someros portarían poblaciones heterogéneas de antecristales heredados, recrecidas por fenocristales formados en condiciones polibáricas durante el ascenso. Además, estos magmas experimentarían fraccionación durante el ascenso y emplazamiento, que se produciría a bajas profundidades y a favor de fracturas principalmente sub-horizontales. Teniendo en cuenta el reducido espesor de las intrusiones, el magma debió enfriarse y cristalizar de forma rápida. Se desarrollaron bordes enfriados en contacto con la roca encajante y la carga de macrocristales (fundamentalmente antecristales) se acumuló hacia las zonas inferiores por sedimentación gravitatoria, produciendo la zonación vertical que se observa en los sills. Se demuestra pues, que la acumulación gravitatoria de cristales es un proceso significativo en la generación, incluso a escala centimétrica, de zonación composicional en intrusiones ígneas.

Además de la caracterización del sistema y de los procesos magmáticos, el estudio del cortejo de lamprófidos cretácicos de las Cadenas Costero Catalanas ha demostrado que una comprensión detallada de los patrones de zonación mineral desvela procesos magmáticos que, de otra forma, permanecerían ocultos. Además, la acumulación de antecristales afecta significativamente las composiciones en roca total, por lo que es necesario realizar una cuidada evaluación petrográfica antes de considerar aquellas

muestras más enriquecidas en MgO y elementos compatibles como las más representativas de fundidos primitivos.

## 8.5. Coeficientes de reparto entre clinopiroxeno, anfíbol y fundidos camptoníticos

Por primera vez, se ha calculado un conjunto de coeficientes de reparto internamente consistentes para clinopiroxeno y anfíbol en fundidos de tipo lamprófido alcalino. Se han utilizado pares de equilibrio fenocristal-mesostasia y fenocristal-fenocristal en muestras naturales del cortejo de lamprófidos cretácicos de las Cadenas Costero Catalanas, y los resultados se han comprobado con modelos cristal-químicos.

Los coeficientes de reparto anfíbol-líquido son, en general, consistentes con los obtenidos en sistemas basálticos, en tanto que los coeficientes de reparto clinopiroxeno-líquido son ligeramente superiores a los obtenidos en sistemas basálticos. Comparados entre sí, clinopiroxeno y anfíbol muestran un reparto similar para la mayoría de elementos traza. En el caso de las tierras raras, la cristalización fraccionada de estos minerales produce un incremento en la concentración de tierras raras ligeras (LREE) y pesadas (HREE) en el fundido, en tanto que la concentración de tierras raras intermedias (MREE) se mantiene relativamente constante.

## 8.6. Enfoque multi-método

Además de las metodologías clásicas para el estudio de resultados geoquímicos, se han llevado a cabo modelos cuantitativos y un análisis de componentes principales (PCA) de las bases de datos composicionales.

La cuantificación del aporte composicional de los antecristales a la composición global de las rocas porfídicas mediante modelos geoquímicos ha probado la hipótesis de que las composiciones de roca total están significativamente influenciadas por la acumulación de antecristales y la variación composicional en roca total puede explicarse en base a la proporción modal y tipo de antecristales en la muestra. Dadas unas concentraciones en elementos traza en antecristales y en la muestra que los contiene, el modelo devuelve la composición global de la mesostasia de la muestra. Esta composición ha resultado muy útil para el estudio de la zonación composicional de cuerpos ígneos, así como para la determinación de las condiciones de equilibrio mineral-fundido y para el cálculo de coeficientes de reparto.

El análisis de componentes principales (PCA) es una herramienta con gran potencial para el estudio de bases de datos geoquímicos. Se trata de un método multivariante que evalúa las relaciones entre datos composicionales teniendo en cuenta todos los contenidos elementales de interés. Por tanto, mejora la evaluación bivariante clásica de los datos y permite realizar interpretaciones basadas en la similitud o diferencia global de los resultados y, por ende, de los procesos magmáticos que han actuado.

En lo relativo a la preparación de las muestras, se ha desarrollado un método muy sencillo, económico y eficaz para la separación óptica de granos de anfíbol de tipo kaersutita y granos de clinopiroxeno rico en magnesio, ya que estos minerales presentan propiedades físicas muy similares. Las aplicaciones potenciales podrían ser muy variadas y, en el presente proyecto de investigación, el método se ha utilizado para purificar separados minerales de anfíbol para experimentos $^{40}Ar/^{39}Ar$ con el fin de obtener la edad de las rocas.

# References

*River bed close to Molí d'en Ponç, northern Catalonian Coastal Ranges*

Adam, J., Green, T. (1994). The effects of pressure and temperature on the partitioning of Ti, Sr and REE between amphibole, clinopyroxene and basanitic melts. *Chemical Geology* 117, 219–233.

Adam, J., Green, T. (2006). Trace element partitioning between mica- and amphibole-bearing garnet lherzolite and hydrous basanitic melt: 1. Experimental results and the investigation of controls on partitioning behaviour. *Contributions to Mineralogy and Petrology* 152, 1–17.

Akinin, V.V., Sobolev, A.V., Ntaflos, T., Richter, W. (2005). Clinopyroxene megacrysts from Enmelen melanephelinitic volcanoes (Chukchi Peninsula, Russia): application to composition and evolution of mantle melts. *Contributions to Mineralogy and Petrology* 150, 85–101.

Albarède, F., Michard-Vitrac, A. (1978). Age and significance of the North Pyrenean metamorphism. *Earth and Planetary Science Letters* 40, 327–332.

Alibert, C. (1985). A Sr-Nd isotope and REE study of late Triassic dolerites from the Pyrenees (France) and the Messejana Dyke (Spain and Portugal). *Earth and Planetary Science Letters* 73, 81–90.

Allègre, C.L., Schiano, P., Lewin, E. (1995). Differences between oceanic basalts by multi-trace element ratio topology. *Earth and Planetary Science Letters* 129, 1–12.

Annen, C. (2011). Implications of incremental emplacement of magma bodies for magma differentiation, thermal aureole dimensions and plutonism–volcanism relationships. *Tectonophysics* 500, 3–10.

Aoki, K., Kushiro, I. (1968). Some clinopyroxenes from ultramafic inclusions in Dreiser Weiher, Eifel. *Contributions to Mineralogy and Petrology* 18, 326–337.

Araña, V., Aparicio, A., Martín-Escorza, C., Garcia-Cacho, L., Ortiz, R., Vaquer, R., Barberi, F., Ferrara, G., Albert, J., Gassiot, X. (1983). El volcanismo neógeno-cuaternario de Catalunya: caracteres estructurales, petrológicos y geodinámicos. *Acta Geológica Hispánica* 18, 1–17.

Ariskin, A.A., Konnikov, E.G., Kislov, E.V. (2003). Modelling of the equilibrium crystallization of ultramafic rocks with application to the problems of formation of phase layering in the Dovyren pluton, Northern Baikal region, Russia. *Geochemistry International* 41, 107–129.

Arranz, E., Lago, M. (2004). El plutonismo sin- y tardi-varisco en los Pirineos. In: Vera, J.A. (Ed.), *Geología de España*. SGE-IGME, Madrid, 263–266.

Arranz, E., Lago, M., Galé, C., Ubide, T., Pocoví, A., Larrea, P., Tierz, P. (2011). Eventos Tectono-Mágmaticos Alpinos en el Registro Geológico de los Pirineos: Inferencias sobre la Evolución del Manto Superior en una Zona Activa. *Revista de la Real Academia de Ciencias de Zaragoza* 66, 31–61.

Aulinas, M., Gimeno, D., Fernández-Turiel, J.L., Pérez-Torrado, F.J., Rodríguez-González, A., Gasperini, D. (2010). The Plio-Quaternary magmatic feeding system beneath Gran Canaria (Canary Islands, Spain): constraints from thermobarometric studies. *Journal of the Geological Society London* 167, 785–801.

Aulinas, M., Gisbert, G., Gimeno, D., Gasperini, D. (2013). Cannibalization of previous Na-rich clinopyroxenes by ascending basic magmas of the Garrotxa Volcanic Field (NE, Spain). *Mineralogical Magazine* 77 (5), 631.

Azambre, B., Fabriès, J. (1989). Mesozoic evolution of the upper mantle beneath the eastern Pyrenees: evidence from xenoliths in Triassic and Cretaceous alkaline volcanics of the eastern Corbières (France). *Tectonophysics* 170 (3–4), 213–230.

Azambre, B., Rossy, M. (1981). Caractère alcalin du magmatisme triasique des Corbières orientales. *Bulletin de la Société Géologique de France* 23 (3), 253–262.

Azambre, B., Rossy, M., Albarède, F. (1992). Petrology of the alkaline magmatism from the Cretaceous North-Pyrenean Rift Zone (France and Spain). *European Journal of Mineralogy* 4, 813–834.

Azambre, B., Rossy, M., Lago, M. (1987). Caractéristiques pétrologiques des dolérites tholéitiques d´âge triasique (ophites) du domaine pyrénéen. *Bulletin de Minéralogie* 110 (4), 379–396.

Bea, F., Fershtater, G.B., Montero, P., Smirnov, V.N., Molina, J.F. (2005). Deformation-driven differentiation of granitic magma: the Stepninsk pluton of the Uralides, Russia. *Lithos* 81, 209–233.

Beattie, P., Drake, M., Jones, J., Leeman, W., Longhi, J., McKay, G., Nielsen, R., Palme, H., Shaw, D., Takahashi, E., Watson, B. (1993). Terminology for trace-element partitioning. *Geochimica et Cosmochimica Acta* 57, 1605–1606.

Beaumont, C., Muñoz, J.A., Hamilton, J., Fullsack, P. (2000). Factors controlling the Alpine evolution of the central Pyrenees inferred from a comparison of observations and geodynamical models. *Journal of Geophysical Research – Solid Earth* 105 (B4), 8121–8145.

Bernard-Griffiths, J., Gruau, G., Cornen, G., Azambre, B., Macé, J. (1997). Continental lithospheric contribution to alkaline magmatism: isotopic (Nd, Sr, Pb) and geochemical (REE) evidence from Serra de Monchique and Mount Ormonde complexes. *Journal of Petrology* 38 (1), 115–132.

Béziat, D., Joron, J.L., Monchoux, P., Treuil, M., Walgenwitz, F. (1991). Geodynamic implications of geochemical data for the Pyrenean ophites (Spain-France). *Chemical Geology* 89 (3–4), 243–262.

Bianchini, G., Beccaluva, L., Bonadiman, C., Nowell, G., Pearson, G., Siena, F., Wilson, M. (2007). Evidence of diverse depletion and metasomatic events in harzburgite–lherzolite mantle xenoliths from the Iberian plate (Olot, NE Spain): Implications for lithosphere accretionary processes. *Lithos* 94, 25–45.

Bixel, F. (1988). Le volcanisme stéphano-permien des Pyrénées Atlantiques. *Bulletin Centre Recherches Exploration-Production Elf-Aquitaine* 12, 661–706.

Blundy, J., Wood, B. (1994). Prediction of crystal-melt partition coefficients from elastic moduli. *Nature* 372, 452–454.

Blundy, J., Wood, B. (2003). Partitioning of trace elements between crystals and melts. *Earth and Planetary Science Letters* 210, 383–397.

Bodinier, J.L., Fabriès, J., Lorand, J.P., Dostal, J., Dupuy, C. (1987). Geochemistry of amphibole pyroxenite veins from the Lherz and Freychinède ultramafic bodies (Ariège, French Pyrénées). *Bulletin de Minéralogie* 110, 345–358.

Bonin, B. (1988). From orogenic to anorogenic environments: evidence from associated magmatic episodes. *Schweizerische Mineralogische und Petrographische Mitteilungen* 68, 301–311.

Bottazzi, P., Tiepolo, M., Vannucci, R., Zanetti, A, Brumm, R., Foley, S.F., Oberti, R. (1999). Distinct site preferences for heavy and light REE in amphibole and the prediction of $^{Amph/L}D_{REE}$. *Contributions to Mineralogy and Petrology* 137, 36–45.

Brice, J.C. (1975). Some thermodynamic aspects of the growth of strained crystals. *Journal of Crystal Growth* 28, 249–253.

Brouxel, M. (1991). Geochemical consequences of flow differentiation in a multiple injection dyke (Trinity ophiolite, N. California). *Lithos* 26, 245–252.

Bullard, E.C., Everett, J.E., Smith, A.G. (1965). The fit of the continents around the Atlantic. *Philosophical Transactions of the Royal Society A* 258, 41–51.

Cabanis, B., Le Fur-Balouet, S. (1989). Les magmatismes stéphano-permiens des Pyrénées marqueurs de l´évolution géodynamique de la chaîne. *Bulletin Centre Recherches Exploration-Production Elf-Aquitaine* 13, 105–130.

Cabanis, B., Le Fur-Balouet, S. (1990). Le magmatisme crétacé des Pyrénées – Apport de la géochimie des éléments en traces – Conséquences chronologiques et géodynamiques. *Bulletin Centre Recherches Exploration-Production Elf-Aquitaine* 14 (1), 155–184.

Calderón, S., Cazurro, M., Fernández-Navarro, L. (1907). Memoria sobre las formaciones volcánicas de la Provincia de Gerona. *Memorias de la Real Sociedad Española de Historia Natural* IV 5, 159–489.

Carey, W.S. (1958). The orocline concept in Geotectonics. *Proceedings of the Royal Society of Tasmania* 89, 255–288.

Carracedo, M., Larrea, F.J., Sarrionandia, F., Jiménez, R. (2000). Estructura y organización de las coladas volcánicas submarinas: relación entre coladas tabulares y lavas almohadilladas cretácicas en la Cordillera Vasco-Cantábrica (País Vasco). *Revista de la Sociedad Geológica de España* 13 (1), 45–53.

Carracedo Sánchez, M., Sarrionandia, F., Juteau, T., Gil-Ibarguchi, J.I. (2012). Structure and organization of submarine basaltic flows: sheet flow transformation into pillow lavas in shallow submarine environments. *International Journal of Earth Sciences* 101, 2201–2214.

Castañares, L.M., Robles, S. (2004). El vulcanismo del Albiense-Santoniense en la Cuenca Vasco-Cantábrica. In: Vera, J.A. (Ed.), *Geología de España*. SGE-IGME, Madrid, 306–308.

Castañares, L.M., Robles, S., Gimeno, D., Vicente Bravo, J.C. (2001). The submarine volcanic system of the Errigoiti Formation (Albian-Santonian of the Basque-Cantabrian Basin, northern Spain): stratigraphic framework, facies, and sequences. *Journal of Sedimentary Research* 71 (2), 318–333.

Castañares, L.M., Robles, S., Vicente Bravo, J.C. (1997). Distribución estratigráfica de los episodios volcánicos submarinos del Albiense-Santoniense en la Cuenca Vasca (sector Gernika-Plentzia, Bizkaia). *Geogaceta* 22, 43–46.

Castro, A., Corretgé, L.G., De la Rosa, J., Enrique, P., Martínez, F.J., Lago, M., Arranz, E., Galé, C., Fernández, C., Donaire, T., López, S. (2002). Palaeozoic magmatism. In: Gibbons, W., Moreno, T. (Eds.), *The geology of Spain*. Geological Society, London, 117–154.

Cebriá, J.M., López-Ruiz, J., Doblas, M., Oyarzun, R., Hertogen, J., Benito, R. (2000). Geochemistry of the Quaternary alkali basalts of Garrotxa (NE Volcanic Province, Spain): a case of double enrichment of the mantle lithosphere. *Journal of Volcanology and Geothermal Research* 102, 217–235.

Charlier, B.L.A., Bachmann, O., Davidson, J.P., Dungan, M.A., Morgan, D.J. (2007). The upper crustal evolution of a large silicic magma body: evidence from crystal-scale Rb-Sr isotopic heterogeneities in the Fish Canyon magmatic system, Colorado. *Journal of Petrology* 48 (10), 1875–1894.

Charlier, B.L.A., Wilson, C.J.N., Lowenstern, J.B., Blake, S., Van Calsteren, P.W., Davidson, J.P. (2005). Magma generation at a large, hyperactive silicic volcano (Taupo, New Zealand) revealed by U–Th and U–Pb systematics in zircons. *Journal of Petrology* 46 (1), 3–32.

Cheng, Q., Bonham-Carter, G., Wang, W., Zhang, S., Li, W., Qinglin, X. (2011). A spatially weighted principal component analysis for multi-element geochemical data for mapping locations of felsic intrusions in the Gejiu mineral district of Yunnan, China. *Computers & Geosciences* 37, 662–669.

Chessex, R., Delaloye, M., Krummenacher, D., Vuagnat, M. (1965). Sur l'âge des roches granitiques de la région de Palamós-Palafrugell (Costa-Brava, Espagne). *Bulletin Suisse de Minéralogie et Pétrologie*, 15–17.

Chistyakova, S.Y., Latypov, R.M. (2009*a*). Fine-scale chemical zonation in small mafic dykes, Kestiö Island, SW Finland. *Geological Magazine* 146, 485–496.

Chistyakova, S.Y., Latypov, R.M. (2009*b*). Two independent processes responsible for compositional zonation in mafic dykes of the Åland-Åboland dyke swarm, Kestiö Island, SW Finland. *Lithos* 112, 382–396.

Chistyakova, S.Y., Latypov, R.M. (2010). On the development of internal chemical zonation in small mafic dykes. *Geological Magazine* 147, 1–12.

Choukroune, P. (1992). Tectonic evolution of the Pyrenees. *Annual Review of Earth and Planetary Sciences* 20, 143–158.

Cortés, J.A., Palma, J.L., Wilson, M. (2007). Deciphering magma mixing: The application of cluster analysis to the mineral chemistry of crystal populations. *Journal of Volcanology and Geothermal Research* 165, 163–188.

Cuevas, J., Garrote, A., Tubia, J.M. (1981). Análisis y significado de diferentes tipos de estructuras en el magmatismo del Cretácico superior de la cuenca Vasco-Cantábrica (1ª parte). *Munibe* 33 (1-2), 1–20.

Cuevas, J., Tubia, J.M. (1984). Análisis y significado de diferentes tipos de estructuras en el magmatismo del Cretácico superior de la cuenca Vasco-Cantábrica. *Munibe* 36, 93–97.

Dalpé, C., Baker, D.R. (2000). Experimental investigation of large-ion-lithophile-element-, high-field-strength-element- and rare-earth-element-partitioning between calcic amphibole and basaltic melt: the effects of pressure and oxygen fugacity. *Contributions to Mineralogy and Petrology* 140, 233–250.

Dautria, J.M., Liotard, J.M., Bosch, D., Alard, O. (2010). 160 Ma of sporadic basaltic activity on the Languedoc volcanic line (Southern France): A peculiar case of lithosphere-asthenosphere interplay. *Lithos* 120, 202–222.

Davidson, J.P., Morgan, D.J., Charlier, B.L.A., Harlou, R., Hora, J.M. (2007). Microsampling and isotopic analysis of igneous rocks: implications for the study of magmatic systems. *Annual Review of Earth and Planetary Sciences* 35, 273–311.

De Beni, E., Wijbrans, J.R., Branca, S., Coltelli, M., Groppelli, G. (2005). New results of $^{40}Ar/^{39}Ar$ dating constrain the timing of transition from fissure-type to central volcanism at Mount Etna (Italy). *Terra Nova* 17, 292–298.

Debon, F., Zimmermann, J.L. (1993). Mafic dykes from some plutons of the Western Pyrenean Axial Zone (France, Spain): markers of the transition from late-Variscan to early-Alpine events. *Schweizerische Mineralogische und Petrographische Mitteilungen* 73, 421–433.

Deer, W.A., Howie, R.A., Zussman, J. (1966). *An introduction to the rock-forming minerals*. Longman, London.

Demant, A., Suarez, M., De La Cruz, R., Bruguier, O. (2010). Early Cretaceous Surtseyan volcanoes of the Bano Nuevo Volcanic Complex (Aysen Basin, Eastern Central Patagonian Cordillera, Chile). *Geologica Acta* 8 (2), 207–219.

Downes, H. (2001). Formation and modification of the shallow sub-continental lithospheric mantle: a review of geochemical evidence from ultramafic xenolith suites and tectonically emplaced ultramafic massifs of western and central Europe. *Journal of Petrology* 42, 233–250.

Downes, H., Bodinier, J.L., Thirlwall, M.F., Lorand, J.P., Fabriès, J. (1991). REE and Sr-Nd isotopic geochemistry of Eastern Pyrenean Peridotite Massifs: sub-continental lithospheric mantle modified by continental magmatism. *Journal of Petrology*, Special Volume (2), 97–115.

Droop, G.T.R. (1987). A general equation for estimating $Fe^{3+}$ concentrations in ferromagnesian silicates and oxides from microprobe analyses, using stoichiometric criteria. *Mineralogical Magazine* 51, 431–435.

Dubois, P., Seguin, J.C. (1978). Les flyschs crétacé et éocène de la zone commingeoise et leur environnement. *Bulletin de la Société Géologique de France* 20 (5), 657–671.

Enrique, P. (1990). The Hercynian intrusive rocks of the Catalonian Coastal Ranges (NE Spain). *Acta Geológica Hispánica* 25 (1-2), 39–64.

Enrique, P. (2009). Las espesartitas, camptonitas y bostonitas del complejo intrusivo de Aiguablava (Cadenas Costeras Catalanas): cartografía y composición. *Geogaceta* 47, 125–128.

Faure, G. (1991). *Principles and applications of inorganic geochemistry*. Macmillan Inc., New Jersey.

Fernández-Mendiola, P.A., García-Mondéjar, J. (2003). Carbonate platform growth influenced by contemporaneous basaltic intrusión (Albian of Larrano, Spain). *Sedimentology* 50, 961–978.

Filleaudeau, P.Y., Mouthereau, F., Pik, R. (2011). Thermo-tectonic evolution of the south-central Pyrenees from rifting to orogeny: insights from detrital zircon U/Pb and (U-Th)/He thermochronometry. *Basin Research* 23, 1–17.

Fitzgerald, P.G., Muñoz, J.A., Coney, P.J., Baldwin, S.L. (1999). Asymmetric exhumation across the Pyrenean orogen: implications for the tectonic evolution of a collisional orogen. *Earth and Planetary Science Letters* 173, 157–170.

Foley, S.F., Jackson, S.E., Fryer, B.J., Greenough, J.D., Jenner, G.A. (1996). Trace element partition coefficients for clinopyroxene and phlogopite in an alkaline lamprophyre from Newfoundland by LAM-ICP-MS. *Geochimica et Cosmochimica Acta* 60, 629–638.

Forster, H.J., Davis, J.C., Tischendorf, G., Seltmann, R. (1999). Multivariate analyses of Erzgebirge granite and rhyolite composition: implications for classification of granites and their genetic relations. *Computers & Geosciences* 25 (5), 533–546.

Francalanci, L., Avanzinelli, R., Nardini, I., Tiepolo, M., Davidson, J.P., Vannucci, R. (2012). Crystal recycling in the steady-state system of the active Stromboli volcano: a 2.5-ka story inferred from in situ Sr-isotope and trace element data. *Contributions to Mineralogy and Petrology* 163, 109–131.

Francis, D., Minarik, W. (2008). Aluminum-dependent trace element partitioning in clinopyroxene. *Contributions to Mineralogy and Petrology* 156, 439–451.

Freeley, T.C., Wilson, L.F., Underwood, S.J. (2008). Distribution and compositions of magmatic inclusions in the Mount Helen dome, Lassen Volcanic Center, California: Insights into magma chamber processes. *Lithos* 106, 173–189.

Frenkel, M.Y., Yaroshevsky, A.A., Ariskin, A.A., Barmina, G.S., Koptev-Dvornikov, E.V., Kireev, B.S. (1989). Convective-cumulative model simulating the formation process for stratified intrusions. In: Bonin, N., Didier, J., Le Fort, P., Propach, G., Puga, E., Vistelius, A. B. (Eds.), *Magma-Crust Interactions and Evolution*. Theophrastus Publication, Athens, Greece, 3–88.

Frey, F.A., Green, D.H., Roy, S.D. (1978). Integrated models of basalt petrogenesis: a study of quartz tholeiites to olivine melilitites from south eastern Australia utilizing geochemical and experimental petrological data. *Journal of Petrology* 19, 463–513.

Fulmer, E.C., Nebel, O., van Westrenen, W. (2010). High-precision high field strength element partitioning between garnet, amphibole and alkaline melt from Kakanui, New Zealand. *Geochimica et Cosmochimica Acta* 74, 2741–2759.

Furman, T., Graham, D. (1999). Erosion of lithospheric mantle beneath the East African Rift system: geochemical evidence from the Kivu volcanic province. *Lithos* 48, 237–262.

Galán, G., Oliveras, V., Paterson, B.A. (2008). Types of metasomatism in mantle xenoliths enclosed in Neogene-Quaternary alkaline mafic lavas from Catalonia (NE Spain). In: Coltorti, M., Grégoire, M. (Eds.), *Metasomatism Oceanic and Continental Lithospheric Mantle*. Geological Society, London, Special Publications 293, 121–153.

Galé, C. (2005). *Evolución geoquímica, petrogenética y de condiciones geodinámicas de los magmatismos pérmicos en los sectores central y occidental del Pirineo*. PhD Thesis, Universidad de Zaragoza.

Galé, C., Arranz, E. (2001). Volcaniclastic Cretaceous magmatism in the Southern Pyrenees: preliminary age and source data. *Journal of Conference Abstracts EUG XI* 6 (1), 577.

Galé, C., Lago, M., Arranz, E. (2000). Petrología del magmatismo alcalino básico del sector de Denuy (Huesca). *Geotemas* 1, 245–249.

Gao, S., Luo, T.C., Zhang, B.R., Zhang, H.F., Han, Y.W., Zhao, Z.D., Hu, Y.K. (1998). Chemical composition of the continental crust as revealed by studies in East China. *Geochimica et Cosmochimica Acta* 62, 1959–1975.

García-Senz, J. (2002). *Cuencas extensivas del Cretácico inferior en los Pirineos centrales, formación y subsecuente inversión*. PhD Thesis, Universidad de Barcelona.

Garrido-Megías, A., Ríos-Aragüés, L.M. (1972). Síntesis geológica del Secundario y Terciario entre los ríos Cinca y Segre. *Boletín Geológico y Minero* 83, 1–47.

Gasperini, D., Gisbert, G., Gimeno, D., Aulinas, M., Macera, P., Bosch, D. (2013). Mantle source heterogeneity beneath the Garrotxa Volcanic Field (NE Spain). *Mineralogical Magazine* 77 (5), 1146.

Gee, J.S., Kent, D.V. (2007). Source of oceanic magnetic anomalies and the geomagnetic polarity timescale. In: Kono, M. (Ed.), *The Treatise on Geophysics 5: Geomagnetism*. Elsevier, Amsterdam, 455–507.

Gibb, F.G.F., Henderson, M.B. (1992). Convection and crystal settling in sills. *Contributions to Mineralogy and Petrology* 109, 358–545.

Gibb, F.G.F., Henderson, M.B. (2006). Chemistry of the Shiant Isles Main Sill, NW Scotland, and wider implications for the petrogenesis of mafic sills. *Journal of Petrology* 47, 191–230.

Gil-Imaz, A., Lago-San José, M., Galé, C., Pueyo-Anchuela, O., Ubide, T., Tierz, P., Oliva-Urcia, B. (2012). The Permian mafic dyke swarm of the Panticosa pluton (Pyrenean Axial Zone, Spain): simultaneous emplacement with the late-Variscan extension. *Journal of Structural Geology* 42, 171–183.

Gill, J., Reagan, M., Tepley, F., Malavassi, E. (2006). Arenal volcano, Costa Rica. Introduction. *Journal of Volcanology and Geothermal Research* 157, 1–8.

Gimeno, D. (2002). Estructura y mecanismos intrusivos de los lamprófidos de Sa Planassa – Punta d'Es Mut (Costa Brava, Cordillera Litoral Catalana): su interés didáctico. *Travalls del Museu de Geologia de Barcelona* 11, 105–133.

Gisbert, G., Gimeno, D., Aulinas, M., Fernández-Turiel, J.L., Gasperini, D., Hernández de la Cruz, A. (2011). Origin of green clinopyroxene cores of lavas from the Garrotxa Volcanic Field (Spain). *Macla* 15, 101–102.

Gisbert, G., Gimeno, D., Fernández-Turiel, J.L. (2009). Eruptive mechanisms of the Puig De La Garrinada volcano (Olot, Garrotxa volcanic field, Northeastern Spain): A methodological study based on proximal pyroclastic deposits. *Journal of Volcanology and Geothermal Research* 180, 259–276.

Golberg, J.M., Maluski, H., Leyreloup, A.F. (1986). Petrological and age relationship between emplacement of magmatic breccia, alkaline magmatism, and static metamorphism in the North Pyrenean Zone. *Tectonophysics* 129, 275–290.

Goldschmidt, V.M. (1937). The principles of distribution of chemical elements in minerals and rocks. *Journal of the Chemical Society London* 655, 655–673.

Gong, Z., Langereis, C.G., Mullender, T.A.T. (2008). The rotation of Iberia during the Aptian and the opening of the Bay of Biscay. *Earth and Planetary Science Letters* 273, 80–93.

Gong, Z., Van Hinsbergen, D.J.J., Vissers, R.L.M., Dekkers, M.J. (2009). Early Cretaceous syn-rotational extension in the Organyà basin — New constraints on the palinspastic position of Iberia during its rotation. *Tectonophysics* 473, 312–323.

Hammer, Ø., Harper, D.A.T., Ryan, P.D. (2001). PAST: Paleontological Statistics Software Package for Education and Data Analysis. *Palaeontologia Electronica* 4 (1), 9pp. http://palaeo-electronica.org/2001_1/past/issue1_01.htm

Harrison, T.M., McDougall, I. (1980). Investigations of an intrusive contact, northwest Nelson, New Zealand—II. Diffusion of radiogenic and excess $^{40}$Ar in hornblende revealed by $^{40}$Ar/$^{39}$Ar age spectrum analysis. *Geochimica et Cosmochimica Acta* 44 (12), 2005–2020.

Hart, S.R, Dunn, T. (1993). Experimental cpx/melt partitioning of 24 trace elements. *Contributions to Mineralogy and Petrogy* 113, 1–8.

Hauri, E.H., Wagner, T.P., Grove, T.L. (1994). Experimental and natural partitioning of Th, U, Pb and other trace elements between garnet, clinopyroxene and basaltic melts. *Chemical Geology* 117, 149–166.

Henry, P., Azambre, B., Montigny, R., Rossy, M., Stevenson, R.K. (1998). Late mantle evolution of the Pyrenean sub-continental lithospheric mantle in the light of new $^{40}$Ar–$^{39}$Ar and Sm–Nd ages on pyroxenites and peridotites (Pyrenees, France). *Tectonophysics* 296, 103–123.

Hildreth, W., Wilson, C.J.N. (2007). Compositional zoning of the Bishop Tuff. *Journal of Petrology* 48 (5), 951–999.

Hill, E., Blundy, J.D., Wood, B.J. (2011). Clinopyroxene–melt trace element partitioning and the development of a predictive model for HFSE and Sc. *Contributions to Mineralogy and Petrology* 161, 423–438.

Hofmann, A.W. (1988). Chemical differentiation of the Earth: The relationship between mantle, continental crust, and oceanic crust. *Earth and Planetary Science Letters* 90, 297–314.

Hofmann, A.W. (1997). Mantle geochemistry: the message from oceanic volcanism. *Nature* 385, 219–229.

Huppert, H.E., Sparks, R.S.J. (1980). Restrictions on the compositions of mid-ocean ridge basalts: a fluid dynamical investigation. *Nature* 286, 46–48.

Huppert, H.E., Sparks, R.S.J. (1989). Chilled margins in igneous rocks. *Earth and Planetary Science Letters* 92, 397–405.

Ijlst, L. (1973). Laboratory overflow-centrifuge for heavy liquid mineral separation. *American Mineralogist* 58, 1088–1093.

Ionov, D.A., Griffin, W.L., O'Reilly, S.Y. (1997). Volatile-bearing minerals and lithophile trace elements in the upper mantle. *Chemical Geology* 141, 153–184.

Irving, A.J., Frey, F.A. (1984). Trace element abundances in megacrysts and their host basalts: constraints on partition coefficients and megacryst genesis. *Geochimica et Cosmochimica Acta* 48, 1201–1221.

Jacobsen, S.B., Wasserburg, G.J. (1984). Sm-Nd evolution of chondrites and achondrites, *II. Earth and Planetary Science Letters* 67, 137–50.

Jaeger, J.C. (1968). Cooling and solidification of igneous rocks. In: Hess, H.H., Poldervaart, A. (Eds.), *Basalts: The Poldervaart treatise on rocks of basaltic compositions*. Wiley Interscience, New York, 503–536.

Jammes, S., Lavier, L., Manatschal, G. (2010). Extreme crustal thinning in the Bay of Biscay and the Western Pyrenees: From observations to modelling. *Geochemistry Geophysics Geosystems* 11.

Jammes, S., Manatschal, G., Lavier, L., Masini, E. (2009). Tectonosedimentary evolution related to extreme crustal thinning ahead of a propagating ocean: example of the western Pyrenees. *Tectonics* 28.

Janousek, V., Braithwaite, C.J.R., Bowes, D.R., Gerdes, A. (2004). Magma-mixing in the genesis of Hercynian calc-alkaline granitoids: an integrated petrographic and geochemical study of the Sázava intrusion, Central Bohemian Pluton, Czech Republic. *Lithos* 78, 67–99.

Jerram, D.A., Martin, V.M. (2008). Understanding crystal populations and their significance through the magma plumbing system. In: Annen, C., Zellmer, G.F. (Eds.), *Dynamics of crustal magma transfer, storage and differentiation*. Geological Society, London, Special Publications 304, 133–148.

Joliffe, I.T. (2002). *Principal Component Analysis, Second Ed*. Springer Series in Statistics, New York.

Juez-Larré, J., Andriessen, P.A.M. (2002). Post Late Paleozoic tectonism in the southern Catalan Coastal Ranges (NE Spain), assessed by apatite fission track analysis. *Tectonophysics* 349, 113–129.

Juez-Larré, J., Andriessen, P.A.M. (2006). Tectonothermal evolution of the northeastern margin of Iberia since the break-up of Pangea to present, revealed by low-temperature fission-track and (U–Th)/He thermochronology. A case history of the Catalan Coastal Ranges. *Earth and Planetary Science Letters* 243, 159–180.

Jurewicz, A., Watson, E.B. (1988). Cations in olivine, Part 1: Calcium partitioning and calcium-magnesium distribution between olivines and coexisting melts, with petrologic applications. *Contributions to Mineralogy and Petrology* 99, 176–185.

Koppers, A.A.P. (2002). ArArCALC-software for $^{40}Ar/^{39}Ar$ age calculations. *Computers & Geosciences* 28, 605–619.

Koppers, A.A.P., Staudigel, H., Wijbrans, J.R. (2000). Dating crystalline groundmass separates of altered Cretaceous seamount basalts by the $^{40}Ar/^{39}Ar$ incremental heating technique. *Chemical Geology* 166, 139–158.

Kretz, R., Hartree, R., Garrett, D. (1985). Petrology of the Grenville swarm of gabbro dikes, Canadian Precambrian Shield. *Canadian Journal of Earth Sciences* 22, 53–71.

Kuiper, K.F., Deino, A., Hilgen, F.J., Krijgsman, W., Renne, P.R., Wijbrans, J.R. (2008). Synchronizing rock clocks of earth history. *Science* 320, 500–504.

Kushiro, I. (2001). Partial melting experiments on peridotite and origin of Mid-Ocean Ridge Basalt. *Annual Reviews of Earth and Planetary Sciences* 29, 71–107.

Lagabrielle, Y., Bodinier, J.L. (2008). Submarine reworking of exhumed subcontinental mantle rocks: field evidence from the Lherz peridotites, French Pyrenees. *Terra Nova* 20, 11–21.

Lagabrielle, Y., Labaume, P., de Saint Blanquat, M. (2010). Mantle exhumation, crustal denudation, and gravity tectonics during Cretaceous rifting in the Pyrenean realm (SW Europe): Insights from the geological setting of the lherzolite bodies. *Tectonics* 29.

Lago, M., Arranz, E., Pocovi, A., Galé, C., Gil-Imaz, A. (2004*a*). Permian magmatism and basin dynamics in the Southern Pyrenees: a record of transition from late Variscan transtension to early Alpine extension. In: Wilson, M., Neumann, E.R., Davies, G.R., Timmerman, M.J., Heeremans, M. and Larsen, B.T. (Eds.), *Permo-Carboniferous magmatism and rifting in Europe*. Geological Society, London, Special Publications 223, 439–464.

Lago, M., Arranz, E., Pocovi, A., Galé, C., Gil-Imaz, A. (2004*b*). Lower Permian magmatism of the Iberian Chain, Central Spain, and its relationship to extensional tectonics. In: Wilson, M., Neumann, E.R., Davies, G.R., Timmerman, M.J., Heeremans, M. and Larsen, B.T. (Eds.), *Permo-Carboniferous magmatism and rifting in Europe*. Geological Society, London, Special Publications 223, 465–490.

Lago, M., De la Horra, R., Ubide, T., Galé, C., Galán-Abellán, B., Barrenechea, J.F., López-Gómez, J., Benito, M.I., Arche, A., Alonso-Azcárate, J., Luque, F.J., Timmerman, M.J. (2012). First report of a Middle-Upper Permian magmatism in the SE Iberian Ranges: characterisation and comparison with coeval magmatisms in the western Tethys. *Journal of Iberian Geology* 38 (2), 331–348.

Lago, M., Pocovi, A., Bastida, J., Arranz, E., Vaquer, R., Dumitrescu, R., Gil-Imaz, A., Lapuente, M.P. (1996). El magmatismo alcalino, Hettangiense, en el dominio nor-oriental de la Placa Ibérica. *Cuadernos de Geología Ibérica* 20, 109–138.

Lago San José, M., Galé Bornao, C., Arranz Yagüe, E., Gil Imaz, A., Pocovi Juan, A., Vaquer Navarro, R. (2000). The Triassic alkaline dolerites of the Valacloche-Camarena Area (SE-Iberian Chain, Teruel): Geodynamic implications. *Estudios Geológicos* 56, 211–228.

Larrea, P., França, Z., Lago, M., Widom, E., Galé, C., Ubide, T. (2013). Magmatic Processes and the Role of Antecrysts in the Genesis of Corvo Island (Azores Archipelago, Portugal). *Journal of Petrology* 54 (4), 769–793.

Larrea, P., Galé, C., Ubide, T., Widom, E., Lago, M., França, Z. (submitted). Magmatic evolution of Graciosa island (Azores, Portugal). *Journal of Petrology*.

LaTourrette, T., Hervig, R.L., Holloway, J.R. (1995). Trace element partitioning between amphibole, phlogopite, and basanite melt. *Earth and Planetary Science Letters* 135, 13–30.

Latypov, R.M. (2003*a*). The origin of marginal compositional reversals in basic-ultrabasic sills and layered intrusions by Soret fractionation. *Journal of Petrology* 44, 1579–1618.

Latypov, R.M. (2003*b*). The origin of basic-ultrabasic sills with S-, D- and I-shaped compositional profiles by in situ crystallization of a single input of phenocryst-poor parental magma. *Journal of Petrology* 44, 1619–1656.

Latypov, R. (2009). Testing the validity of the petrological hypothesis 'No phenocrysts, No post-emplacement differentiation'. *Journal of Petrology* 50 (6), 1047–1069.

Latypov, R., Chistyakova, S. (2009). Phase equilibria testing of a multiple pulse mechanism for origin of mafic–ultramafic intrusions: a case example of the Shiant Isles Main Sill, NW Scotland. *Geological Magazine* 146 (6), 851–875.

Latypov, R.M., Chistyakova, S.Y., Alapieti, T.T. (2007). Revisiting problem of chilled margins associated with marginal reversals in mafic–ultramafic intrusive bodies. *Lithos* 99, 178–206.

Latypov, R., Hanski, E., Lavrenchuk, A., Huhma, H., Havela, T. (2011). A'Three-Increase Model' for the origin of the marginal reversal of the Koitelainen Layered Intrusion, Finland. *Journal of Petrology* 52 (4), 733–764.

Le Bas, M.J., Le Maitre, R.W., Streckeisen, A., Zanettin, B. (1986). A chemical classification of volcanic rocks based on the total alkali–silica diagram. *Journal of Petrology* 27, 745–750.

Le Maitre, R.W. (Ed.) (2002). *Igneous Rocks. A Classification and Glossary of Terms*. Cambridge University Press, Cambridge.

Leake, B.E., Woolley, A.R., Arps, C.E.S., Birch, W.D., Gilbert, M.C., Grice, J.D., Hawthorne, F.C., Kato, A., Kisch, H.J., Krivovichev, V.G., Linthout, K., Laird, J., Mandarino, J.A., Maresch, W.V., Nickel, E.H., Rock, N.M.S., Schumacher, J.C., Smith, D.C., Stephenson, N.C.N., Ungaretti, L., Whittaker, E.J.W., Youzhi, G. (1997). Nomenclature of amphiboles: Report of the Subcommittee on Amphiboles of the International Mineralogical Association, Commission on New Minerals and Mineral Names. *American Mineralogist* 82, 1019–1037.

López-Moro, F.J., Murciego, A., López-Plaza, M. (2007). Silurian/Ordovician asymmetrical sill-like bodies from La Codosera syncline, W Spain: A case of tholeiitic partial melts emplaced in a single magma pulse and derived from a metasomatized mantle source. *Lithos* 96, 567–590.

Losantos, M., Montaner, J., Solà, J., Mató, E., Samsó, J.M., Picart, J., Calvet, F., Enrique, P., Ferrés, M., Solé, J. (2000). Mapa geològic de Catalunya 1:25000. *Palafrugell 335-1-1* (79–25). Institut Cartogràfic de Catalunya (Servei Geològic de Catalunya).

Losantos, M., Roqué, C., Pallí, L. (2004). Mapa geològic de Catalunya 1:25000. *Calella de Palafrugell 335-1-2* (76–26). Institut Cartogràfic de Catalunya (Servei Geològic de Catalunya).

Manhès, G., Minster, J.F., Allègre, C.J. (1987). Comparative U-Th-Pb and Rb-Sr study of the Saint Séverin amphoterite: consequence for early solar system chronology. *Earth and Planetary Science Letters* 39, 14–24.

Marsh, B.D. (2000). Magma chambers. In: Sigurdsson, H., Houghton, B., McNutt, S.R., Rymer, H., Stix, J. (Eds.), *Encyclopedia of Volcanoes*. Academic Press, San Diego, California, 191–206.

Marsh, B.D. (2013). On some fundamentals of igneous petrology. *Contributions to Mineralogy and Petrology* 166, 665–690.

Martel, C., Ali, A.R., Poussineau, S., Gourgaud, A., Pichavant, M. (2006). Basalt-inherited microlites in silicic magmas: Evidence from Mount Pelée (Martinique, French West Indies). *Geology* 34, 905–908.

Martínez González, R.M., Lago San José, M., Valenzuela Ríos, J.I., Vaquer Navarro, R., Salas, R., Dumitrescu, R. (1997). El volcanismo triásico y jurásico del sector SE de la Cadena Ibérica y su relación con los estadíos de rift mesozoicos. *Boletín Geológico y Minero* 108 (4-5), 367–376.

Matton, G., Jébrak, M. (2009). The Cretaceous Peri-Atlantic Alkaline Pulse (PAAP): Deep mantle plume origin or shallow lithospheric break-up? *Tectonophysics* 469, 1–12.

McClay, K., Muñoz, J.A., García-Senz, J. (2004). Extensional salt tectonics in a contractional orogen: A newly identified tectonic event in the Spanish Pyrenees. *Geology* 32, 737–740.

McCoy-West, A.J., Baker, J.A., Faure, K., Wysoczanski, R. (2010). Petrogenesis and origins of Mid-Cretaceous continental intraplate volcanism in Marlborough, New Zealand: Implications for the long-lived HIMU magmatic mega-province of the SW Pacific. *Journal of Petrology* 51, 2003–2045.

McDonough, W.F., Sun, S.S. (1995). The composition of the Earth. *Chemical Geology* 120, 223–253.

McDougall, I., Harrison, T.M. (1999). *Geochronology and Thermochronology by the $^{40}Ar/^{39}Ar$ Method*. Oxford University Press, New York.

McKenzie, D., O'Nions, R.K. (1991). Partial melt distributions from inversion of rare earth element concentrations. *Journal of Petrology* 32, 1021– 1091.

Mey, P.H.W. (1968). Geology of the Upper Ribargozana and Tor valleys, Central Pyrenees (Spain). *Leidse Geologische Mededelingen* 41, 229–292.

Montigny, R., Azambre, B., Rossy, M., Thuizat, R. (1982). Etude K / Ar du magmatisme basique lié au Trias supérieur des Pyrénées. Conséquences méthodologiques et paléogéographiques. *Bulletin de Minéralogie* 105, 673–680.

Montigny, R., Azambre, B., Rossy, M., Thuizat, R. (1986). K-Ar study of Cretaceous magmatism and metamorphism in the Pyrenees: age and length of rotation of the Iberian Peninsula. *Tectonophysics* 129, 257–273.

Morimoto, N., Fabries, J., Ferguson, A.K., Ginzburg, I.V., Ross, M., Seifert, F.A., Zussman, J., Aoki, K., Gottardi, G. (1988). Nomenclature of pyroxenes. *Mineralogical Magazine* 52, 535–550.

Mukasa, S.B., Shervais, J.W., Wilshire, H.G., Nielson, J.E. (1991). Intrinsic Nd, Pb, and Sr isotopic heterogeneities exhibited by the Lherz Alpine Peridotite Massif, French Pyrenees. *Journal of Petrology*, Special Volume (2), 117–134.

Muñoz, J.A. (1992). Evolution of a continental collision belt: ECORS-Pyrenees crustal balanced cross-section. In: McClay (Ed.), *Thrust Tectonics.* Chapman & Hall, London, 235–246.

Nakada, S., Motomura, Y. (1999). Petrology of the 1991–1995 eruption at Unzen: effusion pulsation and groundmass crystallization. *Journal of Volcanology and Geothermal Research* 89, 173–196.

Nimis, P. (1995). A clinopyroxene geobarometer for basaltic systems based on crystals-structure modeling. *Contributions to Mineralogy and Petrology* 121, 115–125.

Nimis, P., Taylor, W.R. (2000). Single clinopyroxene thermobarometry for gamet peridotites. Part 1: Calibration and testing of a Cr-in-cpx barometer and an enstatite-in-cpx thermometer. *Contributions to Mineralogy and Petrology* 139, 541–554.

O'Connor, J.M., Stoffers, P., Wijbrans, J.R., Worthington, T.J. (2007). Migration of widespread long-lived volcanism across the Galápagos Volcanic Province: Evidence for a broad hotspot melting anomaly?. *Earth and Planetary Science Letters* 263, 339–354.

Olin, P.H., Wolff, J.A. (2010). Rare earth and high field strength element partitioning between iron-rich clinopyroxenes and felsic liquids. *Contributions to Mineralogy and Petrology* 160, 761–775.

Oliva-Urcia, B., Casas, A.M., Soto, R., Villalaín, J.J., Kodama, K. (2011). A transtensional basin model for the Organyà basin (central southern Pyrenees) based on magnetic fabric and brittle structures. *Geophysical Journal International* 184, 111–130.

Olivet, J.L. (1996). La cinématique de la plaque Ibérique. *Bulletin Centre Recherches Exploration-Production Elf-Aquitaine* 20, 131–195.

Onuma, N., Higuchi, H., Wakita, H. (1968). Trace element partition between two pyroxenes and the host volcanic rocks. *Earth and Planetary Science Letters* 5, 47–51.

Orejana, D., Villaseca, C., Billström, K., Paterson, B.A. (2008). Petrogenesis of Permian alkaline lamprophyres and diabases from the Spanish Central System and their geodynamic context within western Europe. *Contributions to Mineralogy and Petrology* 156, 477–500.

Orejana, D., Villaseca, C., Paterson, B.A. (2004). Trace element partitioning in alkaline lamprophyres. *Geochimica et Cosmochimica Acta* 68 (Supp. 1).

Orejana, D., Villaseca, C., Paterson, B.A. (2007). Geochemistry of mafic phenocrysts from alkaline lamprophyres of the Spanish Central System: implications on crystal fractionation, magma mixing and xenoliths entrapment within deep magma chambers. *European Journal of Mineralogy* 19, 817–832.

Ortí, F., Vaquer, R. (1980). Volcanismo jurásico del sector valenciano de la Cordillera Ibérica. Distribución y trama estructural. *Acta Geológica Hispánica* XV (5), 127–130.

Pallí, L. (1980). *Mapa Geològic de Castell d'Aro – Platja d'Aro 1:10.000*. Col·legi Universitari de Girona.

Pallí, L., Roqué, C. (1990). *Mapa Geològic de Palafrugell 1:10.000*. Universitat Autònoma de Barcelona.

Pallí, L., Roqué, C. (1991). *Mapa Geològic de Begur 1:10.000*. Universitat Autònoma de Barcelona.

Pallí, L., Roqué, C. (1996). *Itinerari Geològic pel Camí de Ronda de S´Agaró*. Universitat de Girona.

Pallí, L., Roqué, C., Capellá, I. (1993). *Mapa Geològic de Sta. Coloma de Farners 1:10.000*. Universitat de Girona.

Pearce, J.A. (1983). Role of the sub-continental lithosphere in magma genesis at active continental margins. In: Hawkesworth, C.J., Norry, M.J. (Eds.), *Continental Basalts and Mantle Xenoliths*. Shiva Publishing Ltd., Cambridge, Mass., 230–249.

Peterson, R., Francis, D. (1977). The origin of sulfide inclusions in pyroxene megacrysts. *American Mineralogist* 62, 1049–1051.

Petrelli, M., Perugini, D., Poli, G. (2011). Transition to chaos and implications for time-scales of magma hybridization during mixing processes in magma chambers. *Lithos* 125, 211–220.

Pin, C., Bassin, C. (1992). Evaluation of a strontium-specific extraction chromatographic method for isotopic analysis in geological materials. *Analytica Chimica Acta* 269, 249–255.

Pin, C., Briot, D., Bassin, C., Poitrasson, F. (1994). Concomitant separation of strontium and samarium-neodymium for isotopic analysis in silicate samples, based on specific extraction chromatography. *Analytica Chimica Acta* 298, 209–217.

Pin, C., Santos-Zalduegui, J.F. (1997). Sequential separation of LREE, Th and U by miniaturized extraction chromatography: application to isotopic analyses of silicate rocks. *Analytica Chimica Acta* 339, 79–89.

Pirajno, F. (2010). Intracontinental strike-slip faults, associated magmatism, mineral systems and mantle dynamics: examples from NW China and Altay-Sayan (Siberia). *Journal of Geodynamics* 50 (3–4), 325–346.

Piromallo, C., Gasperini, D., Macera, P., Faccenna, C. (2008). A late Cretaceous contamination episode of the European–Mediterranean mantle. *Earth and Planetary Science Letters* 268, 15–27.

Poujol, M., Boulvais, P., Kosler, J. (2010). Regional-scale Cretaceous albitization in the Pyrenees: evidence from in situ U–Th–Pb dating of monazite, titanite and zircon. *Journal of the Geological Society London* 167, 751–767.

Puigdefàbregas, C., Souquet, P. (1986). Tecto-sedimentary cycles and depositional sequences of the Mesozoic and Tertiary from the Pyrenees. *Tectonophysics* 129, 173–203.

Putirka, K.D. (2008). Thermometers and barometers for volcanic systems. *Reviews in Mineralogy and Geochemistry* 69, 61–120.

Rayleigh, J.W.S. (1896). Theoretical considerations respecting the separation of gases by diffusion and similar processes. *Philosophical Magazine* 42, 77–107.

Renne, P.R., Deino, A.L., Hames, W.E., Heizler, M.T., Hemminge, S.R., Hodges, K.V., Koppers, A.A.P., Mark, D.F., Morgan, L.E., Phillips, D., Singer, B.S., Turrin, B.D., Villa, I.M., Villeneuvem, M., Wijbrans, J.R. (2009). Data reporting norms for $^{40}Ar/^{39}Ar$ geochronology. *Quaternary Geochronology* 4, 346–352.

Rhodes, J.M., Dungan, M.A., Blanchard, D.P., Long, P.E. (1979). Magma mixing at mid-ocean ridges: Evidence from basalts drilled near 228N on the Mid-Atlantic Ridge. *Tectonophysics* 55, 35–61.

Ridolfi, F., Renzulli, A. (2012). Calcic amphiboles in calc-alkaline and alkaline magmas: thermobarometric and chemometric empirical equations valid up to 1,130 ºC and 2.2 GPa. *Contributions to Mineralogy and Petrology* 163, 877–895.

Roberts, M.P., Pin, C., Clemens, J.D., Paquette, J.L. (2000). Petrogenesis of mafic to felsic plutonic rock associations: the calc-alkaline Quérigut complex, French Pyrenees. *Journal of Petrology* 41 (6), 809–844.

Rock, N.M.S. (1982). The Late Cretaceous Alkaline Igneous Province in the Iberian Peninsula, and its tectonic significance. *Lithos* 15, 111–131.

Rock, N.M.S. (1991). *Lamprophyres*. Blackie, Glasgow and London.

Roeder, P.L., Emslie, R.F. (1970). Olivine-liquid equilibrium. *Contributions to Mineralogy and Petrology* 29, 275–289.

Rollinson, H. (1993). *Using geochemical data: evaluation, presentation, interpretation*. Pearson Education Limited, Harlow (England).

Rosenbaum, G., Lister, G.S., Duboz, C. (2002). Relative motions of Africa, Iberia and Europe during Alpine orogeny. *Tectonophysics* 359, 117–129.

Rossi, P., Cocherie, A., Fanning, C.M., Ternet, Y. (2003). Datation U–Pb sur zircons des dolérites tholéiitiques pyrénéennes (ophites) à la limite Trias–Jurassique et relations avec les tufs volcaniques dits « infra-liasiques » nord-pyrénéens. *Comptes Rendus Geoscience* 335, 1071–1080.

Rossy, M., Azambre, B., Albarède, F. (1992). REE and Sr-Nd isotope geochemistry of the alkaline magmatism from the Cretaceous North Pyrenean Rift Zone (France-Spain). *Chemical Geology* 97 (1–2), 33–46.

Sakyi, P.A., Tanaka, R., Kobayashi, K., Nakamura, E. (2012). Inherited Pb isotopic records in olivine antecryst-hosted melt inclusions from Hawaiian lavas. *Geochimica et Cosmochimica Acta* 95, 169–195.

Salas, R., Casas, A. (1993). Mesozoic extensional tectonics, stratigraphy and crustal evolution during the Alpine cycle of the eastern Iberian basin. *Tectonophysics* 228, 33–55.

San Miguel Arribas, A. (1952). Observations pétrologiques sur les roches lamprophyriques de la Costa Brava Catalane (Bagur). *Congrès Géologique International Alger Comptes Rendus* 19 (6), 77–99.

San Miguel de la Cámara, M. (1930). Novedades sobre petrografía de Cataluña. *Memorias de la Real Academia de Ciencias y Artes de Barcelona* 12 (9). Barcelona.

San Miguel de la Cámara, M. (1936). Estudio de las rocas eruptivas de España. *Memorias de la Academia de Ciencias de Madrid* 6. Madrid.

Sanz, T., Lago, M., Gil, A., Galé, C., Ramajo, J., Ubide, T., Pocoví, A., Tierz, P., Larrea, P. (2013). The Upper Triassic alkaline magmatism in the NW Iberian Chain (Spain). *Journal of Iberian Geology* (in press).

Scarrow, J.H., Molina, J.F., Bea, F., Montero, P., Vaughan, A.P.M. (2011). Lamprophyre dikes as tectonic markers of late orogenic transtension timing and kinematics: A case study from the Central Iberian Zone. *Tectonics* 30.

Schärer, U., de Parseval, P., Polvé, M., de Saint Blanquat, M. (1999). Formation of the Trimouns talc-chlorite deposit (Pyrenees) from persistent hydrothermal activity between 112 and 97 Ma. *Terra Nova* 11, 30–37.

Schoeffler, J., Henry, J., Villanova J. (1964). État des travaux de cartographie géologique réalisés par la Société nationale des pétroles d'Aquitaine (SNPA) dans les Pyrénées occidentals. *Compte Rendu Sommaire des séances de la Société Géologique de France* 7, 241–246.

Shane, P., Smith, V.C. (2013). Using amphibole crystals to reconstruct magma storage temperatures and pressures for the post-caldera collapse volcanism at Okataina volcano. *Lithos* 156–159, 159–170.

Shannon, R.D. (1976). Revised effective ionic-radii and systematic studies of interatomic distances in halides and chalcogenides. *Acta Crystallographica* A 32, 751–767.

Shaw, C.S.J., Eyzaguirre, J. (2000). Origin of megacrysts in the mafic alkaline lavas of the West Eifel volcanic field, Germany. *Lithos* 50, 75–95.

Shervais, J.W. (1982). Ti–V plots and the petrogenesis of modern and ophiolitic lavas. *Earth and Planetary Sciences Letters* 59, 101–118.

Shirley, D.N. (1987). Differentiation and compaction in the Palisades sill. *Journal of Petrology* 28, 833–865.

Sibuet, J.C., Srivastava, S.P., Spakman, W. (2004). Pyrenean orogeny and plate kinematics. *Journal of Geophysical Research – Solid Earth* 109.

Solé, J., Pi, T., Enrique, P. (2003). New geochronological data on the late Cretaceous alkaline magmatism of the northeast Iberian Peninsula. *Cretaceous Research* 24, 135–140.

Srivastava, S.P., Sibuet, J.C., Cande, S., Roest, W.D., Reid, I.D. (2000). Magnetic evidence for slow seafloor spreading during the formation of the Newfoundland and Iberian margins. *Earth and Planetary Science Letters* 182, 61–76.

Steiger, R.H., Jäger, E. (1977). Subcommission on geochronology: convention on the use of decay constants in geo- and cosmochronology. *Earth and Planetary Science Letters* 36, 359–362.

Stormer, J. (1973). Calcium zoning in olivine and its relationship to silica activity and pressure. *Geochimica et Cosmochimica Acta* 27, 1815–1821.

Streck, M. (2008). Mineral textures and zoning as evidence for open system processes. *Reviews in Mineralogy and Geochemistry* 69, 595–622.

Sun, C., Liang, Y. (2012). Distribution of REE between clinopyroxene and basaltic melt along a mantle adiabat: effects of major element composition, water, and temperature. *Contributions to Mineralogy and Petrology* 163, 807–823.

Thirlwall, M.F. (1991). Long-term reproducibility of multicollector Sr and Nd isotope ratio analysis. *Chemical Geology* 94, 85–104.

Thompson, G.M., Malpas, J. (2000). Mineral/melt partition coefficients of oceanic alkali basalts determined on natural samples using laser ablation-inductively coupled plasma-mass spectrometry (LAM-ICP-MS). *Mineralogical Magazine* 64 (1), 85–94.

Tiepolo, M., Bottazzi, P., Foley, S.F., Oberti, R., Vannucci, R., Zanetti, A. (2001). Fractionation of Nb and Ta from Zr and Hf at mantle depths: the role of titanian pargasite and kaersutite. *Journal of Petrology* 42, 221–232.

Tiepolo, M., Vannucci, R., Bottazzi, P., Oberti, R., Zanetti, A., Foley, S. (2000). Partitioning of rare earth elements, Y, Th, U, and Pb between pargasite, kaersutite and basanite to trachyte melts: Implications for percolated and veined mantle. *Geochemistry Geophysics Geosystems* 1.

Tyson, R.M., Chang, L.L.Y. (1984). The petrology and sulfide mineralization of the Partridge River troctolite, Duluth Complex, Minnesota. *Canadian Mineralogist* 22, 23–38.

Ubide, T., Arranz, E., Galé, C., Lago, M. (2009). Variación vertical de la composición de un sill de lamprófido: influencia de fases xenocristalinas. *Macla* 11, 191-192.

Ubide, T., Arranz, E., Lago, M., Galé, C., Larrea, P. (2012*a*). The influence of crystal settling on the compositional zoning of a thin lamprophyre sill: A multi-method approach. *Lithos* 132-133, 37–49.

Ubide, T., Galé, C., Arranz, E., Lago, M. (2008). Composition of the Aiguablava camptonite sill (Costa Brava batholith). *Macla* 9, 349-350.

Ubide, T., Galé, C., Arranz, E., Lago, M., França, Z., Larrea, P., Tierz, P. (2011). Subduction-related signature in late-Variscan lamprophyres from the Catalonian Coastal Ranges (northeast Spain). *XXV IUGG General Assembly*, abstract #1924, 209.

Ubide, T., Galé, C., Arranz, E., Lago, M., Larrea, P. (under review *b*). Clinopyroxene and amphibole crystal populations in a lamprophyre sill: a record of magma history and a window to mineral-melt partitioning. *Lithos*.

Ubide, T., Galé, C., Arranz, E., Lago, M., Larrea, P., Tierz, P., Sanz, T. (2012*b*). Enriched mantle source for the Cretaceous alkaline lamprophyres from the Catalonian Coastal Ranges (NE Spain). *Mineralogical Magazine* 76 (6), 2475.

Ubide, T., Lago, M., Arranz, E., Galé, C., Larrea, P. (2010*b*). The lamprophyric sub-vertical dyke swarm from Aiguablava (Catalonian Coastal Ranges): petrology and composition. *Geogaceta* 49, 83–86.

Ubide, T., Van Elsas, R., Wijbrans, J.R., Arranz, E., Lago, M., Galé, C., Larrea, P. (2010*a*). A visual method for separating amphibole (kaersutite) and Mg-clinopyroxene. *Macla* 13, 217–218.

Ubide, T., Wijbrans, J.R., Galé, C., Arranz, E., Lago, M., Larrea, P. (under review *a*). Age of the Cretaceous alkaline magmatism in northeast Iberia: implications for the Alpine cycle in the Pyrenees. *Tectonics*.

Van der Voo, R. (1969). Paleomagnetic evidence for the rotation of the Iberian Peninsula. *Tectonophysics* 7, 5–56.

Velde, D., Tournon, J. (1970). La camptonite de San Feliu de Buxalleu (Province de Gérone, Espagne). *Bulletin de la Société Française de Minéralogie et de Cristallographie* 93, 482–487.

Veldkamp, A., Buis, E., Wijbrans, J.R., Olago, D.O., Boshoven, E.H., Marée, M., van den Berg van Saparoea, R.M. (2007). Late Cenozoic fluvial dynamics of the River Tana, Kenya, an uplift dominated record. *Quaternary Science Reviews* 26, 2897–2912.

Vergés, J., Fernández, M., Martínez, A. (2002). The Pyrenean orogen: pre-, syn-, and postcollisional evolution. *Journal of the Virtual Explorer* 8, 57–76.

Vissers, R.L.M., Meijer, P.Th. (2012*a*). Mesozoic rotation of Iberia: Subduction in the Pyrenees?. *Earth-Science Reviews* 110, 93–110.

Vissers, R.L.M., Meijer, P.Th. (2012*b*). Iberian plate kinematics and Alpine collision in the Pyrenees. *Earth-Science Reviews* 114, 61–83.

Vitrac-Michard, A., Albarède, F., Azambre, B. (1977). Age Rb-Sr et $^{39}$Ar-$^{40}$Ar de la syénite néphélinique de Fitou (Corbières orientales). *Bulletin de la Société Française de Minéralogie et de Cristallographie* 100, 251–254.

Vogel, T.A., Hidalgo, P.J., Patino, L.C., Tefend, K.S., Ehrlich, R. (2008). Evaluation of magma mixing and fractional crystallization using whole-rock chemical analyses: polytopic vector analyses. *Geochemistry Geophysics Geosystems* 9.

Walker, J.D., Geissman, J.W., compilers (2009). *Geologic Time Scale*. The Geological Society of America.

Walker Jr., B.A., Klemetti, E.W., Grunder, A.L., Dilles, J.H., Tepley, F.J., Giles, D. (2013). Crystal reaming during the assembly, maturation, and waning of an eleven-million-year crustal magma cycle: thermobarometry of the Aucanquilcha Volcanic Cluster. *Contributions to Mineralogy and Petrology* 165, 663–682.

Wasserburg, G.J., Jacobsen, S.B., DePaolo, D.J., McCulloch, M.T., Wen, T. (1981). Precise determination of Sm/Nd ratios, Sm and Nd isotopic abundances in standard solutions. *Geochimica et Cosmochimica Acta* 45, 2311–2323.

Wedepohl, K.H. (1995). The composition of the continental crust. *Geochimica et Cosmochimica Acta* 59, 1217–1232.

Whitchurch, A.L., Carter, A., Sinclair, H.D., Duller, R.A., Whittaker, A.C., Allen, P.A. (2011). Sediment routing system evolution within a diachronously uplifting orogen: insights from detrital zircon thermochronological analyses from the south-central Pyrenees. *American Journal of Science* 311, 442–482.

Whitney, D.L., Evans, B.W. (2010). Abbreviations for names of rock-forming minerals. *American Mineralogist* 95, 185–187.

Wijbrans, J.R., McDougall, I. (1988). Metamorphic evolution of the Attic Cycladic Metamorphic Belt on Naxos (Cyclades, Greece) utilizing $^{40}$Ar/$^{39}$Ar age spectrum measurements. *Journal of Metamorphic Geology* 6, 571–594.

Wijbrans, J., Németh, K., Martin, U., Balogh, K. (2007). $^{40}$Ar/$^{39}$Ar geochronology of Neogene phreatomagmatic volcanism in the western Pannonian Basin, Hungary. *Journal of Volcanology and Geothermal Research* 164, 193–204.

Wilson, M. (1989). *Igneous Petrogenesis. A Global Tectonic Approach*. Unwin Hyman, London.

Winchester, M.A., Floyd, P.A. (1977). Geochemical discrimination of different magma series and their differentiation products using inmobile elements. *Chemical Geology* 20, 325–343.

Winter, J.D. (2001). *An introduction to igneous and metamorphic petrology*. Prentice Hall, New Jersey.

Wood, B.J., Blundy, J.D. (1997). A predictive model for rare earth element partitioning between clinopyroxene and anhydrous silicate melt. *Contributions to Mineralogy and Petrology* 129, 166–181.

Woodhead, J. (1996). Extreme HIMU in an oceanic setting: the geochemistry of Mangaia Island (Polynesia), and temporal evolution of the Cook-Austral hotspot. *Journal of Volcanology and Geothermal Research* 72, 1–19.

Woodland, A.B., Jugo, P.J. (2007). A complex magmatic system beneath the Deves volcanic field, Massif Central, France: evidence from clinopyroxene megacrysts. *Contributions to Mineralogy and Petrology* 153 (6), 719–731.

Woolley, A.R., Bergman, S.C., Edgar, A.D., Le Bas, M.J., Mitchell, R.H., Rock, N.M.S., Scott Smith, B.H. (1996). Classification of lamprophyres, lamproites, kimberlites and the kalsilitic, melilitic

and leucitic rocks: recommendations of the IUGS Subcommission on the Systematics of Igneous Rocks. *The Canadian Mineralogist* 34, 175–186.

Wyllie, P.J. (1981). Plate tectonics and magma genesis. *International Journal of Earth Sciences* 70, 128–153.

Yao, L., Sun, C., Liang, Y. (2012). A parameterized model for REE distribution between low-Ca pyroxene and basaltic melts with applications to REE partitioning in low-Ca pyroxene along a mantle adiabat and during pyroxenite-derived melt and peridotite interaction. *Contributions to Mineralogy and Petrology* 164, 261–280.

Ziegler, P.A., Cloetingh, S. (2004). Dynamic processes controlling evolution of rifted basins. *Earth-Science Reviews* 64, 1-50.

Zindler, A., Hart, S.R. (1986). Chemical geodynamics. *Annual Review in Earth and Planetary Sciences* 14, 493–571.

# Electronic supplement

Supplementary files for this PhD Thesis can be obtained on request to the author (teresaubide@gmail.com) and include the PDF file of this PhD dissertation and the following auxiliary material:

- Chapter 3: full $^{40}Ar/^{39}Ar$ data results.

- Chapter 4: detailed mineral assemblages and crystallisation sequences for all of the rock types.

- Chapter 5: electron microprobe results and structural formulae for clinopyroxene (Table 5.I), amphibole (Table 5.II), feldspars (Table 5.III), spinel (Table 5.IV), ilmenite (Table 5.V), olivine (Table 5.VI), biotite (Table 5.VII), analcime (Table 5.VIII) and apatite (Table 5.IX). LA-ICP-MS results for clinopyroxene and amphibole (Table 5.X).

- Chapter 6: principal component analysis results for mineral together with whole-rock data (Table 6.I).

- Chapter 7: electron microprobe results, structural formulae and calculations of pressure, temperature and water content in the melt in equilibrium for clinopyroxene (Table 7.I) and amphibole (Table 7.II). Principal component analysis results for clinopyroxene (Table 7.III) and amphibole (Table 7.IV).

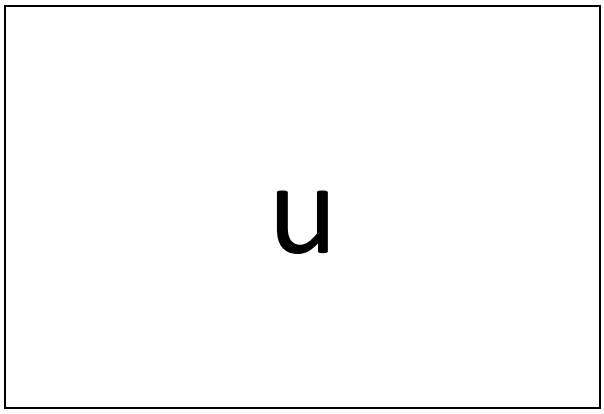


*¿Cómo desarrollo una Tesis Doctoral?*

Adaptado de un jeroglífico de Pedro Ocón de Oro